Physical Modelling and the Associated Acoustic Behaviour of Trumpets and Trombones

by

Janelle Resch

A thesis
presented to the University of Waterloo
in fulfillment of the
thesis requirement for the degree of
Doctor of Philosophy
in
Applied Mathematics

Waterloo, Ontario, Canada, 2019

Examining Committee Membership

The following served on the Examining Committee for this thesis. The decision of the Examining Committee is by majority vote.

Supervisor(s):	Lilia Krivodonova
	Professor, Applied Mathematics, University of Waterloo.
	John Vanderkooy
	Professor, Physics & Astronomy, University of Waterloo.
Internal Member(s):	Michael Waite
	Professor, Applied Mathematics, University of Waterloo.
	Francis Poulin
	Professor, Applied Mathematics, University of Waterloo.
Internal-External Member:	Christopher Batty
	Professor, Computer Science, University of Waterloo.
External-External Member:	Chris Waltham
	Professor, Physics & Astronomy, University of British Columbia.

Author's Declaration

I hereby declare that I am the sole author of this thesis. This is a true copy of the thesis, including any required final revisions, as accepted by my examiners.

I understand that my thesis may be made electronically available to the public.

Abstract

Accurately modelling the production of realistic musical notes in brass instruments is no easy task. Compared to woodwind instruments, brass instruments are considerably longer and constructed with bends, valves or coils, a mouthpiece with a cup rather than a reed or double-reed, as well as a large flare. Mathematically, this means that the sound wave propagation through the instrument could exhibit various nonlinear behaviours that are not examined within the field of linear acoustics. In this thesis, we attempt to accurately model the timbre of musical notes produced on the trumpet and trombone and study the associated acoustic behaviours of both instruments. To accomplish this, we investigate the relevance of the interaction between the player and instrument to ensure the problem is computationally reasonable, as we need to decipher what aspects and parameters can be neglected, and which are essential to consider. This was done through a series of physical experiments and numerical studies, which also provided verification of previous claims and findings published in the literature. Ultimately, we determined there are factors more essential to incorporate over modelling vibroacoustic and thermoviscous effects. We therefore focus on these components and model the nonlinear wave propagation through the instruments in the time-domain using the compressible Euler equations, and numerically solve the system via the discontinuous Galerkin method. Several musical notes played at various dynamic levels are simulated. The numerical solutions are compared against the measured data to evaluate how well the timbre of the different musical tones can be recreated. Although several simplifying assumptions were made, we found that our model produces the most accurate results compared to previous findings. Furthermore, to our knowledge, we are the first to numerically reproduce (from real data) the production of shock waves in the trombone, thereby theoretically and numerically verifying the experimental work published by Hirschberg *et al.* in 1996 (https://doi.org/10.1121/1.414698).

Acknowledgements

Firstly, I want to thank my supervisors, Lilia Krivodonova and John Vanderkooy, for all your guidance and patience. Lilia, I thank you for making me a stronger woman and writer in this field. Having you as a female role model has been very inspiring to me. John, I especially want to thank you for all the additional feedback and help (both scientific and emotional) you have provided me over the last year. It is greatly appreciated and has kept me motivated to see this through to the end. Thanks also to my PhD committee members, Mike Waite and Francis Poulin, for all your discussions and support. You went above and beyond your roles as committee members and I am very grateful. Thanks also to the internal and external examiners, Christopher Batty and Chris Waltham, for all your valuable feedback and for taking part in my defense.

Secondly, I want to give a special thank you to my mentor, Conrad Hewitt, for the countless discussions and positive support that you have provided me over the years. Whenever things were tough or when I needed guidance, I have always been able to count on you. Also, to Francine Vinette and Michael Barnett-Cowan, thank so much for all your guidance, openness and kindness. It is greatly cherished.

Thirdly, I need to thank all my classmates, who I have to say, are some of the most positive and supportive people. From what I have heard from others completing their post-secondary degrees, it is not uncommon for peers to be cold due to competitiveness. I am very grateful for the supportive atmosphere you all created. I especially want to thank my office mate, Andrew Giuliani, for all the computing and emotional support. Thanks Andrew for constantly answering questions, sending me positive text messages, and teaching me how to debug (most valuable day ever)! Also, thank you Kevin Church for all your help both in and out of class. Without you, I don't know how I would have been able to function or travel between Waterloo and London. To Nathan Zavaglia and Jenny Kang, thank you for your discussions and positive energy. Last, but certainly not least, I especially want to thank my core support network:

To my partner in life and science, Eric Ocelewski: For all your love, support, amazing cups of tea, and encouragement as you fought for your own life during these last few years.

To my brother, Corbin Resch: For always having a funny story, listening to my math rants, sensing when I was upset, and for you and Devin giving me a safe haven for writing.

To my nephew and niece, Oliver and Vivianne Resch: For continually giving me perspective and motivation through your innocent exploration of the world, adorable smiles, and hugs.

To my purple sister, Keehan Koorn: For always making me laugh, feel confident in my abilities, being there for me, and being so patient as I wrote this PhD!

Dedication

In loving memory of my Grandmother, *Dorothy Benson.*
My information will always love and cherish your information.
May you rest in peace, Grandma.

November 12, 1922 - May 5, 2019.

Table of Contents

List of Tables

List of Figures

Nomenclature

a - acceleration [m/s^2]

A - area [m^2]

c - speed of sound [m/s]

c_p - specific heat at constant pressure [J/kg·K]

c_v - specific heat at constant volume [J/kg·K]

d_v - viscous boundary layer thickness [m]

d_t - thermal boundary layer thickness [m]

E - energy [J]

f - frequency [Hz]

f_i - the i$^{\text{th}}$ harmonic [Hz]

f_s - sampling frequency [Hz]

$\frac{f_s}{2}$ - Nyquist frequency [Hz]

$\vec{F}$ - force [J]

$F(t)$ - force source term

I_a - acoustic intensity [W/m^2]

k - wave number

L_{thermal} - thermal loss per unit area

L_{viscous} - viscous loss per unit area

m_d - effective mass [kg]

n - number of moles of gas

p - pressure [Pa]

p_0 - atmospheric pressure [Pa]

p_i - incident pressure [Pa]

p_r - reflected pressure [Pa]

p_t - transmitted pressure [Pa]

P - power [W]

P_{lost} - power lost [W]

q - relative power loss

Q_w - source strength

$Q(t)$ - mass source term [kg/s]

r - radius [m]

$R(f)$ - reflection coefficient

s - displacement [m]

S - entropy [J/K]

t - time [s]

T - temperature [K]

$T(f)$ - transmission coefficient

u - velocity in x direction [m/s]

U - volume flow [m^3/s]

$\mathbf{U}$ - vector of conservative variables

v - velocity in y direction [m/s]

V - volume [m^3]

w - velocity in z direction [m/s]

x_s - shock distance [m]

α - loss factor

$\alpha_t = \frac{\kappa}{\rho c_p}$ - thermal diffusivity [m^2/s]

$\gamma = \frac{c_p}{c_v}$ - specific heat ratio

η - bulk modulus [Pa·s]

κ - thermal conductivity [W/m·K]

μ - dynamic viscosity [Pa· s]

$\nu = \frac{\mu}{\rho}$ - kinematic viscosity [m^2/s]

ρ - density of medium [kg/m^3]

τ - simulation time

ϕ - phase angle

$\omega = 2\pi f$ - angular frequency [Hz]

Ω - computational domain

$\partial\Omega$ - computational boundary

$\mathcal{A}$ - volume acceleration

$\mathcal{C}_{\pm}$ - characteristic curves

$\mathbb{L}_2$ - L_2 norm

$\mathcal{P}$ - Fourier transform of pressure

$\mathcal{P}_i$ - Fourier transform of incident pressure

$\mathcal{P}_r$ - Fourier transform of reflected pressure

$\mathcal{P}_t$ - Fourier transform of transmitted pressure

$\mathcal{R}$ - universal gas constant

$\mathcal{R}_{\pm}$ - Riemann invariant

$\mathcal{U}$ - Fourier transform of velocity

BC - boundary condition

DG - discontinuous Galerkin

MSM - machine shop measurements

RIBC - Riemann invariant boundary condition

rms - root mean square

SPL - sound pressure level

Chapter 1

Introduction

Each musical instrument has its own tonal character or sound quality. This is referred to as the *timbre* of the sound and is a psychoacoustic phenomenon that is measurable via the spectral envelope of the sound wave. The spectral envelope describes how the produced sound energy of the wave profile is distributed amongst the harmonic components [190]. Although instruments of the same category (e.g., woodwinds, brass, string, percussion, etc.) have similar tonal qualities, each instrument has its own distinguishable timbre. Brass instruments for instance are usually characterized as 'brassy' or 'bright' where the brassiness is dependent on the dynamic level (i.e., the volume) of the played sound. In particular, when the pressure disturbance entering the horn is a significant fraction of atmospheric pressure[1], it will undergo nonlinear wave steepening as it travels along the bore[2]. This excites the higher harmonic components and produces a brassier sound. Assuming the bore is long enough and the pressure amplitude is large enough, it is also possible for shock waves to develop within the instrument [38], [99], [132], [180], [190], [192]. This has been experimentally observed for the trombone by Hirschberg *et al.* in [99].

Modelling the state of a musical instrument during play, i.e., simulating realistic musical notes, is equivalent to recreating the timbre produced by the vibrating air-column [190]. However, this is a challenging and computationally intensive problem. To accomplish such a task, the factors that influence timbre must first be understood. There are several aspects that contribute to creating specific timbres, such as the player or the dynamic level and thus, the shape of the pressure profile entering the horn [99]. Some claim that the timbre

[1] Where an atmosphere, or 1 atm for short, is 101325 Pa.

[2] The terms 'bore', 'horn', 'air-column', and 'tubing' are used interchangeably in acoustics literature [30].

is also affected by the thermoviscous losses [38], [94], as well as the vibroacoustics of the flare [109], [113]. The most significant factor however is the geometry of the bore, as it will accentuate or attenuate certain spectral components of the propagating sound waves [38], [99], [132], [180], [190], [192].

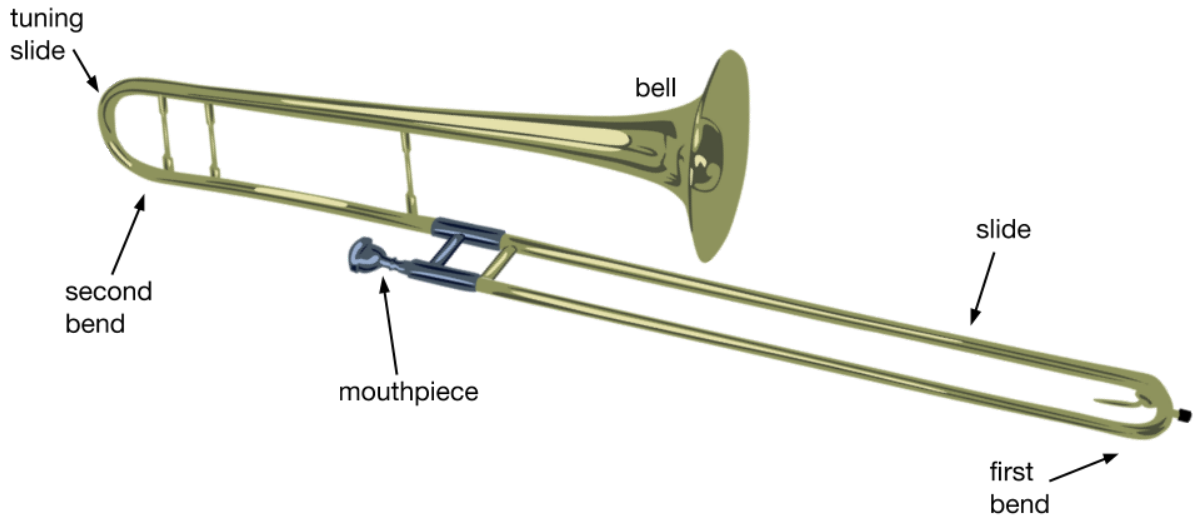

Figure 1.1: An image of the trombone with some of its parts labelled.

Generally speaking, the purpose of this thesis is to experimentally and numerically study the acoustics of sound production and propagation within brass instruments, and then attempt to model the wave propagation of realistic musical notes produced on the trumpet and trombone[3]. An image of these instruments with some of their parts labelled are shown in Figures 1.1 and 1.2[4]. The problem will be approached through an aeroacoustical perspective, i.e., by examining the interaction between the acoustic field and gasdynamic flow induced vibrations. Ideally, aeroacoustic simulations would be formulated in the time-domain where the full compressible Navier-Stokes equations would be numerically solved. This would include coupling the three-dimensional (3D) system to the thin boundary layers near the walls, the oscillating lip behaviour and the vibroacoustic wall effects [159], [113]. A subset of the fluid solution would be the acoustic sound pressure waves. Implementing all such aspects of the problem however would be difficult [159]. Therefore, this thesis also aims to determine the necessary physical components needed to formulate a reasonable model that describes the sound propagation and radiation. An

[3] Specifically, the sound pressure waves of notes that were measured in the lab.

[4] The trumpet and trombone shapes were obtained from https://www.shutterstock.com.

overview on the acoustics of brass instruments will first be given.

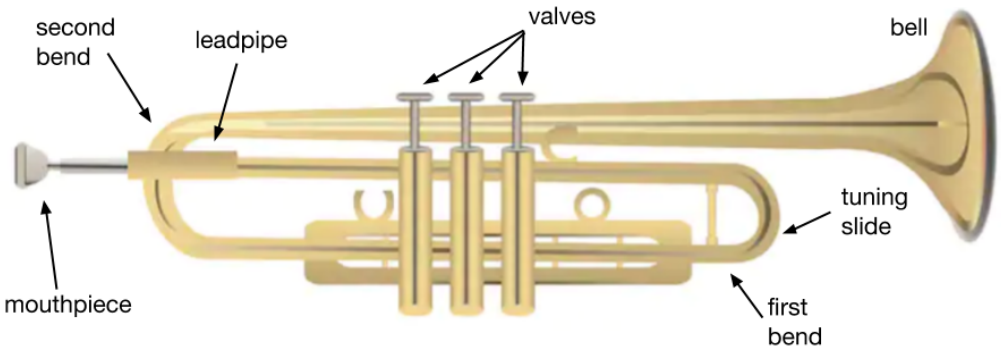

Figure 1.2: An image of the trumpet with some of its parts labelled.

1.1 Sound Production in Brass Instruments

When a musician produces a musical tone on a brass instrument, the lungs act as a source of constant pressure. The air travels to the pressure control valve, which is the coupling of the lips to the instrument. More precisely, the tubing of the instrument can be thought of as the *acoustic resonator*, whereas the lips act as a *mechanical valve* controlling the airflow into the mouthpiece [66][5]. The flow progressing into the instrument is modulated by the opening and closing of the lips [47], [66]. The dynamics of the lips can be described as a double mass system that is coupled by the player's embouchure (muscles in the mouth) where the corresponding restoring force would be some nonlinear function. To a first approximation, the dynamic properties of the lips may be deduced by considering the idealization of a mass, spring, damper system [1], [2], [54].

As the oscillatory pressure disturbance travels through the horn, in reality, it undergoes attenuation. However, the majority of energy dissipation from thermoviscous effects occurs within the thin boundary layers near the walls of the instrument. The thickness of the boundary layer is proportional to $\frac{1}{\sqrt{f}}$ where f is frequency, which implies losses are frequency dependent [38], [180]. Once the pressure waveform approaches the expanding flare region, a portion of the sound energy will either be reflected with a change of sign or

[5] The flow of air is able to enter the bore because of the static overpressure in the player's mouth [47]. It has been reported in [54] and [68] that the steady pressure in the mouth for a brass instrument is approximately 3 kPa - 13 kPa.

transmitted. The reflected waves will then interact with the forward moving ones. This forms a standing wave pattern with amplitude ratios that depend on the relative strength of the reflections from the bell region [20]. A steady note would then be heard radiating from the bore due to the self-sustained oscillations of the instruments. Mathematically, this can be thought of as the acoustic system being in steady state. A schematic of the process is shown in Figure 1.3.

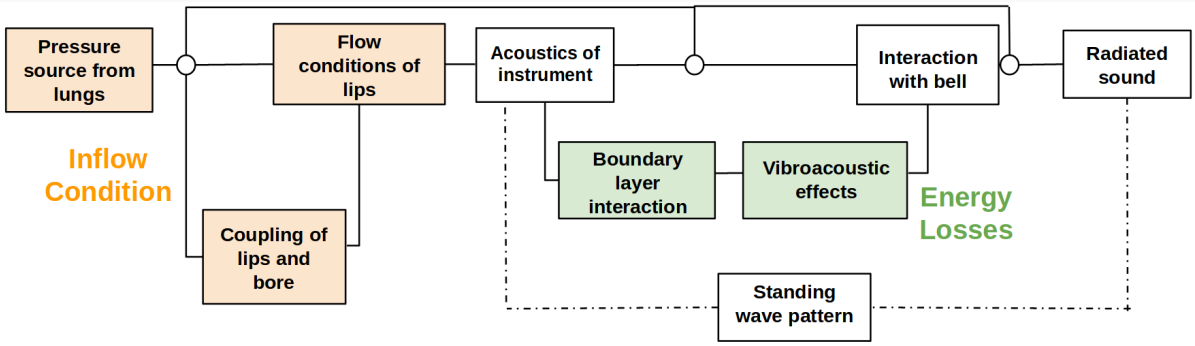

Figure 1.3: A schematic outlining sound production and propagation in brass instruments.

1.1.1 The Coupling of the Lips to the Bore

Several experiments to better understand the lip motion cycles have already been conducted. These experiments obtained measurements of the area and height of the lips as well as the upper lip trajectories using stroboscopes (e.g., [31], [45], [202], [225]). In [45] for instance, it was found that for quiet notes, the aperture height (i.e., how much the lips opened) reached a maximum of approximately 2.6 mm, whereas for the loud notes, the maximum height was near 4.5 mm. Although the mathematical description of the nonlinear coupling between the lips and mouthpiece is still under investigation, some experiments have been conducted to better understand the mechanism. In general, experiments have indicated the following properties regarding the lip motion and corresponding pressure waveforms produced in the mouthpiece [54]:

i. The lower the pitch, the less sinusoidal the produced time pressure waveform will be. This is due to the large amplitude of the lip vibrations.

ii. The amplitude of vibration is larger for lower pitch notes.

iii. The lip motion is practically sinusoidal.

iv. The lips close once every cycle for the pitch produced.

We have not independently conducted experiments to verify the third and fourth property, however we present our own experimental findings in Section 2.3 confirming the first two claims. From reviewing the experimental evidence for claims (iii) and (iv) presented in [31], [54], [202], [225], and discussing these ideas with our brass instrument playing colleagues, claims (iii) and (iv) will be assumed a posteriori. These assumptions will be of great benefit in developing a mathematical model to describe realistic sound wave propagation, as simplifying assumptions can be drawn from such observations. In particular, if a quasi-steady state is simulated then the coupling of the bore to the lips represents the input pressure and velocity source and so, this coupling can be neglected. Others have also taken this approach (e.g., [161], [184], [185], [188], [204])[6]. Therefore, a sinusoidal input representing the airflow being injected into the system can be considered at a periodic rate that corresponds to the fundamental frequency of the musical note being simulated.

1.1.2 The Geometry of the Instrument

Often in the literature, the tubing before the bell of the trumpet or trombone is assumed to be a uniform cylindrical tube, especially if the mathematical description of sound wave propagation is reduced to two dimensions or even one dimension (e.g., [25], [58], [140], [160], [184], [215]). This assumption is a natural starting point to model a brass instrument since finite-amplitude standing waves and acoustic wave propagation in uniform cylindrical tubes have been studied for quite some time. Some of the initial work was done by Weiner [216]. He examined the consequences of nonlinear wave propagation in air-columns such as wave steepening and the formation of shock waves. Further discussions can be found in [104] and [179]. But as we will see in Section 5.5, neglecting the changes in radius of the tubing leading up to the flare, especially near the mouthpiece end, greatly influences the wave motion. Properly modelling these regions is necessary to obtain accurate numerical simulations. Additionally, in Section 5.6 we numerically demonstrate that considering the bends does not greatly influence the sound wave propagation. We suspect this is partly because the cross-sectional area of the tubing is constant through the trumpet and trombone bends, and the bend radius is much less than the wavelengths of the played notes.

The flare expansion also plays a crucial role in producing the timbre associated with brass instruments. One of the most significant properties of the bell is how it influences

[6] In addition, the sound emission process is not influenced by the distant far-field but rather, by the motion of the oscillating lips relative to the mean flow. According to [85], this implies that the source can be considered stationary relative to the surroundings.

the reflections of the sound pressure waves [66], [179], [183], [184]. The location at which the harmonic waves reflect in the bell is dependent on their frequency. The acoustic discontinuity at the bell reflects the lower frequencies whose wavelengths are considerably larger than the bell diameter, whereas higher frequencies propagate out of the bell [20], [210]. The smooth transition of the harmonic waves that are reflected versus transmitted from the flare is referred to as the *cutoff frequency* of the bell [210]. Below this transition phase, the vibration pattern inefficiently radiates sound, whereas above this range, spectral components are transmitted from the flare with very little or no reflection [58], [182][7]. This has also been examined experimentally and findings have consistently indicated that the radiation efficiency of the trumpet and trombone flare show characteristics of a high-pass filter [20], [157], [182]. In Section 5.8, we compare the cutoff frequency of the trumpet and trombone bell and compare our findings with values previously reported.

When it comes to modelling brass instrument flares, it is common in the literature to approximate the shape by various functions or combinations of functions, e.g., exponential functions, hyperbolic functions, etc. [20], [66], [132]. However, if the travelling waves are sensitive to the bell's curvature, approximating its geometry may not be sufficient, especially if the last couple of centimeters are poorly modelled [36]. Such simplifications could result in exaggerated discrepancies when numerically solving the chosen set of equations. Previously in [184], we demonstrated that precisely modelling the flare shape is necessary to accurately model the wave propagation through the flare region. We further showed in [185] that simplifying the problem to a two-dimensional (2D) model does not properly describe the spreading of the sound waves through the flare and therefore, does not properly model the interactions between the backward and forward moving waves.

1.1.3 The Role of Nonlinear Wave Propagation

If a note is played softly on the trumpet or trombone, then its tonal character is typically expressed with respect to the first few harmonics [37]. In acoustics, words such as 'mellow' or 'dull' have been used to characterize such timbres [20]. But as the loudness or playing dynamic of the note increases, the sound quality becomes more 'rich' or 'bright' [132], [20], [66], [180]. This brightness of sound has been characterized as the *brassiness* of the produced sound. Some have proposed ways to quantify the associated timbre via the *brassiness parameter* or *brassiness coefficient* (e.g., [37], [76], [77], [174], [179]). The brassiness parameter is defined with respect to the bore geometry and is a measure of the

[7] This means that higher frequency notes better radiate from the instrument [179].

relative effects that arise as a consequence of nonlinear propagation[8].

The primary focus of this thesis will be on loudly played notes where the amplitude of the pressure disturbance entering the bore is at least 5% of atmospheric pressure. Such waves are classified as *finite-amplitude* waves or *nonlinear* sound waves and play a significant role in understanding the acoustic behaviour [30], [159][9]. As Rendon *et al.* explain in [179], the nonlinear propagation is associated with the "*large-scale distortion of a sound wave through the cumulative effect over a long distance or time of locally small nonlinear effects.*" Although such wave propagation can be produced in both woodwind and brass instruments, nonlinear behaviour is much more prominent in brass instruments [183]. This is because brass instruments are considerably longer and constructed with a mouthpiece cup rather than a curved mouthpiece with a reed or double reed [99], [167].

As briefly mentioned, the acoustic consequence of nonlinear wave propagation is the distortion of the waveform's shape as it travels through the tubing of the instrument. In particular, the crest of the pressure wave will travel faster than the trough causing the wave to steepen. The acoustic consequence of this phenomena is referred to as *spectral enrichment* [37], [38], [99], [180], [183]. Although in the literature it is rather common for researchers in the field to describe or interpret spectral enrichment as a 'change' or a 'transfer of energy from the lower frequency components to the higher ones,' we want to be more precise and clear with our language. The nonlinear process reduces the energy associated with lower frequency components, while higher frequency components increase. So, in a sense, steepening does remove energy from the low to high frequencies but the nonlinear action does not focus on this. In other words, there is not a mechanism per se that transfers energy[10], rather it is a consequence of a nonlinear process by which the waves change shape[11]. An example of this is shown in Figure 1.4, which plots the solution of Burgers' equation with viscosity, which states

$$\frac{\partial u}{\partial t} + u\frac{\partial u}{\partial x} = \nu\frac{\partial^2 u}{\partial x^2}, \tag{1.1a}$$

$$u(x,0) = e^{-\left(\frac{x}{0.15}\right)^2} \tag{1.1b}$$

[8] The brassiness parameter was first discussed by Pyle and Myers [174] in 2006, and then Gilbert [76] developed the theory and performed the first experiments to determine the brassiness for various musical instruments. In 2007, Gilbert *et al.* conducted further experiments to confirm previous findings [77].

[9] Comparatively, *linear* sound waves or *acoustic* waves are defined as pressure waves whose shape does not change as they travel. In other words, the amplitude can only be a small fraction of atmospheric pressure and mathematically, this implies the equations of motion can be linearized.

[10] Or as my supervisor likes to say, "there is no robbing Peter to pay Paul" [210].

[11] We will spend more time examining this experimentally in Section 2.3.1 and numerically in Section 5.9.

over the interval $[-1,\ 1]$ where ν is the kinematic viscosity, t is time, and u is the transport property profile [29]. The upper plots at each time shows the wave profile with respect to the spatial coordinate; the bottom plots depict the corresponding spectrum with respect to the wavenumber[12].

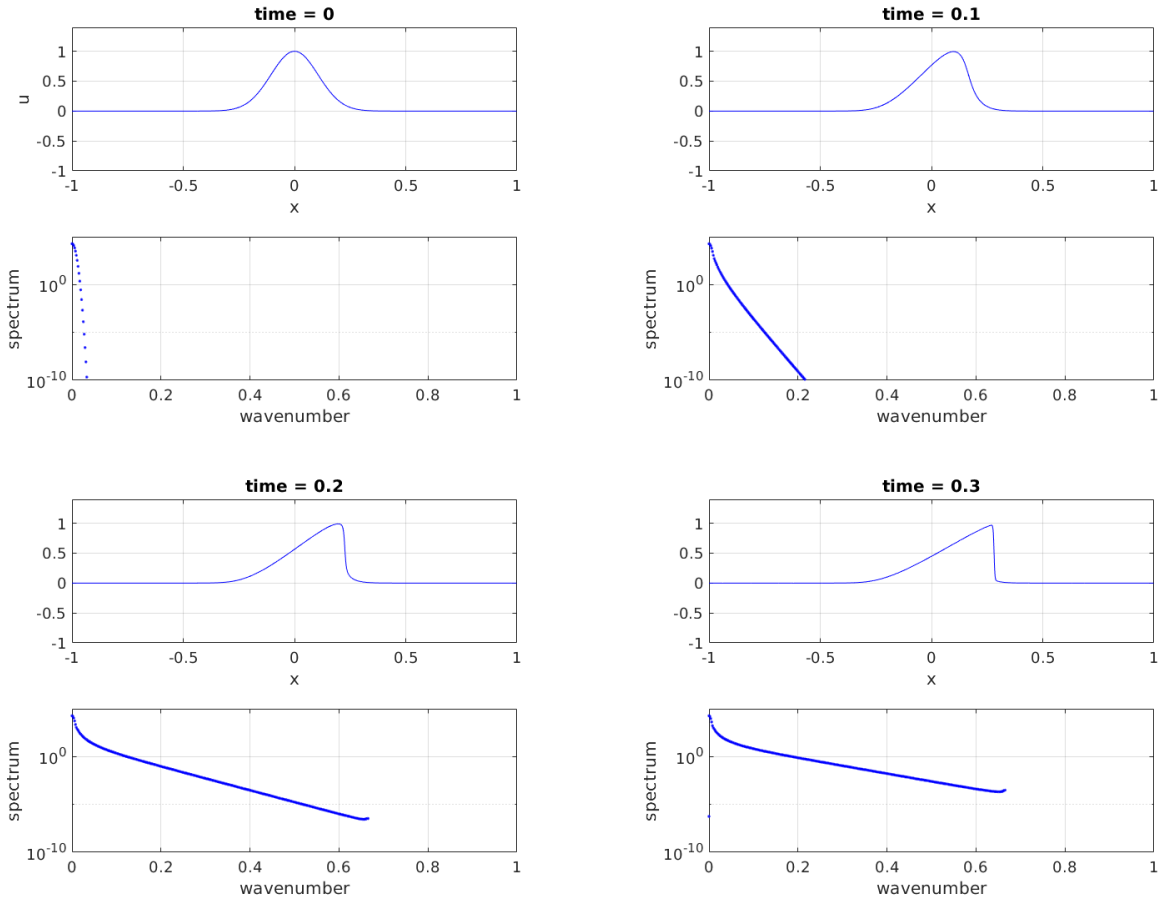

Figure 1.4: An example of the effects due to wave steepening when solving Burgers' equation.

Theoretically, with respect to brass instruments, if the bore is of sufficient length, it is also possible that the steepening waves could develop into shock waves [30], [99], [179]. A

[12] These outputs were obtained by following an online Matlab tutorial to solve Burgers' equation with viscosity using the spectral method [29], [30], [65].

shock wave is a propagation disturbance that physically can be thought of as a plane or curved discontinuous flow structure [131], [176]. For an ideal gas[13], the *Rankine-Hugoniot relations* are conditions that examine how various quantities change at a shock [29]. For the idealized situation where we have a plane shock wave that is normal to the x-axis and positioned at $x = x_s(t) \in [x_L,\ x_R]$ (as shown in Figure 1.5), the *Rankine-Hugoniot jump condition* states that for a conserved physical quantity w,

$$\frac{dx_s(t)}{dt} = \frac{F(w_L) - F(w_R)}{w_L - w_R}, \tag{1.2}$$

where $w(x_L, t) = w_L$, $w(x_R, t) = w_R$, and F denotes the flux function. For the problem to remain physically consistent, the characteristics must intersect or enter the shock rather than merge from the discontinuity. For physical problems where the shock wave is travelling, the jump condition must satisfy

$$\frac{F(w) - F(w_L)}{w - w_L} \leq \frac{dx_s(t)}{dt} \leq \frac{F(w) - F(w_R)}{w - w_R}, \tag{1.3}$$

$\forall w \in [w_L,\ w_R]$.

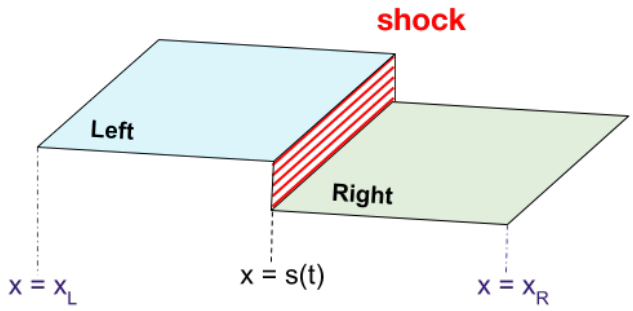

Figure 1.5: Depiction of a shock wave positioned at $x = s(t)$.

For the trombone, shock waves have been known to form when playing certain notes at specific volumes as experimentally shown by Hirschberg *et al.* in [99]. It is often assumed that shock waves are also produced in the trumpet[14]. However, there is some uncertainty due to the length of the instrument. Some results in the literature suggest that the shock

[13] That is, no heat can be transferred between fluid particles.

[14] Pandya *et al.* for instance say they were able to observe shocks exiting the trumpet when using Schlieren imaging techniques [167]. However, there is some uncertainty whether they were observing actual shocks or just the sound wavefront [88].

distance for a loudly played B_3^b is roughly the length of the trumpet (e.g., [167], [183], [204]). Sections 2.3.1 and 5.9 will also investigate such phenomenon.

For problems where the propagation disturbance is mathematically described using the Euler equations, the jump condition defined in (1.3) is obtained by enforcing conservation of mass, momentum and energy in integral form and must be satisfied in the neighbourhood of the shock wave. If ρ, p, u, and E denotes the density, pressure, velocity and energy, respectively, then the jump conditions can be expressed by [29], [30]:

$$\rho_L \bar{u}_L = \rho_R \bar{u}_R, \tag{1.4}$$

$$\rho_L \bar{u}_L^2 + p_L = \rho_R \bar{u}_R^2 + p_R, \tag{1.5}$$

$$\left(\frac{1}{2}\rho_L \bar{u}_L^2 + \rho_L E_L + p_L\right)\bar{u}_L = \left(\frac{1}{2}\rho_R \bar{u}_R^2 + \rho_R E_R + p_R\right)\bar{u}_R, \tag{1.6}$$

where $\bar{u} = \left(u - \frac{dx_s(t)}{dt}\right)$. These Rankine-Hugoniot relations state that the flux of mass, momentum and energy must be continuous at a shock, while the pressure, density and internal energy of the gas may not be continuous [29].

1.2 Previous Proposed Models

Several models to describe nonlinear wave propagation in brass instruments have been proposed. Some have been formulated with respect to the input impedance or radiation impedance[15]. In theory, this approach seems quite reasonable since the peaks of the impedance curves correspond to the resonant frequencies of the bore, which characterizes acoustic behaviour [117]. However, the impedance either has to be measured or calculated by using acoustic pulse reflectometry methods [118]. Such formulations can be problematic for brass instruments because the slope of the horn expansion can quickly become too large as discussed in [27] and [58]. Transmission line models have had some success at modelling sound production in brass instruments [58], [49], [159]. Bilbao *et al.* for instance, considered a finite-difference scheme to compare a one-dimensional (1D) plane and spherical model using a transmission-matrix method. This is typically done for linear propagation though some have attempted to incorporate nonlinearities, e.g., [160].

Time-domain models have also been considered. One that is commonly referenced is proposed by Msallam *et al.* for the trombone [147]. The tubing prior to the flare was modelled as a uniform tube and the radiated sound was processed by a linear filter that

[15] Which is defined as the ratio of the acoustic pressure to the air volume flow rate.

represented the bell. Another model was proposed by Menguy and Gilbert that used generalized Burgers' equations and was numerically solved using a finite-difference method [141]. The authors were able to uncouple the forward and backward moving waves. Their results were interpreted to mean that local linear approximations are reasonable so long as the waves in both directions are properly modelled [110]. A recent 1D model that builds upon [141] is proposed by Berjamin *et al.* in [24]. Other examples of time-domain models can be found in [24], [113], [110], [184], [185].

Frequency-domain models are typically used to describe linear wave propagation. In principle, there is no problem to consider nonlinear effects, and some have attempted to do so. For example, Gilbert *et al.* considered a frequency-domain model based on the generalized Burgers' equation [78]. Simulations were performed on geometries constructed after a bass trombone where the bore before the flare was modelled by a cylindrical tube. Another recent model considered by Noreland *et al.* introduces a hybrid scheme [160]. For the flare region, a 2D finite-element method was considered where the inviscid Helmholtz equation was used. The tubing prior to the flare was modelled as a cylindrical tube where the propagation was modelled using a 1D inviscid transmission line model. Although the model seemed reasonable for low frequency notes, the authors concluded that for high frequencies, a more accurate model was needed. A frequency model that does consider some of the geometric features near the mouthpiece of a brass instrument is proposed by Thompson *et al.* in [204]. The authors considered a nonlinear model for the trombone using the 1D Burgers' equation where the shape of the instrument was approximated by a sequence of 152 cylindrical tubes.

1.3 Thesis Outline

This thesis is structured as follows: Chapter 2 is focused on acoustic experiments that were carried out in John Vanderkooy's Audio Research Lab. The purpose of the four performed experiments was to verify previous findings, examine the differences between the trumpet and trombone, determine the significance of the bell vibrations, and to investigate how the timbre of a musical note changes under certain playing conditions. To achieve these goals, sound pressure measurements were recorded along the instruments using sensitive condenser microphones and accelerometers were mounted on the flare. The full setup of the experiments will be discussed in Section 2.2.4. The experimental results corresponding to the sound pressure measurements as well as the collected accelerometer data will be presented in Sections 2.3 and 2.3.3, respectively. Section 2.3.1 will be dedicated to investigating the timbre differences associated with quietly and loudly played tones. Several

notes produced on the trombone were played at a loud enough dynamic to observe (what we think to be) shock waves. The analysis of these notes is done in Section 2.3.1.

Chapter 3 introduces the mathematical model (Section 3.1), and the formulation of the numerical method (Section 3.2). The full derivations of the equations of motion are included in Appendix D for convenience so that this document is self contained. For the simulations presented in this thesis, a GPU implementation of the discontinuous Galerkin (DG) method was used. The code itself was implemented by previous students of Lilia Krivodonova. I personally only implemented the different boundary conditions and inflow conditions used for the simulations presented in this thesis. So, to be clear, this thesis does *not* focus on the implementation of the numerical method[16]. I instead wanted to test the robustness of the code and apply it to a physical problem by using the experimental data to initialize simulations. To then evaluate how well we could reproduce the playing conditions and associated timbre of the instruments, the numerical solutions were compared against the experimental data outside the flares.

Our proposed model however does not include energy losses for a couple of main reasons. Firstly, and most obviously, they are not implemented in the DG method we are using. Secondly, there is still uncertainty surrounding their importance and whether they have a significant *audible effect*, i.e., whether the timbre is sufficiently influenced so that one could perceive the difference in sound quality. Therefore, Chapter 4 is dedicated toward evaluating whether it is reasonable to neglect losses due to thermoviscous and vibroacoustic effects. With respect to vibroacoustic effects, several papers have recently been published (all as collaborations with Kausel) about the importance of bell vibrations (e.g., [108], [109], [110], [112], [113]), though not everyone agrees that there is an audible effect, as discussed in Brackett's thesis [32]. According to Kausel, wall and bell vibrations are more difficult to generalize because theoretically, vibrational effects could either dampen or amplify certain harmonic components within the instrument or as they are transmitted through the bell [109], [113]. Nonetheless, he states that wall vibrations contain all the frequency components of the radiated sound where the magnitude of the oscillations are dependent on the fourth power of the wall thickness[17] resulting in a lower pitch [109].

Kausel also explains that dampening effects from the walls causes the pressure transfer function to change sign. For the trumpet for instance, he reports that this shift in pressure takes place around 500 Hz and again near 1500 Hz. In particular, for spectral components below 500 Hz and above 1500 Hz, the bell vibrations have an absorbing effect.

[16] Though, we still review the theoretical setup of the DG method in Section 3.2.

[17] He further states that for frequency components larger than the resonant frequencies, the wall displacement is out of phase with pressure [109].

The components in-between are not influenced as much and are more prominent in the radiated power [108], [109], [112], [113]. Although we cannot verify these claims, we have conducted experiments to study and better understand the vibroacoustics of the trumpet and trombone flare. Our results will be presented in Section 2.3.

In reality, there are also energy losses in the instruments due to viscous friction and the transfer of energy in the form of heat from the wave to the walls. However, with respect to these thermoviscous effects, no physical experiments were conducted for this thesis to study such losses, which would be most prominent in the narrow regions of the instrument [108], [146], [217]. But for completeness purposes, a numerical study was done in COMSOL [162], a commercial finite element software program, and will be presented in Section 4.2.2. However, a couple of disclaimers: firstly, this was done for linear wave propagation and secondly, we do *not* attempt to justify the validity of the modelling utilized in COMSOL. We are merely using it as a tool since it is commonly used by the research community (including Kausel) and includes the linearized Navier-Stokes model. We do however make an approximation on the relative power loss from such effects prior to the flare expansion by using the theory discussed in Morse and Ingard [146]. This is done in Section 4.2.3 and allows us to check whether the theoretical and computed approximations are consistent with one another.

Chapter 5 presents a collection of numerical studies that were done to break the problem up into smaller parts, to develop an intuitive understanding of the behaviour associated with the wave propagation, and to use the developed software for a "real life" problem[18]. The influence of the trumpet's and trombone's physical features were studied. We wanted to examine how the initial tubing shape near the mouthpiece (Section 5.5), the bends (Section 5.6), the flare expansion (Section 5.8.1), and the mouthpiece cup (Section 5.8.2) influences the wave propagation through the instrument and consequently, how important each aspect is to accurately model the timbre. This was accomplished either through simulating certain periodic sound waves (i.e., musical notes) or using acoustic pulses (i.e., using pulse reflectometry methods), as outlined in Section 5.1. Section 5.9 is dedicated to numerically investigating the claims made in the literature as well as the ones we made in Section 2.3.1 about spectral enrichment. The hypotheses put forward in Section 2.3.1 about the development of shock waves are discussed in Sections 5.5.3. The cutoff frequency (or transitional range) of the trumpet and trombone is numerically examined in Section 5.8 and compared with values reported in the literature. Finally, we determine whether

[18] In computational fluid dynamics or aeroacoustics, there is a large focus (and for good reason) on testing benchmarks and "toy-problems" which are not always physical. This thesis however extends this evaluation process by testing the practicality of using the implemented method on a real-life, physical problem.

the 3D mathematical description of the equations of motion can be simplified to a lower-dimensional model (Section 5.7), and also determine what simplifications can be made to the computational domain to reduce runtime while preserving the integrity of the computed solution (Section 5.4).

Chapter 6 examines how to prescribe the boundary conditions in a way that permits us to incorporate the experimental data. To define the measured pressure at the inlet of the computational instruments, we need to relate the acoustic pressure and velocity. The different approaches taken in the literature to do so are reviewed in Section 6.1, specifically Bernoulli's equation (6.1.1), the planar relationship (Section 6.1.2), and using Riemann invariants (Section 6.1.3). These approaches are then tested and compared in Section 6.2. The boundary condition that yielded the best results in Section 6.2 was further tested on multiple trumpet and trombone notes in Section 6.3. In Section 6.4.3, we theorize possible ways to obtain a better relationship between acoustic velocity and pressure and complete the first step in our proposed approach.

Chapter 7 wraps up the thesis and in Section 7.1, we evaluated the simulated pitches against the experimental data measured outside the bell and compared our results with previously published work. To our knowledge, our proposed approach gives the most accurate simulations to reproduce the timbre of a real musical note played by a musician.

Chapter 2

Acoustic Experiments

2.1 Purpose and Motivation

To test the reproducibility of previous experimental findings[1], sound pressure measurements and vibrational data were collected while specific musical notes were produced on the trombone and trumpet by a musician. The other motivational factors behind the four separate experiments that were conducted was to:

1. Be confident of findings reported in the literature.
2. Determine if there are significant differences between the behaviour associated with sound waves propagating through the trumpet and trombone.
3. Determine the playing levels where nonlinear effects become more prominent and study how wave steepening influences the radiated spectrum, i.e., the timbre, of certain musical notes.
4. Test for ourselves if shock waves could be observed radiating from the bell of either instrument, and if so, under what conditions.
5. Collect data for numerical simulations to examine the validity of the model that will be used to describe the wave propagation.

[1] Such a measure is sometimes referred to as the *statistical power* of an experiment.

6. Determine whether bell vibrations are significant for either instrument, and if so, for what frequencies/volumes.

2.2 Acoustic Experiments

The experiments conducted for this thesis were carried out at the Audio Research Lab at the University of Waterloo with John Vanderkooy. All experiments were done with live players, specifically: Philip Rempel, Noel Chalmers, Ben Storer and Benjamin Winger. The trumpet and trombone used during the acoustic experiments are shown in Figure 2.1. The different experimental trials are summarized below.

Figure 2.1: Placement of the microphones on the trombone (left) and trumpet (right).

2.2.1 Experiment #1: trumpet sound pressure measurements

Three microphones were used to measure sound pressure waveforms at various locations along the B^b Barcelona BTR-200LQ trumpet. A GRAS 40BP quarter-inch microphone was mounted on the mouthpiece-shank, a B&K 4135 quarter-inch microphone was mounted before the first bend, and a half-inch B&K 4133 microphone was placed 16 cm - 17 cm outside the bell along the central axis. All the microphones recorded the data simultaneously and were connected to three channels of a four channel digital Tektronix oscilloscope with quantized 8-bit converters. We therefore might expect the microphone data to have a maximum of 256 levels. However, due to the large oversampling rate of the internal converters, many samples were added together producing output samples with much better resolution. We found that our data displayed over 2000 levels, so the data was captured approximately with 11-bit precision with a signal-to-noise ratio[2] of about 66 dB. Due to

[2] Which is defined as the ratio of the signal power to the noise power in decibels.

the number of samples per period however (which was 412 for the B_3^b), the noise level in each FFT bin is 26 dB less than the straight 66 dB offered by the resolution of each sample. We find that the acoustical noise in our measurements limits the analysis more than the resolution of the measurement system.

2.2.2 Experiment #2: trombone sound pressure measurements

Four microphones were used to record sound pressure waveforms at several locations along the Mendini MTB-L B^b tenor slide trombone. A B&K 4136 quarter-inch microphone was mounted on the mouthpiece-shank, a B&K 4135 was mounted before the second bend, a GRAS 40BP quarter-inch microphone was positioned at the exit of the bell in the center position, and a half-inch B&K 4133 microphone was placed 16 cm - 17 cm outside the trombone bell along the central axis. All outputs from the microphones used were recorded simultaneously using a USB data acquisition system (DAQ) from Measurement Computing with a 1608FS+ DAQ card, which has eight channels with 16-bit resolution. The DAQ was used at a sampling frequency of 100 kHz. This means that frequencies up to the Nyquist frequency of 50 kHz are properly sampled but components above this are aliased back below the Nyquist frequency. Typically, anti-aliasing filters are needed to prevent this however this was not necessary in our case for several reasons. Although the microphones used at the mouthpiece and bend are capable of reproducing acoustic signals even above 100 kHz, the actual spectra showed almost no signal above 30 kHz thus, aliasing does not occur[3]. The microphone used outside the bell has a sharp roll-off above 40 kHz meaning it acts as its own anti-aliasing filter. This is fortunate since for the trombone we did find that a shock wave was produced and had extremely high spectral components. The signal from this microphone does not suffer from aliasing, although it will suffer from bandwidth reduction due to its operation.

2.2.3 Experiment #3: trumpet and trombone sound pressure measurements with a single accelerometer

Three separate microphones were used to measure sound pressure waveforms along both the B^b Barcelona BTR-200LQ trumpet and Mendini MTB-L B^b tenor slide trombone. For both musical instruments, the B&K 4136 quarter-inch microphone was mounted on the mouthpiece-shank, the GRAS 40BP quarter-inch microphone was mounted before the first

[3] So only the 40 BP quarter-inch microphone is possibly compromised, as it goes up to 70 kHz.

and second bend of the trumpet and trombone, respectively, and a half-inch B&K 4133 microphone was placed 16 cm - 22 cm outside the bells along the central axis. In addition, a Knowles BU 1771 accelerometer with a nominal sensitivity of -45 dBV/g was mounted with beeswax on the outside of each brass instrument flare near the rim as shown in Figure 2.2. The acceleration data was collected as a function of time while the notes were being played. The signals from all microphones as well as the accelerometer were collected using the DAQ from Measurement Computing mentioned in the Experiment #2 description.

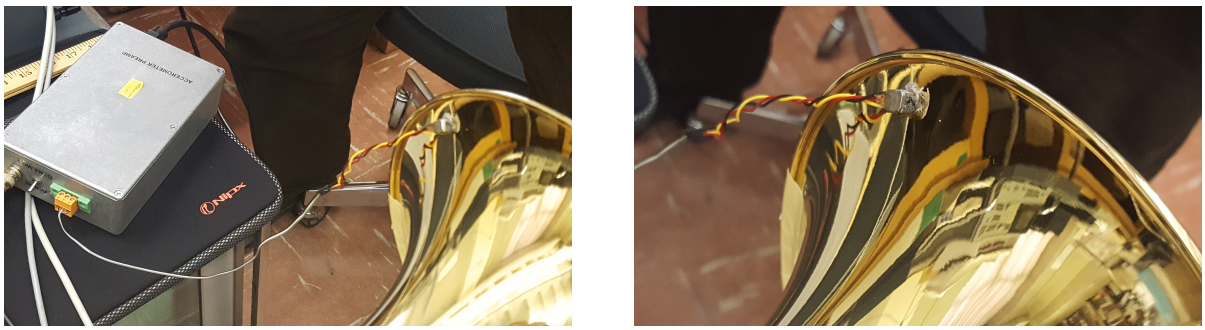

Figure 2.2: Placement of the accelerometer on the trombone bell.

2.2.4 Experiment #4: trumpet and trombone sound pressure measurements with two accelerometers

Three separate microphones were used to measure sound pressure waveforms along the B^b Barcelona BTR-200LQ trumpet and Mendini MTB-L B^b tenor slide trombone. For both instruments, a GRAS 40BP quarter-inch microphone was mounted on the mouthpiece-shank, the B&K 4136 quarter-inch microphone was mounted before the first and second bend of the trumpet and trombone, respectively, and a half-inch B&K 4133 microphone was positioned 16 cm - 22 cm outside the bells along the central axis. In addition, two Knowles BU 1771 accelerometers with a nominal sensitivity of -45 dBV/g were mounted orthogonal to each other (i.e., separated by 90^o) with beeswax on the outside of each brass instrument flare near the rim. The acceleration data was again collected as a function of time while a note was being played. Similar to the second and third experiments, the data was collected using the same DAQ system.

2.2.5 Experimental Setup

The positions of the microphones along the bore are reported in Table 2.1. For convenience, the microphones located at the different positions will be referred to as Mic $_{\text{Mouthpiece}}$, Mic $_{\text{Bend}}$, Mic $_{\text{Bell-Exit}}$ and Mic $_{\text{Outside-Bell}}$ for all experiments for both instruments as defined in Table 2.1[4].

Table 2.1: Location of the microphones along the trumpet and trombone bore shown in Figure 2.1 from the mouthpiece entrance.

Instrument	Mic $_{\text{Mouthpiece}}$	Mic $_{\text{Bend}}$	Mic $_{\text{Bell-Exit}}$	Mic $_{\text{Outside-Bell}}$
Trumpet	4.5 cm	37.5 cm	NA	16 - 17 cm outside bell
Trombone	4.5 cm	179 cm	1-3 cm outside the bell	16-22 cm outside bell

Mic $_{\text{Mouthpiece}}$ and Mic $_{\text{Bend}}$ were mounted on each instrument by cutting quarter-inch diameter holes into the tubing. In an attempt to not alter the acoustic properties of each instrument, a compressible o-ring was used at each location to seal the hole once the microphones were in place. For Experiment #2, #3 and #4, the voltage measured from each microphone was collected and saved simultaneously using TracerDAQ Pro, a multipurpose software package that we used in strip-chart mode, while the musicians held and played the instruments in a normal playing position. Each note was recorded for three seconds with a sampling frequency of $f_s = 100$ kHz. For Experiment #1, the sampling rate was $f_s = 50$ kHz and only a few periods were saved to the local computer using software implemented by John Vanderkooy[5]. Once the data were collected, the raw data were then imported into Matlab and converted into a pressure waveform from voltage to pressure, denoted by $p(t)$, which was measured in Pascals (Pa) as a function of time, t, measured in seconds (s). The corresponding calibrations for each microphone and the Matlab script written for this process can be found in Appendix A and E, respectively.

The vibration/acceleration amplitude can also be examined in the frequency-domain using a discrete Fourier transform (DFT) to compute the spectrum. In practice, this is accomplished using the fast Fourier transform (FFT) algorithm[6]. We take N to be the length of the signal, denoted by $x(n)$, where $1 \leq n \leq (N-1)$. An expression for the

[4] The Mic $_{\text{Bell-Exit}}$ was only used during Experiment #2.

[5] During the fourth experiment, the building's central heating system turned on. To ensure low frequency noise levels would not influence the collected time pressure waveform data, frequencies below 100 Hz were filtered out from the signal using a fifth order Butterworth filter.

[6] Which in Matlab is done using the `fft()` function.

number of frequency lines or bins is equal to

$$I = \begin{cases} \frac{N}{2} + 1 & \text{if the Nyquist frequency was odd,} \\ \frac{N}{2} & \text{if the Nyquist frequency was even,} \end{cases}$$

occurring in intervals of Δf, which is equal to the sampling rate of the raw waveform (f_s) divided by the number of samples (N). In other words, the frequency resolution is equal to the inverse of the total acquisition time, denoted by τ:

$$\Delta f = \frac{1}{\tau} = \frac{f_s}{N}. \tag{2.1}$$

The lowest frequency tested is 0 Hz, the direct current (DC) component (which is in bin 1 when using Matlab), and the highest frequency is the Nyquist frequency, $\frac{f_s}{2}$, which is in bin I. To ensure the amplitude of the sinusoidal component is correct, the DFT is multiplied by a factor of $\frac{2}{N}$, where the factor of two is needed since the amplitude components are double-sided[7]. Finally, to obtain the rms value[8], the magnitude is multiplied by a factor of $\frac{1}{\sqrt{2}}$[9].

Several different notes were played at various dynamic levels, e.g., piano (quiet), mezzo-piano (medium-quiet), mezzo-forte (medium-loud), forte (loud) or double-forte (very loud) and recorded for analysis. In musical notation, these volumes are denoted as *p*, *mp*, *mf*, *f*, and *ff*, respectively. However, there is no precise scientific measure to define each playing level[10], but rather there is a general consensus within the music and acoustic community. Within this thesis, we will therefore define the volume of a musical note with respect to the sound pressure level (SPL) in decibels (dB) obtained from the Mic $_{\text{Mouthpiece}}$ measurements. The measured pressure waveforms in Pa can be converted into SPL dB for each frequency component according to

$$\text{SPL} = 20 \log_{10} \left(\frac{\sqrt{2}\mathcal{P}}{2 \times 10^{-5}} \right) \text{ [dB]}, \tag{2.2}$$

where $\mathcal{P} = \left(\frac{1}{N}\right) \texttt{fft}(p)$, which is then multiplied by a factor of $\sqrt{2}$ to obtain the rms value. The decibel ranges used to define the volume of each recorded note can be found in Table 2.2.

[7] In other words, each frequency has both positive and negative components. We take the magnitude of the complex amplitude because typically, the phase will not be zero. Also note that the DC component is not multiplied by two.

[8] This is a logarithmic measure of the effective sound pressure relative to a reference value [210].

[9] Hence, the amplitude of the DFT is multiplied by $\frac{2}{N\sqrt{2}} = \frac{\sqrt{2}}{N}$.

[10] There is not an exact sound pressure level (SPL) range that corresponds to each playing dynamic.

Table 2.2: Proposed playing volume level definitions for the measured musical notes, which are defined with respect to the total SPL measured at Mic $_{\text{Mouthpiece}}$.

Total SPL dB Obtained at Mic $_{\text{Mouthpiece}}$	Corresponding Volume Definition
150.0 dB - 154.9 dB	*p*
155.0 dB - 159.9 dB	*mp*
160.0 dB - 164.9 dB	*mf*
165.0 dB - 167.5 dB	*f*
167.6 dB - 171.9 dB	*ff*

Data were also collected for notes while the instruments were played in various tubing configurations. For instance, trombone notes were produced while the slide was in position 1 (i.e., when the slide is not extended), position 5 (i.e., when the slide is extended by half its length), and position 7 (i.e., when the slide is fully extended). Notes were also played and recorded when the trombone was in position 3 and position 6. For the trumpet, notes were played while the valves were either all opened or all compressed. The first valve increases the tubing length to lower the pitch by one whole step, the second valve by one half step, and the third valve by one and a half steps. The overall length of the trombone and trumpet depending on the bore configuration can be found in Table 2.3.

Table 2.3: Length of trumpet and trombone bore in different tubing configurations.

Instrument	Tubing Configuration	Overall Length
Trombone	position 1	2.87 m
	position 3	2.99 m
	position 5	3.12 m
	position 6	3.23 m
	position 7	3.35 m
Trumpet	no valves	1.48 m
	valves 1, 2, 3	2.22 m

Between all the experiments that were conducted, a total of 37 measurements (i.e., musical notes) were recorded for the trombone, and 33 were collected for the trumpet. Table 2.4 summarizes the experimental trials. A subset of these measurements will be presented in the next section[11].

[11] Note that '→' in Table 2.4 denotes either a change in dynamic level or tubing configuration.

Experiment	Instrument	Musical Note	Volume	Tubing Configuration
2	Trombone	B_3^b	f	position 1
2	Trombone	B_3^b	p	position 1
2	Trombone	F_3	mp	position 1
2	Trombone	A_3	mp	position 6
2	Trombone	F_3	mf	position 1
2	Trombone	A_3	mf	position 6
2	Trombone	B_3^b	mf	position 1
2	Trombone	B_3^b	p	position 1
2	Trombone	B_4^b	mp	position 1
2	Trombone	B_2^b	ff	position 1
2	Trombone	A_2	f	position 3
2	Trombone	A_1	mf	position 6
2	Trombone	B_2^b	f	position 1
2	Trombone	F_3	$p \rightarrow ff$	position 1
2	Trombone	F_3	ff	position 1
3	Trombone	F_3	f	position 1
3	Trombone	F_3	$mf \rightarrow f$	position 1
3	Trombone	F_3	f	position 1
3	Trombone	F_3	$p \rightarrow mp$	position 1
3	Trombone	F_3	f	position 1
3	Trombone	F_3	f	position 6
3	Trombone	F_3	f	position 6
3	Trombone	F_3	f	position 6
3	Trombone	F_3	crescendo f	position 1
3	Trombone	F_3	f	position 1
3	Trombone	F_3	$p \rightarrow ff$	position 1
3	Trombone	B_3^b	f	position 6
3	Trombone	B_3^b	p	pos 6 $\rightarrow$ pos 1
4	Trombone	B_3^b	f	position 1
4	Trombone	B_3^b	p	position 1
4	Trombone	B_3^b	mp	position 1
4	Trombone	B_3^b	mp	position 1
4	Trombone	$A_3^\#$	mf	position 5
4	Trombone	$A_3^\#$	mf	position 5

4	Trombone	A_3	*mf*	position 7
4	Trombone	A_3	*mp*	position 7
4	Trombone	B_3^b	*ff*	position
1	Trumpet	B_3^b	*f*	no valves
1	Trumpet	B_3^b	*f*	no valves
1	Trumpet	B_3^b	*mf*	no valves
1	Trumpet	B_3^b	*mf*	no valves
1	Trumpet	D_4^b	*mp*	valves 1, 2, 3
1	Trumpet	D_4^b	*mf*	no valves
1	Trumpet	B_4^b	*mp*	no valves
1	Trumpet	B_4^b	*mf*	no valves
1	Trumpet	B_3^b	*mf*	no valves
1	Trumpet	F_4	*mf*	no valves
1	Trumpet	F_4	*f*	no valves
1	Trumpet	B_4^b	*f*	no valves
1	Trumpet	B_4^b	*f*	no valves
1	Trumpet	F_4	*f*	no valves
3	Trumpet	B_3^b	*f*	no valves
3	Trumpet	B_3^b	*mf*	no valves
3	Trumpet	B_3^b	*mp*	no valves
3	Trumpet	F_4	*ff*	no valves
3	Trumpet	B_3^b	*mf*	valves 1, 2, 3
3	Trumpet	$A_4^\#$	*f*	valves 1, 2, 3
4	Trumpet	B_4^b	*ff*	no valves
4	Trumpet	B_4^b	*mf*	no valves
4	Trumpet	E_2	*mp*	no valves
4	Trumpet	B_3^b	*mf*	no valves
4	Trumpet	B_3^b	*ff*	no valves
4	Trumpet	F_5	*mf*	no valves
4	Trumpet	F_5	*mp*	no valves
4	Trumpet	B_3	*ff*	no valves
4	Trumpet	$B_3^\#$	*f*	valves 1, 2, 3
4	Trumpet	B_5	*p*	no valves

Table 2.4: Summary of the musical notes played during the four different experimental runs.

2.3 Experimental Results

The musical notes that will be presented within this section are summarized in Tables 2.5 and 2.6 for the trombone and trumpet. The total SPLs at each microphone are also reported. Figures 2.3 to 2.13 display the trombone notes stated in Table 2.5 in the order they are listed. Similarly, Figures 2.14 to 2.21 depict the trumpet notes listed in Table 2.6. For all the figures, the data presented represents one period of the recorded pressure waveforms once the note being played was steady. We isolated a single period to make the comparison between notes more straight-forward. These graphs show deviation of the sound wave pressure from atmospheric pressure. The spectra of the pressure waves are also shown.

Table 2.5: Musical notes played on the trombone and the total SPLs measured at the different microphone positions.

Note	Tube Config.	Volume	Mic $_{\text{Mouthpiece}}$	Mic $_{\text{Bend}}$	Mic $_{\text{Bell-Exit}}$	Mic $_{\text{Outside-Bell}}$
B_3^b	Position 1	p	152.0 dB	135.0 dB	129.7 dB	108.3 dB
B_3^b	Position 1	f	165.6 dB	155.7 dB	149.7 dB	129.5 dB
F_3	Position 1	p	152.5 dB	143.0 dB	-	105.9 dB
F_3	Position 1	mp	154.0 dB	146.3 dB	-	107.3 dB
F_3	Position 1	mf	163.5 dB	155.7 dB	143.5 dB	121.6 dB
F_3	Position 1	ff	169.9 dB	164.2 dB	154.9 dB	124.4 dB
B_2^b	Position 1	ff	169.0 dB	166.0 dB	151.5 dB	130.1 dB
B_4^b	Position 1	mp	160.0 dB	158.4 dB	148.7 dB	124.5 dB
A_1	Position 6	mf	161.9 dB	159.0 dB	140.4 dB	121.0 dB
A_2	Position 3	f	166.4 dB	164.6 dB	147.8 dB	127.8 dB
A_3	Position 6	mf	162.6 dB	159.4 dB	144.4 dB	123.5 dB

When examining the loudly played notes measured at Mic $_{\text{Outside-Bell}}$, one of the most striking observations was that the SPL of the first few harmonics behaves similar to an increasing function[12], i.e., $f_1 \leq f_2 \leq f_3 \leq \ldots$. The louder the note is played, the more the harmonics progressively increase in SPL, e.g., see the f B_3^b (Figure 2.4), ff F_3 (Figure 2.8), f B_2^b (Figure 2.9) trombone notes as well as the mf B_3^b (Figures 2.15), f B_3^b (Figures 2.16), f B_4^b (Figure 2.18), f F_4 (Figure 2.20) trumpet notes. Similarly, the quieter a note is played, the more the spectrum behaves like an decreasing function, i.e., $f_1 \geq f_2 \geq f_3 \geq \ldots$.

[12] In other words, the first few harmonics get progressively louder.

Table 2.6: Musical notes played on the trumpet and the total SPLs measured at the various microphone positions.

Note	Tube Config.	Volume	Mic $_{\text{Mouthpiece}}$	Mic $_{\text{Bend}}$	Mic $_{\text{Outside-Bell}}$
B_3^b	no valves	*mp*	156.6 dB	139.3 dB	114.9 dB
B_3^b	no valves	*mf*	166.5 dB	158.2 dB	116.8 dB
B_3^b	no valves	*f*	167.1 dB	159.7 dB	117.6 dB
B_4^b	no valves	*mf*	165.2 dB	160.4 dB	115.8 dB
B_4^b	no valves	*f*	167.2217 dB	162.7 dB	119.5 dB
B_5	no valves	*p*	151.9 dB	141.8 dB	111.1 dB
F_4	no valves	*f*	165.4 dB	160.8 dB	115.2 dB
F_5	no valves	*mf*	162.3 dB	158.0 dB	112.4 dB

For the *p* F_3 (Figure 2.5), *mp* B_4^b (Figure 2.10) trombone notes, and the *p* B_5 (Figure 2.19) trumpet note, we find the spectra acts as a strictly decreasing function for the first six to eight harmonics.

For the louder notes, we suspect these observations are a consequence of wave steepening, and for the notes mentioned at *ff*, perhaps even the result of a shock wave (since these pressure waveforms at Mic $_{\text{Outside-Bell}}$ in the time-domain have sharp peaks)[13]. The next section will be dedicated to exploring and verifying these hypotheses.

[13] This is particularly evident for the *ff* F_3 played on the trombone (Figure 2.8). We also notice the harmonic spectrum measured at Mic $_{\text{Bell-Exit}}$ exceeds the Mic $_{\text{Mouthpiece}}$ and Mic $_{\text{Bend}}$ spectra for the higher harmonic components. This observation seems reasonable if a shock formed within the bore before exiting the bell.

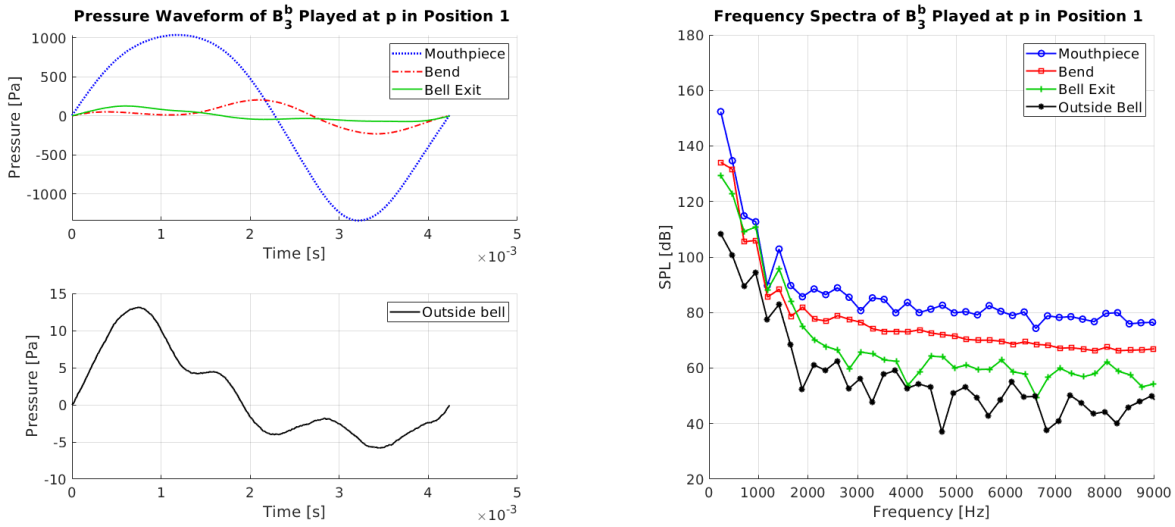

Figure 2.3: Time pressure waveforms (left) and the corresponding spectral components (right) of the B_3^b played at p on the trombone in position 1.

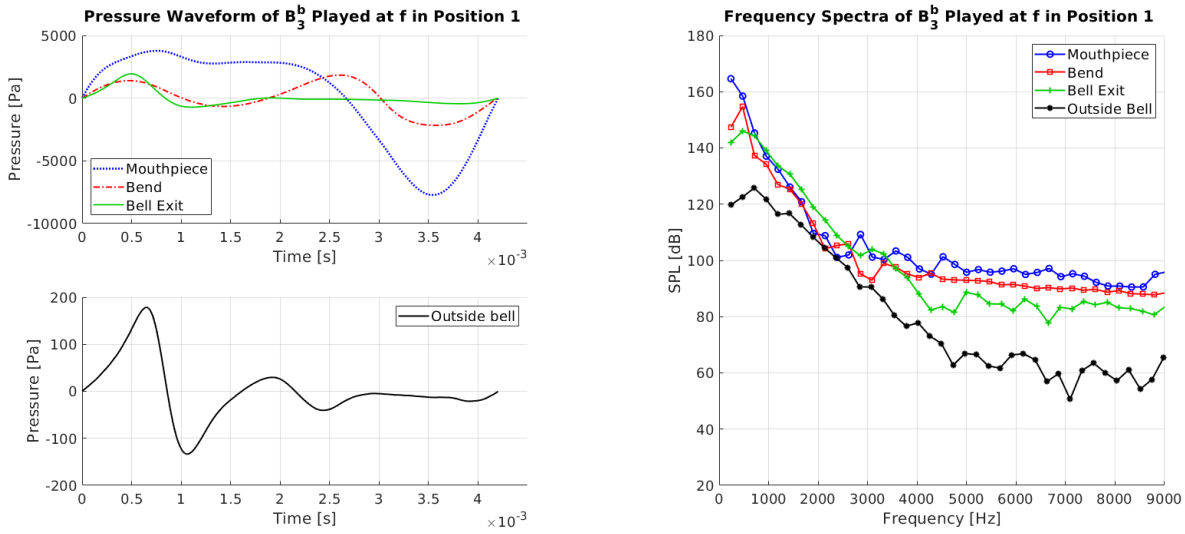

Figure 2.4: Time pressure waveforms (left) and the corresponding spectral components (right) of the B_3^b played at f on the trombone in position 1.

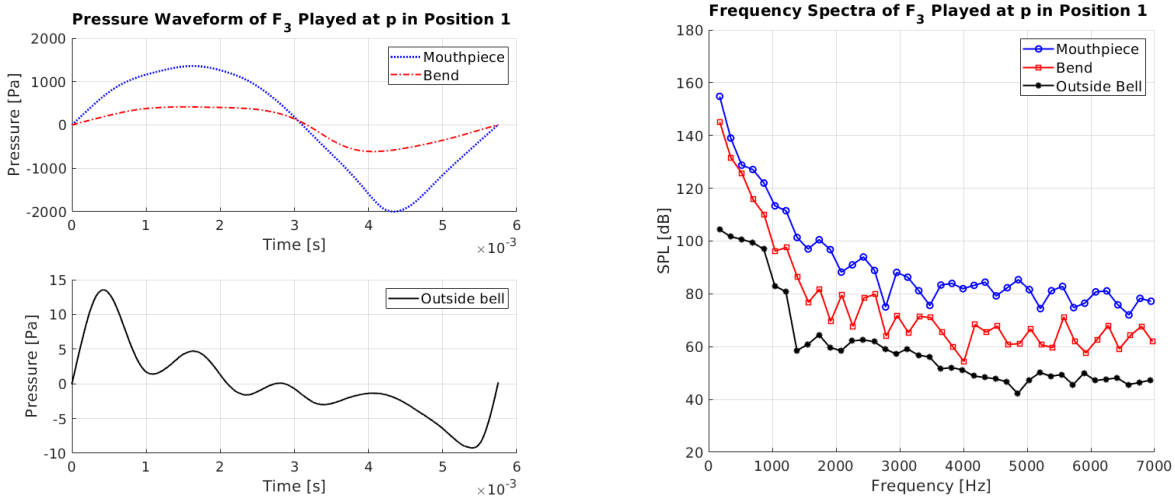

Figure 2.5: Time pressure waveforms (left) and the corresponding spectral components (right) of the F_3 played at p on the trombone in position 1.

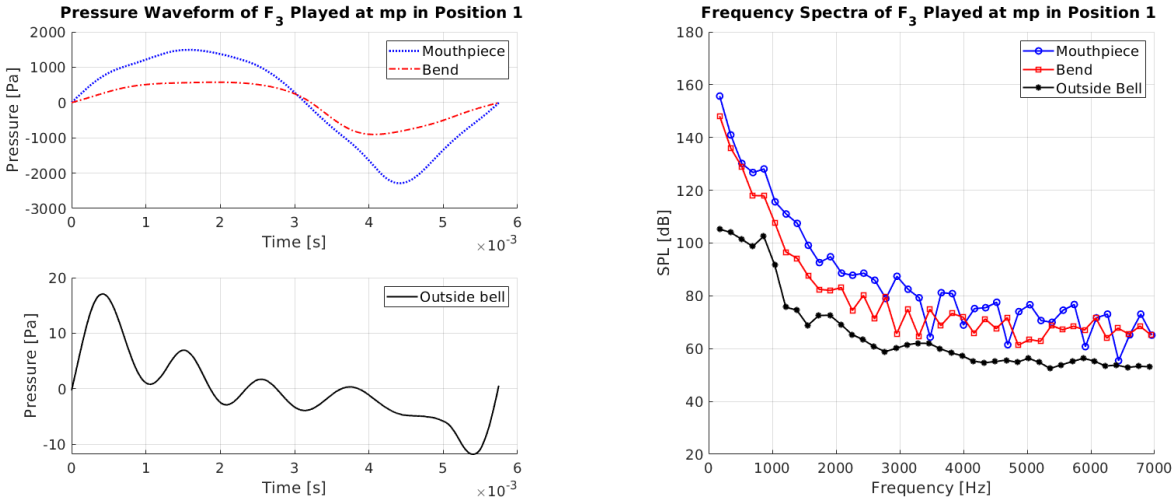

Figure 2.6: Time pressure waveforms (left) and the corresponding spectral components (right) of the F_3 played at mp on the trombone in position 1.

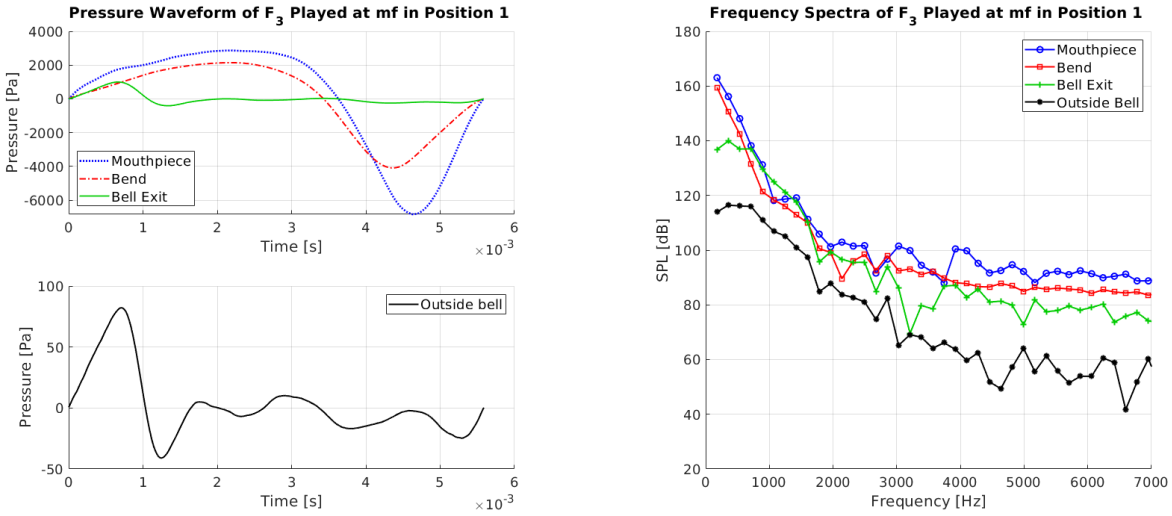

Figure 2.7: Time pressure waveforms (left) and the corresponding spectral components (right) of the F_3 played at *mf* on the trombone in position 1.

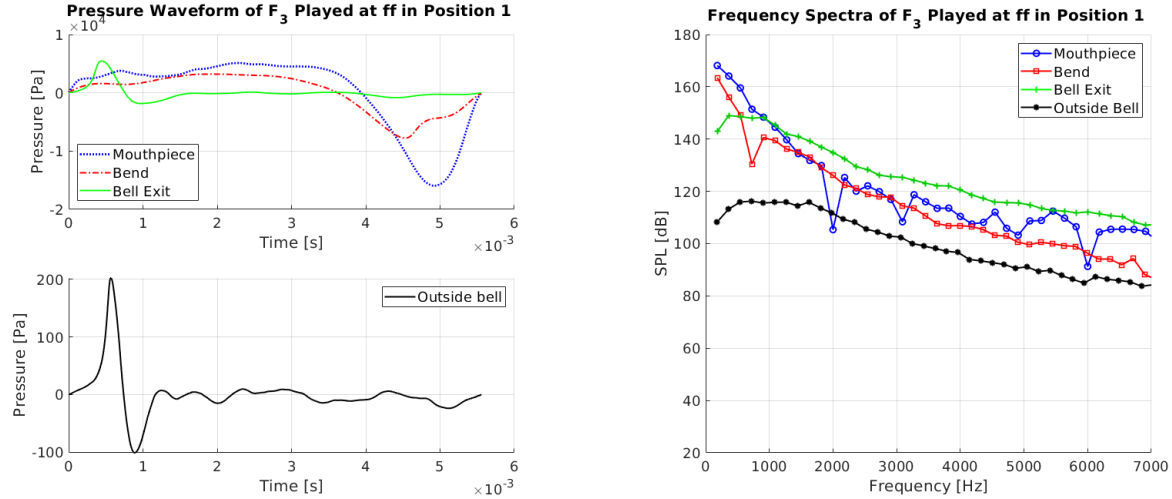

Figure 2.8: Time pressure waveforms (left) and the corresponding spectral components (right) of the F_3 played at *ff* on the trombone in position 1.

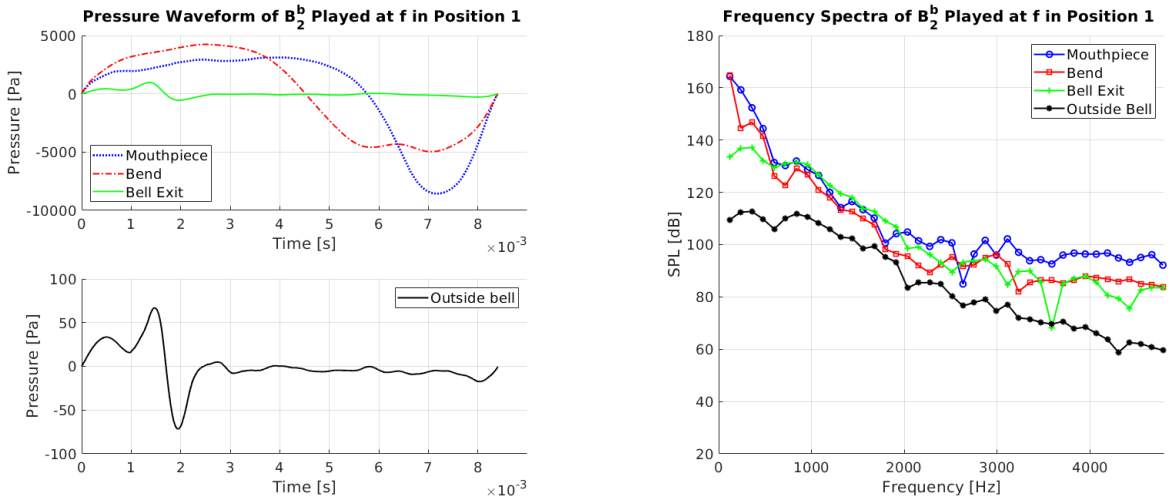

Figure 2.9: Time pressure waveforms (left) and the corresponding spectral components (right) of the B_2^b played at f on the trombone in position 1.

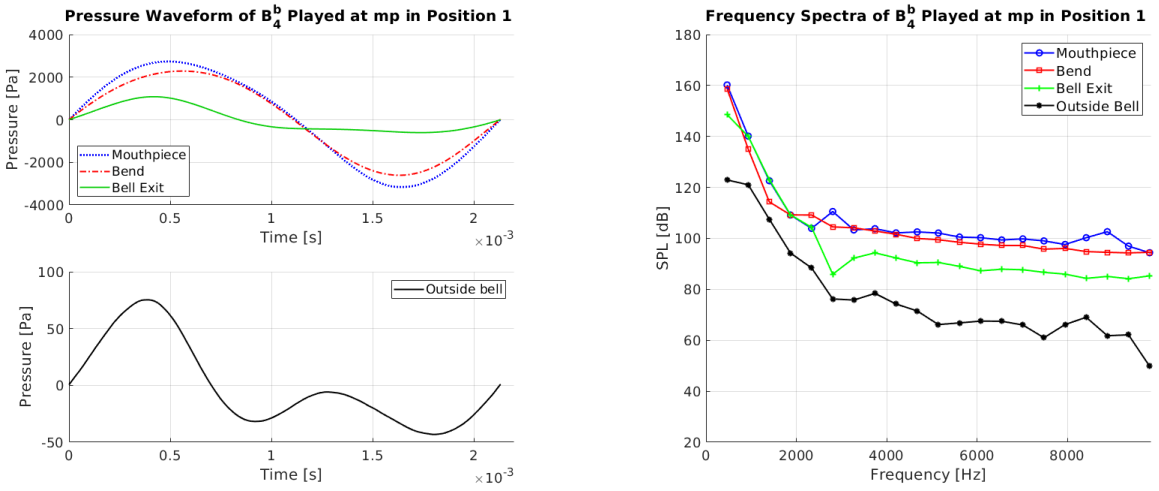

Figure 2.10: Time pressure waveforms (left) and the corresponding spectral components (right) of the B_4^b played at mp on the trombone in position 1.

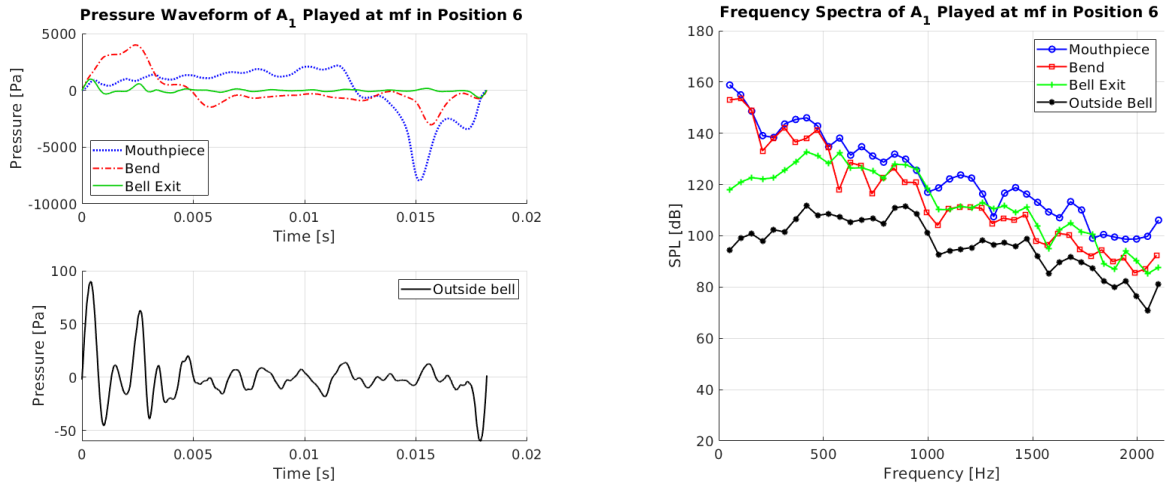

Figure 2.11: Time pressure waveforms (left) and the corresponding spectral components (right) of the A_1 played at *mf* on the trombone in position 6.

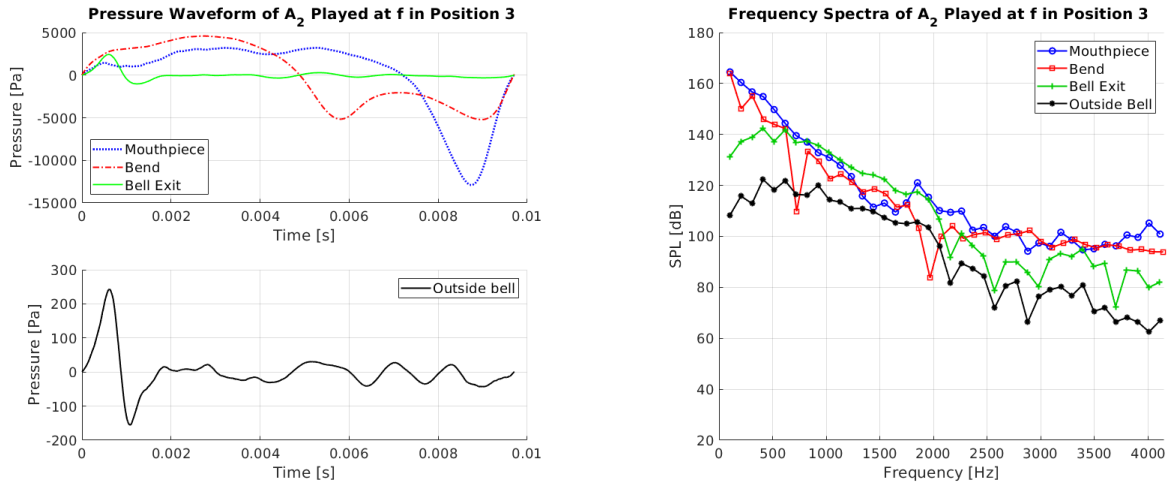

Figure 2.12: Time pressure waveforms (left) and the corresponding spectral components (right) of the A_2 played at *f* on the trombone in position 3.

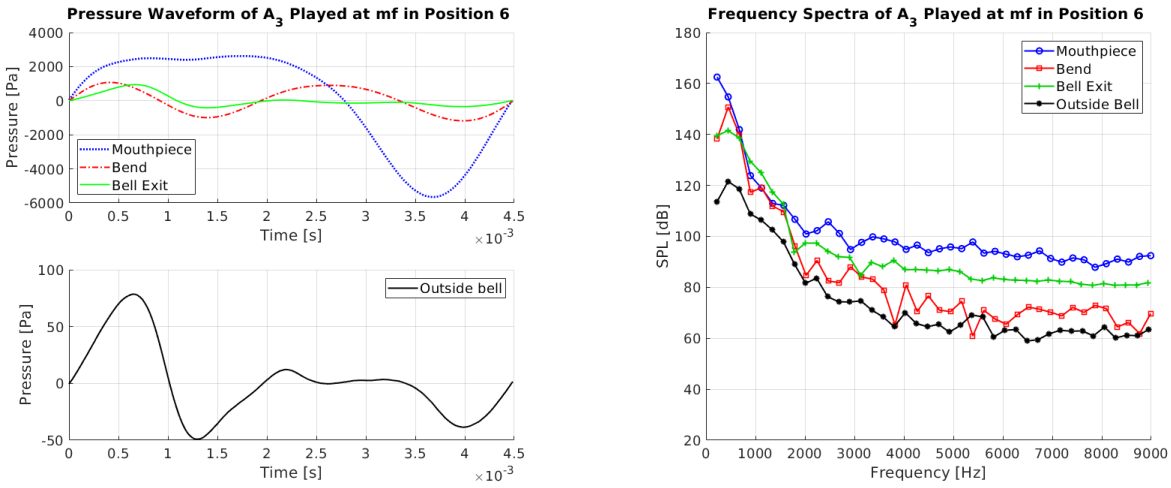

Figure 2.13: Time pressure waveforms (left) and the corresponding spectral components (right) of the A_3 played at *mf* on the trombone in position 6.

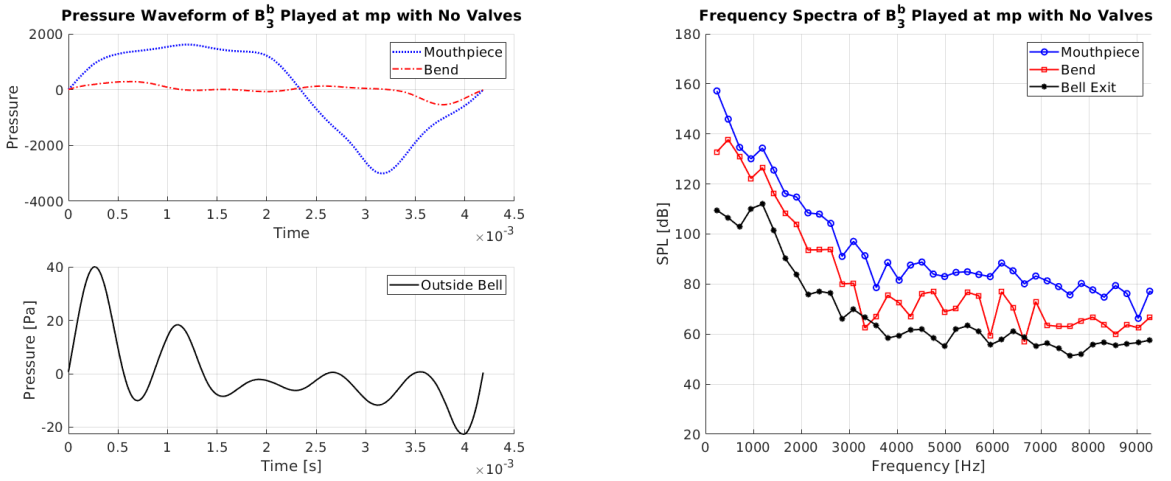

Figure 2.14: Time pressure waveforms (left) and the corresponding spectral components (right) of the B_3^f played at *mp* on the trumpet where no valves are compressed.

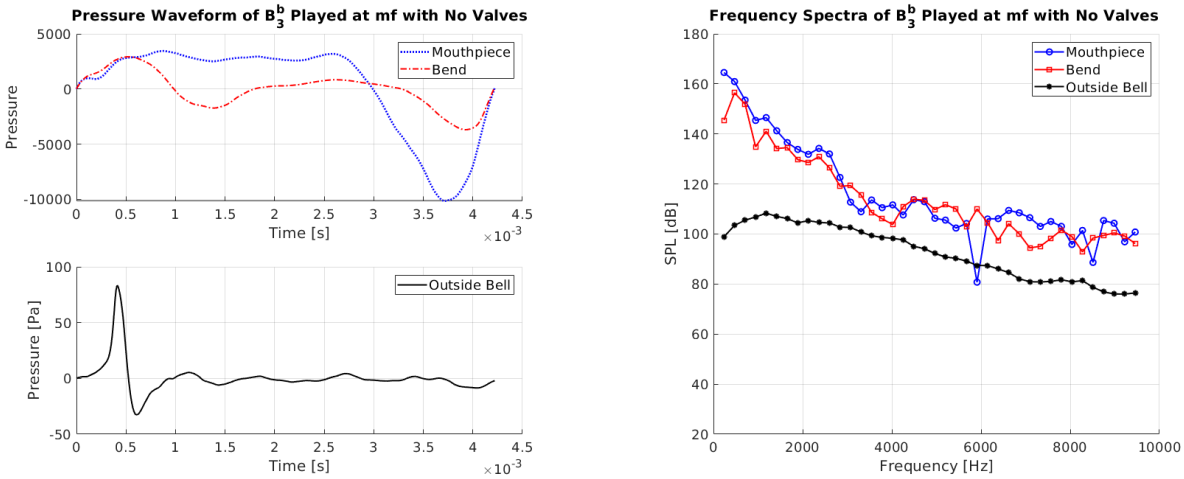

Figure 2.15: Time pressure waveforms (left) and the corresponding spectral components (right) of the B_3^b played at *mf* on the trumpet where no valves are compressed.

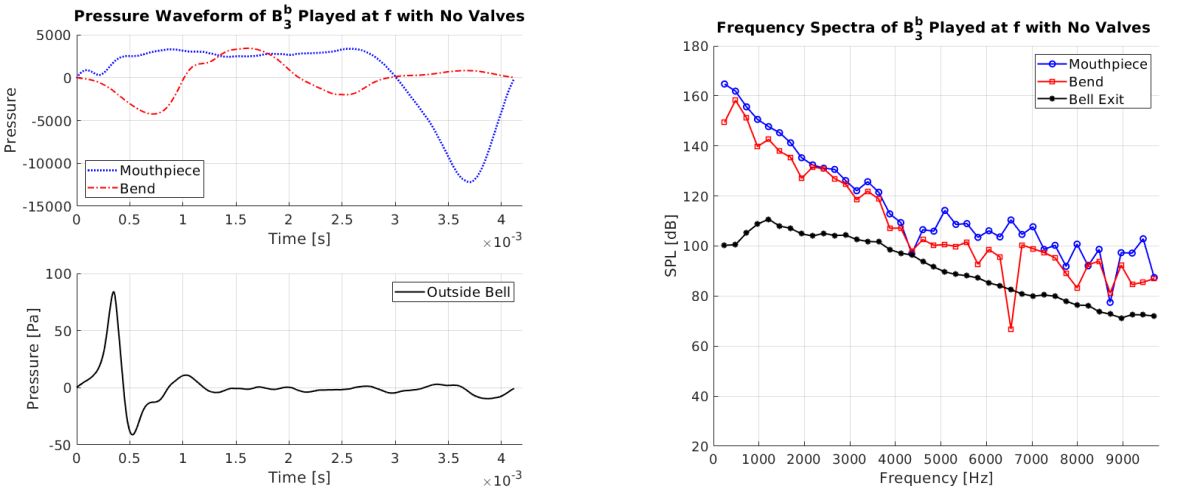

Figure 2.16: Time pressure waveforms (left) and the corresponding spectral components (right) of the B_3^b played at *f* on the trumpet where no valves are compressed.

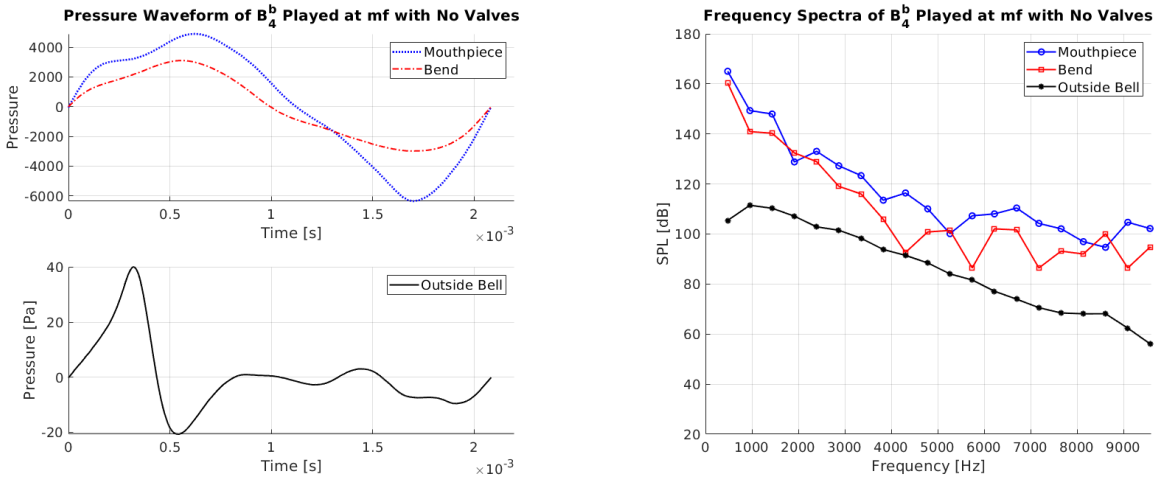

Figure 2.17: Time pressure waveforms (left) and the corresponding spectral components (right) of the B_4^b played at *mf* on the trumpet where no valves are compressed.

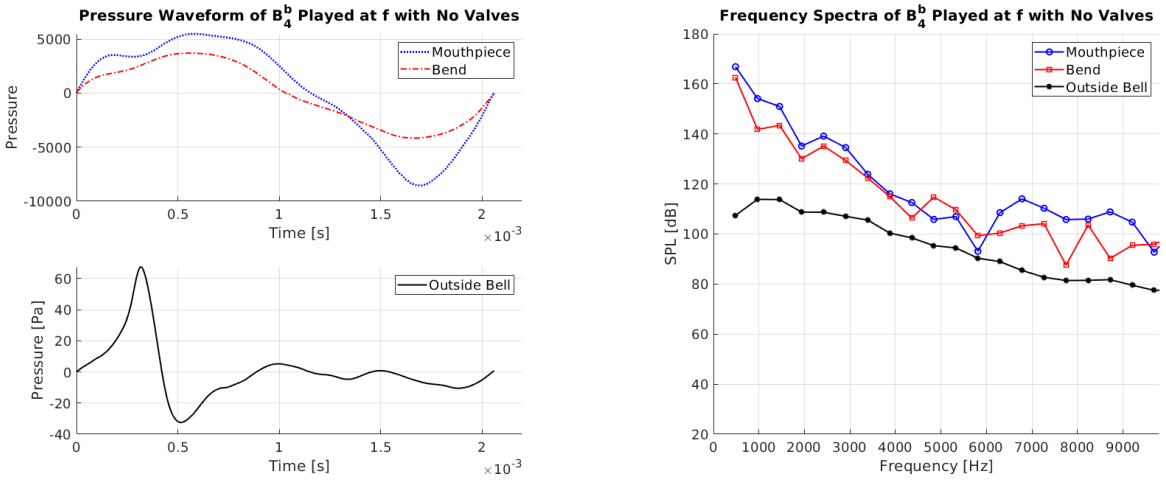

Figure 2.18: Time pressure waveforms (left) and the corresponding spectral components (right) of the B_4^b played at *f* on the trumpet where no valves are compressed.

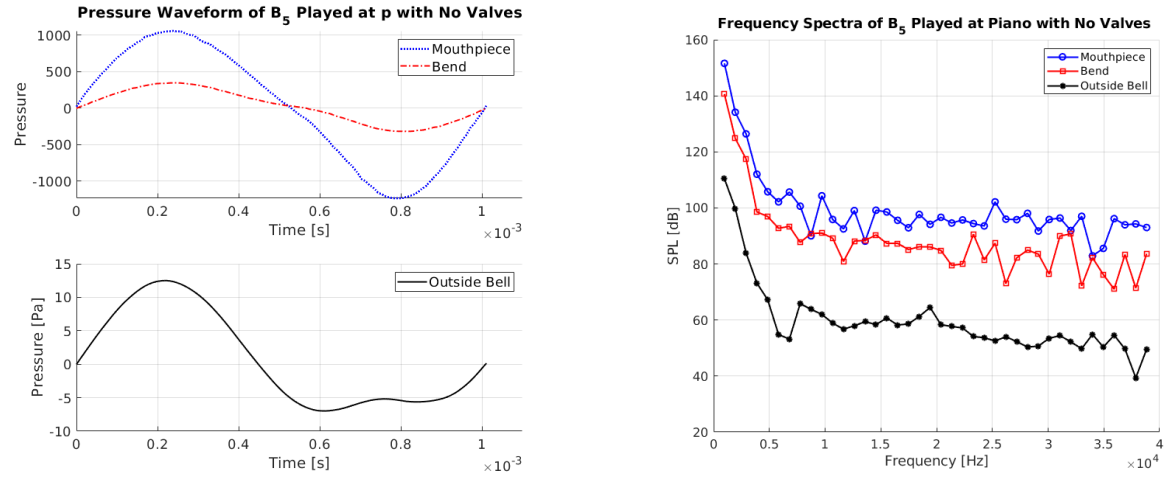

Figure 2.19: Time pressure waveforms (left) and the corresponding spectral components (right) of the B_5 played at p on the trumpet where no valves are compressed.

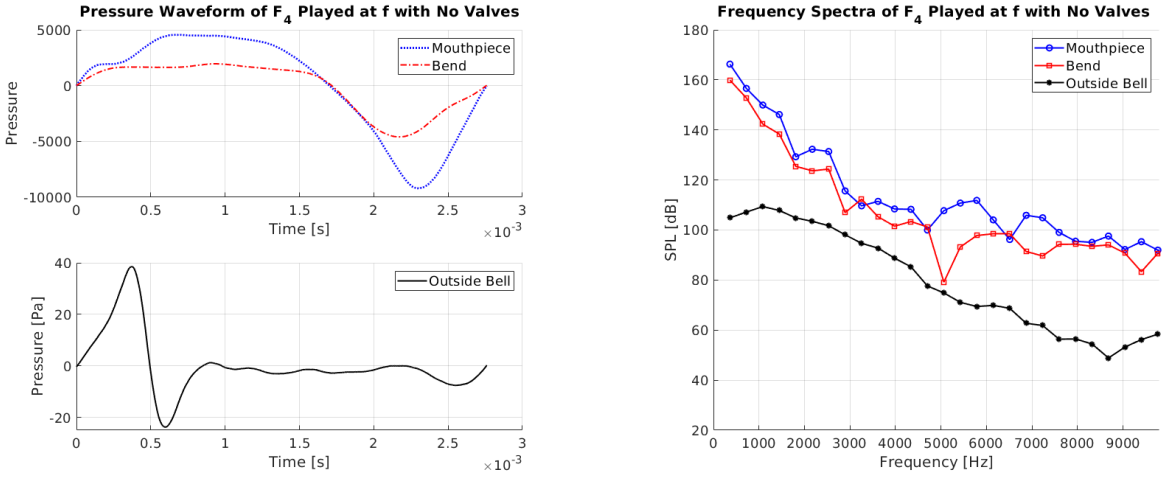

Figure 2.20: Time pressure waveforms (left) and the corresponding spectral components (right) of the F_4 played at f on the trumpet where no valves are compressed.

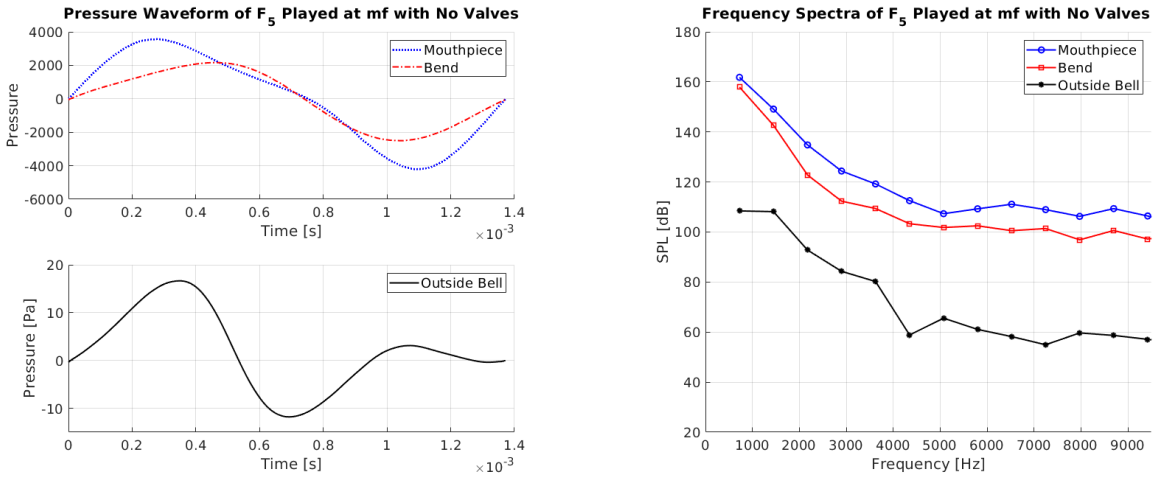

Figure 2.21: Time pressure waveforms (left) and the corresponding spectral components (right) of the F_5 played at *mf* on the trumpet where no valves are compressed.

2.3.1 Verifying Spectral Enrichment for Loudly Played Notes

Previous findings suggest that loudly played musical tone

An F_3 in position 1 was played on the trombone over a duration of three seconds with a sampling frequency of $f_s = 100$ kHz. The musician began at a playing dynamic of *p* and then applied a steady crescendo until the volume level reached *f*. The purpose of this experimental trial was to investigate how the harmonic spectrum changed in time while steadily increasing the SPL. In such situations, i.e., where the vibration frequency of the collected data changes with time, a spectrogram can be useful to analyze the information. It is a visual representation of the spectral power as it changes with time where the time data is partitioned and the power at any instant is represented by colour. A FFT is applied to the data in each time interval and then can be overlapped to visualize how both the amplitude and frequency vary over time [146], [210].

The recorded pressure waveforms collected at Mic $_{\text{Mouthpiece}}$, Mic $_{\text{Bend}}$ and Mic $_{\text{Outside-Bell}}$ are therefore depicted along with their spectrograms in Figure 2.22. All the spectrograms clearly demonstrate that as the playing volume increases, more of the higher harmonic components are excited. This is particularly evident near $t = 2.5$ s.

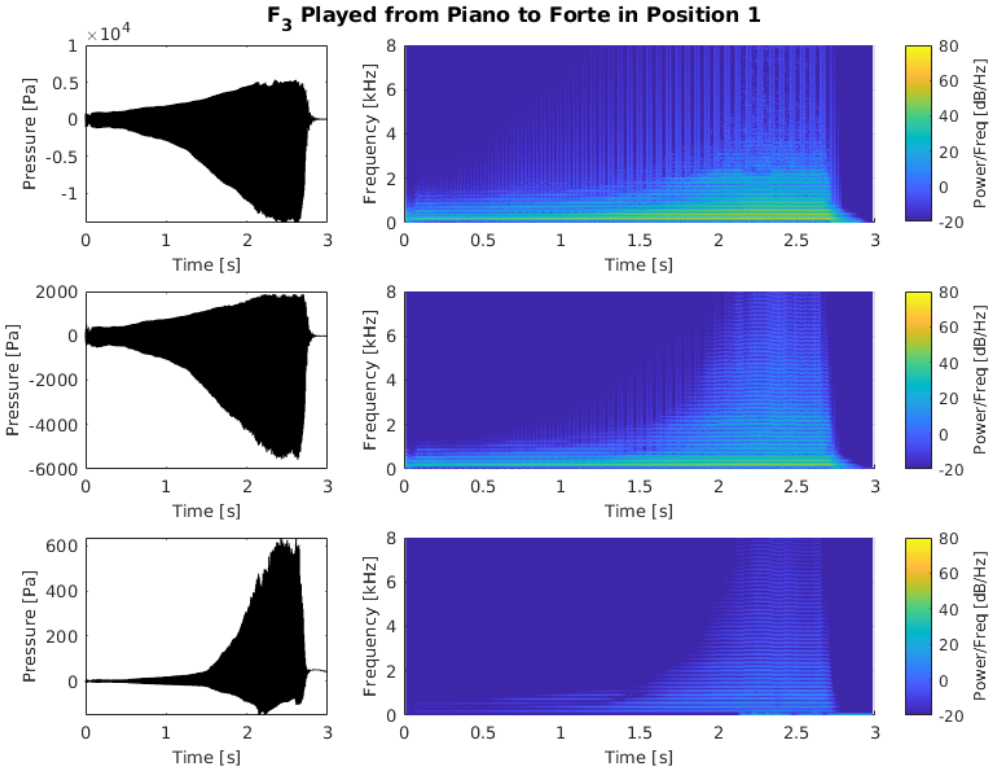

Figure 2.22: F_3 note played on the trombone in position 1 where the volume changes from $p \rightarrow f$. The time pressure waveforms recorded at Mic $_{\text{Mouthpiece}}$, Mic $_{\text{Bend}}$, and Mic $_{\text{Outside-Bell}}$ are shown (left) along with their spectrograms (right).

To further justify the claim that loudly played notes lead to spectral enrichment, B_3^b notes were played at *mp* and *ff* on the trombone in position 1 and recorded once the note was steady. Similarly, a *mp* and *f* B_3^b was produced on the trumpet when the valves were uncompressed. The purpose of this experiment was to compare the harmonic distribution between quiet and loud notes and determine whether the findings are consistent between the different instruments.

Since each cycle of the sound wave is essentially periodic, a single period of each B_3^b note was isolated manually and transformed into the frequency-domain to make the analysis more straight-forward. The number of points, denoted by N, was determined by manually finding the length of a period. The sampling frequency was again $f_s = 100$ kHz. The DFT of pressure, denoted by $\mathcal{P}$, was determined by using the expression $\mathcal{P} = \left(\frac{1}{N}\right)\texttt{fft}(p)$ and

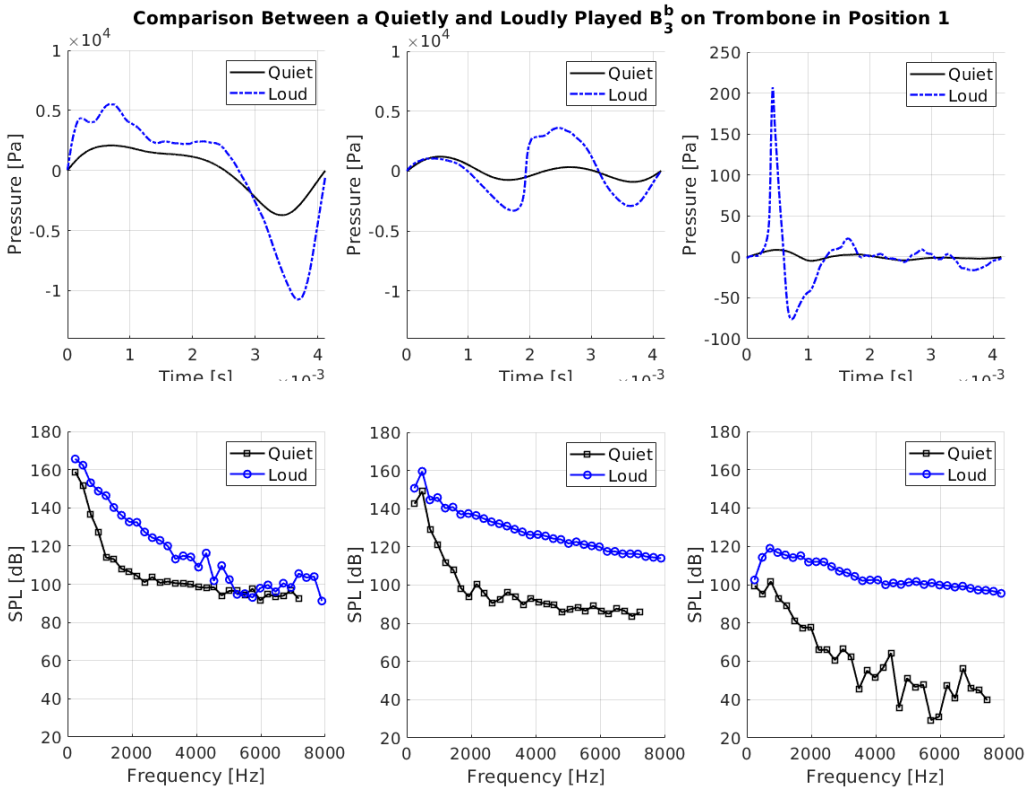

Figure 2.23: B_3^b note played on the trombone in position 1 at *mp* and *ff*. The spectral components of one period of the time pressure waveforms measured at Mic $_{\text{Mouthpiece}}$ (left), Mic $_{Bend}$ (middle) and Mic $_{\text{Outside-Bell}}$ (right) are shown.

the corresponding amplitude for each harmonic component of the pressure was converted to SPL dB using equation (2.2).

One period of the pressure waveforms and their spectra are shown in Figures 2.23 and 2.24 for the trombone and trumpet, respectively. From these plots, it is clear to see the difference in the harmonic distribution between the playing dynamics, especially at Mic $_{\text{Outside-Bell}}$. In particular, outside the bell we observe much more energy in all frequency components from f_2 onward for both instruments. We also see very similar characteristics in the time-domain between the B_3^b's produced on the trumpet versus the trombone. However, we found that the *ff* trombone wave measured at Mic $_{\text{Outside-Bell}}$ has a much higher pressure peak (∼200 Pa) compared to the trumpet B_3^b (∼80 Pa). At first, this may seem odd but recall, the trombone bore is much longer than the trumpet's, so the wave has

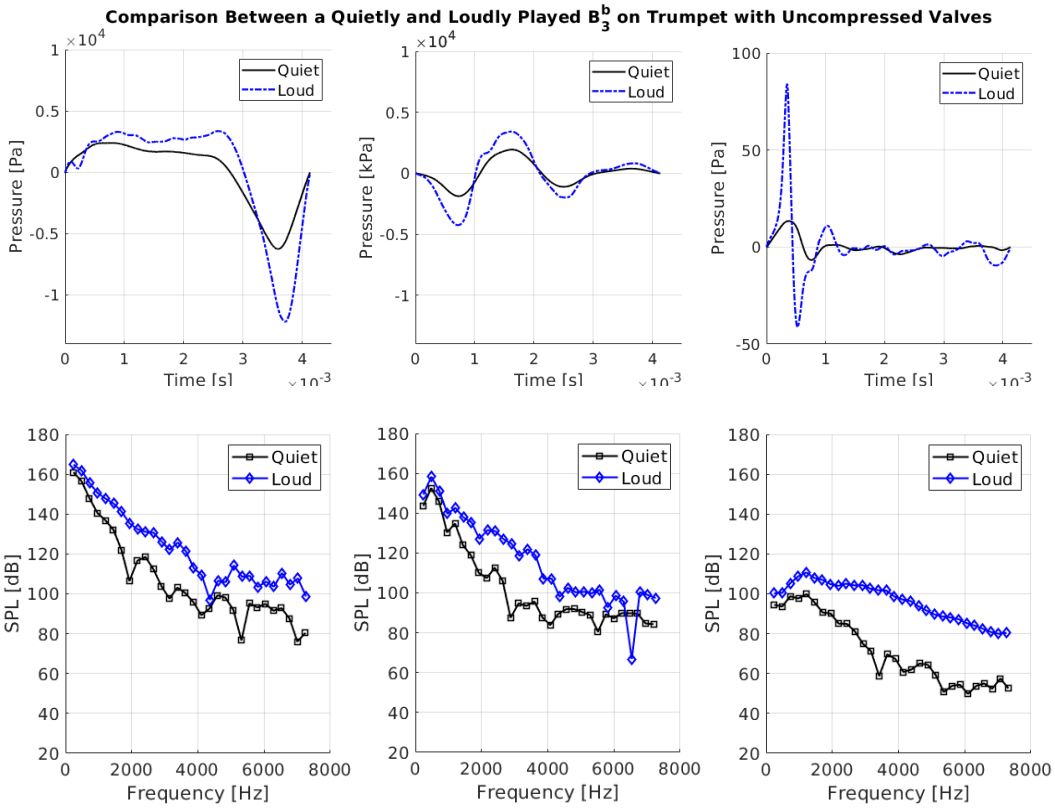

Figure 2.24: B_3^b note played on the trumpet with no valve compression played at *mp* and *f*. The spectral components of one period of the time pressure waveforms measured at Mic $_{\text{Mouthpiece}}$ (left), Mic $_{\textit{Bend}}$ (middle) and Mic $_{\text{Outside-Bell}}$ (right) are shown.

"more room/time" to steepen[14]. This means more of the associated effects due to wave steepening accumulate thereby producing a brassier sound. Moreover, a very steep jump in the trombone pressure can be seen at the Mic $_{\text{Bend}}$ and Mic $_{\text{Outside-Bell}}$ positions (Figure 2.23). The jump in pressure is so steep that it resembles a discontinuity. This could imply that a shock was produced within the instrument[15] (we will discuss this in more detail

[14] The trombone flare is also much larger than the trumpet bell, which directly influences what harmonic components of a signal are transmitted and reflected throughout the flare region. For the trumpet, frequencies greater than 1300 Hz - 1500 Hz mostly radiate from the bell. For the trombone however, frequencies larger than 700 Hz are mostly transmitted [20], [166].

[15] Typically, a physical shock is detected by checking whether the Mach number, which is the ratio of the moving object over the speed of sound, is greater than one [29], [30], [164]. However, we did not measure these parameters.

shortly).

From reviewing Figures 2.23 and 2.24 alone, it is difficult to determine which instrument is more prone to wave steepening. Therefore, an analysis outlined in [13] will be conducted to better understand the effects of nonlinear wave propagation. Let $\mathrm{SPL}_{\mathrm{total}}$ be the total SPL of all harmonics for a note measured at some position along the instrument, and SPL_{f_i} denote the SPL corresponding to the i^{th} harmonic component. Then, the ratio of the SPL associated with the i^{th} harmonic is

$$\varrho_{\mathrm{location}} = \frac{\mathrm{SPL}_{f_i}}{\mathrm{SPL}_{\mathrm{total}}}. \tag{2.3}$$

We then consider the ratio

$$\Phi = \frac{\varrho_{\mathrm{outlet}}}{\varrho_{\mathrm{inlet}}}. \tag{2.4}$$

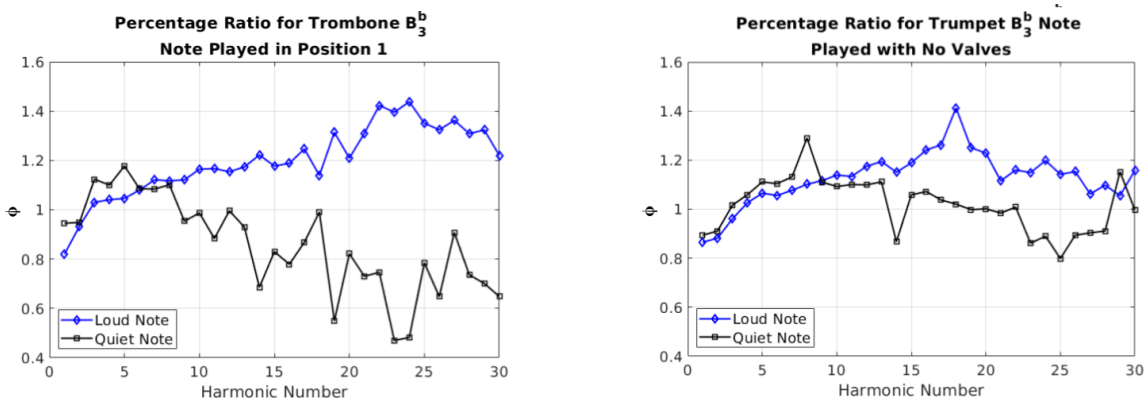

Figure 2.25: Harmonic percentage ratio, Φ from equation (2.4), for quietly and loudly played B_3^b notes produced on the trombone and trumpet from the data shown in Figures 2.23 and 2.24.

Φ is plotted for both instruments in Figure 2.25, and the effects due to wave steepening are rather pronounced, especially for the trombone[16]. The Φ curves (for both instruments) corresponding to the louder notes increase with harmonic number, and are much larger in amplitude compared to the quiet B_3^b notes. This is observed for frequencies above f_{10} and f_6 for the trumpet and trombone, respectively. This is indicative of spectral enrichment

[16] In [13], the authors explain that if $\Phi > 1$ then the instrument transmits the frequency. If the ratio remains constant as the SPL increases, the authors interpreted this to mean that the air-column does not significantly contribute to the wave distortion.

and is more prominent for the waves propagating through the trombone. It leads us to again question whether shock waves were produced for the *ff* note.

2.3.1.1 Generation of Shock Waves

The results presented above demonstrate that wave steepening becomes more prominent within brass instruments as the volume of a signal increases. Although there seem to be indications that a shock wave was produced in the trombone for the loudly played B_3^b, it is still difficult to say with certainty, as we could not measure the Mach number. Since we know that nonlinear wave behaviour leads to spectral enrichment of the higher frequency components, we could examine the number of harmonics needed to reconstruct the pressure waveform that has been transmitted from the bell.

To obtain a continuous expression for the pressure with respect to time, Fourier synthesis was applied to the measured pressure data. The musical notes can be written as a sum of sinusoidal waves with respect to the fundamental frequency, denoted by f_1, and corresponding harmonics, $f_2 = 2f_1$, $f_3 = 3f_1$,..., etc., each with a corresponding amplitude, denoted by A_i, and phase shift, denoted by ϕ_i. A harmonic component can be rewritten as a phase-shifted cosine[17]. Therefore, one period of the entire pressure waveform of a desired note is expressed as

$$p(t) = A_0 + 2\sum_{i=1}^{\frac{f_s}{2}} A_i \cos\left(2\pi f_i t + \phi_i\right), \tag{2.6}$$

where A_0 is the term corresponding to the direct current, and $\frac{f_s}{2}$ denotes the Nyquist frequency [63].

Equation (2.6) was truncated and $p(t)$ was considered with 10, 20, 50, 100, 150 and 200 harmonics. The reconstructed waveforms are plotted against the measured B_3^b pressure profiles in Figures 2.26 and 2.27. Upon visual inspection, there is little difference between the truncated data and experimental curves when 50 or more harmonics are considered[18].

[17] In particular, as a superposition of the real and imaginary parts with amplitudes a and b, i.e.,

$$a_i \cos(\omega_i t) + b_i \sin(\omega_i t) = A_i \cos\left(2\pi f_i t + \phi_i\right), \tag{2.5}$$

where $\omega_i = 2\pi f_i$ is the angular frequency. The amplitude is defined as $A_i = \sqrt{(a_i^2 + b_i^2)}$, and the corresponding phase angle is $\phi_i = \arctan\left(\frac{b_i}{a_i}\right)$.

[18] In previous studies, it is typical for only six to ten harmonics to be considered when describing a note, e.g., [13], [99], [179].

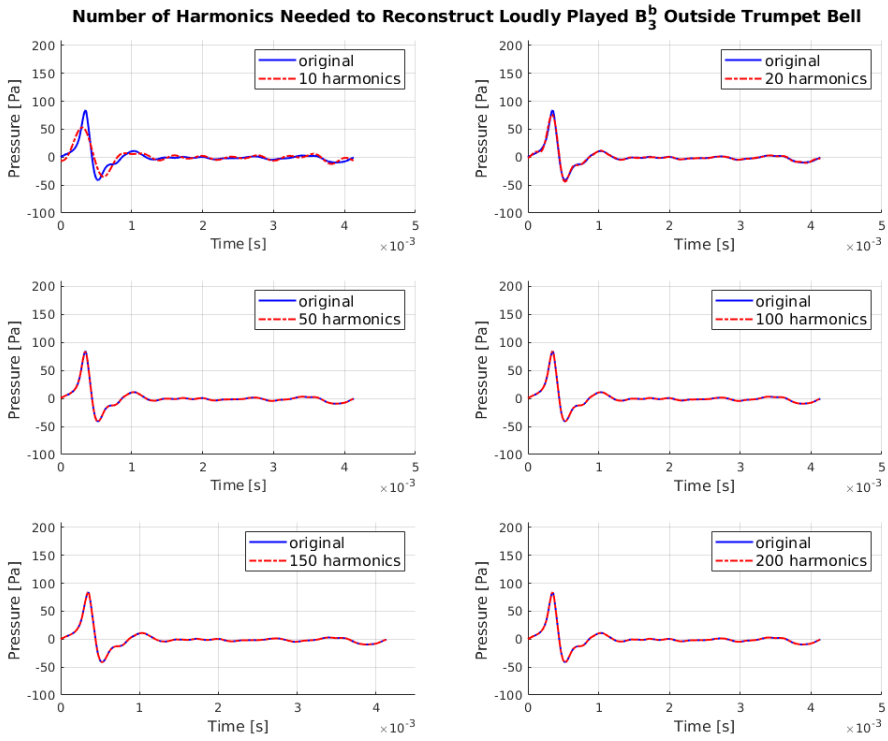

Figure 2.26: Reconstructed time pressure waveform of a loudly played B_3^b trumpet note measured at Mic $_{\text{Outside-Bell}}$ defined by equation (2.6) where 10, 20, 50, 100, 150 and 200 harmonics are considered. The $\mathbb{L}_2$ error for each reconstructed waveform can be found in Table 2.7.

But to be more rigorous, the relative error between the measured and truncated waveforms were computed using the $\mathbb{L}_2$ norm and are reported in Table 2.7. For the B_3^b played at *mp*, the relative error was found to be less than 0.1% for both instruments when 100 harmonics were considered. The B_3^b trumpet note played at *ff* had a relative error of 0.16%, but for the trombone, the error was above 4%[19]. As the number of harmonics considered to reconstruct the waveforms increased, the error for the loud trumpet note quickly decreased, whereas this was not the case for the loud trombone note.

Although there is growing evidence to support our suspicion that the pressure waveform

[19] Comparatively, for the *ff* B_3^b trumpet note to have a relative error near 4%, only 30 harmonics were required to reconstruct the waveform.

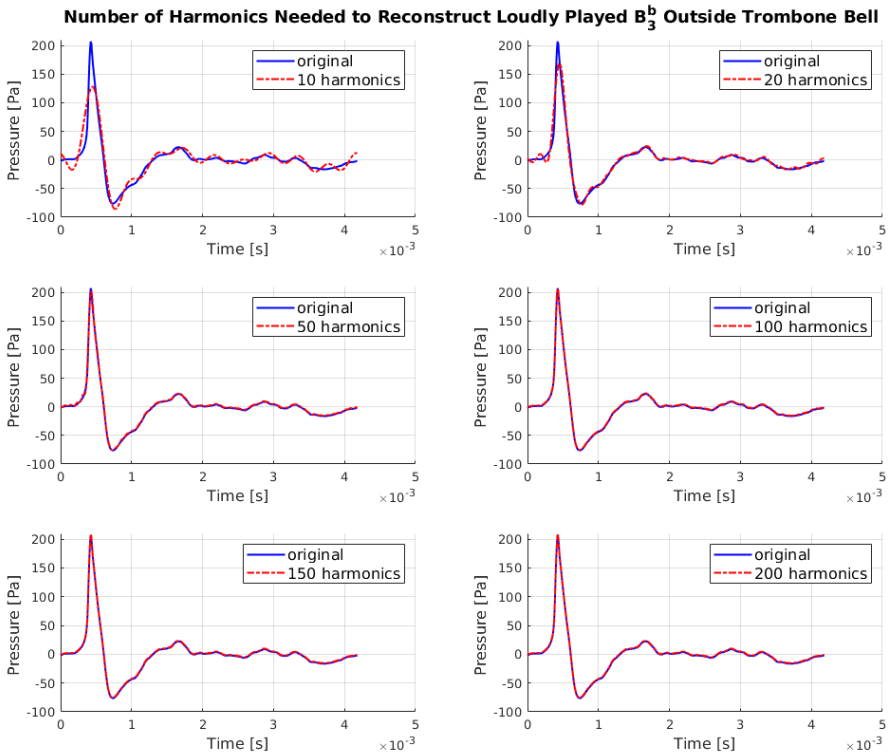

Figure 2.27: Reconstructed time pressure waveform of a loudly played B_3^b trombone note measured at Mic $_{\text{Outside-Bell}}$ defined by equation (2.6) where 10, 20, 50, 100, 150 and 200 harmonics are considered. The $\mathbb{L}_2$ error for each reconstructed waveform can be found in Table 2.7.

outside the trombone bell in Figure 2.27 could be the result of a shock wave, we still need to substantiate this claim mathematically. We will therefore examine whether it is theoretically possible for a shock wave to form within the tubing prior to the bell. The distance at which the shock forms is known as the *shock distance* and can be approximated by

$$x_s = \frac{2\gamma p_0 c}{(1+\gamma)\left(\frac{\partial p}{\partial t}\right)_{max}}, \tag{2.7}$$

where γ is the specific heat ratio for air, c is the speed of sound in air, and p_0 is atmospheric pressure. Equation (2.7) is the standard expression used in the acoustics literature and was considered by Hirschberg *et al.* in [99]. A derivation of x_s can be found in Appendix

Table 2.7: $\mathbb{L}_2$ error associated with the number of harmonics used to reconstruct the pressure waveforms of the B_3^b notes played on the trumpet and trombone that were measured at Mic $_{\text{Mouthpiece}}$. The measured and reconstructed waveforms are compared in Figure 2.26 and 2.27 for the trumpet and trombone, respectively.

Number of Harmonics	Error for Trumpet Notes		Error for Trombone Notes	
At $\text{Mic}_{\text{Outside-Bell}}$	Quiet B_3^b	Loud B_3^b	Quiet B_3^b	Loud B_3^b
10	1.3%	35 %	0.5 %	58 %
20	0.2 %	6.6 %	0.4 %	31 %
50	8.9e-02 %	0.8 %	0.1 %	7.4 %
100	4.2e-02 %	0.2 %	9.9e-02 %	4.6 %
150	2.3e-02 %	9.3e-02 %	7.5e-02 %	4.4 %
200	9.6e-03 %	2.4e-02 %	9.8e-03 %	4.4 %

C. It allows us to determine (in the ideal case) whether a shock could form within a certain region of the instrument given a specific $\frac{\partial p}{\partial t}$ at the inlet. It is unlikely that a shock would form within the bell itself because as the wave travels through the flare expansion, it will spread out thereby decreasing in amplitude.

The values for x_s are reported in Table 2.8 for the B_3^b notes shown in Figures 2.23 and 2.24. Using equation (2.7), we found that it was only possible for a shock to form for the *ff* note produced by the trombone. In particular, we calculated that $x_s = 1.78$ m, which is in the main tubular region prior to the flare expansion. In Section 5.5.3, we will simulate these notes through a computational trumpet and trombone to numerically verify if a shock forms within either instrument.

Table 2.8: Calculated shock distance for the B_3^b notes shown in Figures 2.23 and 2.24.

	Trumpet Notes		Trombone Notes	
	Quiet B_3^b	Loud B_3^b	Quiet B_3^b	Loud B_3^b
$\left(\frac{\partial p}{\partial t}\right)_{\max}$	7.6 MPa/s	13 MPa/s	4.3 MPa	23 MPa/s
x_s	5.30 m	2.96 m	9.44 m	1.78 m

2.3.2 Examining the Change in Bore Length

We were curious to see what would happen if the playing position of the trombone was altered during play while simultaneously increasing the SPL. So we ran another experimental trial where a F_3 note was played while the volume increased from $mf \rightarrow f$. Simultaneously, the player altered the tubing configuration to change from position 6 $\rightarrow$ position 1. The note was held for a duration of approximately one second and $f_s = 100$ kHz.

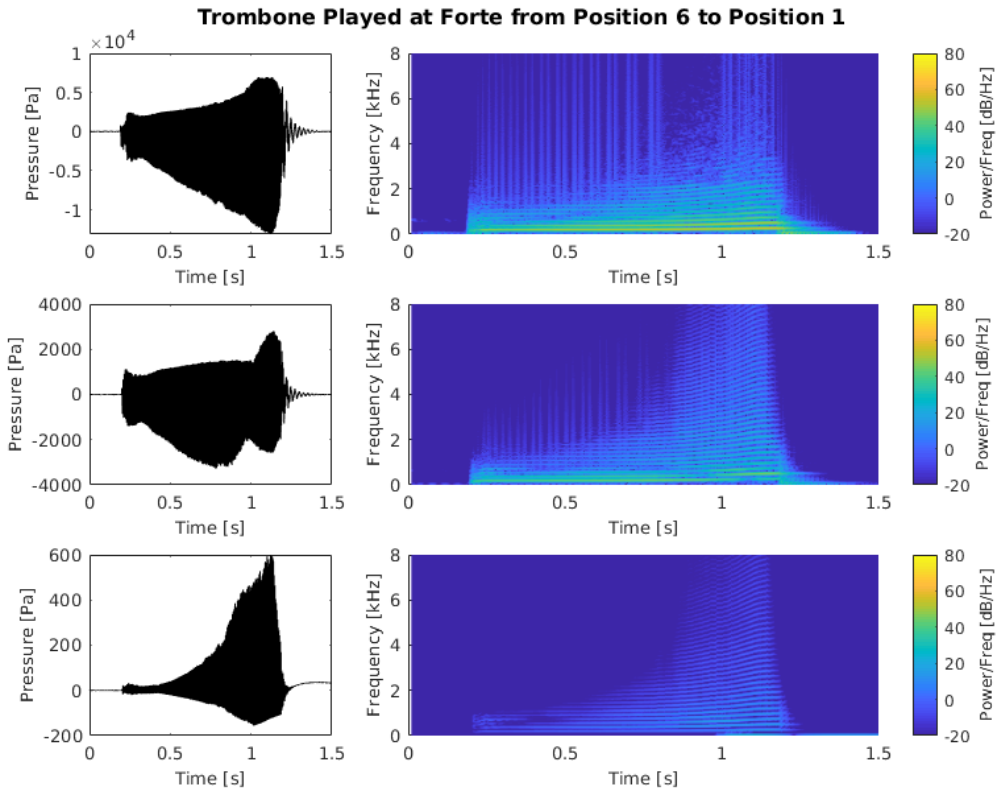

Figure 2.28: F_3 note played at $mf \rightarrow f$ on the trombone while the slide transitioned from position 6 $\rightarrow$ position 1. The time pressure waveforms measured at Mic $_{\text{Mouthpiece}}$ (top), Mic $_{\text{Bend}}$ (middle) and Mic$_{\text{Outside-Bell}}$ (bottom) are shown (left) along with their spectrograms (right).

The recorded pressure waveforms and corresponding spectrograms are shown in Figure 2.28. The spectrograms illustrate that the effect of the crescendo was exaggerated. This is

because while the F_3 note was being played, changing the position of the slide decreased the total length of the instrument by almost 50 cm. Figure 2.28 also captures how the F_3 dies off, i.e., the response in SPL when the note stops being produced. In particular, we see from the Mic $_{\text{Mouthpiece}}$ spectrogram that frequencies over 2000 Pa stop being generated immediately, while the harmonics below 2000 Pa decrease in SPL systematically (from highest to lowest). A similar affect can be seen at Mic $_{\text{Bend}}$. However, for the pressure sampled at Mic $_{\text{Outside-Bell}}$, all frequency components die away nearly at the same time (though, there is a slight lag for the lowest frequency components). This is consistent with findings published in [190] in which the authors describe that "*considering in turn each of the harmonics from the fundamental frequency, the attack tends to be slower and the release faster, so the harmonics seem to appear one after the other and fade out in the opposite way. Therefore, the sound gradually becomes brighter during the attack, until it reaches its maximum in the steady-state and it gets darker during the release*" [190].

2.3.3 Accelerometer Measurements

According to Kausel, the timbre associated with the radiated sound field from a brass instrument is influenced by the structural vibrations of the bore [113]. But, for this effect to be substantial, there must be significant vibrational amplitudes over a range of frequencies. To investigate the vibrational motion of the bell, accelerometers were used to evaluate the importance and prominence of such behaviour.

Accelerometers are also a useful tool for the purpose of studying shock waves and the corresponding vibrational affects [33]. The vibrating structure examined works by converting mechanical energy to electrical energy when experiencing acceleration, which is intrinsically a dynamic variable that is the result from the application of a net force on a body. Acceleration can be expressed in terms of g (equal to 9.81 m/s^2 on Earth) [33]. When analyzing vibration data in the time-domain (amplitude plotted against time), the typical parameters used to quantify the strength of the vibration profile are the amplitude, the peak-to-peak value, and the root mean square (rms) value[20].

The accelerometer results from playing certain notes on the trombone and trumpet will now be presented. All of the following data discussed in this section is from Experiment #4[21]. To review the collected accelerometer data, we filtered out frequencies above 5000

[20] The rms value is defined as the square root of the arithmetic mean of a set of numbers squared. The rms value is usually most useful since it is directly related to the energy content of the vibration profile and thus, the destructive capability of the vibration.

[21] Experiment #3 had similar results but only one accelerometer was used. Since similar findings were obtained from Experiment #4, we trust the collected data and think it is more informative.

Hz via a fifth order Butterworth filter[22].

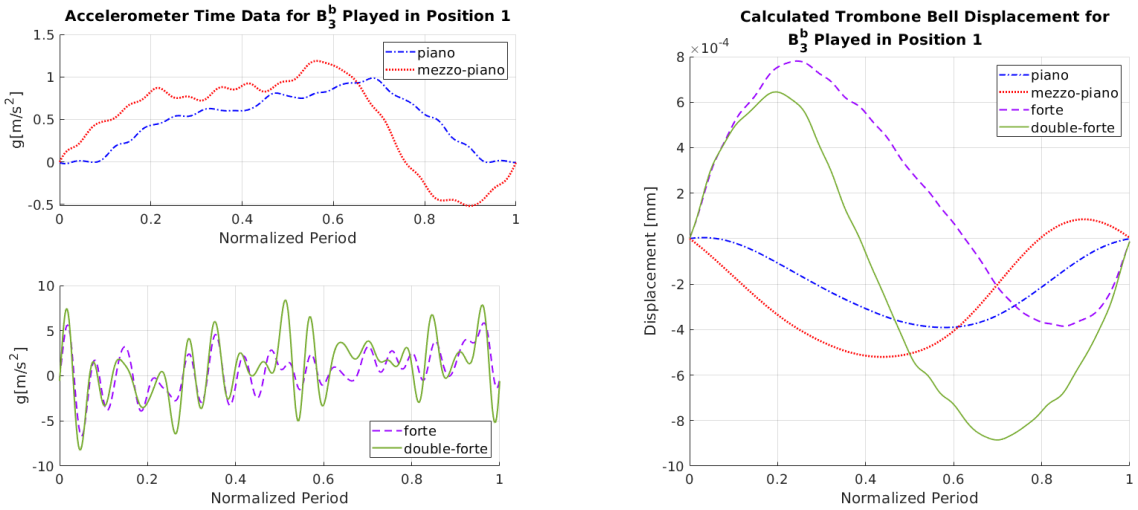

Figure 2.29: Acceleration data (left) and calculated trombone bell displacement (right) for B_3^b played at p, mp, f and ff on the trombone in position 1.

Table 2.9: SNR of accelerometer data corresponding to Figure 2.29.

Instrument	Note	Volume	SNR for Acc. 1	SNR for Acc. 2
Trombone - Position 1	B_3^b	p	19.5 dB	18.2 dB
Trombone - Position 1	B_3^b	mp	22.3 dB	20.5 dB
Trombone - Position 1	B_3^b	f	-6.54 dB	-2.27 dB
Trombone - Position 1	B_3^b	ff	-9.70 dB	-6.56 dB

[22] A fifth order Butterworth filter was used via the `butter()` function in Matlab where the asymptotic roll-off of an nth order is 20n dB/decade. Although we cannot design a filter with zero phase, we can design a "zero phase" filter using the `filtfilt()` function. This processes the accelerometer signal both in the forward and backward direction and will not change the time position of the signal much.

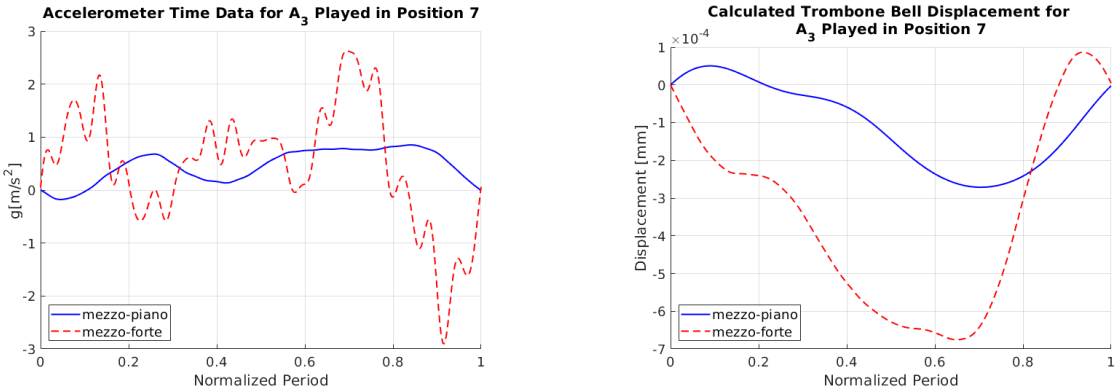

Figure 2.30: Acceleration data (left) and calculated trombone bell displacement (right) for A_3 played at *mp* and *mf* on the trombone in position 7.

Table 2.10: SNR of accelerometer data corresponding to Figure 2.30.

Instrument	Note	Volume	SNR for Acc. 1	SNR for Acc. 2
Trombone - Position 7	A_3	*mp*	17.9 dB	12.4 dB
Trombone - Position 7	A_3	*mf*	-2.18 dB	-1.73 dB

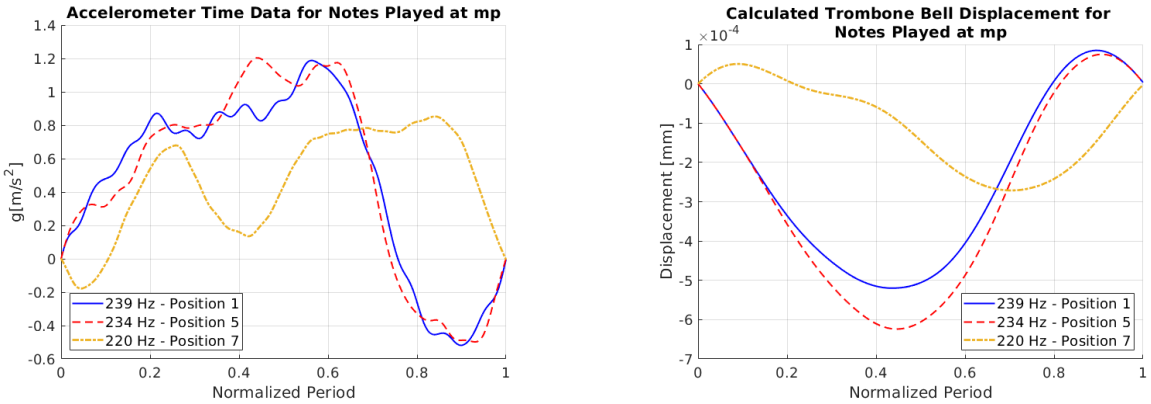

Figure 2.31: Acceleration data (left) and calculated trombone bell displacement (right) for 239 Hz note played in position 1, 234 Hz note played in position 5, and 220 Hz note played in position 7 all at *mp*.

Table 2.11: SNR of accelerometer data corresponding to Figure 2.31.

Instrument	Note	Volume	SNR for Acc. 1	SNR for Acc. 2
Trombone - Position 1	239 Hz	*mp*	19.5 dB	18.2 dB
Trombone - Position 5	234 Hz	*mp*	25.8 dB	20.1 dB
Trombone - Position 7	220 Hz	*mp*	17.9 dB	12.4 dB

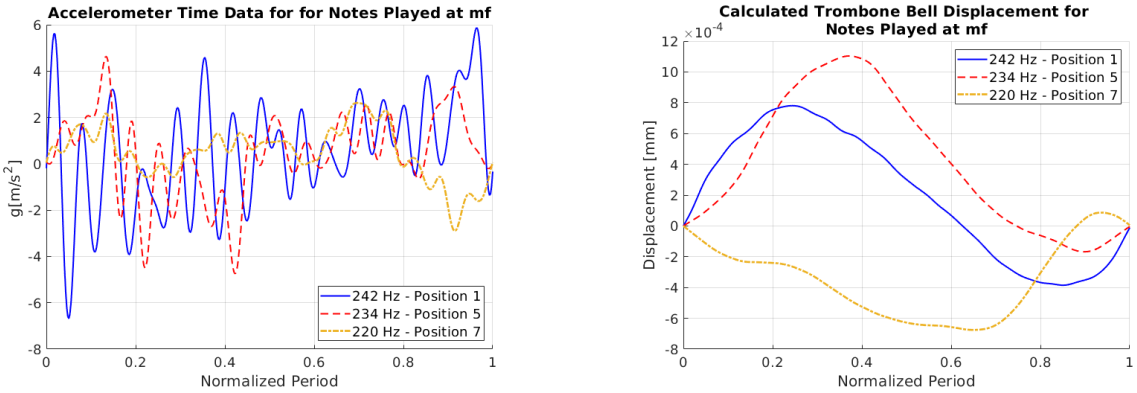

Figure 2.32: Acceleration data (left) and calculated trombone bell displacement (right) for 242 Hz note played in position 1, 234 Hz note played in position 5, and 220 Hz note played in position 7 all at *mf*.

Table 2.12: SNR of accelerometer data corresponding to Figure 2.32.

Instrument	Note	Volume	SNR for Acc. 1	SNR for Acc. 2
Trombone - Position 1	242 Hz	*f*	-6.54 dB	-2.27 dB
Trombone - Position 5	234 Hz	*mf*	-5.05 dB	-2.62 dB
Trombone - Position 7	220 Hz	*mf*	-2.19 dB	-1.73 dB

In addition to examining the acceleration data, the signal-to-noise ratio (SNR), which is defined as the ratio of the signal power to the noise power in decibels, for the accelerometers was calculated in Matlab. If the obtained value is larger than 0 dB it indicates that there is more signal than noise. Analyzing the SNR may give a better indication on whether a shock was produced. In particular, if a shock wave was generated, more noise should be present in the signal.

To better interpret the flare vibrations from a structural analysis perspective, the bell displacement from the accelerometer data was also calculated. To account for drift/noise when numerically integrating, the mean of the acceleration was subtracted from the acceleration signal to obtain velocity. To then find the displacement, the mean of the velocity was subtracted from the velocity signal before the numerical integration was performed[23].

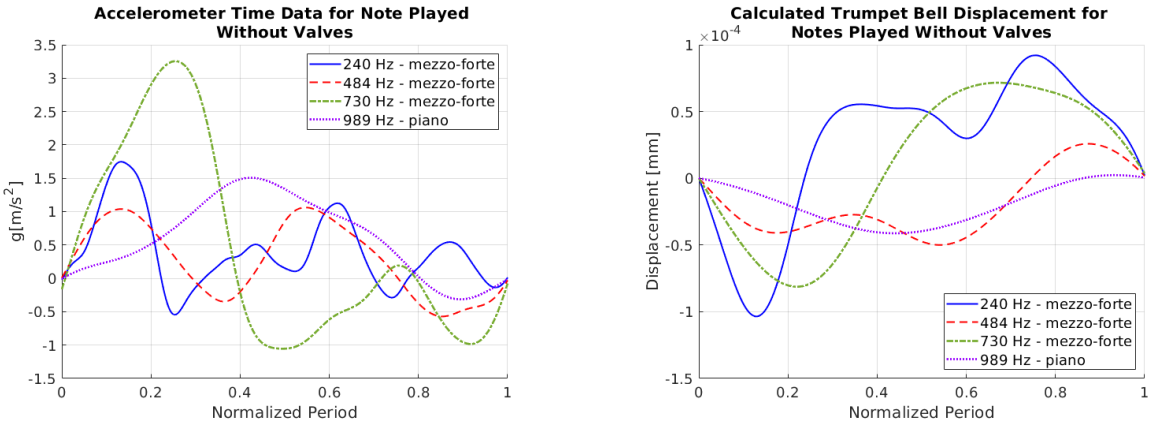

Figure 2.33: Acceleration data (left) and calculated trumpet bell displacement (right) for 240 Hz note played at *mf*, 484 Hz note played *mf*, 730 Hz note played *mf* and 989 Hz note played at *p* where the valves are uncompressed.

Table 2.13: SNR of accelerometer data corresponding to Figure 2.33.

Instrument	Note	Volume	SNR for Acc. 1	SNR for Acc. 2
Trumpet - No Valves	240 Hz	*mf*	-0.933 dB	2.15 dB
Trumpet - No Valves	484 Hz	*mf*	7.81 dB	0.563 dB
Trumpet - No Valves	730 Hz	*mf*	17.4 dB	0.829 dB
Trumpet - No Valves	989 Hz	*p*	6.52 dB	0.768 dB

In Figures 2.29 to 2.36, one period of the accelerometer time data and corresponding bell displacement from equilibrium is shown. Tables 2.9 to 2.16 report the SNR for both accelerometers for the notes in the mentioned figures. The trombone notes in particular are displayed in Figures 2.29 to 2.32 and Tables 2.9 to 2.12, whereas the trumpet information is depicted in Figures 2.33 to 2.36 and Tables 2.13 to 2.16.

[23] An approximation to determine the pressure amplitude associated with the vibrations of the flares can be found in Section 4.1.2.

As a quick remark, Figures 2.35 and 2.36 examine the B_3^b and B_4^b notes where the valves are not used. Both notes were played at *mf* as well as *ff*. We were interested in measuring these specific pitches because in [112], [113], [213], it is reported that the strongest resonant frequencies of the trumpet flare are near a B_4^b ([112], [113]) and B_3^3 ([213]). From comparing the acceleration corresponding to the *ff* B_3^b and B_4^b, we observe that the B_3^b is much more oscillatory (or spectral) but the vibrational amplitudes are similar. The difference between the SNR values of the accelerometers is largest for the *mf* B_4^b (with a difference of approximately 7.3 dB).

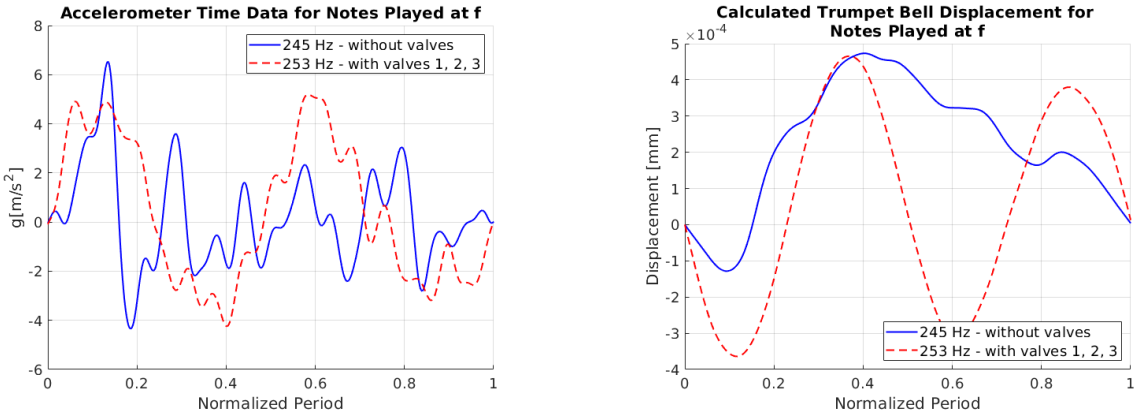

Figure 2.34: Acceleration data (left) and calculated trumpet bell displacement (right) for 245 Hz note played without compressed valves and 253 Hz note played with valves 1, 2, 3 compressed both at *f*.

Table 2.14: SNR of accelerometer data corresponding to Figure 2.34.

Instrument	Note	Volume	SNR for Acc. 1	SNR for Acc. 2
Trumpet - No Valves	245 Hz	*ff*	-3.95 dB	-0.777 dB
Trumpet - Valves 1,2,3	253 Hz	*f*	8.69 dB	-1.18 dB

Overall, if we compare the vibrational data between the trumpet and trombone, we find that generally:

i. As the volume of the note increases, the acceleration data becomes more spectral. This observation is further supported by the SNR values. From our experimental

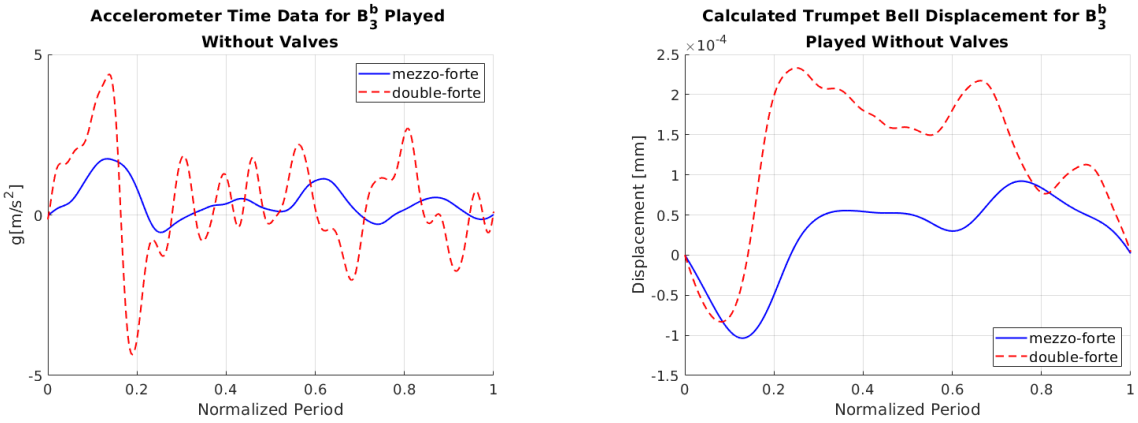

Figure 2.35: Acceleration data (left) and calculated trumpet bell displacement (right) for B_3^b played at *mf* and *ff* where the valves are uncompressed.

Table 2.15: SNR of accelerometer data corresponding to Figure 2.35.

Instrument	Note	Volume	SNR for Acc. 1	SNR for Acc. 2
Trumpet - No Valves	B_3^b	*mf*	-0.934 dB	2.15 dB
Trumpet - No Valves	B_3^b	*ff*	-5.58 dB	-0.834 dB

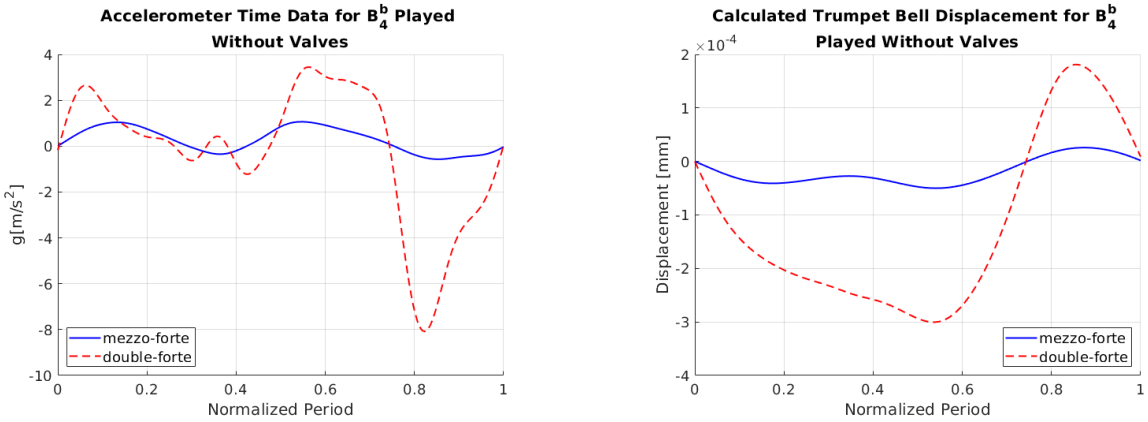

Figure 2.36: Acceleration data (left) and calculated trumpet bell displacement (right) for B_4^b played at *mf* and *ff* where the valves are uncompressed.

Table 2.16: SNR of accelerometer data corresponding to Figure 2.36.

Instrument	Note	Volume	SNR for Acc. 1	SNR for Acc. 2
Trumpet - No Valves	B_4^b	*mf*	7.81 dB	0.563 dB
Trumpet - No Valves	B_4^b	*ff*	2.00 dB	4.36 dB

data, the only exception we see is for the *ff* B_4^b played on the trumpet where no valves are compressed.

ii. As the volume of a note increases, the magnitude of the acceleration and thus, bell displacement increases.

iii The SNR values between the accelerometers differ much more for the trumpet compared to the trombone, especially for the 730 Hz trumpet note, which corresponds to an F_5.

iv. The bell displacements we obtained were on the order of 1 μm, which is consistent with results previously published in the literature, specifically [112], [113]. However, the displacement of the trombone bell was consistently larger than the trumpet flare by approximately two to three times.

We additionally wanted to evaluate the precise resonances contained in the collected vibrational data. Although the acceleration data is roughly periodic, we see from reviewing the SNRs that the louder a note is played, the more noise there is in the signal. Although Fourier transforms can be effectively used to analyze vibration when there is a finite number of dominant frequency components, power spectral densities (PSDs) better characterize random vibration signals[24]. A PSD is computed by multiplying each frequency bin in the FFT by its complex conjugate. This results in having only the real spectrum where the amplitude is expressed as $\frac{(\text{quantity-being-measured})^2}{\text{Hz}}$[25]. This is a key aspect that makes a PSD more practical than a FFT for random vibrational analysis - the amplitude value is normalized to the frequency bin width thereby eliminating the dependency on the bin width. This enables us to compare vibration levels for signals of various lengths [210], [218].

[24] The term 'power' is used because the magnitude of the PSD is the mean-square value of the signal being considered. It does not correspond to the physical quantity power measured in watts.

[25] So for example, the PSD of an acceleration signal would have units of $\frac{g^2}{\text{Hz}}$ with $\frac{g}{\sqrt{\text{Hz}}}$ and could be referred to as the acceleration spectral density [218].

Table 2.17: Musical notes played on the trombone and trumpet where the power spectral densities were calculated for the both accelerometers.

Instrument	Note	Volume Level	Tubing Configuration
Trombone	B_3^b	p	position 1
	B_3^b	mp	position 1
	B_3^b	f	position 1
	B_3^b	ff	position 1
	B_3/B_3^b	mp	position 5
	$A_3^\#/B_3$	mf	position 5
	A_3	mp	position 7
	A_3	mf	position 7
Trumpet	B_3^b	mf	no valves
	B_3^b	ff	no valves
	$B_3^b/B_3^\#$	f	valves 1, 2, 3
	B_4^b	mf	no valves
	B_4^b	ff	no valves
	F_5	mp	no valves
	F_5	mf	no valves
	B_5	p	no valves

Thus, the PSD of the accelerometer data for the notes played on the trombone listed in Table 2.17 are plotted in Figures 2.37 to 2.39. Figures 2.40 to 2.42 show the trumpet notes. An additional plot corresponding to the trumpet notes in Figure 2.33 can be found in Figure 2.43.

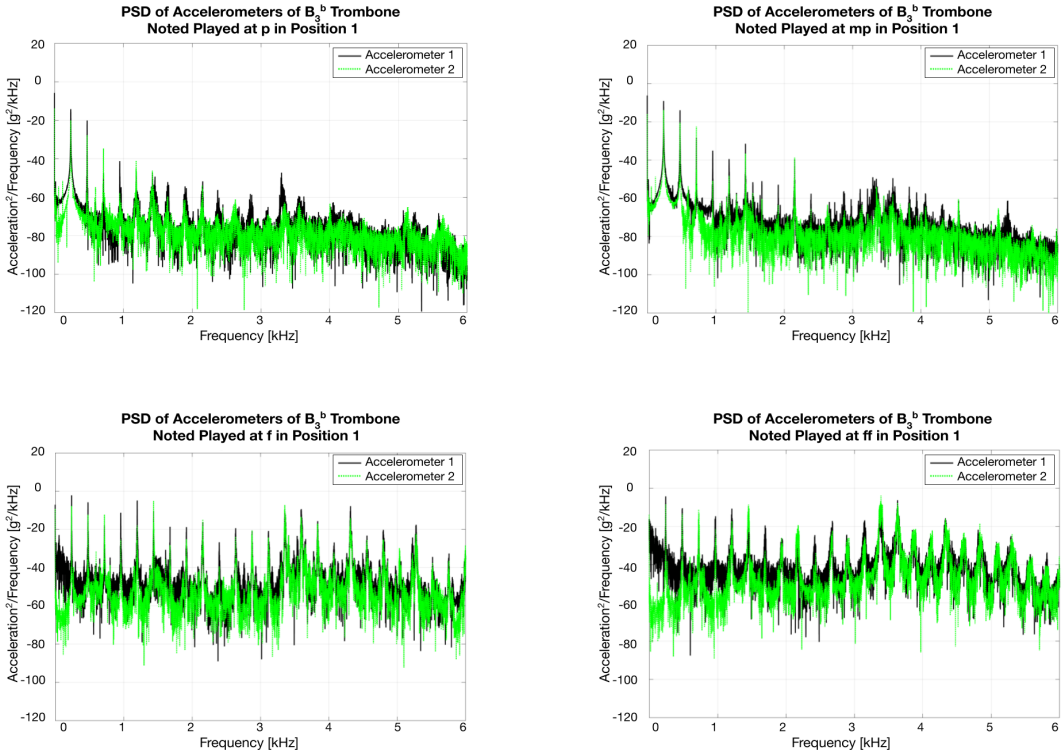

Figure 2.37: Calculated PSD associated with the trombone bell vibrations while playing B_3^b in position 1 at p (top-left), mp (top-right), f (bottom-left) and ff (bottom-right).

Although in Section 4.1.2.3 we will calculate the pressure that is produced from the vibrating bells, the intention behind examining the PSDs beforehand is to confirm which resonance peaks are present in the signals. As expected, the PSDs plots reveal that the peaks correspond with the harmonics of the musical note being played. The other motivation in this analysis was to verify in the frequency-domain that more resonances are excited as the volume of a note increases. We again observe this to be true for all musical notes and is particularly well demonstrated for the trombone in Figure 2.37, i.e., for the B_3^b was played at p, mp, f and ff in position 1, as well as Figure 2.39, i.e., when the trombone A_3 note played at mp and mf in position 7. However, if we consider the trumpet when all valves are compressed (Figure 2.40), the bell resonances become stronger as the volume of the note increases, but this effect is not as pronounced (though the trumpet notes compared were played at a different dynamic level, specifically mf and ff).

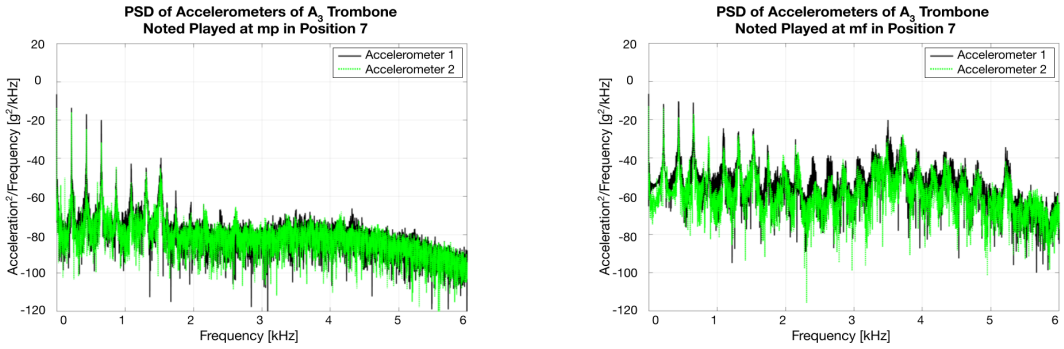

Figure 2.38: Calculated PSD associated with the trombone bell vibrations shown in Figure 2.30 while playing A_3 in position 7 at *mp* (left) and *mf* (right).

Figure 2.43, which plots the 240 Hz, 484 Hz, 730 Hz and 989 Hz trumpet notes, illustrates how the resonances behave as the frequency of the pitch increases. The 240 Hz, 484 Hz and 730 Hz notes were all played at *mf* and all have similar SPLs at Mic $_{\text{Mouthpiece}}$. However, the resonances for 484 Hz (B_4^b) are the strongest followed by the 730 Hz (F_5). The drop off in power of the higher resonances is of similar order but seems to be fastest for the F_5.

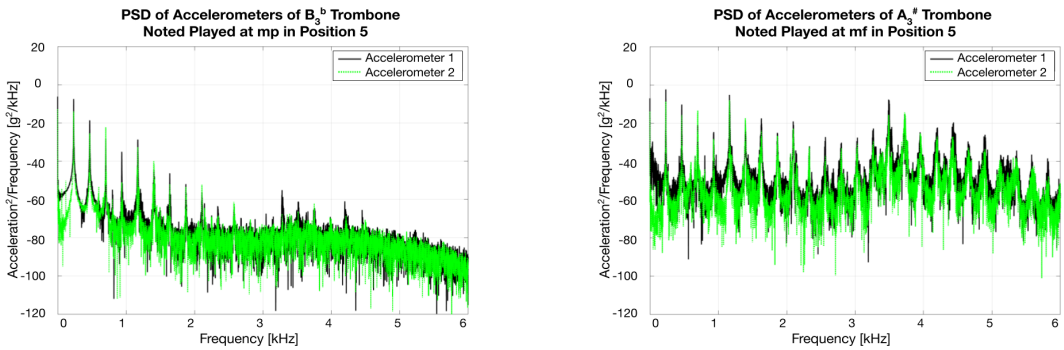

Figure 2.39: Calculated PSD associated with the trombone bell vibrations while playing a 234 Hz note (near B_3/B_3^b) at *mp* (left) and a 220 Hz note (near $A_3^{\#}/B_3$) at *mf* (right) both in position 5.

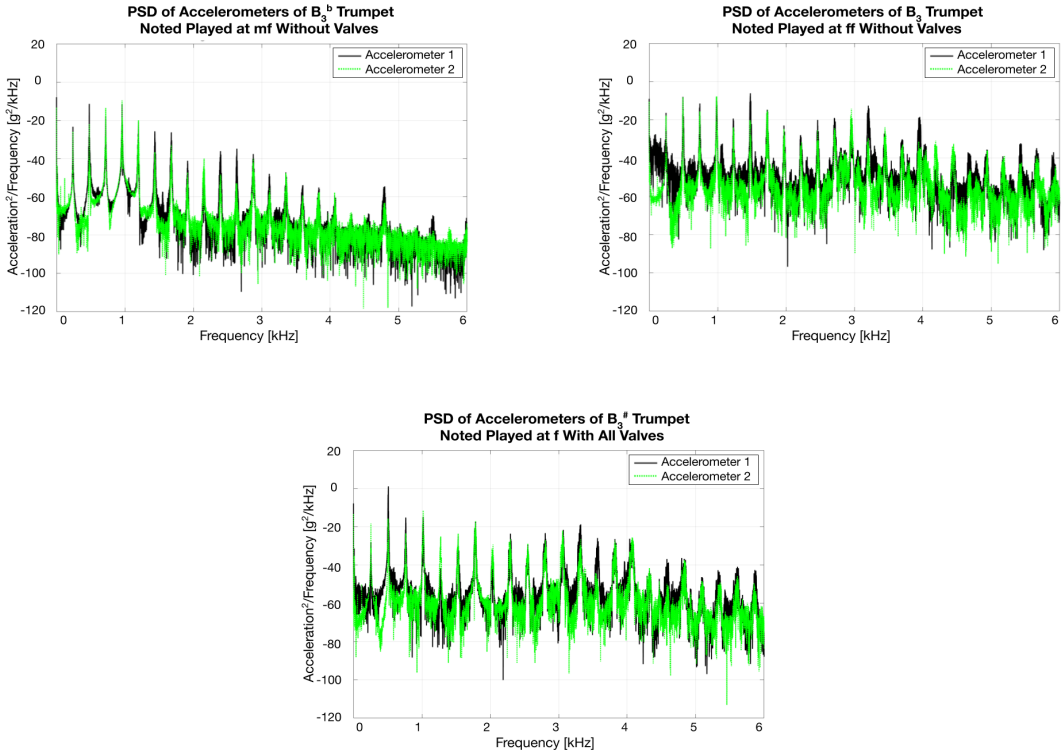

Figure 2.40: Calculated PSD associated with the trumpet bell vibrations while playing B_3^b in neutral position at *mf* (top-left) and *ff* (top-right) and a 245 Hz note (near $B_3^b/B_3^\#$) with all valves compressed at *f* (bottom).

Therefore, from the PSD plots, we have also verified that:

v. The resonances of the bell correspond with the harmonic frequencies of the musical notes being played.

vi. As the volume of a note increases, more of the resonances become excited and increase in amplitude.

Although we cannot verify that the strongest resonant frequency of the trumpet bell is near 484 Hz and that it has a dampening effect on the SPL [112], [113] (potentially decreasing it by as much as 6 dB [109]), our data does suggest that the vibratory effects near 484 Hz is stronger relative to our other measured notes.

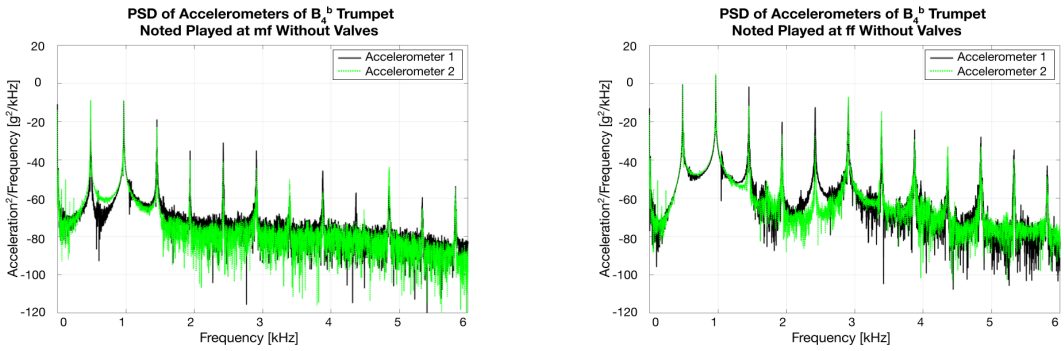

Figure 2.41: Calculated PSD associated with the trumpet bell vibrations while playing B_4^b in neutral position at *mf* (left) and *ff* (right).

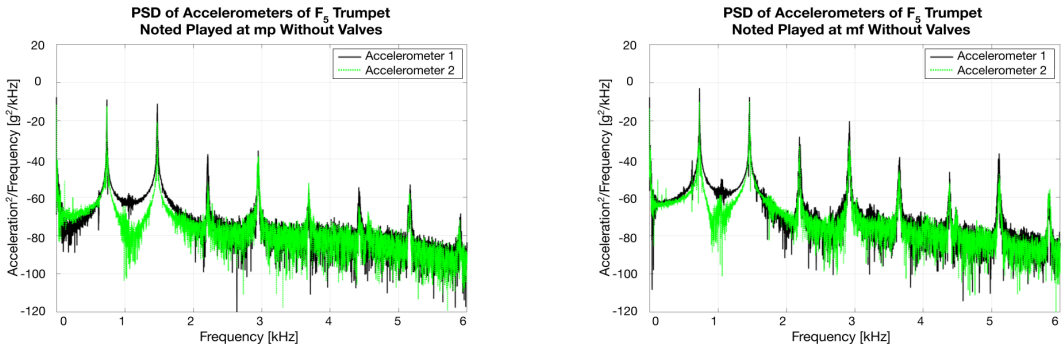

Figure 2.42: Calculated PSD associated with the trumpet bell vibrations while playing F_5 in neutral position at *mf* (left) and *ff* (right).

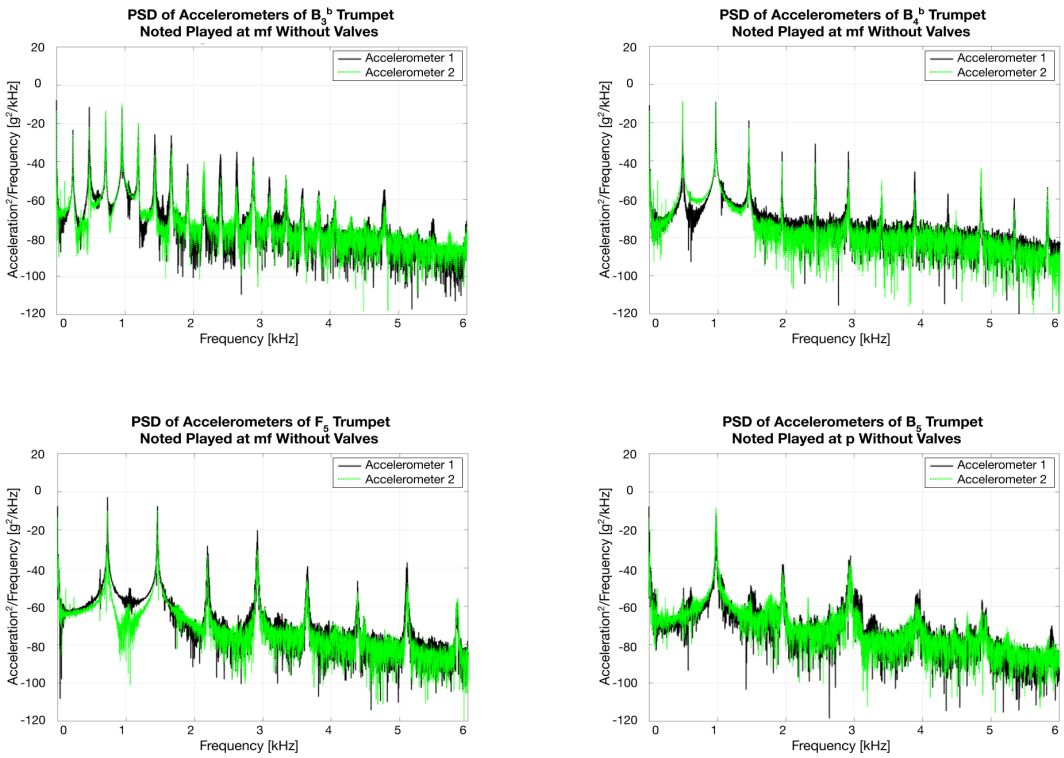

Figure 2.43: Calculated PSD associated with the trumpet bell vibrations while playing B_3^b at *mf* (top-left), B_4^b at *mf* (top-right), F_5 at *mf* (bottom-left) and B_5 at *p* (bottom-right).

Chapter 3

Mathematical and Numerical Fundamentals

This chapter will be dedicated to reviewing the chosen mathematical model and numerical method used to obtain the results presented in this thesis. Musical notes produced by a musician on a trumpet or trombone physically correspond to the creation of longitudinal pressure waves that propagate through air, which is characterized as a compressible fluid. If the air flowing through a horn does not exhibit any tangential stress then there would be no internal friction and no energy would be lost (so viscosity would not be a concern) [143]. Therefore, to model the acoustic behaviour associated with propagating sound waves in brass instruments, the equations from gasdynamics will be used [85].

This field is a branch of fluid mechanics, in which the underlying concepts are based on the conservation laws for mass, momentum and energy. In particular, the behaviour of a fluid is described with respect to the macroscopic properties of velocity $\vec{u}$, pressure p, density ρ, temperature T, and energy E. If one was merely interested in examining the laws at a point, then the equations of motion can be expressed in differential form. If the intent is instead to consider the governing laws in a region, the conservation laws need to be stated in integral form. The conservation laws required to describe the motion of a Newtonian, compressible fluid will be stated below. A more rigorous background of the thermodynamics and a derivation of each conservative law can be found in Appendix D.

3.1 Summary of the Equations of Motion

Consider a Newtonian, compressible, viscous fluid. The equation describing conservation of mass is called the *continuity equation* and is defined by

$$\frac{\partial \rho}{\partial t} + \nabla \cdot (\rho \vec{u}) = Q(t), \tag{3.1}$$

where the right hand side corresponds to the source term if one exists, otherwise $Q(t) = 0$. The equations describing conservation of momentum are referred to as the *Navier-Stokes equations* and written most generally as

$$\rho \left(\frac{\partial \vec{u}}{\partial t} + \vec{u} \cdot \nabla \vec{u} \right) = \nabla \cdot \tau + \vec{F}, \tag{3.2}$$

where $\vec{F} = (X, Y, Z)$ are the body forces, and for a compressible fluid with thermodynamic pressure, p, the stress tensor is defined as

$$\tau_{ij} = \left(-p + \frac{2}{3}\mu \nabla \cdot \vec{v} \right) \delta_{ij} + 2\mu e_{ij}, \tag{3.3}$$

where $i = 1, 2, 3$, μ is the shear viscosity, and e_{ij} is the deformation tensor defined by

$$e_{ij} = \frac{1}{2} \left(\frac{\partial u_i}{\partial x_j} + \frac{\partial u_j}{\partial x_i} \right). \tag{3.4}$$

If viscosity and body forces (e.g., gravity) are neglected, we obtain the *Euler equations*

$$\frac{\partial \vec{v}}{\partial t} + \vec{v} \cdot \nabla \vec{v} = -\frac{1}{\rho} \nabla p. \tag{3.5}$$

Using equations (3.1) and (3.5), the conservation of energy equation for an ideal, inviscid flow can be derived and gives

$$\frac{DE}{Dt} - \frac{p}{\rho^2} \frac{D\rho}{Dt} = 0. \tag{3.6}$$

Assuming the flow is adiabatic, i.e., energy is transferred only as work, then

$$\frac{DS}{Dt} = 0, \tag{3.7}$$

where S denotes entropy. Physically, this means that entropy is advected with the flow and hence, is constant on streamlines. Assuming we have an ideal gas, it implies two things: firstly, that $c^2 = \frac{\gamma p}{\rho}$ and secondly, the molecular diffusivity is zero, i.e., no heat can be transferred between fluid particles, which means entropy must be in a thermodynamic equilibrium. This type of flow is called *isentropic*.

3.2 Numerical Method and Components

The system of partial differential equations (PDEs), which models acoustic wave propagation, can typically be written as a hyperbolic system of conservative laws. Numerically solving these equations of motion can be expensive, especially if discontinuities arise in the solution (which can occur even if the initial wave profile is smooth) [41]. A common approach when numerically simulating acoustic wave propagation is to use either a finite-volume (FV) or finite-element (FE) method [148]. A high-order accurate method that combines aspects from both FV and FE methods is the discontinuous Galerkin (DG) method, which was developed by Cockburn and Shu [41], [42]. This method is particularly useful for modeling hyperbolic systems because numerical fluxes defined along the cell interfaces guarantee stability and local solvability, i.e., at each time step, only information about the neighbouring cells are required. The DG method can also accommodate unstructured meshes, adaptive refinement, [223] and is open to parallel implementations [72].

3.2.1 General Formulation of the Discontinuous Galerkin Method

In order to derive the discontinuous Galerkin method, we write a general hyperbolic system of conservation laws as

$$\frac{\partial \mathbf{u}}{\partial t} + \nabla \cdot \mathbf{F}(\mathbf{u}) = \mathbf{0}, \qquad \mathbf{x} \in \Omega, \qquad t > 0, \tag{3.8a}$$

$$\mathbf{u} = \mathbf{u}^0, \qquad t = 0, \tag{3.8b}$$

with the solution $\mathbf{u}(\mathbf{x}, t) = (u_1, u_2, ..., u_m)^t$, where $(\mathbf{x}, t) \in \Omega \times [0, \tau]$ (τ is the final time), and numerical flux $\mathbf{F}(\mathbf{u})$. The computational domain Ω is partitioned into a collection of non-overlapping elements

$$\Omega = \bigcup_{j=1}^{N_h} \Omega_j, \tag{3.9}$$

where N_h denotes the total number of elements in Ω.

We then construct a Galerkin problem on element Ω_j by multiplying equation (3.8a) by a test function $\mathbf{v} \in (H^1(\Omega_j))^m$, where m is the number of equations in the system [84]. Then integrating the result on Ω_j and using the divergence theorem, we obtain

$$\int_{\Omega_j} \mathbf{v} \frac{\partial \mathbf{u}}{\partial t}\, ds + \int_{\partial\Omega_j} \mathbf{v}\mathbf{F}(\mathbf{u}) \cdot \hat{n}\, d\tau - \int_{\Omega_j} \nabla \mathbf{v} \cdot \mathbf{F}(\mathbf{u})\, ds = \mathbf{0}, \qquad \forall \mathbf{v} \in (H^1(\Omega_j))^m, \tag{3.10}$$

where $\hat{n}$ is the unit outward normal vector to $\partial\Omega_j$. In 3D, each element Ω_j is mapped to the canonical tetrahedron with vertices $(0,0,0)$, $(1,0,0)$, $(0,1,0)$, and $(0,0,1)$ via the transformation

$$\begin{bmatrix} x \\ y \\ z \\ 1 \end{bmatrix} = \begin{bmatrix} x_{j,1} & x_{j,2} & x_{j,3} & x_{j,4} \\ y_{j,1} & y_{j,2} & y_{j,3} & y_{j,4} \\ z_{j,1} & z_{j,2} & z_{j,3} & z_{j,4} \\ 1 & 1 & 1 & 1 \end{bmatrix} \begin{bmatrix} 1-r-s-t \\ r \\ s \\ t \end{bmatrix}, \tag{3.11}$$

where $(x_j, y_j, z_j)_{1,2,3,4}$ are the vertices of Ω_j in the physical space and (r,s,t) are the canonical coordinates. Face 1, face 2, face 3, and face 4 are defined to be the face opposite of vertex $(1,0,0)$, $(0,1,0)$, $(0,0,1)$, and $(0,0,0)$, respectively. The Jacobian of the transformation is defined as

$$J_j = \begin{bmatrix} x_{j,2}-x_{j,1} & x_{j,3}-x_{j,1} & x_{j,4}-x_{j,1} \\ y_{j,2}-y_{j,1} & y_{j,3}-y_{j,1} & y_{j,4}-y_{j,1} \\ z_{j,2}-z_{j,1} & z_{j,3}-z_{j,1} & z_{j,4}-z_{j,1} \end{bmatrix}. \tag{3.12}$$

The solution $\mathbf{u}(\mathbf{x},t)$ on Ω_j is approximated by a vector function $\mathbf{U}_j = (U_{j,1}, U_{j,2}, \ldots, U_{j,m})^T$, where

$$U_{j,k} = \sum_{i=1}^{N_\mathrm{p}} \mathbf{c}_{j,k}\varphi_i, \quad k = 1,2,\ldots,m, \tag{3.13}$$

where N_p is the number of basis vectors and $\mathbf{c}_{j,k} = (c_{j,k,1}, c_{j,k,2}, \ldots, c_{j,k,M})^t$. The polynomial basis $\{\varphi_i\}_{i=1}^{N_\mathrm{p}}$ is chosen to be orthonormal in $\mathcal{L}^2(\Omega_j)$ where p is the order of the orthonormal basis. This will produce a multiple of the identity for the mass matrix on Ω_j when the testing function $\mathbf{v}$ is chosen to be equal to the basis functions consecutively starting with φ_1. In 3D, the linear basis is $\{\varphi_1, \varphi_2, \varphi_3, \varphi_4\}$ where

$$\begin{aligned} \varphi_1 &= \sqrt{6}, \\ \varphi_2 &= -\sqrt{10} + 4\sqrt{10}r, \\ \varphi_3 &= -2\sqrt{5} + 2\sqrt{5}r + 6\sqrt{5}s, \\ \varphi_4 &= -2\sqrt{15} + 2\sqrt{15}r + 1\sqrt{15}s + 4\sqrt{15}t. \end{aligned}$$

Due to the discontinuous nature of the numerical solution, the normal flux $\mathbf{F}_n = \mathbf{F}(\mathbf{u})\cdot\hat{n}$, is not defined on $\partial\Omega_j$. The standard approach is to define it in terms of a numerical flux $\mathbf{F}^*(\mathbf{U}_j, \mathbf{U}_k)$ that depends on the solution $\mathbf{U}_j$ on Ω_j and $\mathbf{U}_k$ on the neighboring element Ω_k sharing the portion of the boundary $\partial\Omega_{jk}$ common to both elements [64]. It is assumed

that the numerical flux is monotone and differentiable. Equation (3.10) can now be written as

$$\begin{aligned}\mathbf{0} =& \frac{\mathrm{d}}{\mathrm{dt}} \int_{\Omega_j} \sum_{i=1}^{N_\mathrm{p}} \mathbf{c}_{j,k} \varphi_i \mathbf{v} \, ds + \sum_{k \neq j} \int_{\partial \Omega_{j,k}} \mathbf{v} \mathbf{F}^*(\mathbf{U}_k, \mathbf{U}_j) \cdot \hat{n}_{k,j} \, d\tau \\ & - \int_{\Omega_j} J_j^{-1} \nabla \mathbf{v} \cdot \mathbf{F}(\mathbf{U}_j) \, |\det(J_j)| \, ds\end{aligned}$$

Taking $\mathbf{v}$ to be φ_i, we obtain

$$\begin{aligned}\frac{\mathrm{d}}{\mathrm{dt}} \int_{\Omega_j} \sum_{i=1}^{N_\mathrm{p}} \mathbf{c}_{j,k} \varphi_i \varphi_i \, ds = & - \sum_{k \neq j} \int_{\partial \Omega_{j,k}} \varphi_i \mathbf{F}^*(\mathbf{U}_k, \mathbf{U}_j) \cdot \hat{n}_{k,j} \, d\tau \\ & + \int_{\Omega_j} J_j^{-1} \nabla \varphi_\mathbf{i} \cdot \mathbf{F}(\mathbf{U}_j) \, |\det(J_j)| \, ds\end{aligned}$$

Using the fact that the basis is orthonormal,

$$\frac{\mathrm{d}}{\mathrm{dt}} \mathbf{c}_{j,k} = \frac{1}{|\det(J_j)|} \left[- \sum_{k \neq j} \int_{\partial \Omega_{j,k}} \varphi_i \mathbf{F}^*(\mathbf{U}_k, \mathbf{U}_j) \cdot \hat{n}_{k,j} \, d\tau + \int_{\Omega_j} \left(J_j^{-1} \nabla \varphi_\mathbf{i} \right) \cdot \mathbf{F}(\mathbf{U}_j) \, |\det(J_j)| \, ds \right] \tag{3.14}$$

Finally, the $\mathcal{L}^2$ volume and surface inner products in equation (3.14) are computed using 2p and 2p+1 order accurate Gauss quadratures [64], [124], respectively. The resulting system of ordinary differential equations (ODEs) is

$$\frac{d\mathbf{c}}{dt} = \mathbf{f}(\mathbf{c}), \tag{3.15}$$

where $\mathbf{c}$ is the vector of unknowns and $\mathbf{f}$ is a nonlinear vector function resulting from the boundary and volume integrals in equation (3.10) [84]. Since the mass matrix is diagonal, it is straight-forward to invert [124].

3.2.2 Local Time-Step

After evaluating the numerical flux to solve equation (3.15), we progress in time via an explicit two-stage, second-order Runge-Kutta (RK) discretization scheme known as Heun's

method. Using the value of $\mathbf{c}$ at the previous time step, i.e., $\mathbf{c}_{n-1} = \mathbf{c}(t^{n-1})$, at level t^n we have

$$\begin{aligned}\mathbf{c}^{(1)} &= \mathbf{c}_{n-1} + \Delta t\ f(\mathbf{c}_{n-1}) \\ \mathbf{c}_n &= \mathbf{c}_{n-1} + \frac{\Delta t}{2}\big(f(\mathbf{c}_{n-1}) + f(\mathbf{c}^{(1)})\big).\end{aligned}$$

In order to maintain stability, a small enough Δt needs to be chosen. For the DG method with RK integration scheme of (p + 1), we require the global Courant-Friedrichs-Lewy (CFL) condition to be

$$\Delta t^n \leq \min_j \left(\frac{h_j}{(2\mathrm{p}+1)\ |\lambda_\mathrm{j}|}\right) \tag{3.16}$$

where $|\lambda_j|$ is the maximum wave speed on cell j, and h_j is the minimum radius of the inscribed sphere of the cell [124]. In our case, we require

$$\Delta t^n \leq \min_j \left(\frac{h_j}{3\ |\lambda_j|}\right). \tag{3.17}$$

For the discretization in space, we used the local Lax-Friedrichs Riemann solver, i.e., we write

$$\mathbf{F}^*(\mathbf{U}_k, \mathbf{U}_j) = \frac{1}{2}\big(\mathbf{f}(\vec{U}_L) + \mathbf{f}(\vec{U}_R)\big) + \lambda\big(\vec{U}_L - \vec{U}_R\big), \tag{3.18}$$

where $\lambda = \max\big(|\mathbf{f}'(u)|\big)$. This particular numerical flux is first-order accurate and thus, dissipative in nature. However, since shocks can be produced within the trombone, it seems appropriate to use over a limiter. Using a higher-order approximation does not seem necessary to improve the accuracy of our numerical results, as the mesh resolution must be fine enough to resolve certain regions of the computational instruments to ensure the frequency components of the waveform can be captured. Improving the numerical accuracy over that of the experiment did not seem worthwhile.

3.2.3 Few Remarks Regarding the Software

The DG method used for this thesis was a GPU implementation done by former students of Lilia Krivodonova[1]. Full details of their implimentation and algorithms used can be

[1] Marty Fuhry first coded the method for the linear advection equation, Maxwell's equations, the shallow water equations and the Euler equations in 1D and 2D for his master's thesis. Andrew Giuliani then extended the work to 3D during his PhD and implemented the Euler equations using a 2D axisymmetric model.

found in [72], [84], [124]. Therefore, to be clear, this thesis is not focused on implementing the software itself or running benchmarks. Instead, I aimed to utilize and test the code on a real life problem using actual measured data. However, we briefly mention some of the main aspects below for completeness[2].

The DG method used was written with CUDA, which is a parallel computing platform and programming model created by NVIDIA. It was specifically designed to work with programming languages such as C, C++ and Fortran. In addition, CUDA supports programming frameworks such as OpenCL and OpenACC as well as third party wrappers that are available for Matlab, Python, Java, Perl, Ruby, etc. [165].

The unit of computation in CUDA is known as a *thread* and is assigned a unique index. Threads are clustered into groups of 32, known as *wraps*, which can be further grouped into *blocks*. The number of wraps per block is determined by the coder. Functions that are executed on the GPU are called *kernels* and are run by many threads in parallel. The general procedure to run a CUDA program is as follows [165]:

1. Declare and allocate the CPU and GPU memory.
2. Initialize the CPU data.
3. Transfer the data from the CPU to the GPU[3].
4. Execute the desired kernels and upon completion, terminate the kernels.
5. Send results from the GPU to the CPU.

The simulations throughout this thesis were mostly run on the NVIDIA Tesla K40 (12 GB) through the University of Waterloo's GPU cluster, the Shared Hierarchical Academic Research Computing Network (SHARCNET)[4], or by using a Titan Xp (8 GB) GPU on a local computer kindly donated by NVIDIA.

3.3 Computational Geometry

The meshes used for the various numerical experiments will be discussed independently in each section. All the computational geometries were constructed in GMSH using the

[2] Also in case the reader is not familiar with CUDA.
[3] Data is transferred between the CPU and GPU via the PCIe bus.
[4] Which is a high performance computing environment stationed in Ontario.

Delaunay algorithm to generate the elements, and the Netgen optimization algorithm to improve the mesh quality.

Non-uniform meshes were used with smaller elements near the bell and the mouthpiece end to better resolve the trumpet and trombone geometry. For accurate resolution, a sufficient number of cells in the radial direction is also required. Consequently, there were approximately 90 elements in the radial direction in the narrowest region of the instrument. We then also had a high number of elements per wavelength in the axial direction. We verified that a finer mesh did not improve our simulation results and believe the resolution is sufficient, i.e., the numerical error is smaller than the modeling error.

Chapter 4

Examination of Energy Losses

Incorporating sound attenuation into our problem is a difficult task, especially when using a time-domain model to describe the propagation of finite-amplitude sound waves. This leads us to ask: how important are these losses and is it necessary to include them in our model? From an aeroacoustics perspective, the three main mechanisms that could contribute to sound energy losses are [20], [39], [66], [90], [109], [146]:

1. Thermal losses or heat conduction caused by the diffusion of heat from the sound field into the boundaries.
2. Viscous losses caused by the friction the fluid experiences at the boundary.
3. Vibroacoustic losses caused by the vibrations of the instrument.

Although most researchers agree that there exists some quantifiable effect from vibroacoustic and thermoviscous (or viscothermal) losses, there is not yet a consensus among the entire acoustic community whether such phenomena have a noticeable influence on the timbre of a played sound [90], [159]. In this chapter, some of the key findings in the literature will be reviewed. Then, using COMSOL, we will verify some of these claims previously made about boundary layer losses in narrow, uniform tubes. In particular, we used this finite-element solver to compare the linearized Navier-Stokes and Euler systems. These results will be discussed in Section 4.2.2. The consequences of neglecting losses in the trumpet and trombone will also be explored theoretically, as we attempt to quantify the amount of energy that could potentially be lost (from the played sound) in a worst-case scenario. Using the collected accelerometer data, we also estimate the significance of the vibroacoustic effects examined in Section 2.3.3. Then, in Section 4.2.3, using the theory discussed in [146], we approximate the power lost due to viscous and thermal effects.

4.1 Vibroacoustic Effects

The radiated or external sound field produced from a brass instrument is the consequence of the sound emitted from acoustic oscillations of the air-column as well as the sound emitted from wall and bell vibrations [157], [213]. If the structural resonance of the instrument walls happen to coincide with one of the acoustical resonances of the air-column, the two couple vibroacoustically [156]. In principle, it is possible that such vibroacoustic effects could result in sound radiation being transmitted into the surrounding internal or external fluid flow [156]. But overall, the acoustical contributions from the air-column are much more significant. According to Moore, sound produced by the vibrating bell of a trombone is on the order of 10,000 times less powerful than the sound energy from the resonating air-column [144]. Similar claims regarding lateral wall vibrations are made by Gautier and Tahani in [81].

4.1.1 Review of the Literature

With respect to wall vibrations, there has been a 100+ year debate on their importance and whether they produce an audible effect on the sound[1] [90]. Researchers at least seem to agree that although the material and thickness of the instrument's wall does influence the vibroacoustics, such effects are very small and compared to the instrument's geometry, are negligible [12], [73], [156], [173], [199]. But otherwise, some postulate the vibroacoustic effects can influence the timbre of certain types of bores such as organ pipes [9], [10], [142], [156][2]. However, even for simple bores (including organ pipes), others do not agree. For instance, Backus and Hundley state that "*the wall vibrations in organ pipes as commonly constructed have negligible influence on the steady pipe tone, and probably little on the transient buildup as well*" [11].

For brass instruments in particular, a number of experiments were done between 2005 - 2018 to investigate whether wall or bell vibrations could significantly influence the played sound, e.g., [108], [109], [112], [113], [144], [156], [157], [182]. Several of these experiments were run where an instrument was excited in two different situations: one where the bell was free to vibrate and another where it was dampened with sand bags (e.g., [108], [109], [112], [113], [144]). Other experiments have used scanning laser vibrometers (e.g., [156],

[1] Brackett believes that the disagreements in the literature are partly due to how the research has been carried out. Some work for instance has been done numerically, while physical experiments have also been carried out (using artifical mouthpieces, loudspeakers or live players) but using different instruments with various materials and wall thickness [32].

[2] But for organ pipes, wall effects are approximately 40 dB below the main sound intensity [9], [10].

[157]), or have been numerical investigations (e.g., [112], [113], [157]). From the outcomes of these experiments, some believe vibroacoustic interactions with the instrument's internal acoustic field are unlikely to occur since fluid-structure vibroacoustic interactions are weak [156]. Others however say their experiments indicated that the sound distribution of the relative power was altered by the bell and wall vibrations. For example, Moore claimed that for the trumpet, the relative power in the fundamental may change by more than 3 dB when the bell vibrations were damped[3] [144], and Kausel observed that "*differences in the power contained in individual overtones can exceed 6 dB in some cases*" [109]. However, Kausel *et al.* also acknowledged that their numerical results were not consistent with their measurements [112]. Moreover, these experiments were not done with a live player. This implies that the observed vibrational behaviour of the instruments in the lab may not be representative of how brass instruments respond in reality. For example, musicians hold a trombone or trumpet with both hands thereby naturally dampening some of the vibroacoustic effects[4]. The other main claims made in these papers are summarized below.

i. For the trumpet in particular, bell vibrations 2.5 cm from the rim of the bell were recorded to be 200 $\pm$ 20 μm by Moore [144]. However, Kausel obtains much lower values, approximately on the order of 1μm [112], [113].

ii. Again for the trumpet, Kausel calculated in [113] that the radial displacement of the bore prior to the flare was between 0.01 nm - 0.4 nm (1e-5 μm - 4e-4 μm).

iii. The outer and inner pressure fields produced in brass instruments are most influenced by the oscillation mode that corresponds to the physical length of the flare region [113]. For the trumpet and trombone, this corresponds to approximately 750 Hz and 900 Hz, respectively.

iv. Though the influence is small, the input impedance and transfer function can be effected via bell vibrations by several decibels if the bell's resonance corresponds with the musical note being produced. In addition, the vibrations can influence the brassiness of transmitted waves by dampening all radiated components [144], [112], [113].

v. Structural resonance can increase the effects of wall vibrations, specifically in the lower frequency range [112] .

[3] For the B_4^b specifically, Moore found that the wall vibrations decreased the power of the fundamental and second harmonic but increased the power of the higher frequencies [144].

[4] This may influence the trumpet more than the trombone since the player's hand covers more surface area due to the instrument's size and tubing configuration.

vi. As stated in Section 1.3, the dampening effect from the walls causes the pressure transfer function to change sign. This shift in pressure is near 500 Hz and again at 1500 Hz. For components below 500 Hz and above 1500 Hz, the bell vibrations have an absorbing effect. The components in-between are not affected as much and are more prominent in the radiated power [108], [109], [112], [113].

Comparing some of these findings with our own results presented in Section 2.3.3, we found that bell vibrations near the rim were on the order of 0.05 μm - 1 μm. These values are more consistent with Kausel's findings [112], [113], rather than Moore's when the bell was free to vibrate [144]. When the bell was damped with the sandbags however, Moore found that the vibrations were reduced to 20 $\pm$ 10 μm [144].

4.1.2 Examining Vibroacoustic Effects in Brass Instruments

We suspect that the SPL lost from bell vibrations is negligible relative to the direct sound. But, to assess and quantify how the radiated pressure amplitude is influenced by the wall vibrations (which would be most prominent at the bell, specifically the bell rim [113]), we will estimate what the damping effect should be from theory and then calculate the pressure fluctuations produced from our measured bell vibrations.

4.1.2.1 Monopole Approximation

The surface of a pressure front exiting the bell at worst acts like a monopole at the highest radiation efficiency. The radiated sound energy from a brass instrument can then be approximated as a monopole source centered at the bell exit. This approximation will be sufficient so long as the waveform's wavelength is smaller than the diameter of the flare [54], [120], [146]. For the trumpet and trombone, this corresponds to 2500 Hz and 1700 Hz, respectively. As the frequency of the waves increase beyond this, the approximation breaks down, as the sound energy becomes more biased toward the central radiation axis [120]. Others have also made this approximation such as [120], [132], [134], [152]. Furthermore, recent experimental evidence (e.g., [134] (using Schlieren imaging) and [120] (using an array of microphones)) as well as numerical findings (e.g., [120]) support the validity of this setup.

As illustrated in Figure 4.1, we consider the sound pressure, denoted by p, a distance R from the bell exit along the central axis. Let D denote the bell diameter and a = iωu be the acceleration of the flare where ω is the angular frequency and u is the axial velocity at the

bell rim. We are interested in determining the sound pressure produced by the monopole at position O a distance R from the bell exit with respect to a particular frequency, f. The highest radiation sound effect produced from the acceleration can be calculated assuming that it all adds up from the bell area. Although the wave propagation within the trumpet or trombone bore is nonlinear, the transmitted sound waves travel through free space and propagate in a more-or-less linear fashion. Hence, the following analysis can be made.

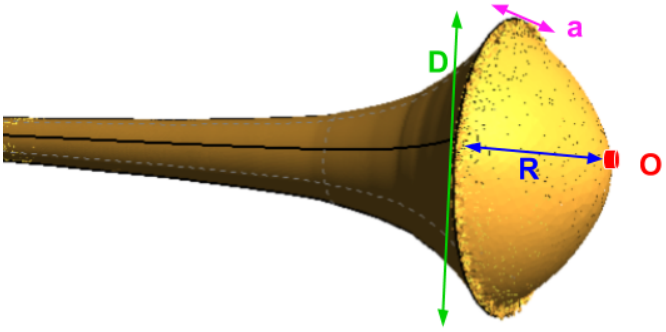

Figure 4.1: A diagram illustrating the fluctuating pressure that arises from the vibrating bell when approximated as a monopole source.

At the bell exit, the pressure produced by a monopole source is

$$p(r,t) = -\frac{k\rho c}{4\pi R} Q_w e^{-ikR}, \tag{4.1}$$

where k denotes the wavenumber, ρ is the density, c is the speed of sound, and Q_w denotes the strength of the monopole, which can be written as the product of the surface area and normal surface velocity [198]. Writing the surface area of the hemispheric wavefront with radius r_0, the source strength is defined as

$$Q_w = 2\pi r_0^2 u.$$

Since we have the acceleration of the bell rim, we can write $u = i\frac{\mathrm{a}}{\omega}$ and hence,

$$Q_w = \frac{2\pi r_0^2 \mathrm{a}}{\omega}.$$

Substituting Q_w into (4.1), we obtain

$$\begin{aligned} p(r,t) &= -\frac{k\rho c}{4\pi R}\left(\frac{2\pi \mathrm{a}}{\omega} r_0^2\right) e^{-ikR} \\ &= -\frac{\rho r_0^2}{2R} \mathrm{a} e^{-\mathrm{ikR}}. \end{aligned} \tag{4.2}$$

4.1.2.2 The Suspended Disk Approximation (Skudrzyk and Pierce)

Perhaps a more suitable approximation can be made since the bell vibrations cause an expanding and contracting effect, which introduces and withdraws air periodically thereby, producing a pressure field[5]. We will approximate the end of the bell as a thin, suspended vibrating disk of radius r_0 along the axis of the instrument, as illustrated in Figure 4.2.

We are primarily interested with the pressure variations along the dipole axis. The net force exerted on the fluid by the disk due to the transverse oscillations will be denoted by $\mathbf{F}(t)$. By Newton's third law, the net force will be the surface integral of pressure.

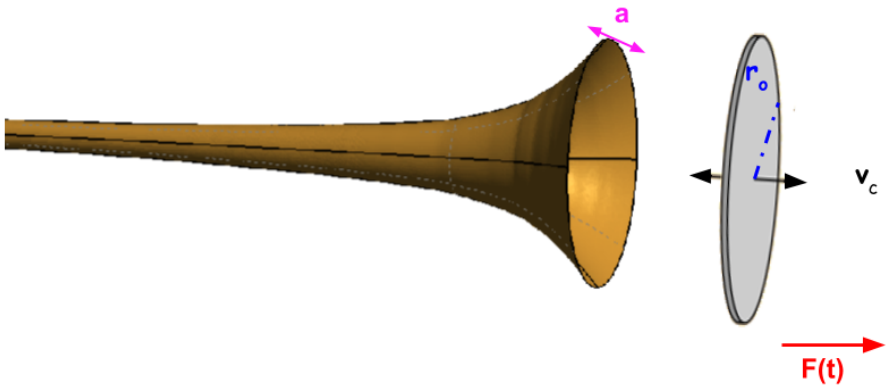

Figure 4.2: A diagram illustrating how to approximate the dipole pressure field associated with the bell vibrations by a suspended vibrating disk of radius r_0 with effective mass m_d.

The force itself can be determined using Newton's second law where the hydrodynamic or effective mass of the thin circular disk moving in the direction of the normal is

$$m_d = \frac{8}{3}\rho r_0^3. \tag{4.3}$$

So by Newton's second law,

$$F(t) = \frac{8}{3}\rho r_0^3 \frac{dv_c}{dt}, \tag{4.4}$$

where v_c is the transverse velocity of the disk [170]. For low frequencies, i.e., when $kr_0 << 1$,

[5] So the sound pressure at the bell is then at least bipolar or multipolar around the central axis [210].

the sound pressure is given in Skudrzyk [198] to be

$$\begin{aligned} p(r,t) &= -\frac{\cancel{\rho} c}{4\pi R} k^2 u \frac{m_d}{\cancel{\rho}} \left(1 + \frac{1}{ikR}\right) e^{-ikR} \\ &= -\frac{1}{4\pi R} k^2 c u \left(\frac{8}{3}\rho r_0^3\right) \left(1 + \frac{1}{ikR}\right) e^{-ikR} \\ &= -\frac{2k\cancel{c}\rho r_0^3}{3\pi R} \left(\frac{\omega}{\cancel{c}}\right) u \left(1 + \frac{1}{ikR}\right) e^{-ikR}, \end{aligned} \tag{4.5}$$

where u is the axial velocity. Multiplying (4.5) by $\frac{S}{\pi r_0^2}$ where S is the source area, we obtain

$$\begin{aligned} p(r,t) &= -\frac{2k\rho\omega\cancel{r_0^3}}{3\pi R} \left(\frac{S}{\pi\cancel{r_0^2}}\right) u \left(1 + \frac{1}{ikR}\right) e^{-ikR} \\ &= -\frac{2k\rho\omega r_0}{3\pi^2 R} \underbrace{(Su)}_{=Q} \left(1 + \frac{1}{ikR}\right) e^{-ikR} \\ &= -\frac{2k\rho r_0}{3\pi^2 R} \underbrace{(Q\omega)}_{=\mathcal{A}} \left(1 + \frac{1}{ikR}\right) e^{-ikR} \\ &= -\frac{2kr_0\rho}{3\pi^2 R} \mathcal{A} \left(1 + \frac{1}{ikR}\right) e^{-ikR}, \end{aligned} \tag{4.6}$$

where Q is the source strength and $\mathcal{A}$ is the volume acceleration[6]. This expression is also obtained by both Pierce [170] and Skudrzyk [198]. Following Morse and Ingard [146], the same expression can be obtained with a change of sign. For further details, see Pierce [170].

[6] When considering $kR \approx 1$, the (complex) factor has a magnitude of $\sqrt{2}$.

4.1.2.3 Pressure Amplitude Associated with Bell Vibrations

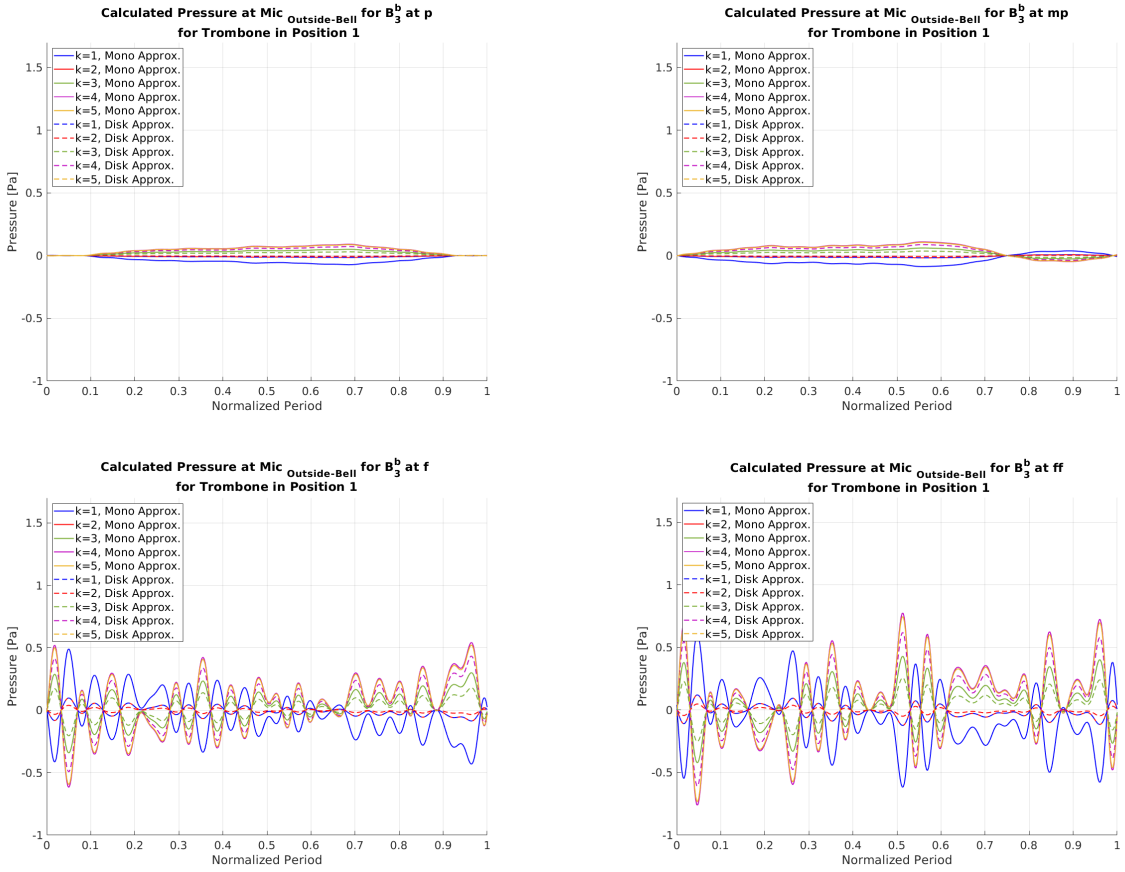

Figure 4.3: Calculated pressure associated with the trombone bell vibrations shown in Figure 2.29 while playing B_3^b in position 1 at *p* (top-left), *mp* (top-right), *f* (bottom-left) and *ff* (bottom-right).

Using the derived expressions (4.2) and (4.6), we can estimate the produced pressure corresponding to the accelerometer measurements presented in Section 2.3.3. For each musical note considered, the resulting pressure for the first five resonant frequencies (f_1-f_5), will be plotted. The trombone results can be found in Figures 4.3 to 4.6 (which shows the pressure associated with the trombone bell vibrations depicted in Figures 2.29 to 2.32). Similarly, the calculated pressure for the trumpet notes are shown in Figures 4.7 to 4.10 (which correspond to the trumpet bell vibrations presented in Figures 2.33 to 2.36). For

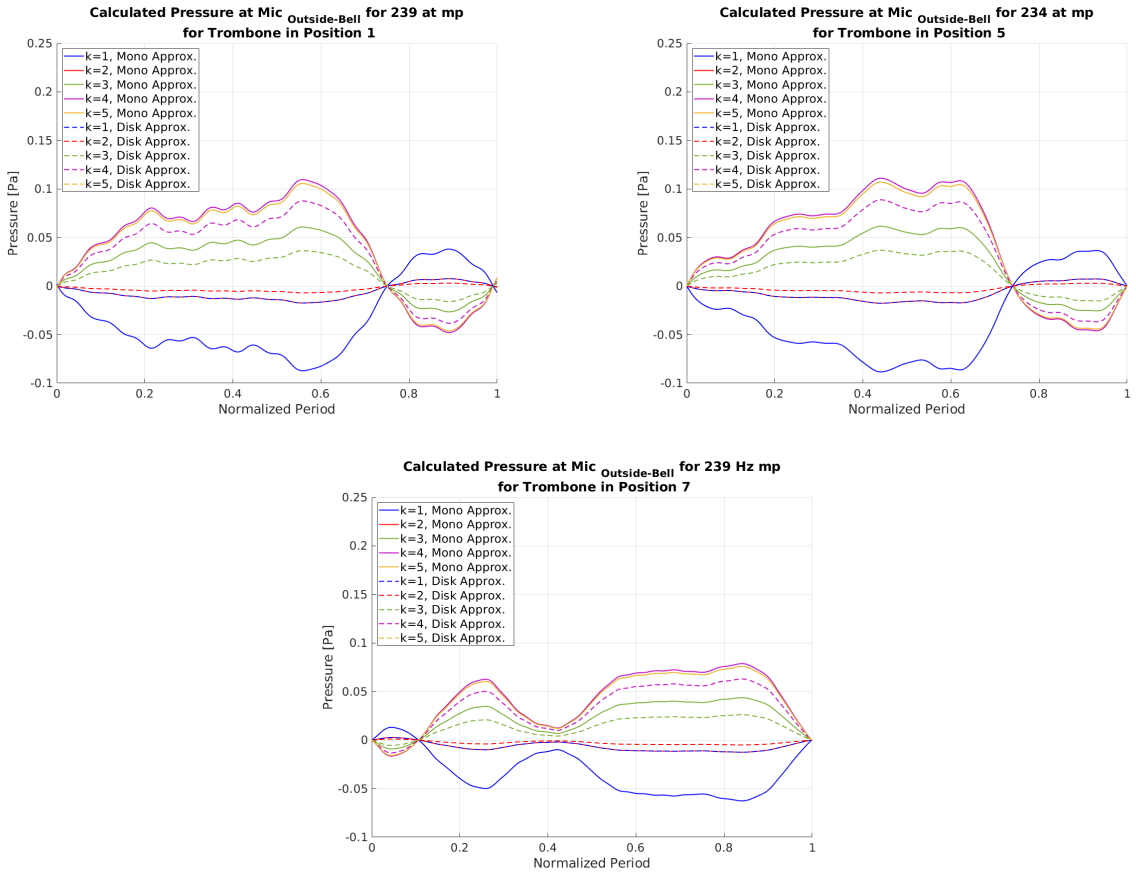

Figure 4.4: Calculated pressure associated with the trombone bell vibrations shown in Figure 2.31 while playing a 239 Hz note in position 1 (top-left), 234 Hz note in position 5 (top-right), and 220 Hz note in position 7 (bottom) all at *mp*.

all plots, the monopole approximation curves correspond to the solid lines (−), whereas the suspended disk approximation is plotted with dashed lines (- -). Instead of individually discussing each plot (since the analysis will be synonymous with the discussion in Section 2.3.3), the focus will be on comparing the trombone versus the trumpet results.

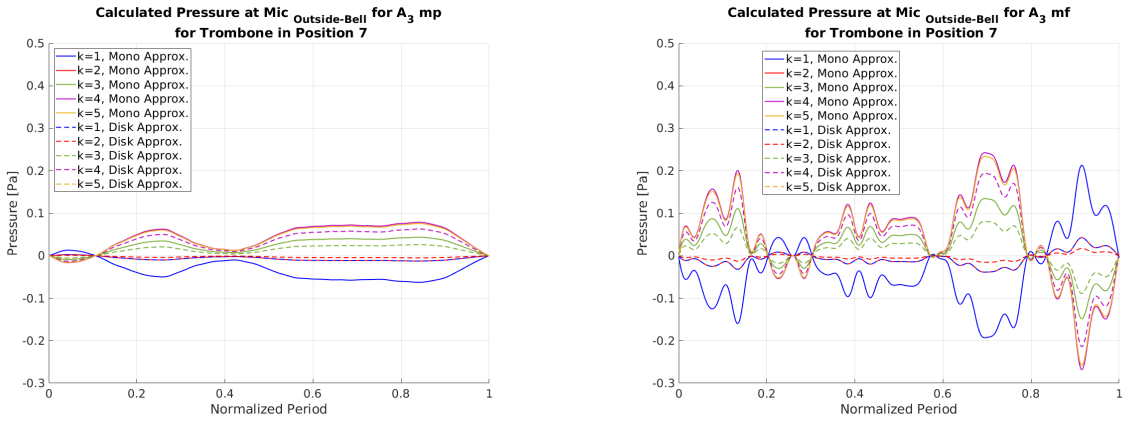

Figure 4.5: Calculated pressure associated with the trombone bell vibrations shown in Figure 2.30 while playing A_3 in position 7 at *mp* (left) and *mf* (right).

From examining all the plots for the trumpet notes, we calculated that the pressures associated with the bell vibrations at Mic $_{\text{Outside-Bell}}$ would have an amplitude of at most 0.6 Pa, regardless of the tubing configuration. This maximum value corresponds to the B_4^b played at *fff* where no valves are compressed (right of Figure 4.10). Recall that in [144], the authors found that the B_4^b was the note which decreased the power of f_1 and f_2, but increased the power of the higher frequencies[7]. For the trombone, the maximum pressure amplitude resulting from the bell vibrations was found to be around 0.8 Pa, and corresponded to the B_3^b being played at *fff* in position 1 (bottom-right of Figure 4.3).

Reviewing Figure 4.7, which depicts the 240 Hz, 484 Hz, 730 Hz (all at *mf*) and 989 Hz (at *p*) trumpet notes, we observe that the sound pressure becomes less spectral as the pitch increases. In addition, we notice that the main pressure peaks for the B_3^b (240 Hz) and B_5 (989 Hz) are close in amplitude despite their different dynamic levels. The maximum pressure amplitude for the F_5 is almost twice as large. For the trombone, we see from comparing Figure 4.4 (the *mp* notes) to Figure 4.6 (the *mf* notes) that as the volume of the played sound increases, the pressure becomes more spectral. This is also evident when examining the B_3^b played at *p*, *mp*, *f* and *fff* in Figure 4.3. The trumpet too displays similar behaviour (left versus right plot in Figure 4.9).

[7] From the numerical results for the B_4^b *f* note shown in Figure 5.21 in Section 5.5, it turns out that the computed spectra for the fundamental was too large by 7 dB and the highest harmonics were underestimated slightly. This in itself does not necessarily imply anything, but I found it to be interesting.

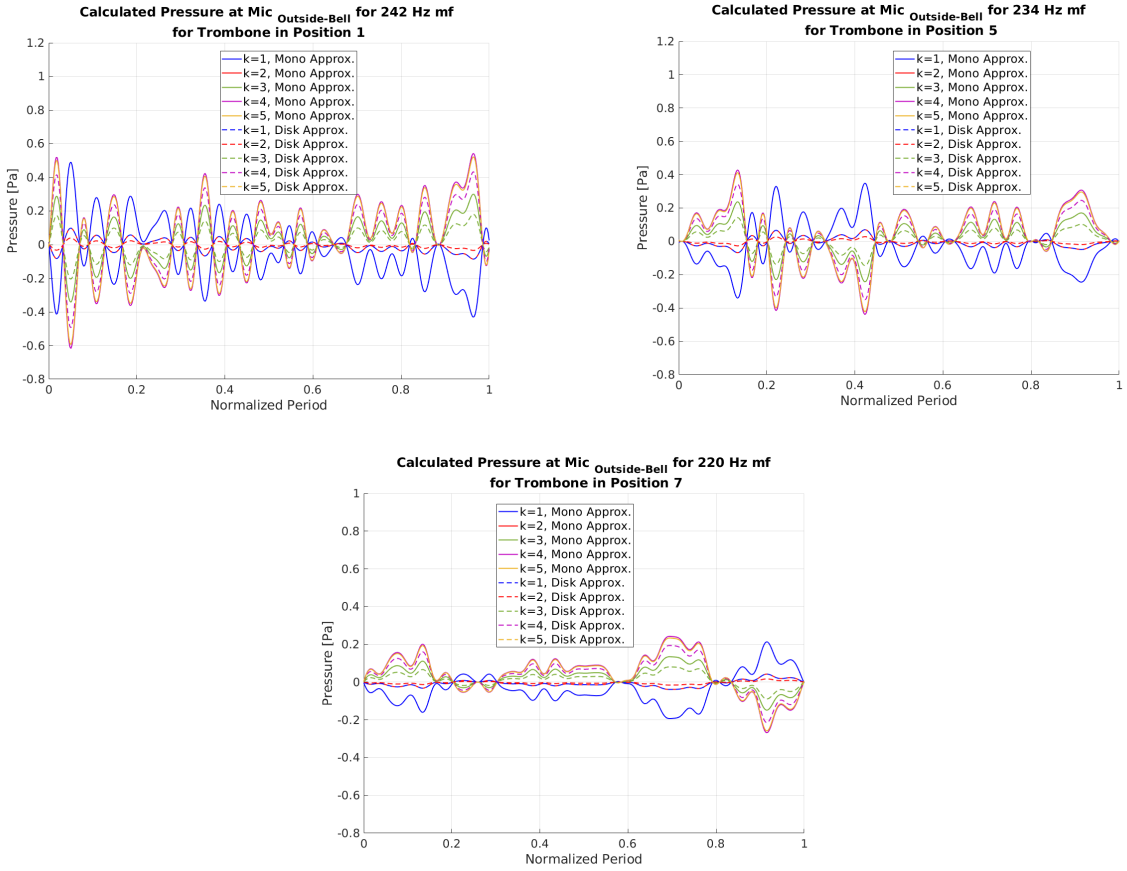

Figure 4.6: Calculated pressure associated with the trombone bell vibrations shown in Figure 2.32 while playing a 242 Hz note in position 1 (top-left), 234 Hz note in position 5 (top-right), and 220 Hz note in position 7 (bottom) all at *mf*.

A commonality that we notice between the trumpet and trombone when playing *mf* to *f* notes is that when the tubing is fully extended, the pressure amplitude is lower than if the equivalent note was played in the instrument's neutral position. This is demonstrated in Figures 4.6 for the trombone (which plots a pitch near A_3/B_3^b at *mf*) and then, in Figure 4.8 for the trumpet (which plots a note near $B_3/B_3^\#$ at *f*). In addition, there seems to be higher resonances present in the pressure waveform when the tubing is fully extended. In particular, the pressure curves do not cross $p = 0$ as often but rather, the perturbations can be seen along the envelope of the amplitude.

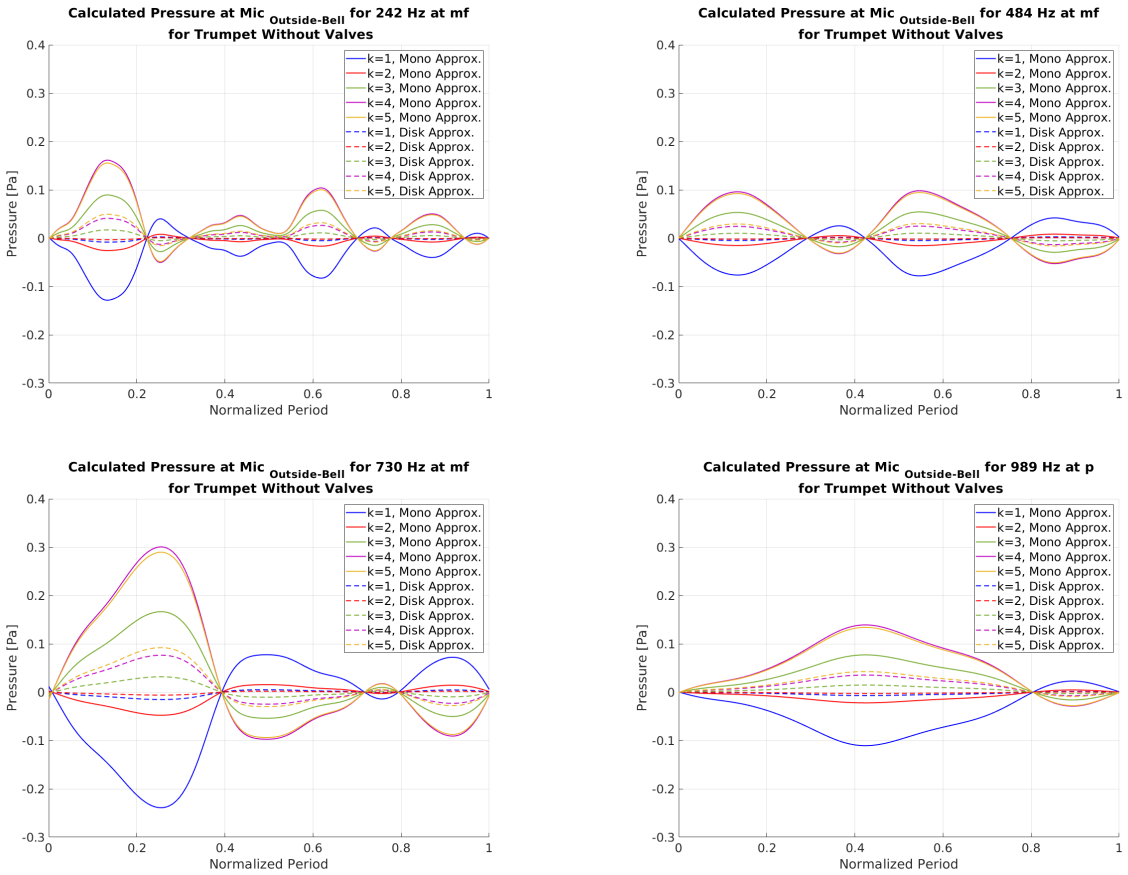

Figure 4.7: Calculated pressure associated with the trumpet bell vibrations shown in Figure 2.33 while playing a 240 Hz note at *mf* (top-left), 484 Hz note at *mf* (top-right), 730 Hz note at *mf* (bottom-left), and 989 Hz note at *p* (bottom-right) where no valves were compressed.

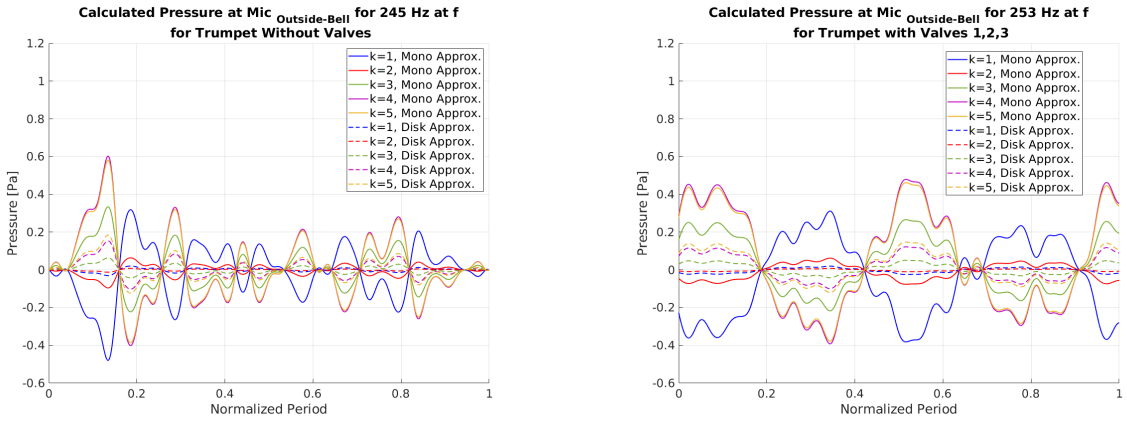

Figure 4.8: Calculated pressure associated with the trumpet bell vibrations shown in Figure 2.34 while playing a 240 Hz note at *mf* (top-left), 245 Hz note played without compressed valves (left), and 253 Hz note played with valves 1, 2, 3 compressed (right) both played at *f*.

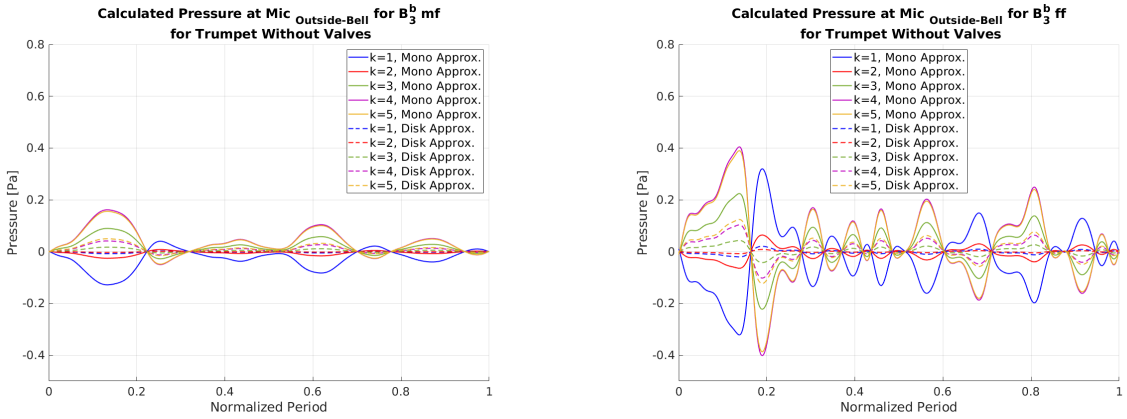

Figure 4.9: Calculated pressure associated with the trumpet bell vibrations shown in Figure 2.35 while playing B_3^b without compressing the valves at *mf* (left) and *ff* (right).

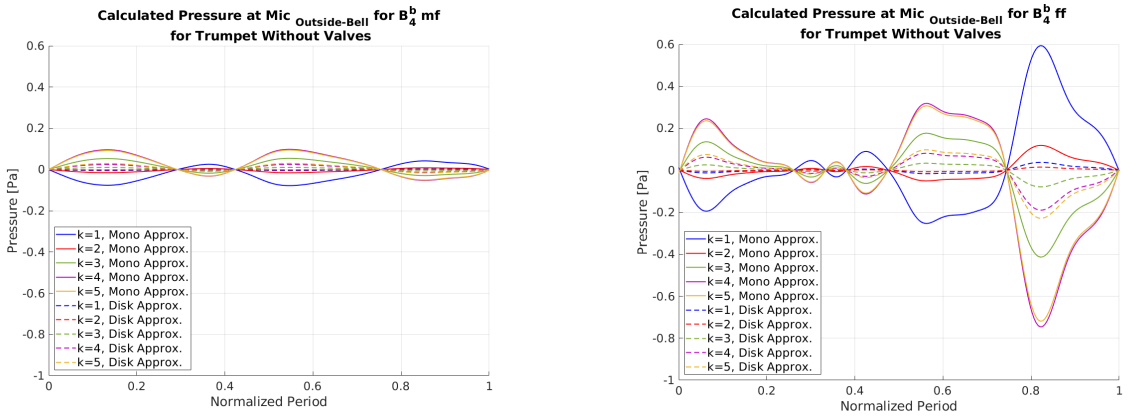

Figure 4.10: Calculated pressure associated with the trumpet bell vibrations shown in Figure 2.36 while playing B_4^b without compressing the valves at *mf* (left) and *ff* (right).

In summary, from comparing the sound pressure produced from the bell vibrations using equations (4.2) and (4.6) we discovered the following:

i. The pressure produced by the bell vibrations at Mic $_{\text{Outside-Bell}}$ for both instruments is less than 1 Pa. As predicted, the sound pressure amplitudes from the trombone are approximately two to three times larger than the pressure disturbances produced by the trumpet bell.

ii. The pressure resulting from the monopole approximation is much larger than the pressure obtained from the suspended disk approximation.

iii. As the volume of the note increases, the pressure becomes more spectral (qualitatively, appears to be more oscillatory), although this is not nearly as drastic for the B_4^b trumpet note played at *ff* in its neutral position.

iv. As the volume of a note increases, the magnitude of the pressure increases.

We could not find in the literature any similar calculations using accelerometer data to examine the effect of the bell vibrations on the radiating sound pressure field. Our findings indicate that the vibroacoustic bell effects would have little influence on the pressure measured at Mic $_{\text{Outside-Bell}}$. In particular, for the notes we considered in the lab, there would be at most a change in pressure of 0.05 Pa - 1 Pa for the first five harmonic waves.

4.1.2.4 Approximation using the Ideal Gas Law (Kausel)

Upon carefully reviewing previous studies, we only found one other similar approximation to the ones discussed above. It was carried out by Kausel *et al.* in [109], [113]. However, the obtained description of the pressure variations due to vibroacoustic effects was more general and not specifically for the bell.

In [109], the authors estimated the pressure fluctuations associated with wall vibrations under isothermal conditions. Then in [113], adiabatic conditions were examined. To obtain the pressure expression, the authors used the equation for an ideal gas which states that if $V(t)$, $p(t)$ and $n(t)$ are the volume, pressure and number of moles of gas at some time t, at some temperature T, then under adiabatic conditions

$$p(t)V(t)^{\gamma} = \mathcal{R}Tn(t), \tag{4.7}$$

where $\mathcal{R}$ is the universal gas constant. Perturbations in pressure and volume were considered to derive an expression describing the extra pressure amplitude produced from the wall oscillations. In particular, they obtained that

$$-\Delta p = \frac{2p_0\gamma}{r}\tilde{s}, \tag{4.8}$$

where γ is the specific heat ratio, r is the radius of the bore, and $\tilde{s}$ denotes the oscillations in the wall displacement in the radial direction. The authors interpreted the negative sign to mean that an on-phase radial wall displacement reduces the sound pressure amplitude [113].

If we apply equation (4.8) to our strongest notes, i.e., the B_4^b *fff* trumpet note and the B_3^b *fff* trombone note, we obtain the pressure profile shown in Figure 4.11, which corresponds to the pressure at the bell rim. The peak pressure is approximately 1 Pa and 2.4 Pa for the trumpet and trombone, respectively. As mentioned however, this approximation would be for the pressure located at the rim of the instruments rather than at Mic $_{\text{Outside-Bell}}$. Therefore, a better comparison of (4.8) with (4.2) and (4.6) would be to consider the near-field solutions. But, the monopole and suspended disk approximations are rather poor here, particularly (4.2). Overall, these values obtained with (4.8) are still relatively small considering B_3^b *fff* trombone and B_4^b *fff* trumpet notes have a maximum pressure at Mic $_{\text{Outside-Bell}}$ of over 200 Pa and 80 Pa. Therefore, the pressure difference would be on the order of 0.01%.

With respect to the wall vibrations, it has been reported that such oscillations are much stronger when there is some sort of asymmetry [213], so perfectly cylindrical pipes tend not

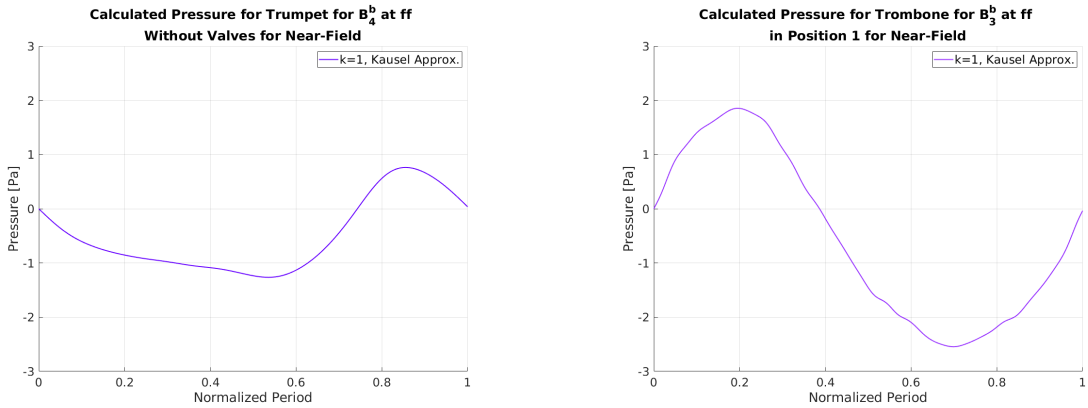

Figure 4.11: Calculated fluctuating pressure disturbance obtained associated with the trumpet vibrations for the B_4^b at *ff* (left), and the trombone vibrations for the B_3^b at *ff* (right) when using Kausel's approximation from [113].

to vibrate [213]. Although, in reality, there are always some flaws when instruments are manufactured [113], [169]. Despite that we did not calculate the vibrations associated with the cylindrical portion of the trumpet or trombone, if we use (4.8), we can approximate the pressure difference in the bore of the instrument at specific radii. Since we did not measure the vibrations in the bore prior to the flare, we would need to use the displacements reported in [113]. For a B_4^b played on the trumpet, the radial displacement of the cylindrical region was calculated to be between 0.01 nm - 0.4 nm. Taking the upper value, the associated pressure from such oscillations would only be approximately 0.02 Pa. Even if we considered the narrow bore oscillations to be much larger, say for instance, on the order of 1000 nm, the resulting pressure change would still only be approximately 45 Pa. In the cylindrical region of the trumpet or trombone, pressures can range from 1500 Pa (for a *p* note) to 20 kPa (for a *ff* note), a 45 Pa difference only corresponds to a potential deviation of 0.2 % - 3 %)[8]. Therefore, our findings demonstrate that even in the worse case, neglecting vibroacoustic effects when modelling the sound propagation would result in an error of at most 1%.

[8] As shown in the accelerometer graphs, the quietly played musical notes have small displacement amplitudes. Hence, 3% is a generous approximation.

4.2 Thermoviscous Effects

When sound is being produced in a brass instrument, the particle velocity or motion of the air through the bore introduces a slipping of adjacent layers of gas [217]. Due to viscosity, this slip generates a sort of internal friction that acts to resist the acceleration of air thereby decreasing kinetic energy [146], [192]. Potential energy is also lost from heat conduction, i.e., the exchange of thermal energy between the wave and the surface of the bore [17], [192]. Though, as stated by Berggren, "*the relative importance of the thermal and viscous losses varies with the type of medium, the wavelength, and the characteristic size of the domain*" [23]. Ideally, the viscous drag/friction and the thermal conduction within a musical instrument can be ignored[9]. However, some in the literature claim (e.g., [30], [38], [103], [141]) that any deformation of small-amplitude waves "*is mainly controlled by thermoviscous losses in the wall boundary layers*" [141]. Consequently, the spectral components are dampened, particularly the higher ones [38], [141].

4.2.1 Review of the Literature

Thermoviscous losses were originally investigated by Helmholtz and Kundt [93], [126], though much of the foundational work was done by Kirchhoff [121], [122], [217]. For instance, Kirchhoff was the first to suggest an expression for the *amplitude attenuation constant* (also referred to as the loss factor, α) finding that if the temperature of the air was 20^o C,

$$\alpha \approx 2.964e-05\frac{\sqrt{f}}{r} \text{ 1/cm} , \tag{4.9}$$

where r denoted the radius of the tube and f is frequency [217][10]. However, equation (4.9) is not sufficient for all types of tubes. As described by Weston, tubes can be classified either as 'narrow', 'wide' or 'very wide' depending on how the thermoviscous losses influence the wave motion [217]. He outlines that for narrow tubes (and low frequencies), the air motion can be described as isothermal and would mostly be governed by viscous effects. For wide

[9] The thermal conductivity of a gas, denoted by κ, is related to the density, ρ, heat capacity per unit mass at constant volume, c_v, speed of sound, c, specific heat ratio, γ, and the mean free path ℓ of the gas molecules. As defined in [146], κ can be approximated by $\kappa \approx \frac{1.6\ell\rho c c_v}{\sqrt{\gamma}}$. The molecular mean free path in atmospheric pressure at 20^o C is $\ell \approx 10^{-5}$ cm [146]. Viscosity is produced by momentum diffusion, i.e., when gas molecules pass each other, the velocity of the particles are subject to a shear stress proportional to the rate of change of the molecules velocity. In this case, the proportionality constant is the coefficient of viscosity, denoted by μ. As defined in [146], μ can be written as $\mu \approx \frac{\ell\rho c}{\sqrt{\gamma}}$.

[10] This work was later reproduced in more detail by Rayleigh [178].

tubes, the air motion would be adiabatic and the sound energy would diffuse evenly across the tube's cross-section with a slight preference near the walls. Finally, for very wide tubes, the majority of the sound energy would be lost near the wall within the thin boundary layers [217]. Equation (4.9) holds for 'wide'[11], or 'very wide' tubes.

Some of the initial work examining the influence of thermoviscous losses in musical instruments was done by Benade for the clarinet. He estimated that as much as 40% of the clarinet's sound energy could be lost. For brass instruments however, Benade approximated that only 10% - 20% of the sound energy would be lost since they are not constructed with holes. Myers obtained a similar approximation for the trombone. In particular, he estimated that wall losses could reduce the amplitude of the transfer function by approximately 18% [152]. With respect to the impedance peaks, Noreland has suggested that for brass instruments, dampening can decrease the frequency (i.e., the pitch) of the lowest impedance peaks by approximately 5%, and lower the amplitude (i.e., volume) of the peaks by several orders of magnitude. However, the relative peak discrepancy from neglecting viscosity through the bell region would only be around 0.02% [158].

Several studies have been done on brass wind instruments, both experimental (e.g., [14], [38], [50], [141]) and numerical (e.g., [21], [36], [39], [106], [101], [141]) to investigate the effects of viscosity and thermal conductivity. However, incorporating the wall losses is more easily done in the frequency-domain due to the frequency dependence [179], [204], and as a result, linear wave propagation is typically considered [179]. Most such problems are formulated in 1D[12] or 2D where the propagation has been modelled using, for instance, acoustic impedance and admittance formulations (e.g., [27], [28]), Webster's horn equation (e.g., [101]), the linearized Navier-Stokes equations (e.g., [94], [106], [107], [155],), modified Burgers' equations (e.g., [89], [92], [141]) and the Helmholtz equation (e.g., [48], [160]). Others have tried to approximate losses with digital filters using transmission line models (e.g., [25], [39]) or wave digital modelling (e.g., [209]). Some have also attempted to setup the problem in the frequency-domain and then convert it into the time-domain (e.g., [25], [27]). Upon this transformation, fractional derivatives appeared with spatially varying coefficients[13] [25], which usually require a finite impulse response (FIR) filter or an infinite impulse response (IIR) filter[14] [25], [205].

[11] Where r is at least 10 times the width of the boundary layer thickness [38].

[12] Some believe it is sufficient for the boundary layer motion to be considered in 1D so long as the transverse component of the particle velocity is small [39]. However, it may be considered an oversimplification because the fluid motion in a resonator with a boundary layer is no longer 1D.

[13] These coefficients are functions of the specific heat ratio, Prandtl's number and shear viscosity (constants discussed in [114]).

[14] Although using FIR fractional delay filters for 'signal-dependent passive nonlinearities' with signal-dependent coefficients has been suggested in the literature [208].

Regardless of the mathematical description, extending such problems to include nonlinear effects has shown to be tricky. One reason for this is that a time-domain model is preferable to properly describe the interaction between the backward and forward moving waves [24], [27] but thermoviscous losses are frequency dependent. Moreover, complications can arise due to numerical stability considerations [27]. One approach to deal with this would be to use artificial viscosity, although it is not ideal. A key issue with artificial viscosity[15] is that (as the name suggests) it is artificial, and used to stabilize discontinuities rather than physically model viscosity [137]. As a consequence, the numerical solution can become too diffusive and distort the resonances of the musical instrument [27]. This is similarly true with limiters [84]. The same outcome can be achieved with other dissipation approaches[16] [137].

When it comes to including both nonlinear and thermoviscous effects, one view in the literature is that these two effects "*act to oppose each other* [38]"[17]. In particular, some believe that as large-amplitude waves undergo spectral enrichment, the "*viscothermal losses in the boundary layer at the tube wall act to dissipate the high frequency energy that is the result of nonlinear wave steepening*" [38] and 'counteract' one another [132]. The effects due to spectral enrichment and losses however should not be equated per se; these factors are different. Thermoviscous losses are more of a linear effect, whereas steepening is nonlinear, i.e., they depend on different factors. Moreover, the presence of wave steepening does not change the wall losses; they will be present regardless of the wave propagation behaviour. But for high dynamic notes, losses typically just have less of an influence compared to the nonlinearities. A few studies examining this phenomenon have already been published. For instance, Menguy and Gilbert investigated the interaction between thermoviscous losses and nonlinearities for planar waves in cylindrical tubes both theoretically and experimentally [141]. Their work outlined which factor (spectral enrichment or losses) would be dominant for acoustic waves of various SPLs. Another more recent (experimental and numerical) study was done by Chick *et al.* for the trombone [38][18].

[15] Although, every numerical method has artificial viscosity, whether it be explicit or implicit.

[16] For instance, using Riemann solvers, which is what we do.

[17] Logie is another who has said that "*the total radiated sound power for a given input pressure will increase with the amount of nonlinear distortion... [but] there is some degree of counteraction to this by the increased wall losses with increasing frequency*" [132].

[18] So perhaps, it is reasonable to neglect boundary layer losses in our case, as nonlinearities are more important to consider.

4.2.2 Numerical Experiment using COMSOL

Carrying out a simple numerical study to examine and compare the effects of sound attenuation on certain size tubes may provide some useful insights. Additionally, it would allow us to verify findings from previous studies, such as those completed by Weston[19]. To accomplish this, the Navier-Stokes equations would need to be used, as they model acoustic wave propagation in the presence of viscous and thermal boundary layers [23]. However, this system of equations has not yet been implemented in the DG code I am using for my work. Within the field of brass instrument acoustics however, it is relatively common for COMSOL to be used for such studies (e.g., [39], [106], [112], [113], [155])[20]. Therefore, to still be able to experiment computationally in a way that is consistent with the literature[21], the *aeroacoustics module* in COMSOL [163] was used to obtain the results discussed in this section only.

In particular, the linearized, compressible, axisymmetric Navier-Stokes and Euler systems for an ideal gas in the time-domain were used to model the wave propagation through various computational tubes. Similar initial and boundary conditions to those used in the studies from [38], [39], [141] will be considered. Initially everything was at rest and at atmospheric pressure. At the inlet of each tube, a sinusoidal pressure function was used for the input, specifically,

$$p(t) = 500 \sin(2\pi \mathrm{ft}) \text{ [Pa]},$$

where $f = 242$ Hz. The wavelength was large relative to the tubes' diameter and no mean flow was considered. At the outlet of each tube, an impedance condition was used[22]. To resolve the boundary layers in COMSOL for the Navier-Stokes system, the tube walls were prescribed the default no-slip and isothermal conditions, i.e., the acoustic velocity and temperature difference was set to zero at the walls of the tubes. If such physical effects do not need to be considered, the COMSOL documentation states that this boundary condition should be changed to the slip and adiabatic option [105]. For the Euler system, the default rigid-wall condition was prescribed.

[19] Running such simulations would also allow us to tailor the setup of the problem according to our own needs, similarly to the study done by Chick *et al.*, i.e., by considering tubes that resemble certain components of the trumpet and trombone bores [38].

[20] Papers have even been published that simply compare the different discretizations available in COMSOL [106].

[21] In this thesis, we do not attempt to justify the adequacy of the model or implementation of the models included in COMSOL.

[22] Pass-through boundary conditions were also used and produced the same results, i.e., the solutions lied on top of each other.

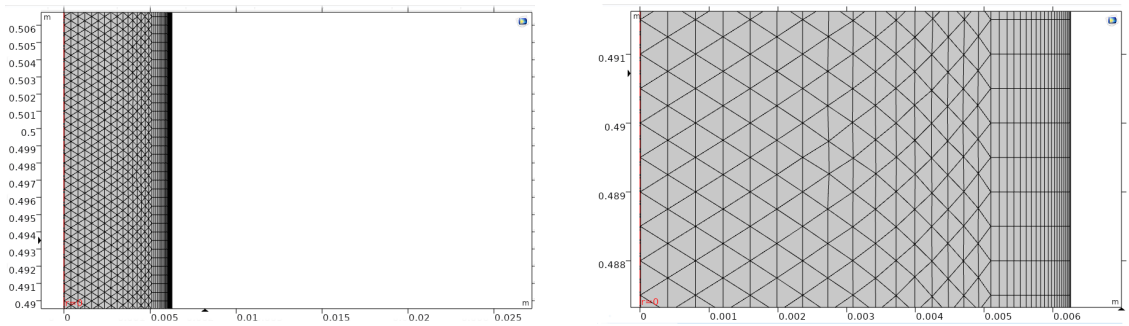

Figure 4.12: A close-up of the mesh generated in COMSOL for the tube of $r = 0.65$ cm with 20 boundary layers near the wall.

Table 4.1: Information regarding the COMSOL simulations discussed in Section 4.2.2. The number of elements and runtime for each simulation is reported.

Radius of Tube	Model	Number of elements	Runtime
$r = 1$ cm	Navier-Stokes Equations	94,253	5h12m58s
	Euler Equations	94,253	3h1m23s
$r = 0.65$ cm	Navier-Stokes Equations	95,279	5h37m55s
	Euler Equations	95,279	3h53m27s
$r = 0.5$ cm	Navier-Stokes Equations	99,679	7h13m58s
	Euler Equations	99,679	4h24m24s
$r = 0.3$ cm	Navier-Stokes Equations	111,043	8h45m0s
	Euler Equations	111,043	4h53m23s

Four computational tubes, all 2 m in length, were constructed. The radii considered were $r = 1$ cm, 0.65 cm, 0.5 cm, 0.3 cm. The corresponding meshes were obtained using COMSOL's built-in mesh generator. To ensure the boundary layers were properly resolved, 20 layers were considered within the 1 mm wide radial region from the inner wall (with a stretch factor of 1.05). An example of this is shown in Figure 4.12, and the total number of elements for each computational tube is reported in Table 4.1. In addition, to test whether the cell refinement was sufficient, a couple of the simulations were rerun on finer meshes. Since the numerical results did not visually change[23], we took this to mean that the original meshes were well resolved and that the simulations did not greatly suffer

[23] In other words, we obtained the same solution.

from numerical diffusion.

4.2.2.1 Computational Results using COMSOL

The numerical solutions obtained in COMSOL when solving the linearized Navier-Stokes and Euler equations were sampled 24 cm and 190 cm away from the inlet of each tube. Since the resulting pressures were periodic, for each solution, one period was isolated, analyzed and then plotted against the others in the time-domain (Figure 4.13) and frequency-domain (Figure 4.14). As expected, the computed pressures obtained via the Euler equations were equivalent regardless of the computational tube's radius. When the Navier-Stokes equations were used, we observe that the pressure amplitude slightly decreases as the tube's radius decreases. More precisely, when comparing the outputs from both systems, the pressure difference between the numerical results for each tube 24 cm and 190 cm from the inlet was,

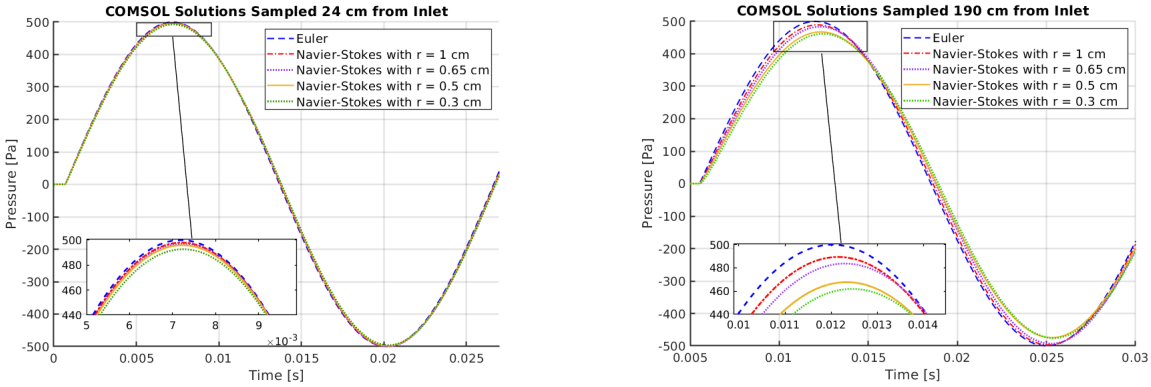

Figure 4.13: COMSOL results from solving the linearized Navier-Stokes and Euler equations in 2 m tubes with radii of $r = 1$ cm, $r = 0.65$, $r = 0.5$ cm and $r = 0.3$ cm sampled 24 cm (left) and 190 cm (right) from the inlet.

r = 0.30 cm: 1.6% and 7.6%[24],

r = 0.50 cm: 0.8% and 6.4%,

[24] This corresponds to the deviation in the pressure peaks by 7 Pa and 38 Pa when sampled 24 cm and 190 cm from the inlet .

r = 0.65 cm: 0.6% and 3.2%,

r = 1.00 cm: 0.4% and 2.2%.

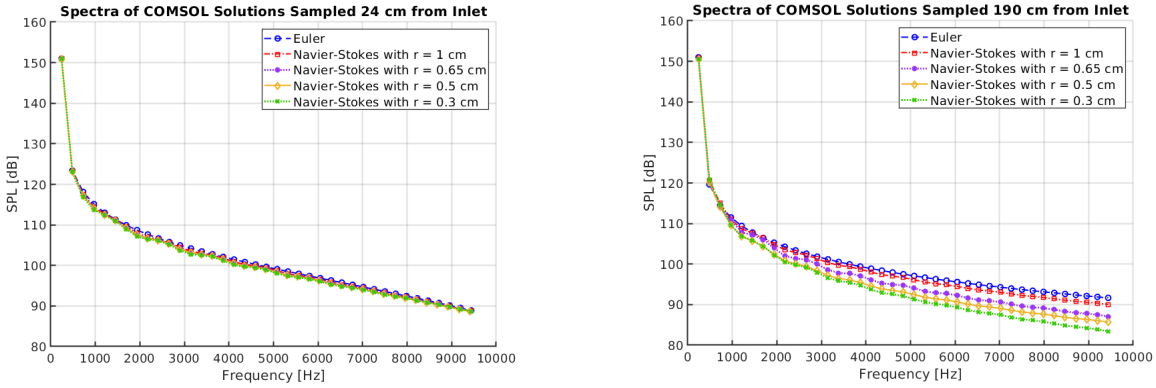

Figure 4.14: Spectral components of the COMSOL results from solving the linearized Navier-Stokes and Euler equations in 2 m long tubes with radii of $r = 1$ cm, $r = 0.65$, $r = 0.5$ cm and $r = 0.3$ cm sampled 24 cm (left) and 190 cm (right) from the inlet.

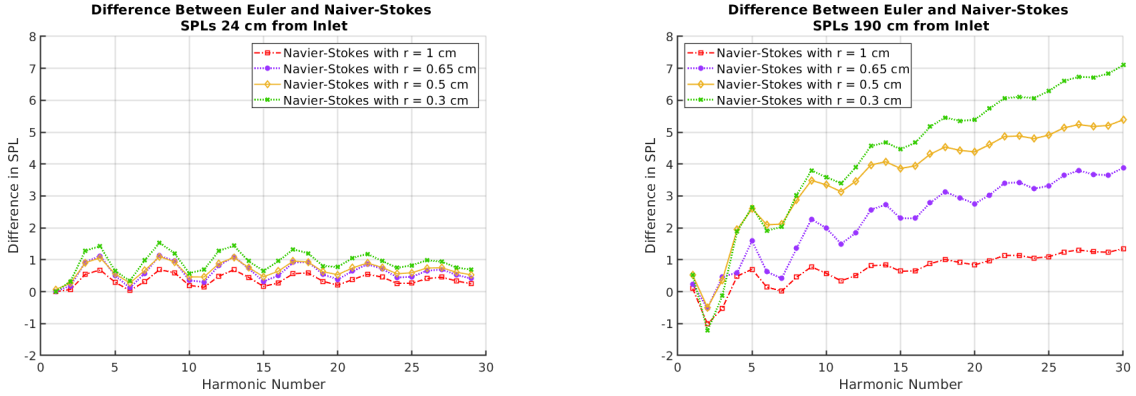

Figure 4.15: The difference in the SPL between the Euler and Navier-Stokes systems solved in COMSOL when considering 2 m long tubes with radii of $r = 1$ cm, $r = 0.65$, $r = 0.5$ cm and $r = 0.3$ cm sampled 24 cm (left) and 190 cm (right) from the inlet.

In Figure 4.15, we plot the difference in SPLs between the Navier-Stokes and Euler equation results for all four tubes considered. We observe that the amplitude variation between the solutions 190 cm from the inlet increases as a function of frequency, as expected.

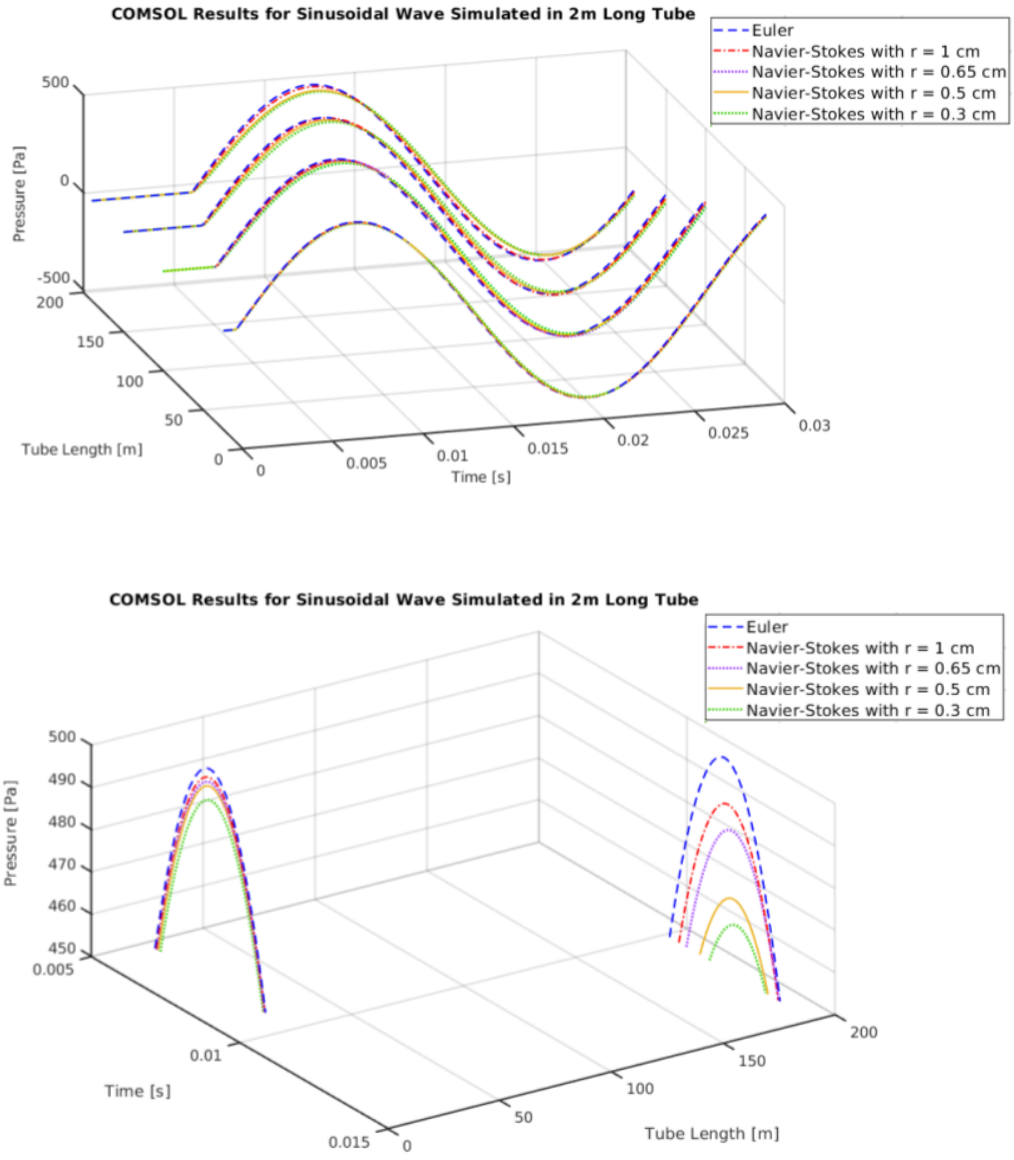

Figure 4.16: The computed pressure obtained from COMSOL when solving the Navier-Stokes and Euler equations. The pressure wave sampled at different locations along each computational tube is shown (top), and a magnification of the pressure peaks sampled 24 cm and 190 cm from the inlet is shown (bottom).

Moreover, the deviation becomes more drastic as the radius of the tube decreases, which is in agreement with Weston [217]. The thermoviscous losses are not nearly as prominent when examining the outputs only 24 cm from the inlet.

To better observe the progression of the pressure waves as they travel through the tubes of varying radii, the profiles are sampled at different locations along the bore and plotted in Figure 4.16. At a distance of 24 cm from the inlet, the results indicate that for the trumpet's narrowest tubing region, i.e., when $r \approx 0.3$ cm, the Euler equations overestimate the pressure of a small-amplitude wave by at most 1.6%. For the trombone's narrowest tubing section, i.e., when $r \approx 0.5$ cm, the difference is at most 0.8%. The main cylindrical portion of the trumpet and trombone that leads into the flare expansion is around 78 cm and 170 cm, respectively. The overestimation in the pressure amplitude from neglecting losses in this tubing section is less than 5% for both instruments.

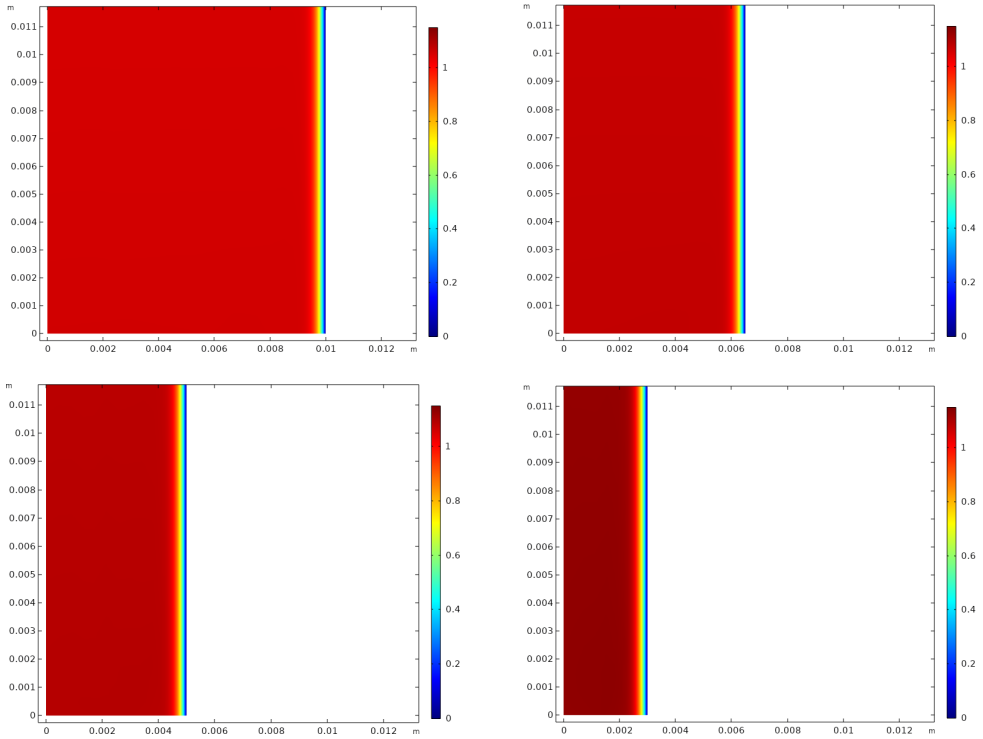

Figure 4.17: Comparison of the boundary layers obtained from the COMSOL solution when using the linearized Navier-Stokes equations for a tube with $r = 1$ cm (top-left), $r = 0.65$ cm (top-right), $r = 0.5$ cm (bottom-left), and $r = 0.3$ cm (bottom-right). Even for the smallest tube, the boundary layer thickness is still small relative to the tube radius.

In Figure 4.17 we also show an image of the boundary layers obtained for each computational tube after solving the Navier-Stokes equations. These outputs of the velocity fields are in agreement with solutions previously published in the literature for the trumpet (e.g., [112]). Furthermore, even for the smallest tube ($r = 0.3$ cm), we notice that the thickness of the boundary layer is still relatively small. More precisely, since the boundary layer thickness is less than a tenth of the tube's diameter, according to Weston, all the tubes can be classified as 'wide' or 'very wide' [217]. As to be expected, boundary layers were not observed after solving the Euler equations (the radial velocity was uniform across the tube). In Table 4.1, the runtimes are reported. As we can see, using the Navier-Stokes equations takes approximately twice as long.

In summary, these findings indicate that the error associated from neglecting thermoviscous losses in the main cylindrical region of the trumpet and trombone corresponds to an error of at most 5%. However, it is difficult to extrapolate these results to the full nonlinear system. We therefore make the following theoretical approximation below.

4.2.3 Energy Loss Approximation for Narrow Bore Regions

According to [38], since the boundary layers that form along the walls of the trumpet and trombone are on the order of 0.1 mm, we can approximate the amplitude loss using equation (4.9) for each of the radii listed in Table 4.1 for specific frequencies. For example, the loss factor as a function of radius was calculated and plotted in Figure 4.18 where $f_1 = 242$ Hz. For all frequencies considered, once the radius of the tube is 1 cm, $\alpha < 0.002$.

A better approximation however would be to have an expression that is written with respect to the boundary layer thickness. Such theory is outlined in [146] by Morse and Ingard, which we will use to estimate the relative power loss of the sound dissipation from the boundary layer effects.

4.2.3.1 Relative Power Loss Approximation

As stated by Morse and Ingard [146], for air, the thickness of the viscous and thermal boundary layers, denoted by d_v and d_h, are

$$d_v = \sqrt{\frac{2\mu}{\rho\omega}} \approx \frac{2.1e\text{-}03}{\sqrt{f}} \text{ m}, \qquad d_h = \sqrt{\frac{2\kappa}{\rho\omega c_p}} \approx \frac{2.5e\text{-}03}{\sqrt{f}} \text{ m}. \tag{4.10}$$

where ρ is the density, ω is the angular frequency, κ is the thermal conductivity, μ is viscosity, and c_p is the heat capacity at constant pressure. A derivation of d_v and d_h can

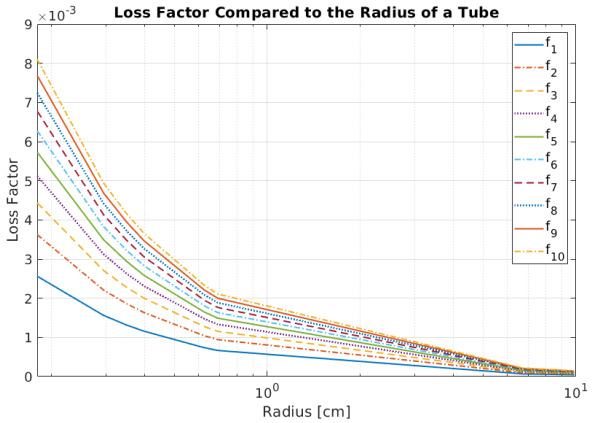

Figure 4.18: The loss factor calculated using equation (4.9) compared to the radius of a tube where $f_1 = 242$ Hz.

be found in [23]. According to Benade however [17], these values are better approximated by

$$d_v \approx \frac{1.6e\text{-}03}{\sqrt{f}} \text{ m}, \qquad d_h \approx \frac{1.9e\text{-}03}{\sqrt{f}} \text{ m}. \tag{4.11}$$

As expected, we observe that $d_v, d_h \propto \frac{1}{\sqrt{f}}$, so the boundary layer thickness gets thinner as the frequency increases. For more specific details on how these expressions were obtained, please refer to [146]. The boundary layer thickness corresponding to the different harmonic components of the B_3^b note are listed in Table 4.2 when using Benade's values.

According to Morse and Ingard [146], the thermal loss per unit area at the boundary along the surface can be approximated by

$$L_{\text{thermal}} \approx \left(\frac{\gamma - 1}{2\rho c^2}\right) \omega d_h \ |p_{\text{surface}}|^2, \tag{4.12}$$

where $|p_{\text{surface}}|^2$ is the rms value of the pressure at the surface. Similarly, the power loss per unit area averaged over the surface area from viscous forces can be approximated by

$$L_{\text{viscous}} \approx \frac{\omega}{2\rho c^2} d_v \ |p_{\text{surface}}|^2. \tag{4.13}$$

By definition, the transmitted power, denoted by P, is defined as

$$P = I_a A = \frac{A}{2\rho c} |p|^2, \tag{4.14}$$

Table 4.2: Calculated viscous boundary layer thickness (d_v) and thermal boundary layer thickness (d_t) with respect to specified frequencies using equation (4.11).

Frequency	Viscous Boundary Layer d_v	Thermal Boundary Layer d_t
242 Hz	2.3499e-04 m	1.6071e-04 m
484 Hz	9.5455e-05 m	1.1364e-04 m
726 Hz	7.7938e-05 m	9.2784e-05 m
968 Hz	6.7497e-05 m	8.0353e-05 m
1210 Hz	6.0371e-05 m	7.1870e-05 m
1452 Hz	5.5111e-05 m	6.5608e-05 m
1694 Hz	5.1023e-05 m	6.0741e-05 m
1937 Hz	4.7727e-05 m	5.6818e-05 m
2179 Hz	4.4998e-05 m	5.3569e-05 m
2421 Hz	4.2689e-05 m	5.0820e-05 m
2663 Hz	4.0702e-05 m	4.8455e-05 m
2905 Hz	3.8969e-05 m	4.6392e-05 m

where I_a is the acoustic intensity and A is the area. Therefore, the total viscous and thermal loss rate at the surface is[25]

$$\begin{aligned} L_{\text{thermal}} + L_{\text{viscous}} &\approx \left(\frac{\omega}{2\rho c^2}\right)\left[(\gamma-1)d_h + d_v\right]\ |p_{\text{surface}}|^2, \\ &\approx \left(\frac{|p_{\text{surface}}|^2\ \pi\sqrt{f}}{\rho c^2}\right)\left[(\gamma-1)\ 1.9e\text{-}03 + 1.6e\text{-}03\right]. \end{aligned} \tag{4.15}$$

The total power lost, denoted by P_{Lost}, is

$$P_{\text{lost}} = \left(L_{\text{thermal}} + L_{\text{viscous}}\right) A_{\text{surface}}. \tag{4.16}$$

We can now consider the ratio of the power lost in the tube to the power transmitted in the tube. Hence, the relative power loss, denoted by q, is defined as

$$q = \frac{P_{\text{lost}}}{P}. \tag{4.17}$$

Although losses become stronger at higher frequencies, the thickness of the boundary layer becomes thinner. Furthermore, for harmonics above the cutoff frequency, no reflections occur. For these reasons, Kausel believes that thermoviscous losses have the greatest

[25] The full derivation of equation (4.15) can be found in [146].

Table 4.3: Approximation of the relative power lost in the bore of the trumpet and trombone prior to the flare expansion for harmonic components corresponding to the B_3^b when using equation (4.11).

Frequency	Relative Power Loss for Trumpet	Relative Power Loss for Trombone
242 Hz	1.70 %	2.20 %
484 Hz	2.40 %	3.11 %
726 Hz	2.94 %	3.81 %
968 Hz	3.39 %	4.40 %
1210 Hz	3.79 %	4.92 %

effect on the lower spectral components of a played sound [110]. If for instance, we consider the harmonics of the B_3^b that are below the cutoff frequency, along with Benade's expressions for d_v and d_h[26], (4.17) can be used to calculate the relative power lost within the tubing prior to the instrument's bell. Table 4.3 listed these q values for the lower spectrum of the B_3^b. If Kausel is correct (that the losses mostly influence the lowest frequencies)[27], then our obtained theoretical approximation is consistent with the COMSOL results for the B_3^b discussed in Section 4.2.2, i.e., losses prior to the bell are approximately 5%. It is encouraging that the results found in Sections 4.2.2 and 4.2.3 are consistent and relatively small. This leads us to believe that nonlinearities would be much more important to model, especially if effects of wave steepening "*act to oppose*" boundary layer losses, as suggested in [38], [132], [141]. However, this is speculation and no conclusive statements about the losses associated with finite-amplitude sound waves can be made from examining small ones.

4.3 Summary of Findings

In this chapter, the consequences of neglecting vibroacoustic and thermoviscous effects have been explored. From our findings, we have come to the following conclusions:

i. Thermoviscous losses are most important in the narrowest region of the instrument, i.e., near the mouthpiece-shank. This section of tubing is only around 24 cm and 4.5

[26] Benade's approximation was chosen over Morse and Ingard's approximation for d_v and d_h (Morse and Ingard assume that temperature will always be fixed and give the basic dependence), as it is used more often, e.g., [192], and is a closer approximation.

[27] Which seems reasonable because these spectral components are mostly confined to the bore.

cm for the trumpet and trombone, respectively. Though, these narrow regions also correspond to where the amplitude of the waveform is largest, i.e., where the SPLs are highest.

ii. The main cylindrical bore portion of the instruments as well as the flare expansions can be considered as 'wide' or 'very wide' tubes. According to [38], [158], [217], wall loss effects are therefore small.

iii. We believe that the SPLs of the tones we are mainly concerned with are in a dynamic range where nonlinearities as well as the cross-sectional area of the instruments are more important to model compared to the vibroacoustic and thermoviscous losses. This is in agreement with the work published in [38], [132], [141], [185][28].

[28] Which will be demonstrated in the next chapter.

Chapter 5

Numerical Experiments

5.1 Prerequisites

The purpose of this chapter is to determine what computational aspects of our problem can be simplified without compromising the integrity or validity of the numerical solutions. Ultimately, we aim to accurately simulate realistic musical notes in brass instruments. However, investigating the numerical challenges of such an endeavour by first solving simpler acoustic problems would be beneficial, as this would allow us to verify the adequacy of our approach. We therefore aim to answer the following questions:

1. What is the optimal computational domain to reduce the simulation runtime while maintaining the integrity of the numerical solution?
2. How accurately does the computational instrument need to be modelled, and how do the different components influence the sound wave propagation? This includes:
    i. The shape of the tubing prior to the flare with a specific focus on the geometry near the mouthpiece-shank.
    ii. The bends.
    iii. The bell.
3. What dimension should the problem be solved in?

The other intention of this chapter is to numerically verify the claims made in Chapter 2 and in the literature. For instance,

4. Is the cutoff frequency of our computational instruments in accord with the physical instrument?

5. Can we numerically verify spectral enrichment thereby supporting the findings discussed in Section 2.3.1?

6. Can we numerically confirm the predictions made in Section 2.3.1.1 regarding the generation of shock waves in the trumpet and trombone for the loudly played B_3^b?

5.2 Discretization of Conservative Euler System

To simulate realistic trumpet or trombone notes, we primarily focused on the effects due to nonlinear wave propagation rather than energy losses. The Euler system is therefore optimal because the formulation is able to handle discontinuities. For a Newtonian, compressible, inviscid fluid, the five equations of motion are defined by

$$\begin{aligned}
\frac{\partial \rho}{\partial t} + \frac{\partial(\rho u)}{\partial x} + \frac{\partial(\rho v)}{\partial y} + \frac{\partial(\rho w)}{\partial z} &= 0, \\
\rho\left(\frac{\partial u}{\partial t} + \vec{v}\cdot\nabla u\right) + \frac{\partial p}{\partial x} &= 0, \\
\rho\left(\frac{\partial v}{\partial t} + \vec{v}\cdot\nabla v\right) + \frac{\partial p}{\partial y} &= 0, \\
\rho\left(\frac{\partial w}{\partial t} + \vec{v}\cdot\nabla w\right) + \frac{\partial p}{\partial z} &= 0, \\
\rho\left(\frac{\partial E}{\partial t} + \vec{v}\cdot\nabla E\right) + p\nabla\cdot\vec{v} &= 0,
\end{aligned}$$

where ρ is the gas density, $\rho\mathbf{u} = (\rho u, \rho v, \rho w)$ are the momenta in the x, y and z direction, respectively, p is the pressure, and E is the total energy. Finally, the parameter γ is the specific heat ratio, which is $\gamma = 1.4$ for air [97]. Writing this set of hyperbolic PDEs in Cartesian coordinates (x, y, z) and in conservative form yields

$$\frac{\partial \mathbf{U}}{\partial t} + \frac{\partial \mathbf{F}(\mathbf{U})}{\partial x} + \frac{\partial \mathbf{G}(\mathbf{U})}{\partial y} + \frac{\partial \mathbf{H}(\mathbf{U})}{\partial z} = \mathbf{0}, \tag{5.1}$$

where $\mathbf{U}$ is the vector of conserved variables and the flux vectors are

$$\mathbf{F}(\mathbf{U}) = \begin{bmatrix} \rho u \\ \rho u^2 + p \\ \rho uv \\ \rho uw \\ u(E+p) \end{bmatrix}, \quad \mathbf{G}(\mathbf{U}) = \begin{bmatrix} \rho v \\ \rho uv \\ \rho v^2 + p \\ \rho vw \\ v(E+p) \end{bmatrix}, \quad \mathbf{H}(\mathbf{U}) = \begin{bmatrix} \rho w \\ \rho uw \\ \rho vw \\ \rho w^2 + p \\ w(E+p) \end{bmatrix}. \tag{5.2}$$

The equation of state for an ideal gas connects E to the other variables and closes the system,

$$E = \frac{p}{\gamma - 1} + \frac{\rho}{2}(u^2 + v^2 + w^2). \tag{5.3}$$

The problem can also be formulated by exploiting the axial symmetry in which the solution is independent from the angular coordinate θ. The equations of motion can then be written as a 2D axisymmetric system (x, r) where r is the radial component and x is the horizontal one. The momenta in the axial and radial directions are described by $\rho\dot{x}$ and $\rho\dot{r}$, respectively. To avoid the singularity at $r = 0$, the surface integral was not computed along the axis of symmetry and $\mathbf{U}$ is multiplied by r. The system (5.1 - 5.2) in (x, r) coordinates is

$$\frac{\partial[r\mathbf{U}]}{\partial t} + \frac{\partial[r\mathbf{F}(\mathbf{U})]}{\partial x} + \frac{\partial[r\mathbf{G}(\mathbf{U})]}{\partial r} = \mathbf{S}(\mathbf{U}), \tag{5.4}$$

where the following source term arises as a consequence of the change of variable

$$\mathbf{S}(\mathbf{U}) = \begin{bmatrix} 0, & 0, & p, & 0 \end{bmatrix}^{\mathbf{T}}. \tag{5.5}$$

5.3 Solving the Compressible Euler Equations

To numerically solve the system (5.1) or (5.5), boundary conditions must be imposed as they contain necessary information regarding how gas enters and exits the computational domain. The normal components of the fluxes determine the transport properties at a surface [97]. If $v_n = \vec{v} \cdot \hat{n}$ denotes the normal velocity component at the surface where $\hat{n}$ is the normal vector pointed toward the flow domain, then at the boundary, the behaviour of the Euler system will be determined by the propagating waves with speeds $(v_n + c)$, v_n, $(v_n - c)$. Speeds $(v_n \pm c)$ correspond to the acoustic waves, whereas v_n are the entropy and vorticity waves. For our computational purposes, the flow at the inlet and at the outer domain (outlet) will be subsonic, i.e., there will not be shocks entering the computational

instrument or exiting the far-field of Ω. Thus, if the value of the wave speed is positive, it means that a physical boundary condition must be imposed. In other words, if information is coming into Ω, then the information must be defined from outside the domain. Conversely, if the wave speed is negative, a numerical boundary condition must instead be used. This implies that if information is leaving Ω, we cannot impose information from the outside [97]. An illustration of this can be found in Figure 5.1.

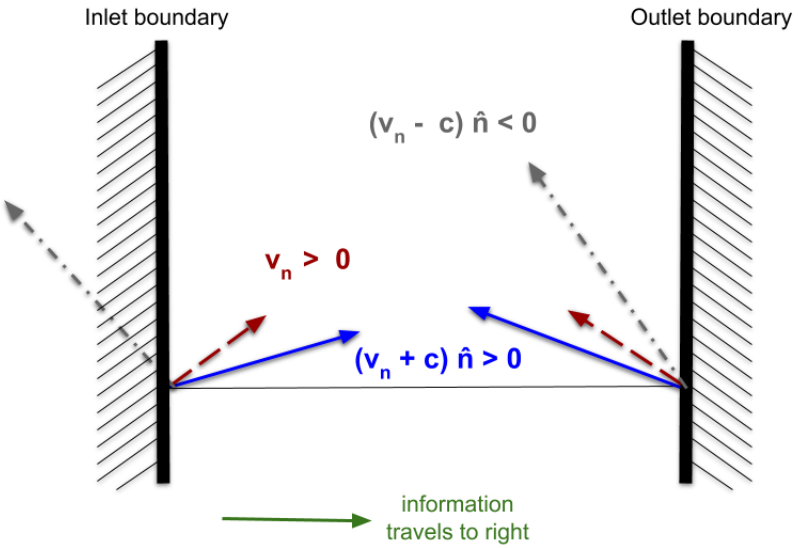

Figure 5.1: For subsonic conditions, the characteristic propagation properties at the inlet and outlet boundary when solving the compressible Euler equations.

Therefore, to numerically solve the Euler system[1], three boundary conditions are required,

1. a solid-wall condition,
2. an inlet condition,
3. an outlet condition,

as well as initial conditions. These boundary conditions must be imposed such that they are physically and acoustically consistent.

[1] It should be stated however that when solving the Euler equations, there is no guarantee that the flow will remain isentropic. But generally speaking, for an inviscid, subsonic flow, entropy remains constant [97].

5.3.1 Numerical Setup for Experiments

All numerical simulations presented in Sections 5.4, 5.5, 5.6 and 5.7 had a similar setup (with respect to the initial and boundary conditions) so, for ease of reading, this setup will first be reviewed.

Initial Conditions (ICs)

For the numerical experiments, we take the flow to initially be at rest and introduce the sound waves or pressure disturbances via the boundary condition. All variables are scaled from physical values to ones more convenient for computation. In particular, the ambient speed of sound, c_0, which is approximately 343 m/s in air, and atmospheric pressure, p_0, are scaled to be equal to 1.0. Assuming that the flow is isentropic, i.e., $c_0 = \sqrt{\frac{\gamma p_0}{\rho_0}}$, the initial density ρ_0 should then be taken to be 1.4. In summary, the initial conditions are given by

$$\left[p_0, \rho_0, u_0, v_0, w_0\right] = \left[1.0, 1.4, 0, 0, 0\right]. \tag{5.6}$$

Boundary Conditions (BCs)

On the inner and outer walls of the trumpet and trombone, excluding the mouthpiece boundary, reflective boundary conditions (i.e., solid-wall BCs) were prescribed. A ghost state was specified so that the normal velocity was reflected with respect to the wall, i.e., taken with a change of sign. The density, pressure and tangential velocity were unchanged from the corresponding values inside the cell. Thus, we have the dimensionless condition

$$\begin{cases} p_{\text{right}} = p_{\text{left}}, \\ \rho_{\text{right}} = \rho_{\text{left}}, \\ u_{\text{right}} = u_{\text{left}} - 2u_{\text{left}}\hat{n}_x, \\ v_{\text{right}} = v_{\text{left}} - 2v_{\text{left}}\hat{n}_y, \\ w_{\text{right}} = w_{\text{left}} - 2w_{\text{left}}\hat{n}_z, \end{cases} \tag{5.7}$$

where $\hat{n}_x$, $\hat{n}_y$, and $\hat{n}_z$ are the components of the outward unit normals in the x, y and z direction, respectively.

Along the far-field boundary, pass-through conditions were used where the ghost state was prescribed to be the initial state defined in (5.6). The computational domain was

large enough to ensure the numerical solution (specifically the waveform exiting the bell) would not be adversely influenced by any reflections from the outer wall, i.e., the waves were able to pass-through with little, to no reflection[2]. At the left vertical boundary of the bore (which corresponds to the mouthpiece boundary), the ghost state was specified to be the inflow condition, which will now be described. To obtain a continuous expression for pressure with respect to time, the procedure outlined in Section 2.3.1.1 to obtain equation (2.6) was carried out for the experimental pressure measured at Mic $_{\text{Mouthpiece}}$ unless otherwise specified. The specific notes used will be mentioned independently in the different sections. We then related velocity to pressure at the mouthpiece through the expression derived from linear acoustic theory for planar waves, i.e.,

$$p - p_0 = \rho_0 c_0 u. \tag{5.8}$$

Simulations using the spherical relationship were also run but the results were equivalent to the outputs obtained when using equation (5.8) and so, will not be discussed here. The linearization is reasonable since the speed of the air particles inside the instrument is low relative to the speed of sound. Velocity measurements for trombones reported in [54], [66] give the maximum speed to be around 17 m/s (i.e., about 5% of the speed of sound) in the throat of the mouthpiece, which is similar to the values observed in our numerical simulations. Moreover, this linearization is only applied locally at the inlet boundary. Everywhere else in the computational domain, the velocity is described through the nonlinear system of equations[3]. Nonetheless, there are some issues using such a setup and Chapter 6 will be dedicated to reviewing such decisions. Finally, the density is computed assuming we have an adiabatic process. Thus, compressible flow theory states that [131]

$$\rho = \gamma p^{\frac{1}{\gamma}}. \tag{5.9}$$

In summary, the dimensionless boundary condition at the inlet of the computational trumpet or trombone is given by

$$\begin{cases} p = A_0 + \sum_{i=1}^{N_f} 2A_i \cos\left(2\pi f_i t + \phi_i\right), \\ \rho = \gamma p^{\frac{1}{\gamma}}, \\ u = \frac{p - p_o}{\rho_o c_o}, \\ v = 0.0, \\ w = 0.0, \end{cases} \tag{5.10}$$

[2] We experimentally determined the necessary size of the domain, this will be discussed in Section 5.4.
[3] Some have claimed in the literature that this is a valid approximation, e.g., [110], [141].

where N_f is the number of frequencies, A_i, f_i, and ϕ_i denote the amplitude, frequency and phase shift, respectively, for each harmonic of the measured notes [184].

In addition to running simulations that have an inflow boundary condition that prescribes a periodic waveform, acoustic pulse simulations were also carried out and are presented in Sections 5.6, 5.8.1 and 5.8.2. The numerical setup is similar except, for how the pressure expression is written in the inflow condition. More details are given below.

5.3.2 Pulse Reflectometry Numerical Tests

Impulse or pulse reflectometry has been a useful way to investigate problems such as stratifications in the earth's crust, measuring the structure of the trachea or lungs, and to study acoustic systems [195]. For instance, pulse reflectometry has been used to examine acoustically significant features of brass and wind instruments (e.g., [6], [7], [18], [51], [138], [195], [196], [214]). This typically includes measuring the instrument's profile as well as the input impedance, which is defined as the ratio of the acoustic pressure to the air volume flow rate at the inlet of the instrument. Pulse reflectometry can also be used numerically for similar purposes. In our case, it could allow us to better evaluate whether our computational instrument is sufficiently accurate to properly model the wave propagation. Reflection and transmission coefficients could also be calculated.

Acoustic pulse reflectometry is carried out by sending an impulse down the bore of a musical instrument. As the pulse travels toward the open end, the incident wave undergoes partial reflection and transmission whenever there is a change in impedance. This is sometimes referred to as a *reflection sequence*. The position that is chosen along the bore to sample the reflection sequence is called the *input impulse response* [195]. The changes in impedance are due to expansions or contractions along the instrument's profile (i.e., when the cross-sectional area of the bore changes).

In Sections 5.6, 5.8.1 and 5.8.2, acoustic pulse reflectometry simulations will be discussed and presented for various purposes. Most of these numerical experiments were setup to generate a pressure pulse at the inlet of the computational instrument[4]. This corresponds to changing the expression for p in equation (5.10) to instead be

$$p = \begin{cases} 1.0 + \mathcal{C}(1 - \cos(\mathcal{D}t)), & \text{if t} < \frac{2\pi}{\mathcal{D}}, \\ 1.0, & \text{otherwise}, \end{cases} \tag{5.11}$$

[4] However, other numerical tests produced an acoustic pulse via a source term. More details can be found in Sections 6.4.2 and 6.4.1.

where $\mathcal{C}$ corresponds to half the amplitude of the pulse and $\mathcal{D}$ defines the duration. For the test cases in this thesis, small amplitude pulses that did not undergo significant (if any) wave steepening were considered.

Reflection and Transmission Coefficients

A standard practice when analyzing pulse reflectometry results is to find the reflection and transmission coefficients. From examining the reflection sequence, the reflection coefficient, denoted by $R(f)$, and can be calculated by taking the frequency content of the reflected pressure, $\mathcal{P}_r$, and dividing it by that of the incident pressure, $\mathcal{P}_i$, i.e., the ratio of the reflected pulse to the incident pulse [197]. The corresponding amplitude is calculated by

$$|R(f)| = \frac{\mathcal{P}_r(f)}{\mathcal{P}_i(f)}. \tag{5.12}$$

The transmission coefficient, denoted by $T(f)$, is the ratio of the radiated pressure, $\mathcal{P}_t(f)$, to the incident pressure. The corresponding amplitude is obtained by

$$|T(f)| = \frac{\mathcal{P}_t(f)}{\mathcal{P}_i(f)}. \tag{5.13}$$

Examining these acoustic parameters in the time-domain can also be useful, especially when studying the influence of specific regions of the instrument such as the bell [55].

5.4 Computational Domain Shape

Describing and simulating acoustic wave propagation can be difficult and time consuming, especially when modelling 3D problems in the time-domain. A computational boundary, denoted by $\partial\Omega$, is defined to construct a computational domain, denoted by Ω. As the propagating waves exit Ω, the amplitude needs to be sufficiently small otherwise reflections can occur from $\partial\Omega$ and influence the numerical solution. This implies that Ω needs to be sufficiently large without being too large[5]. Deciding on the appropriate geometry of the outer boundary can also be challenging for acoustic simulations through ducts such as musical instruments. This is because the "*position and geometry of the domain boundary is governed by the shape of the duct*" [189]. It therefore seems appropriate to investigate whether Ω can be manipulated to reduce reflections while being computationally practical.

[5] Otherwise, it would be too expensive to simulate.

5.4.1 Setup for the First Set of Computational Geometries

Since the trumpet is significantly smaller than the trombone, all the numerical simulations presented in this section were done using a shortened trumpet shape depicted in Figure 5.2. The geometry of the modified instrument was made to accurately model the slowly increasing diameter of the bell and the cylindrical tube leading up to the flare. It was important to have a realistic representation of a bell because as mentioned in [189], the optimal geometry of $\partial\Omega$ will be governed by the shape of the wavefront exiting the bore. The portion of the waveform that radiates from the flare contains mostly higher frequency components where the waves exit the bell with a more-or-less curved wavefront [20], [120]. There will however be a bias as the energy leaves the flare: more will be focused along the central axis rather than along the edges of the flare [55].

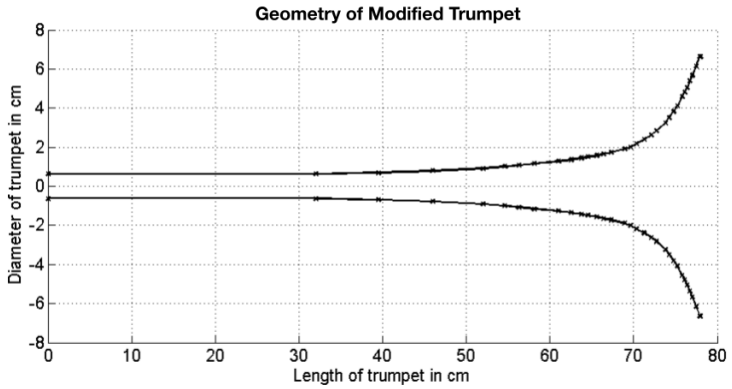

Figure 5.2: The geometry of the modified trumpet used for the simulations in Section 5.4.

For the inlet boundary, the pressure was prescribed to be the experimental data measured at Mic $_{\text{Bend}}$ for the B_3^b played at f (see Figure 5.3). We decided to simulate a periodic waveform rather than a pulse for this test since we aim to eventually simulate musical notes. However, for this numerical experiment, we are only concerned with how the numerical outputs will differ when Ω is manipulated rather than accurately reproducing the experimental data collected at Mic $_{\text{Outside-Bell}}$.

We first consider two types of geometries for Ω to model the trumpet in:

Type A: Whole domain (Ω_{Whole})

Domains that completely encapsulate the modified trumpet.

Type B: Half domain (Ω_{Half})

Domains that only have an area directly in front of the modified trumpet.

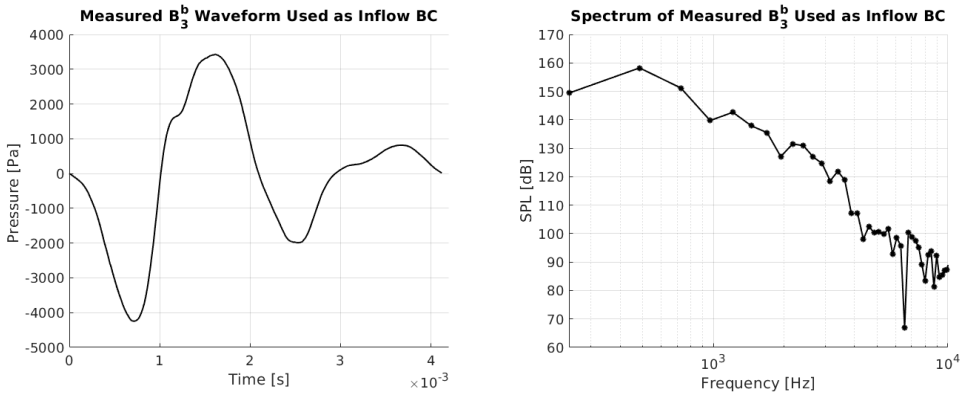

Figure 5.3: The pressure measured at the Mic $_{\text{Bend}}$ on the trumpet, which was used to define the inflow boundary condition. The time pressure waveform (left) and frequency spectrum (right) are shown.

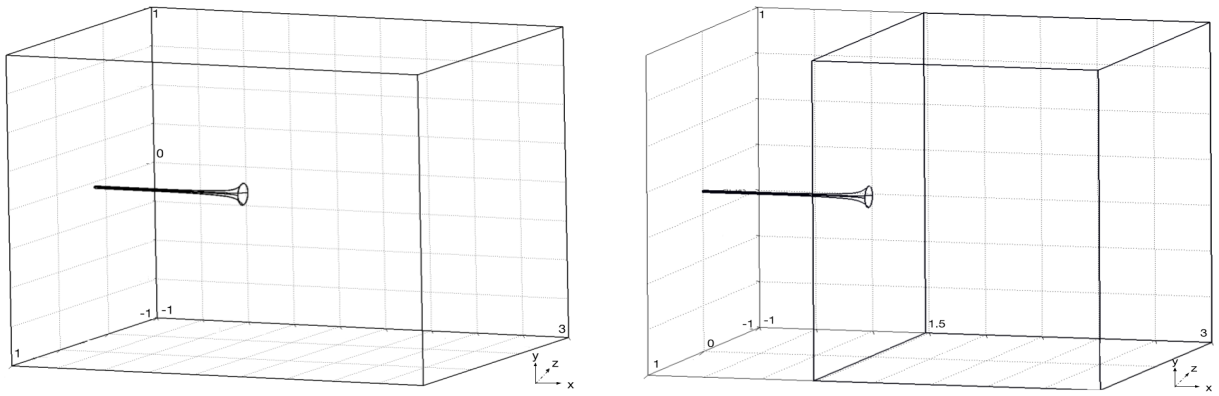

Figure 5.4: Two computational domains that were tested in Sections 5.4.1 and 5.4.2 Left: Ω_{Whole}. Right: Ω_{Half}.

The goal of examining the different volumes for Ω is to address the following inquiries:

1. Is it necessary to consider Ω behind the flare or, can it be neglected since only a small portion of the energy propagates behind the bell?

2. Is it advantageous to simulate a curved acoustic wavefront in a domain where there are no corners (this will be examined in Section 5.4.3)?

The Type A and Type B computational domains are shown in Figure 5.4. The center of the bell exit is located at the coordinate $(x, y, z) = (1.48\text{m}, 0, 0)$ for both Ω_{Whole} and Ω_{Half}. In the y and z directions, the domains are defined in $[-1\text{m},\ 1\text{m}]$. In front of the flare, both domain types extend to $x = 3\text{m}$. For Ω_{Whole}, the x-axis range further extends in the negative direction to $x = -1\text{m}$. So, in summary:

$$\text{For } \Omega_{\text{Whole}}: \ x \in [-1, 3],\ y \in [-1, 1],\ z \in [-1, 1].$$
$$\text{For } \Omega_{\text{Half}}: \ \ x \in [0, 3],\ y \in [-1, 1],\ z \in [-1, 1].$$

With respect to the meshes that were generated using GMSH, the number of elements, the smallest radius of the inscribed sphere[6] (which will be denoted by r_{min}) as well as the memory required for each mesh is reported in Table 5.1.

Table 5.1: The number of elements, minimum radius of the inscribed sphere (r_{min}) and memory required for the meshes generated for the computational domains shown in Figure 5.4.

Name of Domain	Number of Elements	r_{min}	Memory Required
Ω_{Half}	1,130,373	94.5 μm	1.50 GB
Ω_{Whole}	2,277,060	68.3 μm	3.00 GB

5.4.2 Simulation Results on Ω_{Whole} and Ω_{Half}

To analyze our simulation results, point sensors were placed around Ω_{Whole} and Ω_{Half} at various positions in front of the bell exit, as well as directly above and below the flare end. We are specifically interested in examining what happens along the central axis, i.e., $(x, 0, 0)$ where $x \in [0, 3]$. We expect to see some difference in the SPLs between the whole and half domain simulations directly above and below the bell, i.e., at $(1.48\text{m}, y, z)$ where $y, z \in [-1, -1]$.

Before reviewing the numerical solutions along $(x, 0, 0)$ however, we confirmed that the computed pressure radiating from the bell was indeed consistent among the different octants[7]. This demonstrates that the wavefront exiting the bell is symmetric, as expected. For this reason, only the numerical outputs sampled in the first octant (shown in Figure 5.5) will be reviewed here. This is done in both the time- and frequency-domain where the FFT was performed on the entire pressure signal.

[6] The inscribed sphere is a sphere that is contained within a tetrahedral cell which is tangent to each face.

[7] So for $y, z > 0$ or $y, z < 0$ when x is positive.

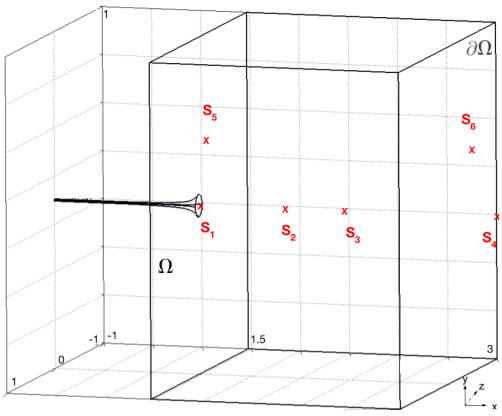

Figure 5.5: Location of point sensors positioned in the domains from Figure 5.4 that will be examined in Section 5.4.2.

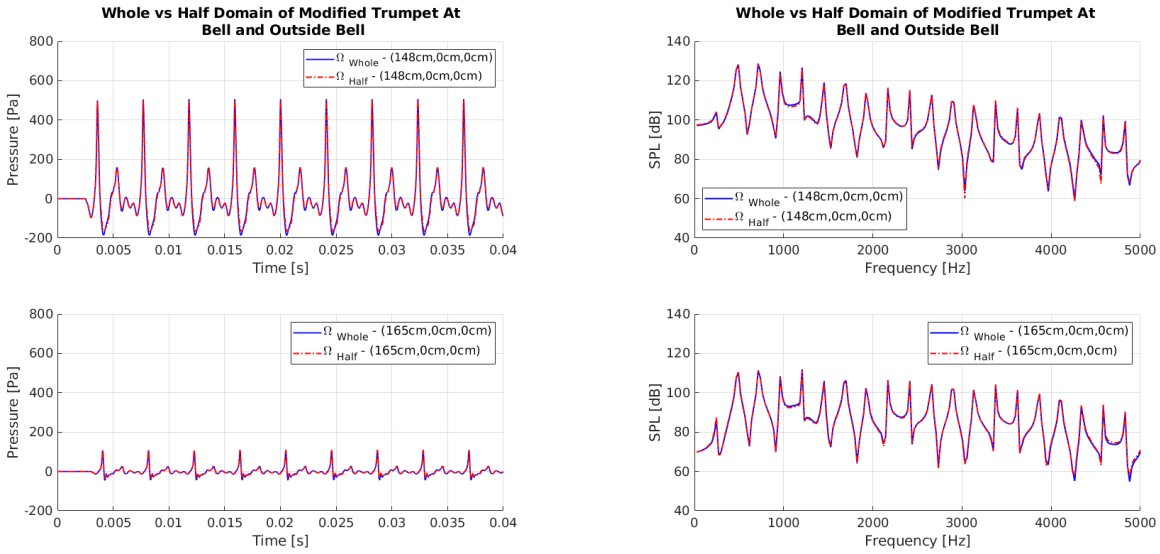

Figure 5.6: The computed pressure using Ω_{Whole} and Ω_{Half} in the time-domain (left) and frequency-domain (right) at positions S_1 (upper-plots) and S_2 (lower-plots) depicted in Figure 5.5.

First, we examine the difference between the Ω_{Whole} and Ω_{Half} simulations at points $(1.48, 0, 0)$ and $(1.65, 0, 0)$. As shown in Figure 5.5, the points at these locations are referred

to as S_1 and S_2[8]. The computed pressure and spectra sampled at S_1 and S_2 are plotted in Figure 5.6. We observe the solutions lie on top of each other, and we interpret this to mean that there is no difference between the outputs.

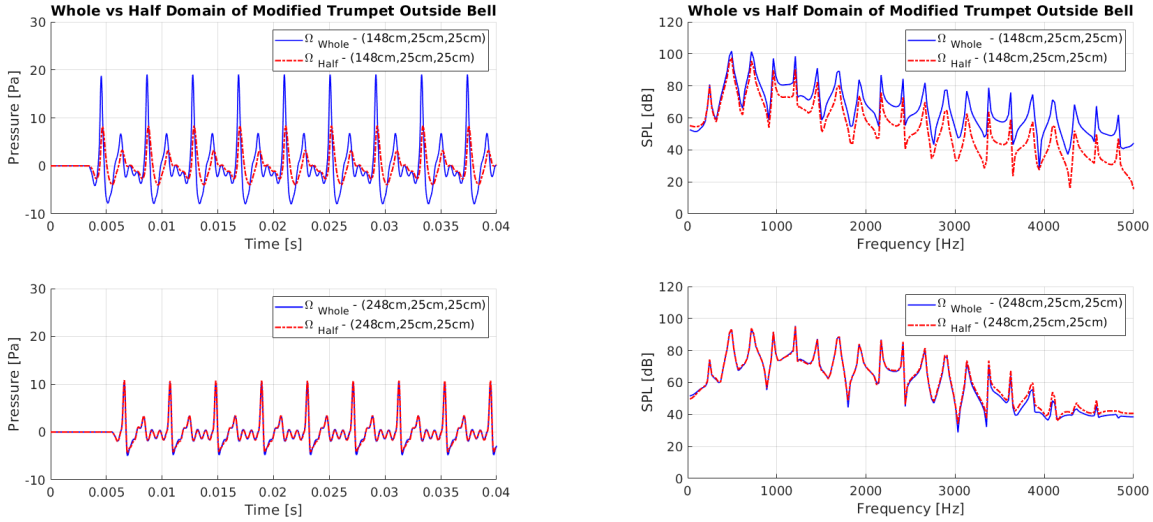

Figure 5.7: The computed pressure using Ω_{Whole} and Ω_{Half} in the time-domain (left) and frequency-domain (right) at positions S_5 (upper-plots) and S_6 (lower-plots) depicted in Figure 5.5.

Next, we review the numerical output sampled above the bell at $S_5 = (1.48, 0.25, 0.25)$ and $S_6 = (2.48, 0.25, 0.25)$ (Figure 5.7). As expected, we observe some variation between the Ω_{Whole} and Ω_{Half} solutions directly above the bell exit at S_5 (upper-left plot). The amplitude of the first peaks align well but the SPLs of the higher components corresponding to the Ω_{Half} solution decrease as a function of frequency. Still, the general behaviour of the spectral curves are comparable. Further away from the bell at S_6, no significant differences are observed between the Ω_{Whole} and Ω_{Half} outputs. More importantly, the computed pressure sampled at S_3 and S_4 (Figure 5.8) are practically indistinguishable at both locations.

In summary, our numerical results indicate that the computational region behind the bell can be neglected. This result is greatly beneficial, as the number of mesh elements is almost cut in half thereby significantly reducing runtime and the memory required.

[8] Where S_2 corresponds to the Mic $_{\text{Outside-Bell}}$ position defined in Chapter 2.

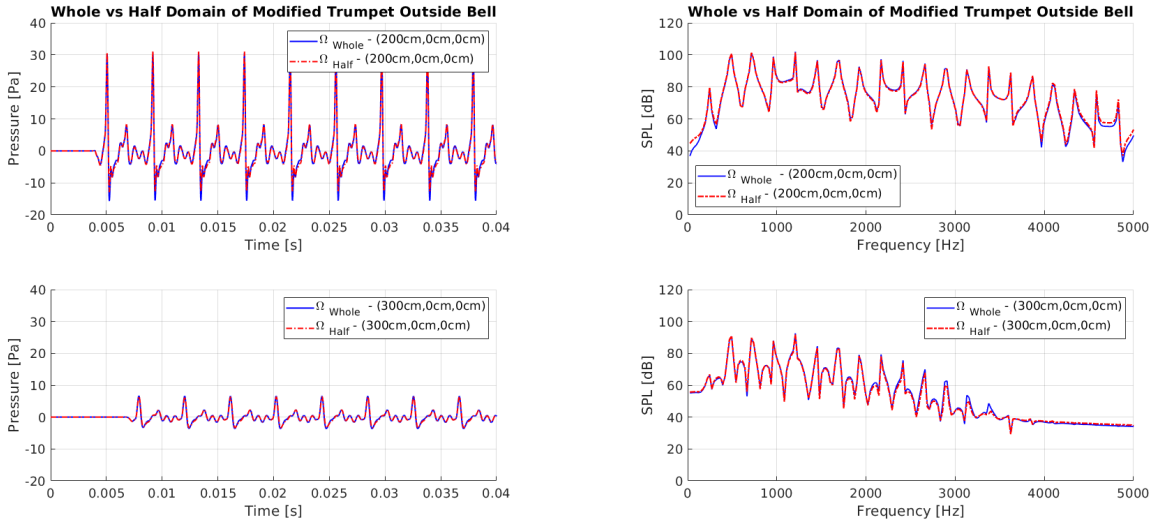

Figure 5.8: The computed pressure using Ω_{Whole} and Ω_{Half} in the time-domain (left) and frequency-domain (right) at positions S_3 (upper-plots) and S_4 (lower-plots) depicted in Figure 5.5.

Consequently, more attention can be directed toward more carefully modelling the initial tubing shape near the mouthpiece-shank, which is extremely narrow, especially for the trumpet.

5.4.3 Setup for Additional Computational Geometries

In this section, we discuss how the shape of the domain at the far-field influences the solution. Although a box-shaped domain is easier to construct, the corners may be problematic. In particular, reflections occurring within the corners can influence the numerical solution. If Ω is sufficiently large, this should not be an issue. Nonetheless, if we could use a smaller domain, runtimes would be faster and we may obtain a cleaner solution.

Therefore, two additional domain shapes were considered: a cylindrical and cylindrical-plus-half-spherical shape, denoted by $\Omega_{\text{Half-Cylinder}}$ and $\Omega_{\text{Half-Sphere}}$, respectively. For convenience, we will now refer to Ω_{Half} as $\Omega_{\text{Half-Box}}$. Since we have already determined that whole domains are not necessary for our purposes, further such simulations will not be

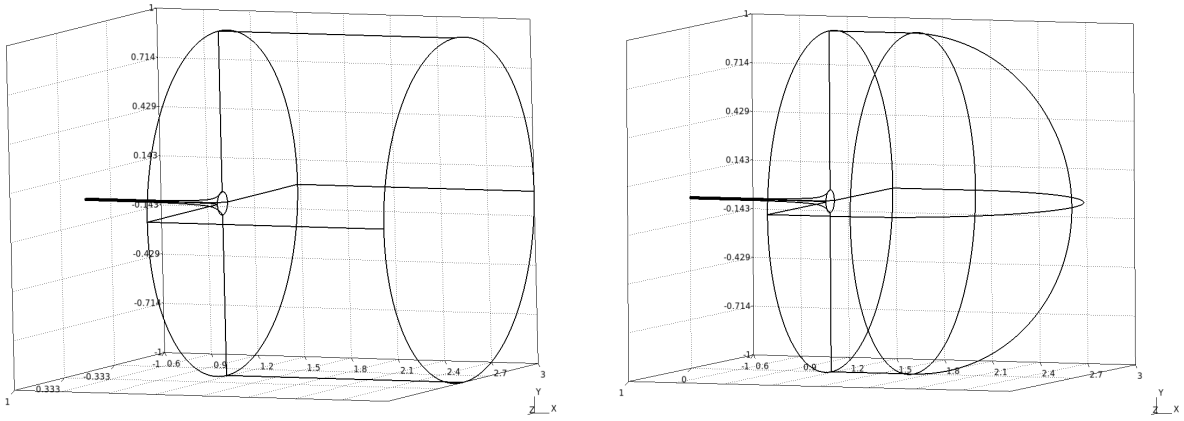

Figure 5.9: Additional half domains that were tested in Sections 5.4.3 and 5.4.4. Left: $\Omega_{\text{Half-Cylinder}}$. Right: $\Omega_{\text{Half-Sphere}}$.

considered here[9]. A picture of the additional domains is shown in Figure 5.9. A summary of all the Type B domains, their geometric shape, their names and mesh properties can be found in Table 5.2.

Table 5.2: The number of elements, minimum radius of the inscribed sphere ($r_{\min}$) and the memory required for meshes generated for the computational domains shown in Figure 5.9.

Domain Shape	Name of Ω	Number of Cells	$r_{\min}$	Mem. Required
Box	$\Omega_{\text{Half-Box}}$	1,130,373	94.5 μm	1.50 GB
Cylinder	$\Omega_{\text{Half-Cylinder}}$	1,128,185	62.7 μm	1.50 GB
Cylinder+$\frac{1}{2}$Sphere	$\Omega_{\text{Half-Sphere}}$	1,100,410	47.7 μm	1.45 GB

5.4.4 Simulation Results on $\Omega_{\text{Half-Box}}$, $\Omega_{\text{Half-Cylinder}}$ and $\Omega_{\text{Half-Sphere}}$

The computed pressure for all three half domains sampled at S_1 and S_2 (Figure 5.10), and S_5 (Figure 5.11) are indistinguishable. At S_6 however, we do observe extremely small

[9] During my PhD, several other whole (and half) domains were considered for a grad class project. The results demonstrated that a half domain of any shape compared to the equivalent whole domain was sufficient to use. These numerical simulations were not included in the thesis due to time constraints. In particular, simulations using a much finer mesh (compared to the initial meshes) were not run for all the whole domains, only for Ω_{Whole}.

amplitude differences in the frequency-domain between the solutions (Figure 5.11 bottom-right). For frequencies greater than 2500 Hz, the SPLs corresponding to the $\Omega_{\text{Half-Sphere}}$ solution are the highest, followed by $\Omega_{\text{Half-Box}}$ and then, $\Omega_{\text{Half-Cylinder}}$. The small variations between the solutions can also be seen in the time-domain, though the differences are slight. However, S_6 is located at the far upper end of the domains where the pressure reaches a maximum of only 12 Pa. It will be more important to see if there are any blatant differences in the numerical solutions along the central axis.

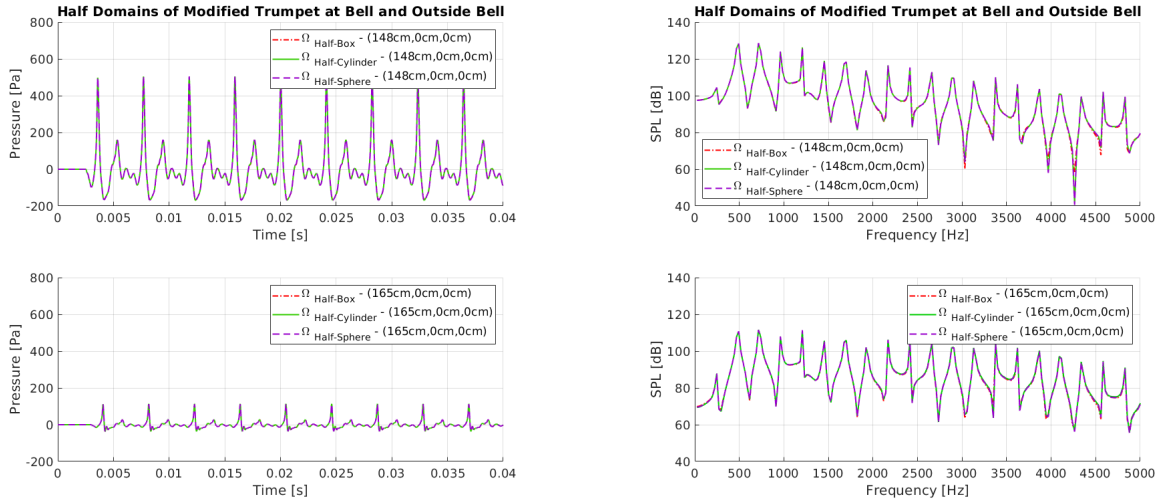

Figure 5.10: The computed pressure on $\Omega_{\text{Half-Box}}$, $\Omega_{\text{Half-Cylinder}}$ and $\Omega_{\text{Half-Sphere}}$ in the time-domain (left) and frequency-domain (right) sampled at S_1 (upper-plots) and S_2 (lower-plots) as depicted in Figure 5.5.

Examining the computed pressure at S_3 and S_4 (Figure 5.13), the outputs in the time-domain sampled at S_3 align rather well. Slight differences can be seen at the peak and dip. But this variation is only 4 Pa and 2 Pa between the $\Omega_{\text{Half-Sphere}}$ and $\Omega_{\text{Half-Cylinder}}$ peaks versus the $\Omega_{\text{Half-Sphere}}$ and $\Omega_{\text{Half-Box}}$ peaks, respectively[10]. In the frequency-domain, this variation is observed in the spectral curve for harmonics larger than 3500 Hz. At S_4, the computed pressures closely align but the pressure peak corresponding to the $\Omega_{\text{Half-Sphere}}$ solutions is approximately 1 Pa larger. In the frequency-domain, this translates to the solution having slightly larger SPLs for harmonics larger than 2500 Hz.

[10] Hence, there is a variation of approximately 6 Pa between the $\Omega_{\text{Half-Sphere}}$ and $\Omega_{\text{Half-Cylinder}}$ peak pressure amplitudes.

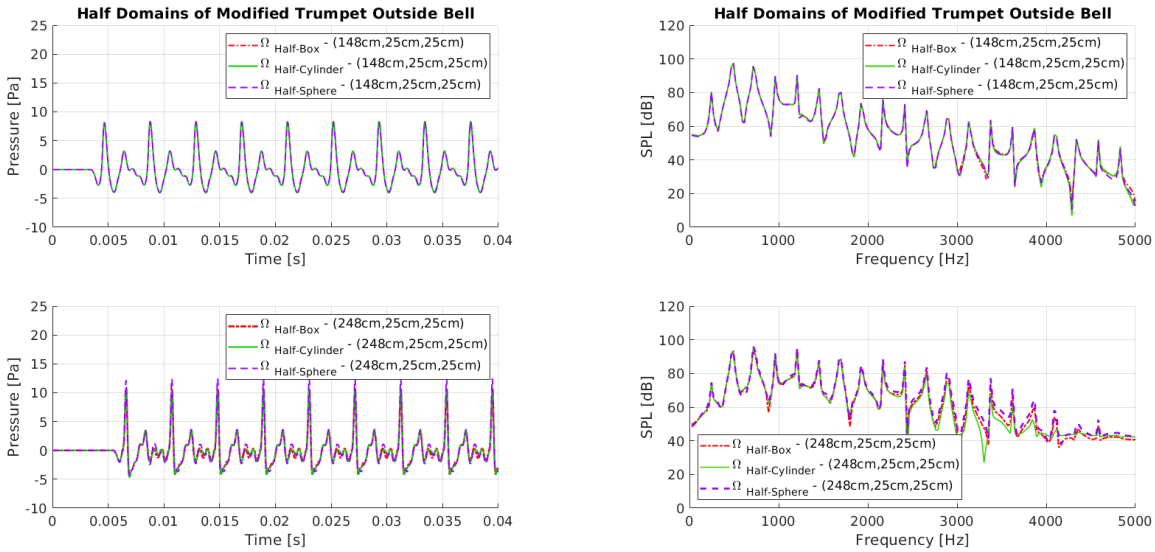

Figure 5.11: The computed pressure on $\Omega_{\text{Half-Box}}$, $\Omega_{\text{Half-Cylinder}}$ and $\Omega_{\text{Half-Sphere}}$ in the time-domain (left) and frequency-domain (right) sampled at S_5 (upper-plots) and S_6 (lower-plots) as depicted in Figure 5.5.

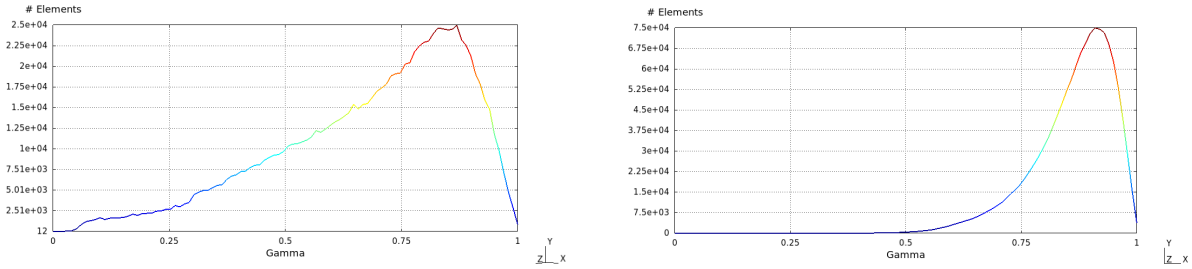

Figure 5.12: Plots generated in GMSH measuring the mesh quality of the domains when the full length trumpet is modelled in $\Omega_{\text{Half-Sphere}}$ (left) and $\Omega_{\text{Half-Cylinder}}$ (right).

In summary, although we notice small deviations in the computed pressures between the different half domain shapes, the differences are observed where the domain is truncated at the far-field. The numerical solutions at the bell exit and at Mic $_{\text{Outside-Bell}}$, i.e., S_1 and S_2, are equivalent, which for our purposes is most important. However, examining the mesh quality rating given by GMSH after the meshes were generated, we found that the quality of $\Omega_{\text{Half-Cylinder}}$ is slightly better. A comparison of the mesh quality plots produced

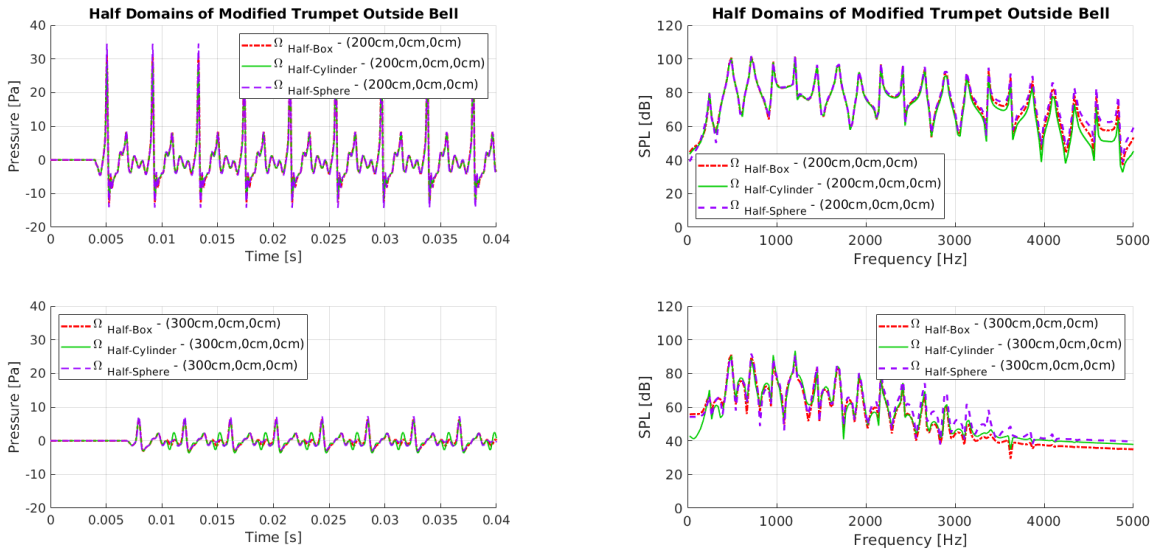

Figure 5.13: The computed pressure sampled on $\Omega_{\text{Half-Box}}$, $\Omega_{\text{Half-Cylinder}}$ and $\Omega_{\text{Half-Sphere}}$ in the time-domain (left) and frequency-domain (right) at positions S_3 (upper-plots) and S_4 (lower-plots) as depicted in Figure 5.5.

by GMSH for $\Omega_{\text{Half-Sphere}}$ and $\Omega_{\text{Half-Cylinder}}$ are shown in in Figure 5.12. The smoother and more skewed the distribution is to the right, the better the mesh quality. Hence, a half cylindrical shaped domain was used for the other simulations presented throughout this thesis[11].

5.5 Importance of the Mouthpiece-Shank Geometry

As argued in [180], [161] and [38], observed nonlinear effects associated with finite-amplitude wave propagation are dependent on the bore of the instrument, i.e., the length of the instrument, the variation in diameter, the flare expansion rate, etc.. For any region in the instrument where the cross-sectional area increases, the amplitude of the propagating waves will decrease since the sound energy spreads out and the particle velocity and pressure both

[11] For the musical notes that were to be simulated, we found that the numerical outputs using $\Omega_{\text{Half-Box}}$ or $\Omega_{\text{Half-Cylinder}}$ gave equivalent spectral components for the frequency range we are concerned about. However, from looking at the isosurfaces, the numerical solutions obtained on $\Omega_{\text{Half-Cylinder}}$ were cleaner.

decrease [152]. The instrument's shape and how the radius of the bore varies needs to be very carefully measured to construct good meshes for computations. It is believed however, that the influence of the instrument's shape on the timbre becomes less prominent when pitches are played at lower dynamic levels [38].

Although the acoustic community has come to a general consensus on how the bell influences the radiated sound and wave propagation within the instrument[12], less attention has been paid to the geometry of the narrow region in-between the mouthpiece-shank and first bend. It is often assumed that the bore prior to the bell is uniform in diameter (e.g., [25], [58], [140], [160], [184], [215]). But close inspection near the trumpet mouthpiece for instance reveals that the inner tubing before the first bend is more complex than alluded to by the outer geometry. For example, if $r_{\text{Mouthpiece-Shank}}$ denotes the radius of the mouthpiece-shank, and r_{Bore} is the radius of trumpet bore 24 cm away from $r_{\text{Mouthpiece-Shank}}$, measurements reveal that r_{Bore} is $2.12 \times r_{\text{Mouthpiece-Shank}}$. For the trombone, r_{Bore} is $1.77 \times r_{\text{Mouthpiece-Shank}}$. Since volume increases by a factor of r^2, neglecting subtle variations in the bore's cross-section could greatly influence the approximated pressure slope entering the main body of the instrument and thus, how much the nonlinear waves distort inside the instrument [20], [99], [123], [147], [180]. In addition, reflections, and the spreading or contracting in nonuniform regions of the tube, can alter the standing waveform pattern.

In this section, we will explore the influence of properly modelling the initial bore geometry. The bends will not be discussed here, but rather in Section 5.6. Slightly more emphasis will be placed on the trumpet due to its shape and smaller size though, simulations for the trombone will also be reviewed.

5.5.1 Initial Bore Shape

We do not attempt to model the pressure and flow behaviour in the mouthpiece cup since pressure measurements were not obtained at this position[13]. Collecting such measurements is also complicated due to the difficulty in placing a microphone at the mouthpiece cup. In addition, the coupling of the lips to the mouthpiece is a highly nonlinear process still being studied (e.g., [20], [99], [147], [158], [181], [204]). Thus, in an attempt to avoid the complicated acoustic behaviour in the mouthpiece cup, we collected pressure measurements

[12] In the trumpet bell, the expansion increases the radius of the instrument by a factor of 10.9; for the trombone it is a factor of 8.9. The flare geometry directly effects the proportion of which spectral components are reflected and transmitted from the bell [20], [99].

[13] A discussion on the mouthpiece cup can be found in Section 5.8.2

(presented in Chapter 2) for our study at the mouthpiece-shank (Mic $_{\text{Mouthpiece}}$), approximately 4.5 cm and 4.7 cm from the beginning of the mouthpiece of the trumpet and trombone, respectively. A general diagram of a trumpet and trombone instrument mouthpiece and the positioning of the microphone is shown in Figures 5.14 and 5.15, respectively. The shaded region represents the beginning of the computational domain.

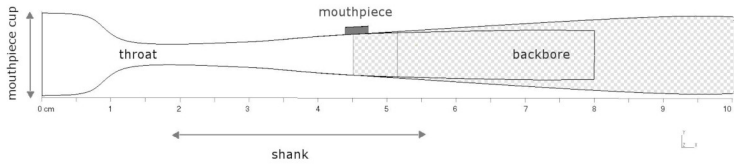

Figure 5.14: A diagram of the first 10 cm of the trumpet mouthpiece. The shaded region corresponds to the beginning of the computational domain where the left vertical wall at 4.5 cm is the mouthpiece boundary. The junction between the trumpet tubing and the mouthpiece is located at 5.2 cm.

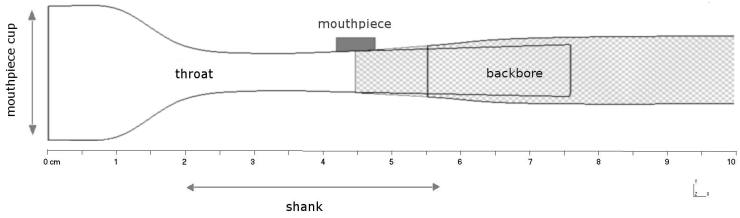

Figure 5.15: A diagram of the first 10 cm of the trombone mouthpiece. The shaded region corresponds to the beginning of the computational domain where the left vertical wall at 4.7 cm is the mouthpiece boundary. The junction between the trombone tubing and the mouthpiece is located at 5.6 cm.

We present here three geometries that approximate the physical shape of the 1.48 m long trumpet shown in Figure 2.1 from Chapter 2. The objective was to create a geometrical representation of the trumpet flare and initial bore shape as accurately as possible. The bell in particular was modelled with great care since the flare expansion influences harmonic reflections of propagating sound pressure waves (this will be examined in Section 5.8.1). Slight inaccuracies in the bell geometry can produce exaggerated discrepancies in numerical simulations as we showed in [185]. For this reason, to obtain a realistic flare shape, a photograph of the trumpet bell was taken. The *grabit* software (Math Works Inc.) was

then used to trace out the trumpet flare by a series of points. We used these points to interpolate the bell shape by cubic splines. The same procedure was carried out for the trombone bell.

The first trumpet geometry we present has an uniform cylindrical bore prior to the flare (top plot of Figure 5.16) and will be referred to as *Geo.1* $_{Trumpet}$. This approximation is often used in the literature (e.g., [27], [58], [140], [158], [160], [215]), which was the motivation behind Geo.1 $_{\text{Trumpet}}$'s construction. The tubing of a real trumpet near the mouthpiece does not have a cylindrical shape. From the outside of the instrument, the radius of the bore from the mouthpiece appears to slowly increase for approximately 24 cm giving a conical-type shape. Then, the tube appears to be cylindrical until it begins to widen again 102 cm from the computational mouthpiece. This geometry configuration will be referred to as *Geo.2* $_{Trumpet}$ and is shown in the middle plot of Figure 5.16.

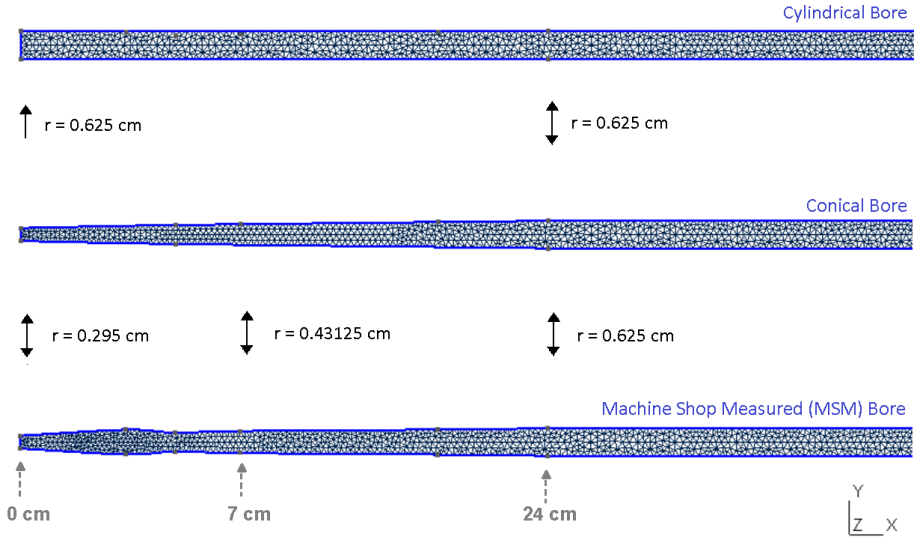

Figure 5.16: A longitudinal cross-section of the geometric shapes of the initial tubing of the computational trumpet used to construct Geo.1 $_{\text{Trumpet}}$ (top), Geo.2 $_{\text{Trumpet}}$ (middle) and Geo.3 $_{\text{Trumpet}}$ (bottom), with reference names *Cylindrical Bore*, *Conical Bore* and *Machine-Shop Measurements (MSM) bore*, respectively. Radii are the same at points indicated by the double arrows.

We have learned that the inner geometry of the trumpet does not always coincide with the outside shape. We attempted to obtain more precise measurements from the university's machine shop to construct a better approximation of the inner tubing of the shank with nine points. This geometric approximation is presented in the bottom plot

of Figure 5.16 and will be called *Geo.3* $_{Trumpet}$. Similarly to Geo.2 $_{\text{Trumpet}}$, the tubing in-between 24 cm - 102 cm is modeled as a cylindrical tube.

Due to the different radii at the mouthpiece, the difference in volume between Geo.1 $_{\text{Trumpet}}$ and the other two computational trumpet geometries is significant. Since the bore radius at the inlet is larger for Geo.1 $_{\text{Trumpet}}$, the surface area at the outlet increases and thus, the volume velocity and associated radiated pressure will be larger [38]. For this reason, we expect that the simulations run on Geo.1 $_{\text{Trumpet}}$ will produce numerical amplitudes that are larger than the measured profiles.

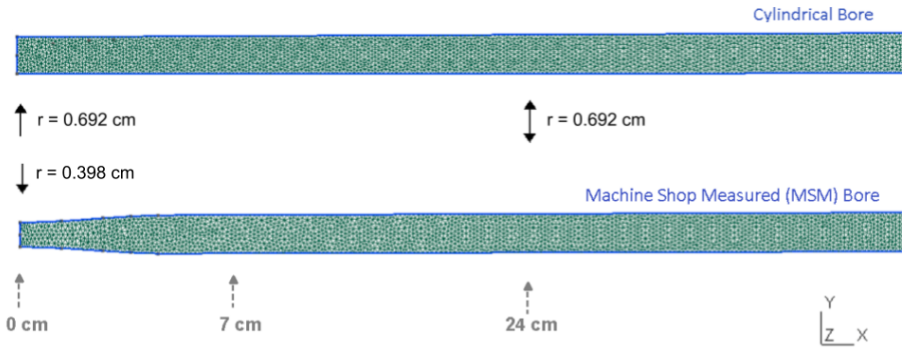

Figure 5.17: A longitudinal cross-section of the geometric shapes of the initial tubing of the computational trombone used to construct Geo.1 $_{\text{Trombone}}$ (top) and Geo.2 $_{\text{Trombone}}$ (bottom), with reference names *Cylindrical Bore*, and *Machine-Shop Measurements (MSM) bore*, respectively. Radius is the same at the point indicated by the double arrow.

Next, two geometries to represent the 2.87 m long trombone shown in Figure 2.1 from Chapter 2 will be presented where the bends are not modelled. Compared to the trumpet, the initial bore shape of the trombone is not nearly as complicated (see Figure 5.16). The trumpet tubing resembles a subtle converging-diverging channel approximately 4.5 cm from the mouthpiece cup entrance. This is not the case for the trombone. The trombone bore is more conical for the initial 4.5 cm (not including the mouthpiece cup). The next 159.5 cm of tubing remains cylindrical (the first bend is within this region). Leading into the second bend however, the trombone tubing slightly increases in radius again. The second bend then immediately leads into the rapidly expanding flare region. Therefore, if the trombone were to be straightened out, between 164 cm to 247 cm, the bore is a conical shape that increases in radius by a factor of 1.59. Thus, for the trombone, two different geometries were considered: one that has a cylindrical bore prior to the flare, which will be called *Geo.1* $_{Trombone}$, and one that accurately models the tubing leading up to the flare, referred to as *Geo.2* $_{Trombone}$ (Figure 5.17).

Summary of Computational Geometries

In summary, we present three computational trumpets and two computational trombones where the initial 24 cm and 247 cm of tubing is modeled differently for each trumpet and trombone geometry as listed below.

Geo.1 $_{\text{Trumpet}}$: *Cylindrical Bore*
The tubing from the mouthpiece boundary to the flare entrance, i.e., $x \in [0 \text{ cm}, 102 \text{ cm}]$, was approximated by a cylindrical bore.

Geo.2 $_{\text{Trumpet}}$: *Conical Bore*
The tubing between $x \in [0 \text{ cm}, 24 \text{ cm}]$ was approximated using three measurements of the radius of the tube: at the mouthpiece microphone position, the shank, and before the first bend. This was followed by a cylindrical bore in the region $x \in [24 \text{ cm}, 102 \text{ cm}]$.

Geo.3 $_{\text{Trumpet}}$: *Machine-Shop Measured (MSM) Bore*
The tubing between $x \in [0 \text{ cm}, 24 \text{ cm}]$ was reconstructed from the nine measurements taken. This was followed by a cylindrical bore in the region $x \in [24 \text{ cm}, 102 \text{ cm}]$.

Geo.1 $_{\text{Trombone}}$: *Cylindrical Bore*
The tubing from the mouthpiece boundary to the entrance of the flare, i.e., $x \in [0 \text{ cm}, 247 \text{ cm}]$ was approximated by a cylindrical bore.

Geo.2 $_{\text{Trombone}}$: *Machine-Shop Measured (MSM) Bore*
The tubing between $x \in [0 \text{ cm}, 4.5 \text{ cm}]$ was reconstructed from the four obtained measurements. This was followed by a cylindrical bore in the region $x \in [4.5 \text{ cm}, 164 \text{ cm}]$. The next section leading into the flare has a slight conical shape from $x \in [164 \text{ cm}, 247 \text{ cm}]$.

For the trumpet and trombone geometries, a half domain shape with a cylindrical far-field was used. Since the bends are not considered here, both instruments can be considered as radially symmetric. Hence, their 3D geometry was created using a rotational extrusion

about the x-axis on the curve outlining the computational instrument as well as the far-field boundary. An example of a trumpet and trombone curve used in GMSH is shown in Figures 5.18 and 5.19, respectively.

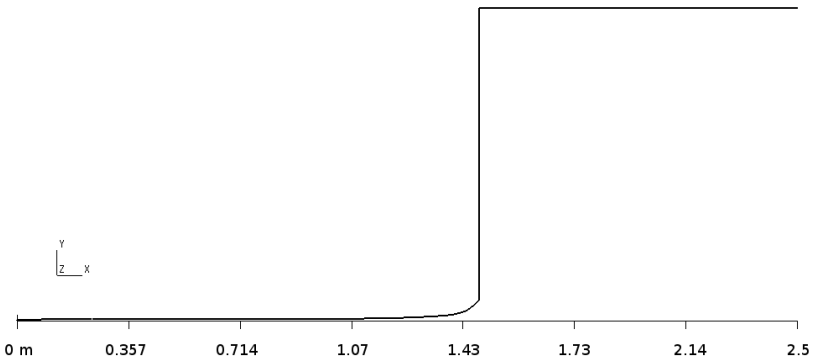

Figure 5.18: The profile used in GMSH to create the Geo.2 $_{\text{Trumpet}}$ and surrounding area via a rotational extrusion about the x-axis.

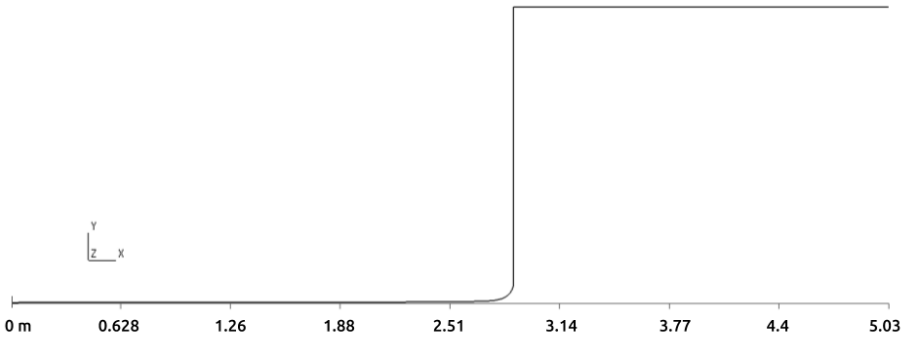

Figure 5.19: The profile used in GMSH to create the Geo.2 $_{\text{Trombone}}$ and surrounding area via a rotational extrusion about the x-axis.

Special care needed to be taken to ensure there were enough cells in the radial direction to obtain accurate simulations. The meshes used ranged from having 603,201 to 2,234,905 tetrahedral elements. The corresponding mesh size spacing was chosen so that our nu-

merical results visually did not vary if a finer mesh was used[14]. The smallest radius of the inscribed sphere for the tetrahedral elements as well as the memory required for each computational geometry is reported in Table 5.3.

Table 5.3: Properties of the computational domains with the corresponding number of elements, minimum radius of the inscribed sphere ($r_{\min}$) and memory required for the computational geometries used in Section 5.5.

Geometry	Bore Shape	Number of Cells	$r_{\min}$	Memory Required
Geo.1 $_{\text{Trumpet}}$	Cylindrical	603,201	38.3 μm	810 MB
Geo.3 $_{\text{Trumpet}}$	Conical	1,302,915	53.3 μm	1.73 GB
Geo.3 $_{\text{Trumpet}}$	MSM	1,317,219	26.7 μm	1.75 GB
Geo.1 $_{\text{Trombone}}$	Cylindrical	830,780	73.5 μm	1.11 GB
Geo.2 $_{\text{Trombone}}$	MSM	2,234,905	51.2 μm	2.97 GB

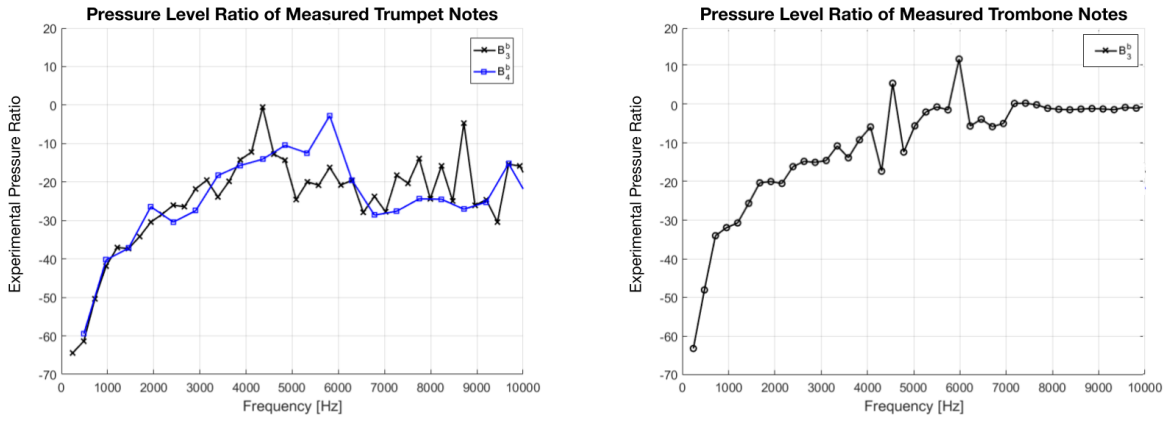

Figure 5.20: Pressure level ratios of the of experimental data, specifically the ratio of the pressure measured at Mic $_{\text{Outside-Bell}}$ over the pressure measured at Mic $_{\text{Mouthpiece}}$. Left: B_3^b and B_4^b at f produced on the trumpet. Right: B_3^b at f produced on the trombone.

The inflow boundary condition considered for the computational trumpets was prescribed to be the B_3^b and B_4^b notes played at f (discussed in Section 2.3.1). For the trombone, numerical simulations were done for the B_3^b played at *ff*. To understand the

[14] We also tested if the refinement was sufficient by simulating a short duration pulse down each computational domain. If the pressure amplitude stayed constant along the length of the bore, we assumed the mesh was good for computation.

wave transmission from the trumpet and trombone flare, and to estimate the noise content of our experimental data, the ratio between the measured pressure levels at Mic $_{\text{Outside-Bell}}$ and Mic $_{\text{Mouthpiece}}$ were determined and plotted in Figure 5.20. For all notes, the curves displays similar character for frequencies up to 4000 Hz. The remaining portion of the signals however appear to be noisy due to the observed zig-zag pattern. We take this to mean that the experimental data up to 4000 Hz is most reliable and does not contain much noise.

5.5.2 Simulated Results for the all Computational Instruments

The equations of motion for the mentioned tones were solved on Geo.1 $_{\text{Trumpet}}$, Geo.2 $_{\text{Trumpet}}$, Geo.3 $_{\text{Trumpet}}$, Geo.1 $_{\text{Trombone}}$ and Geo.2 $_{\text{Trombone}}$. The spectra of the resulting computed pressures sampled at the Mic $_{\text{Outside-Bell}}$ position are shown in Figures 5.21 and 5.22. These spectral curves are compared against the experimental data measured at Mic $_{\text{Outside-Bell}}$ to determine which geometry produces the best result.

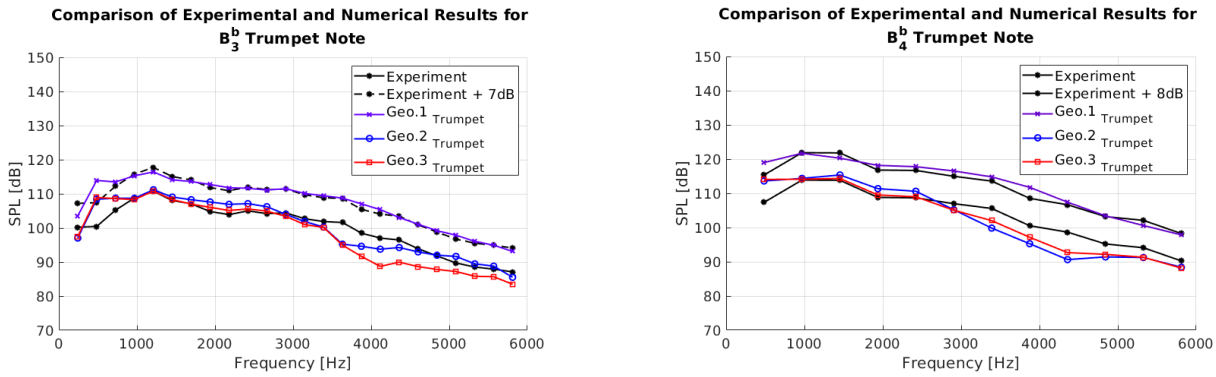

Figure 5.21: Frequency spectra of experimental data versus the Geo.1 $_{\text{Trumpet}}$, Geo.2 $_{\text{Trumpet}}$ and Geo.3 $_{\text{Trumpet}}$ simulation results for the loudly played B_3^b (left) and B_4^b (right) trumpet notes.

For Geo.1 $_{\text{Trumpet}}$, a comparison of the numerical and experimental data shows that the numerical amplitude for the B_3^b and B_4^b notes is overestimated by approximately 7 dB and 8 dB, respectively[15]. To compare the shapes of the experimental and computed spectra,

[15] Recall that the radius of the mouthpiece boundary for Geo.1 $_{\text{Trumpet}}$ is 2.12 times larger than that of Geo.2 $_{\text{Trumpet}}$ and Geo.3 $_{\text{Trumpet}}$. It therefore seems reasonable that the corresponding numerical amplitude values at the bell position for Geo.1 $_{\text{Trumpet}}$ are roughly 7 dB off since $(20 \log_{10}(2.12) \approx 6.5$ dB).

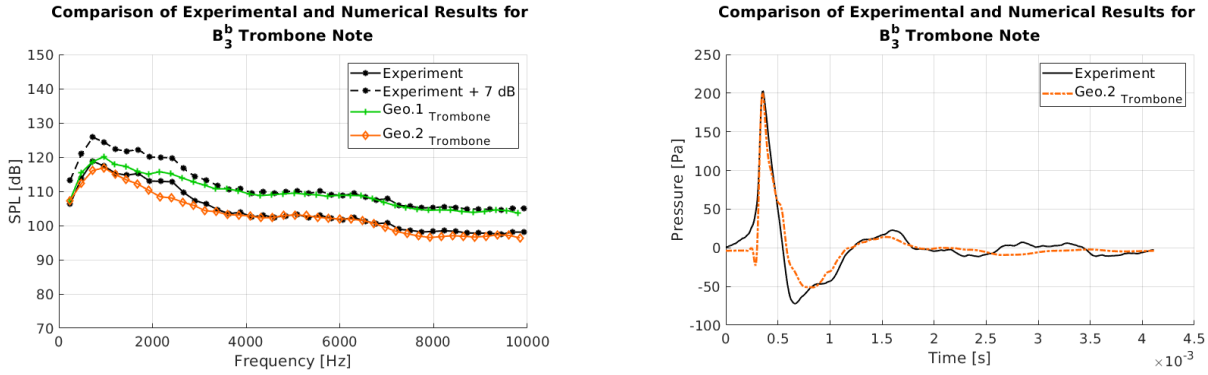

Figure 5.22: Pressure waveform (right) and frequency spectra (left) of experimental data versus the Geo.1 $_{\text{Trombone}}$ and Geo.2 $_{\text{Trombone}}$ simulation results for the loudly played B_3^b trombone note.

the experimental curves were shifted upwards by the amplitude difference and plotted on the same figures. With the shift, we see that the harmonic distribution of the experimental data and numerical solutions are in good agreement for frequency components above 700 Hz. For Geo.1 $_{\text{Trombone}}$, we observe that the SPL of the measured note is overestimated by approximately 7 dB for components above 3000 Hz but the harmonic distributions are very similar. Frequencies f_1, f_2, f_3, f_7 align very closely with the measured trombone data however, frequencies from 1000 Hz to 3000 Hz deviate by 2 dB - 4 dB.

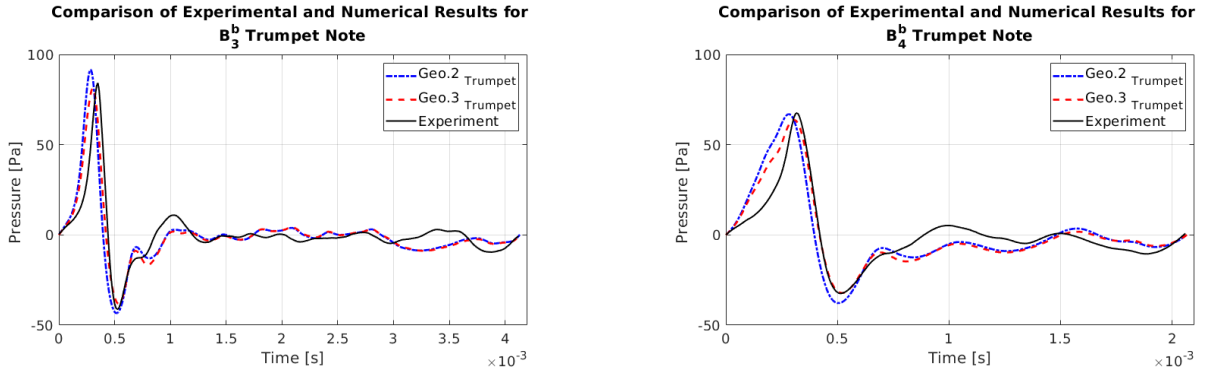

Figure 5.23: Experimental pressure waveform versus the Geo.2 $_{\text{Trumpet}}$ and Geo.3 $_{\text{Trumpet}}$ simulation results for the loudly played B_3^b (left) and B_4^b (right) trumpet notes.

The numerical amplitudes for the Geo.2 $_{\text{Trumpet}}$ and Geo.3 $_{\text{Trumpet}}$ simulations are much

closer to the B_3^b and B_4^b experimental curves compared to the Geo.1 $_{\text{Trumpet}}$ output. In particular, when Geo.3 $_{\text{Trumpet}}$, (which has the *MSM* bore) is used, the simulation closely agrees with the experimental data for components between 900 Hz - 3400 Hz for the B_3^b (left of Figure 5.21), and 900 Hz - 2800 Hz for the B_4^b (right of Figure 5.21). Similar results are obtained for Geo.2 $_{\text{Trumpet}}$ (which has the *conical* bore) however, compared to Geo.3 $_{\text{Trumpet}}$, the frequencies are slightly higher in SPL in the mentioned harmonic ranges. We observe more deviation from the experiment for both geometries for frequencies near 4000 Hz. For spectral components below 900 Hz, Geo.2 $_{\text{Trumpet}}$ and Geo.3 $_{\text{Trumpet}}$ generate almost identical outputs. Both underestimate the fundamental frequency of the B_3^b by roughly 3 dB, whereas the second and third harmonics are roughly 8 dB and 3 dB too high, respectively. For the B_4^b, f_1 (which corresponds to f_2 of the B_3^b) is roughly 7 dB too high.

The Geo.2 $_{\text{Trombone}}$ result also yields a better match to the experimental spectrum compared to the Geo.1 $_{\text{Trombone}}$ solution. With the exception of the slight deviation observed for f_3, we find good agreement for harmonics less than 1800 Hz and greater than 2800 Hz. However, for components in-between, the numerical output underestimates the experimental data where the greatest variation is for f_{11} by 4 dB. Comparatively, in this frequency range, we found that the Geo.1 $_{\text{Trombone}}$ solution better matches the experimental spectrum.

For completeness, in Figure 5.23 (trumpet) and Figure 5.22 (trombone), one period of the most accurate numerical results in the time-domain is plotted against the experimental waveform. From a compressible fluids simulation point of view, the numerical and experimental waveforms match rather well[16]. For the computational trombone, we observe Gibbs type oscillations as the computed pressure approaches the peak. It turns out that this is due to numerical shock waves that formed in the Geo.2 $_{\text{Trombone}}$ bore[17] (which we further discuss below)!

5.5.3 Discussion on Modelling the Initial Bore Geometry

Our findings indicate that properly modelling the bore geometry near the mouthpiece region of a trumpet or trombone is necessary to obtain accurate simulation results. This is

[16] Although for all trumpet geometries there is still some deviation in the lower frequencies, the lower harmonic distribution for these results are significantly more accurate compared to the equivalent 2D numerical solutions presented in our previous work [185].

[17] If a fluid flow problem develops a discontinuity in the numerical solution, spurious oscillations or Gibbs type oscillations are typically present [212]. Other traditional graphical displays that indicate the production of numerical shock waves include concentrated contour lines in the neighbourhood of the discontinuity as well as examining the isosurfaces of the Mach number [222].

especially apparent for the trumpet, yet is often overlooked. We observe that the shape near the trumpet mouthpiece in particular has a large influence on the sound wave reflections within the instrument. The radiated frequencies from the Geo.2 $_{\text{Trumpet}}$ and Geo.3 $_{\text{Trumpet}}$ bells show evidence of this. In particular, the bores for these geometries differ only slightly, yet there are distinguishable differences between the solutions in the frequency domain (e.g., see frequencies 1500 Hz - 2600 Hz in Figure 5.21).

It is difficult to take precise measurements of the entire interior of the instrument. Even in the tubing regions that are more accessible, the measurement error can be large. This creates complications as the computational output is sensitive to the tubing radius at the inflow boundary. For instance, numerical experiments we have done on Geo.1 $_{\text{Trumpet}}$ showed that enlarging the radius of the uniform tube prior to the bell by a mere 0.45 mm alters the spectral amplitude outside the bell by almost 2 dB for the lower frequencies, and between 2 dB - 5 dB for the higher components (see Figure 5.24).

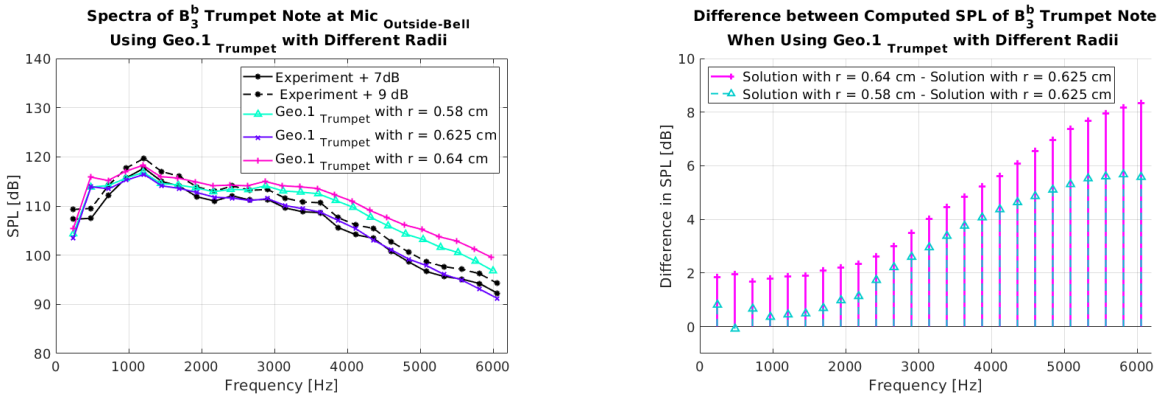

Figure 5.24: Experimental results when simulating the B_3^b on Geo.1 $_{\text{Trumpet}}$ where the initial bore is considered with radii $r = 0.58$ cm, $r = 0.625$ cm and $r = 0.64$ cm. Left: Resulting frequency spectra. Right: Difference in SPL between the numerical outputs.

The trombone results also demonstrate that accurately modelling the initial bore shape is important. However, the Geo.1 $_{\text{Trombone}}$ and Geo.2 $_{\text{Trombone}}$ simulations produce relatively similar SPLs for the lower harmonics (Figure 5.22), which I did not expect to find[18]. It was only the higher components that differed by 7 dB. This reveals that the tubular shape before the flare expansion does not greatly influence the wave as it travels through

[18] I expected to obtain variations similar to those observed in the trumpet results when a cylindrical bore was used, i.e., there would be a difference in the SPLs for all spectral components, not just a subset of them.

the regions that increase in cross-sectional area (i.e., the waves do not undergo as many reflections in the trombone compared to the trumpet). Instead, in the conical regions of Geo.2 $_{\text{Trombone}}$ (between [0 cm, 4.5 cm] and [164 cm, 247 cm]), the amplitude of the wave will spread and hence, decrease the effects due to nonlinearities. This would explain why only the higher frequencies of the Geo.1 $_{\text{Trombone}}$ solution are larger than the Geo.2 $_{\text{Trombone}}$ output, because there was just a higher degree of spectral enrichment.

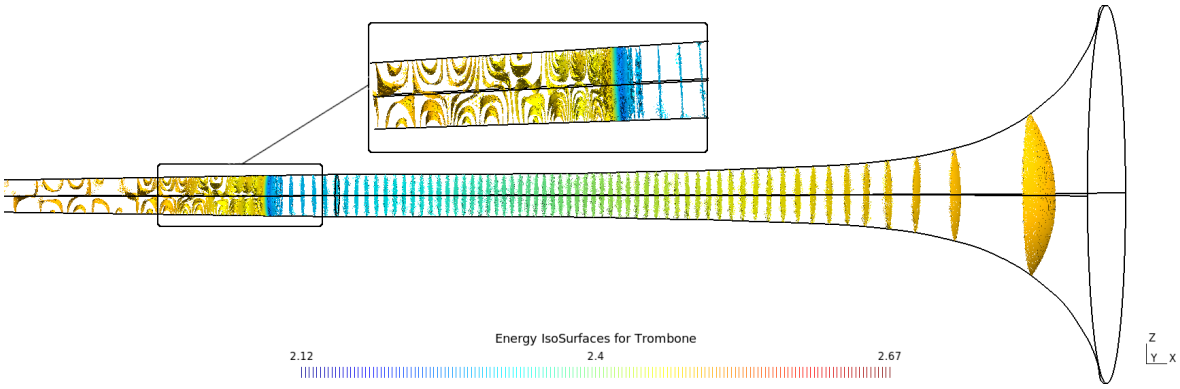

Figure 5.25: Energy isosurfaces of shock approaching the trombone bell. Note the units are scaled (see equations (5.3) and (5.6)).

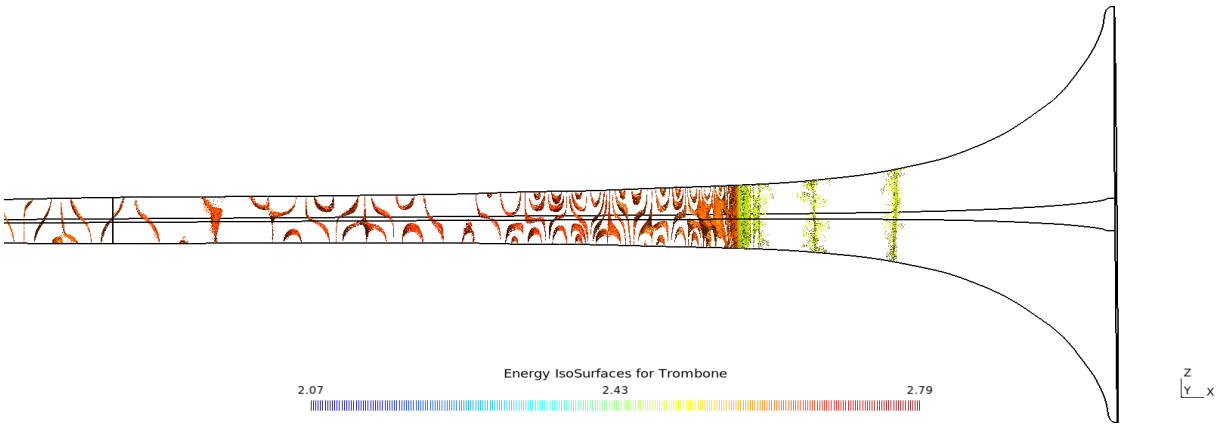

Figure 5.26: Energy isosurfaces of shock entering the trombone flare expansion. Note the units are scaled (see equations (5.3) and (5.6)).

As mentioned above, the nonlinearities corresponding to the B_3^b trombone note were strong enough to develop into shock waves before propagating through the bell. Recall that this simulated note was the same tone discussed in Section 2.3.1.1 from Chapter 2

(see Figures 2.23 and 2.24). We confirmed the production of a shock wave by reviewing both the post-processing files as well as sampling the computed pressure 1 m, 1.78 m and 2 m away from the computational inlet boundary along the central axis. In Figures 5.25 and 5.26, we show the energy isosurfaces produced by the simulation when Geo.2 $_{\text{Trombone}}$ was used. These post-processing images depict concentrated isosurfaces in the neighbourhood of the shock wave as it travels towards the flare and then into the flare expansion.

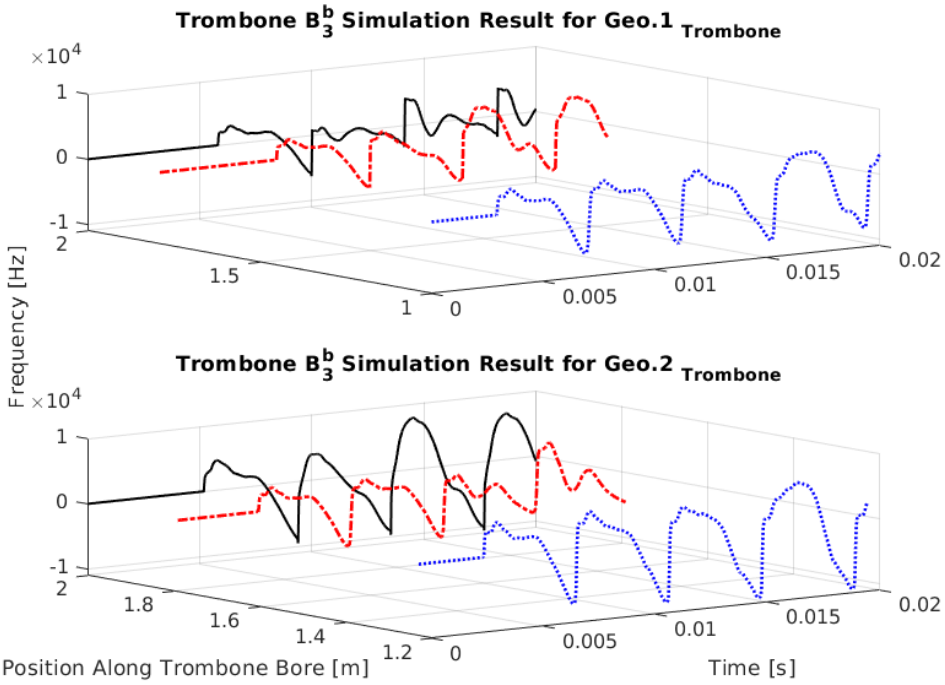

Figure 5.27: Numerical results sampled at the points $(1\text{m}, 0, 0)$, $(1.78\text{m}, 0, 0)$ and $(2\text{m}, 0, 0)$ along the trombone bore for Geo.1 $_{\text{Trombone}}$ (top) and Geo.2 $_{\text{Trombone}}$ (bottom) to observe the development of the shock wave.

Then, in Figure 5.27, a small portion of the computed pressure at the three mentioned points is shown, and a magnification of the pressure waveforms at 1.78 m and 2 m between $t = 0.003$ s and $t = 0.0123$ s can be found in Figure 5.28. These plots depict the computed pressure before reflections occurred at the bell (i.e., when the pressure made its first pass through the computational trombones) at the mentioned points. We notice that for the Geo.1 $_{\text{Trombone}}$ simulation, a shock can be observed at 1.78 m. However, for the Geo.2 $_{\text{Trombone}}$ output, the shock only develops by the time the computed pressure is

sampled again at 2 m. In other words, somewhere in-between 1.78 m - 2 m, the steepening wave fully develops into a shock, as depicted in Figure 5.28.

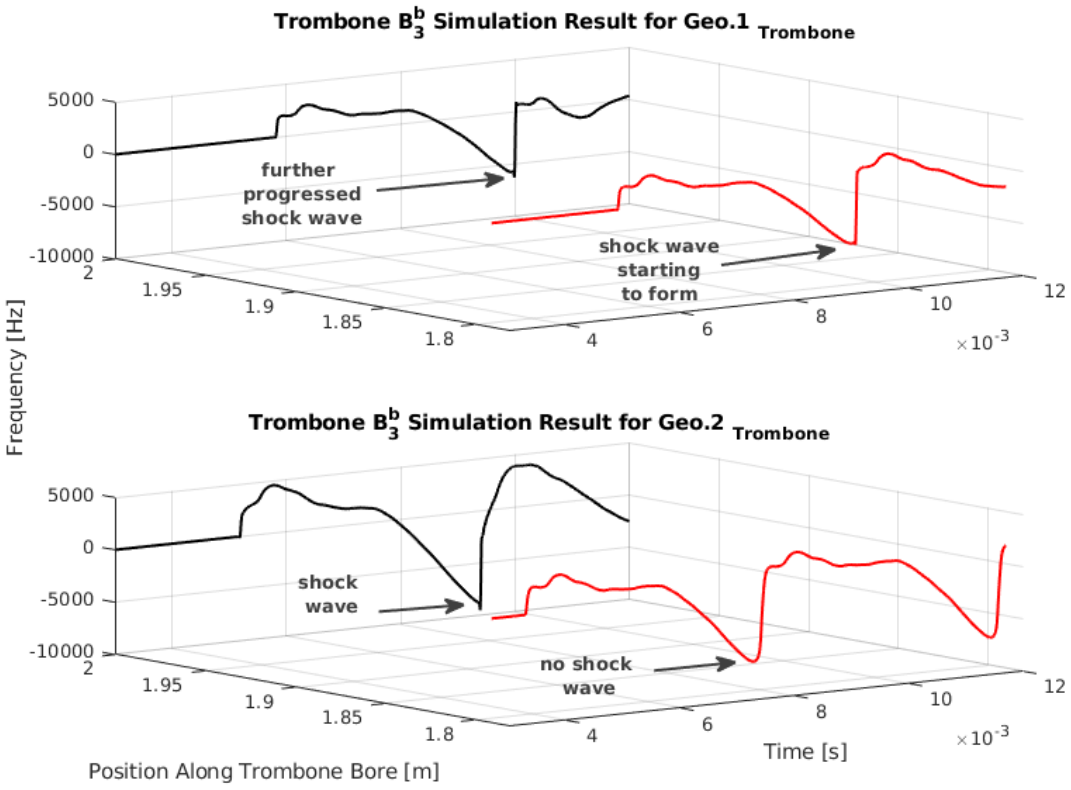

Figure 5.28: Numerical results sampled at positions $(1.78\text{m}, 0, 0)$ and $(2\text{m}, 0, 0)$ along the trombone bore for the Geo.1 $_{\text{Trombone}}$ (top) and Geo.2 $_{\text{Trombone}}$ (bottom) results. Shock waves can been seen for both results at $(2\text{m}, 0, 0)$.

This not only supports the conjectures made in Chapter 2, but to our surprise, also closely agrees with the theoretical approximation made for x_s. In particular, we estimated that (assuming the theory was a good initial approximation), a shock was expected to form in Geo.1 $_{\text{Trombone}}$ approximately 1.78 m - 1.79 m from the mouthpiece given the rate of change of the input pressure wave. Numerically, we found that the computed pressure steepened into a shock wave by the time the solution was sampled 1.79 m from the inlet position. When the trombone bore is properly modelled, the wave has to travel further before developing into a shock. However, this still occurs 47 cm prior to the bell. So even though we neglected losses, because the Geo.2 $_{\text{Trombone}}$ numerical solution so closely

resembles the experiment, it seems entirely reasonable that a shock would form prior to the bell of the real trombone.

However, to further verify this hypothesis, we examined the measured pressure obtained at Mic $_{\text{Bend}}$, which was positioned near the predicted x_s. The recorded pressure wave was then compared against both numerical solutions once a steady state was reached. These outputs can be seen in the time- and frequency-domain in Figure 5.29. Our numerical results show relatively good quantitative agreement with the experimental pressure. Furthermore, in the left plot of Figure 5.29, we clearly observe that the experimental pressure underwent severe wave steepening by the sharp change amplitude near $t = 0.0024$ s. The plot also shows an imminent shock in the Geo.1 $_{\text{Trombone}}$ and Geo.2 $_{\text{Trombone}}$ outputs[19], where the latter shock has just begun to form. To our knowledge, we are the first that have been able to numerically verify using real data that shock waves are produced in the trombone.

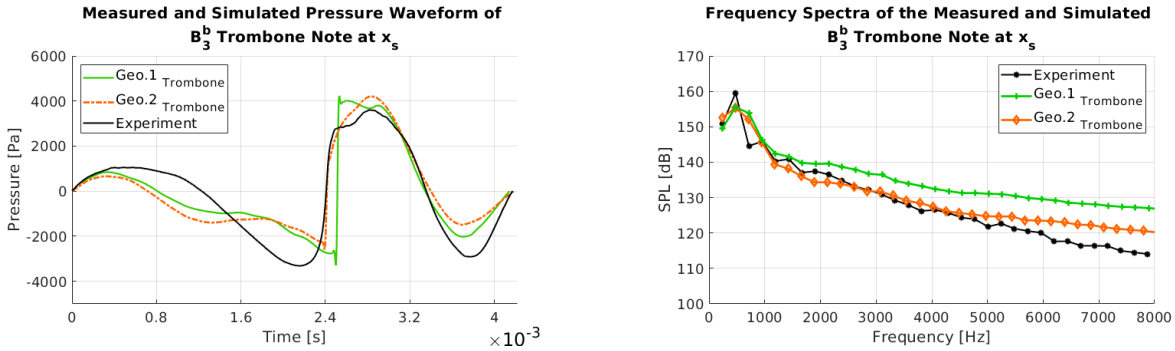

Figure 5.29: Comparison between measured and simulated sound pressure waveforms of the B_3^b sampled inside the trombone approximately 179 cm from the inlet.

In addition, as predicted in Section 2.3.1.1, the nonlinearities associated with the B_3^b trumpet note were not strong enough for shock waves to form within the computational instrument. We again plot the energy isosurfaces corresponding to the Geo.3 $_{\text{Trumpet}}$ loud B_3^b simulation in Figure 5.30. This post-processing image depicts the sound energy propagating through the instrument and radiating from the flare. We notice that the isosurfaces are not concentrated at any position as those observed in Figures 5.25 and 5.26 for the loud B_3^b trombone note.

[19] Which satisfies the jump conditions.

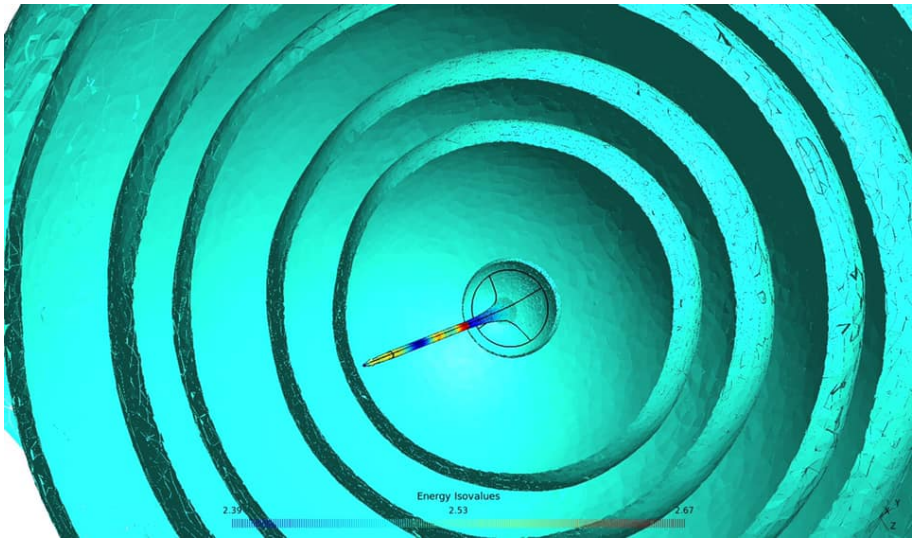

Figure 5.30: Energy isosurfaces of sound waves radiating from the bell as curved wavefronts. Note the units are scaled (see equations (5.3) and (5.6)).

5.6 Importance of Bends

The significance of the trumpet and trombone bends will now be examined to determine if they greatly influence the sound wave propagation. If it is found that they have little effect, it may not be worth the computational expense to include them. Furthermore, it would not be necessary to consider the full 3D model, a 2D axisymmetric one could instead be used. Previously in [184], we investigated the trumpet bends using a 2D model and found they were unnecessary to include. We suspect this will also be the case in 3D and that neglecting the bends will be a reasonable simplifying assumption.

5.6.1 Setup for Bores Prior to the Flare

Before considering the full trumpet and trombone geometries, we first consider simplified versions without the flare. These tubular shapes are referred to as Geo $_{\text{Trump-Bore}}$ and Geo $_{\text{Trom-Bore}}$. which model the instruments prior to the flare if the bends were straightened out. The second trumpet-like tube was constructed with a bend located 37.5 cm from the inlet. The second trombone-like tube includes a bend 69.58 cm from the inlet, and then remains cylindrical for the next 159.5 cm. The second trombone bend was positioned 194.07

cm from the inlet boundary. This additional set of tubes will be called Geo $_{\text{Trump-Bore-Bend}}$ and Geo $_{\text{Trom-Bore-Bends}}$. A picture of each geometry is depicted in Figure 5.31 and Table 5.4 contains information about each mesh.

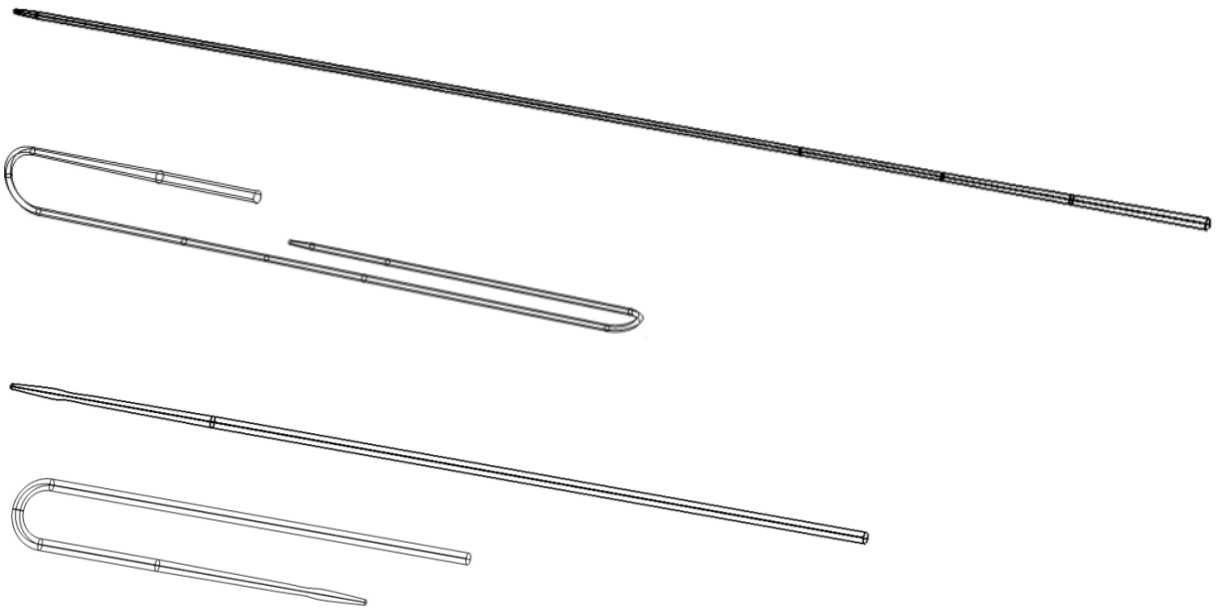

Figure 5.31: Computational trumpet and trombone tubular shapes prior to the flare shown in order from top to bottom: Geo $_{\text{Trom-Bore}}$, Geo $_{\text{Trom-Bore-Bends}}$, Geo $_{\text{Trum-Bore}}$ and Geo $_{\text{Trum-Bore-Bend}}$ used in Sections 5.6.1 and 5.6.2.

Instead of simulating musical notes through these tubes, an acoustic pressure pulse was produced at the inlet boundary and sent down each geometry shown in Figure 5.31. The motivation in doing this was to better understand the behaviour of the bends by examining how the pulses changed as they propagated through each bend. The pressure pulses generated had a peak amplitude corresponding to 2% of atmospheric pressure in an attempt to avoid nonlinear effects. The tubes will not open into a domain but rather, the outlet will be left open (i.e., pass-through boundary conditions). If the tubes being considered were uniform with this outlet condition, the pulse would propagate directly out of the tube without reflections occurring[20]. Although the tubes shown in Figure 5.31 are not uniform in diameter, we still expect that most of the pulse will propagate directly from the tube. The parts of the signal that remain will be due to reflections that have occurred from the variations in the bore's radius.

[20] Simulations have been run to confirm this.

Table 5.4: Properties of the computational tubes shown in Figure 5.31 with the corresponding number of elements, minimum radius of the inscribed sphere (r_{min}) and memory required.

Geometry	Number of Cells	r_{min}	Memory Required
Geo $_{\text{Trump-Bore}}$	1,128,113	36.5 μm	1.51 GB
Geo $_{\text{Trump-Bore-Bend}}$	1,375,359	37.1 μm	1.84 GB
Geo $_{\text{Trom-Bore}}$	1,643,193	52.3 μm	2.21 GB
Geo $_{\text{Trom-Bore-Bends}}$	1,678,023	43.8 μm	2.25 GB

5.6.2 Simulation Results Obtained on Bore Geometries

Analyzing the obtained impulse response curves in the time-domain could be insightful since intricate details of the reflection sequence can be observed. Reviewing such detail in the frequency-domain is not always as practical [28]. The spectrum however does offer a quick way to inspect which frequency components vary between the different numerical outputs.

The computed impulse responses of the pressure pulse sampled at the inlet and outlet of Geo $_{\text{Trum-Bore}}$ and Geo $_{\text{Trum-Bore-Bend}}$ are shown in Figure 5.32. The equivalent Geo $_{\text{Trom-Bore}}$ and Geo $_{\text{Trom-Bore-Bends}}$ outputs are depicted in Figure 5.33. We plot the time-domain curves with respect to simulation time, τ, for convenience since the speed of sound is scaled to be $c_0 = 1$. This implies that when $\tau = 1$, the pressure wave would have propagated for 1 m. The simulations were run until $\tau = 20$. To better see the difference between the incident, reflected, and transmitted portion of the pressure pulse, i.e., $p_i(t)$, $p_r(t)$ and $p_t(t)$, which we plot them separately in Figures 5.34 (trumpet) and 5.35 (trombone). The corresponding frequency content, i.e., $\mathcal{P}_i$, $\mathcal{P}_r$ and $\mathcal{P}_t$, are also shown.

The input impulse responses of the Geo $_{\text{Trum-Bore}}$ and Geo $_{\text{Trum-Bore-Bend}}$ solutions (Figure 5.32) show minimal differences. For the Geo $_{\text{Trum-Bore-Bend}}$ simulation, we see the addition of a small pressure peak immediately followed by a dip of the same magnitude ($\sim$40 Pa) near $\tau = 0.8$, i.e., 2.3 ms. This corresponds to the time it would take for a portion of the pulse to reflect from the bend and return to the inlet. Since the trumpet bore prior to the bell only changes in radius for the initial 24 cm of tubing (which is before the position of the bend), most of the complicated reflections occur early in the simulation, and the majority of the pulse is transmitted from the tube exit after its first pass to the outlet. The small residual pressure from the back-flow can be seen in the left-middle plot of Figure 5.34. The Geo $_{\text{Trum-Bore}}$ and Geo $_{\text{Trum-Bore-Bend}}$ simulations at the outlet (right of Figure 5.32) match rather well, with the exception of there being a slight time delay between the pulses.

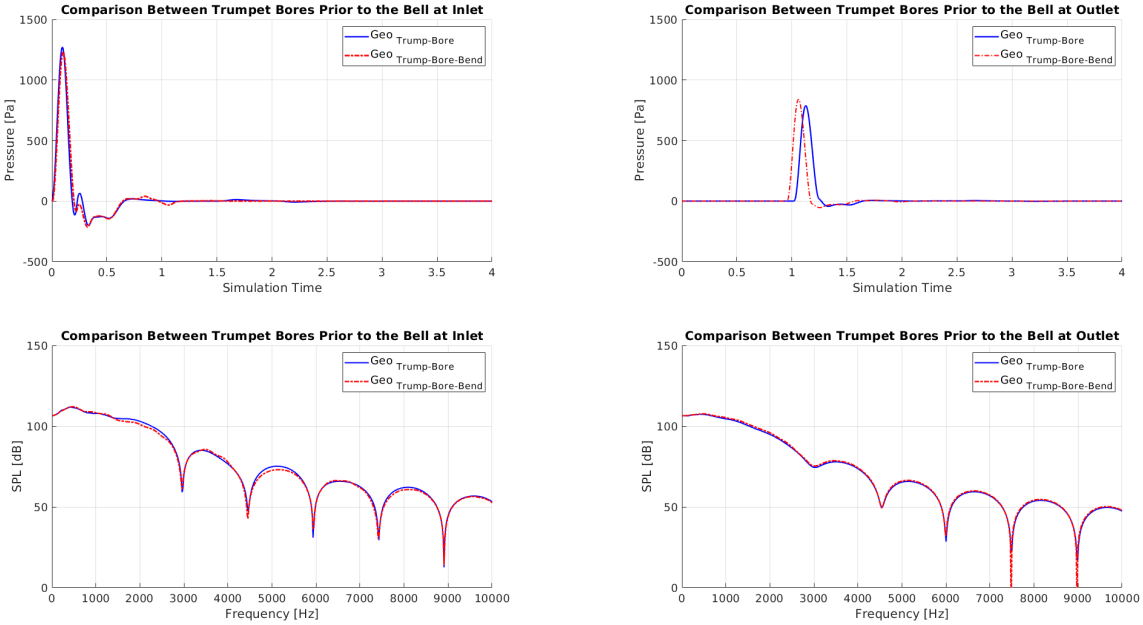

Figure 5.32: Impulse response curves obtained on Geo $_{\text{Trum-Bore}}$ and Geo $_{\text{Trum-Bore-Bend}}$ at the inlet (left) and bell exit (right). A portion of the computed pressure (top) and harmonic spectra of entire impulse (bottom) is shown.

With respect to the trombone, the Geo $_{\text{Trom-Bore-Bends}}$ impulse response (top-left of Figure 5.33) shows a reflection near $\tau = 1.4$, i.e., at 4.1 ms, which aligns well with the time it would take for a small portion of the wave to reflect from the first bend and return to the inlet. As expected, this is not observed in the Geo $_{\text{Trom-Bore}}$ curve because the radius of the trombone bore does not change near the first bend. In fact, the cross-sectional area remains constant for roughly 1.6 m, and then starts to vary again 1.64 m from the mouthpiece boundary. The Geo $_{\text{Trom-Bore}}$ impulse response shows good alignment with this increase in diameter at 1.64 m as seen by the negative reflection. But, in the numerical result for Geo $_{\text{Trom-Bore-Bends}}$, positive as well as negative reflections are observed in the time-domain plot. This is a consequence of having two separate bends. Nonetheless, the main reflection sequences for both Geo $_{\text{Trom-Bore}}$ and Geo $_{\text{Trom-Bore-Bends}}$ mostly vanish by the time $\tau = 5$. In real-time, this is 12.6 ms, which corresponds to the incident wave making a full round trip to the outlet and back in to the inlet. There are some reverberations seen in the numerical output when using Geo $_{\text{Trom-Bore-Bends}}$ but this is just due to the residual signal bouncing around between the bends.

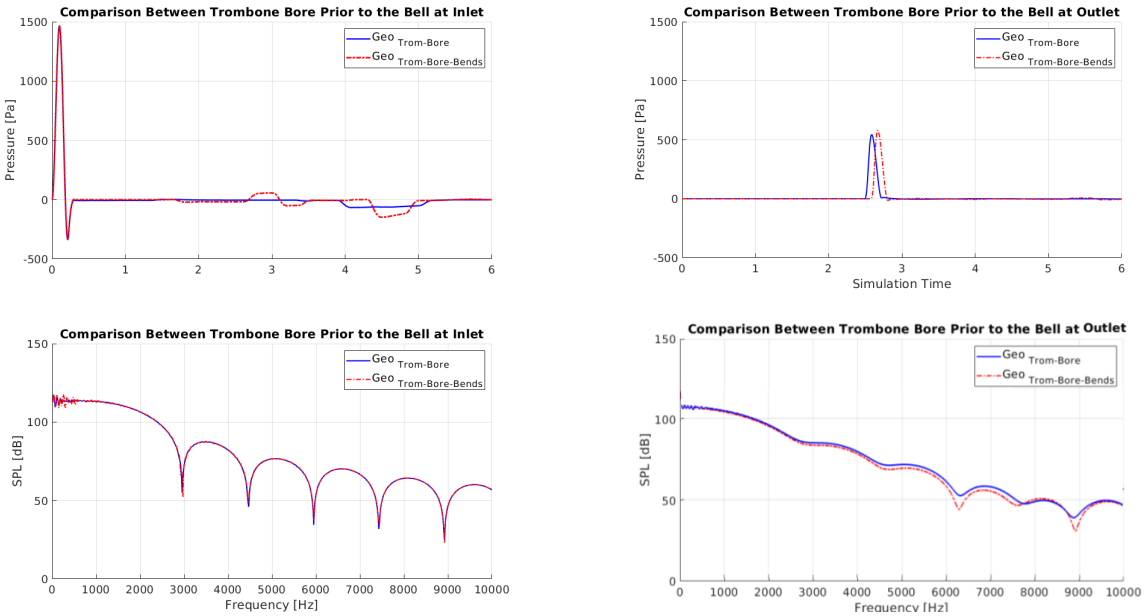

Figure 5.33: Impulse response curves obtained on Geo $_{\text{Trom-Bore}}$ and Geo $_{\text{Trom-Bore-Bends}}$ at the inlet (left) and bell exit (right). A portion of the computed pressure (top) and harmonic spectra of entire impulse (bottom) is shown.

Overall, the impulse response curves obtained from the tubular shapes indicate that the bends do not greatly influence the wave propagation through the bores prior to the flare expansions. There are, of course, slight variations in the reflection sequences when the bends are modelled, but these effects are so small they are barely observable in the spectra. As shown in Section 5.5, the initial bore shape is significantly more influential. Our findings are consistent with work done by Félix *et al.* [62][21].

[21] Authors of [27] and [159] also claim that it is sufficient not including the bends, though they did not carry out specific studies to justify this.

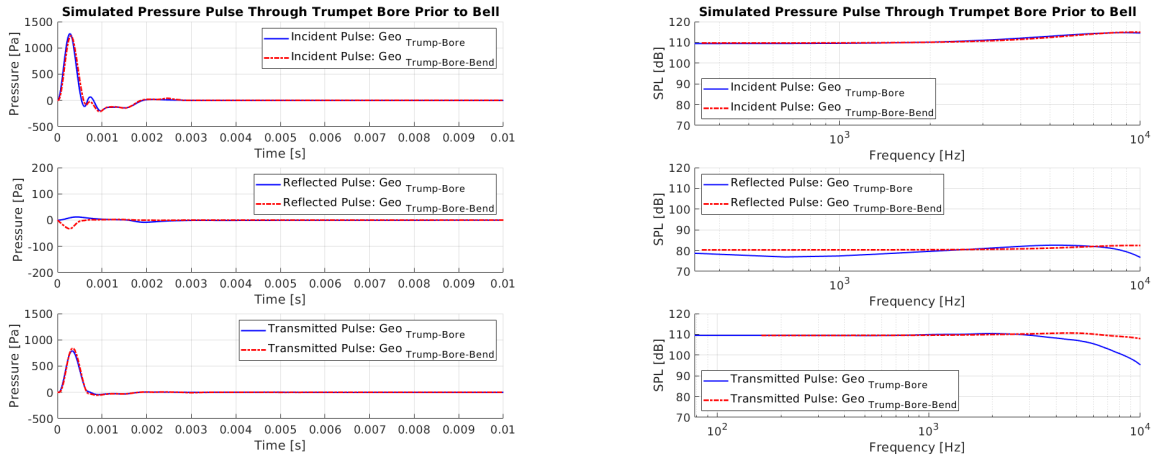

Figure 5.34: Computed impulse response curves of $p_i(t)$ (top) and $p_r(t)$ (middle) at the inlet as well as the $p_t(t)$ at the bell exit obtained on Geo $_{\text{Trum-Bore}}$ and Geo $_{\text{Trum-Bore-Bend}}$. The computed pressure (left) and harmonic spectra (right) are shown.

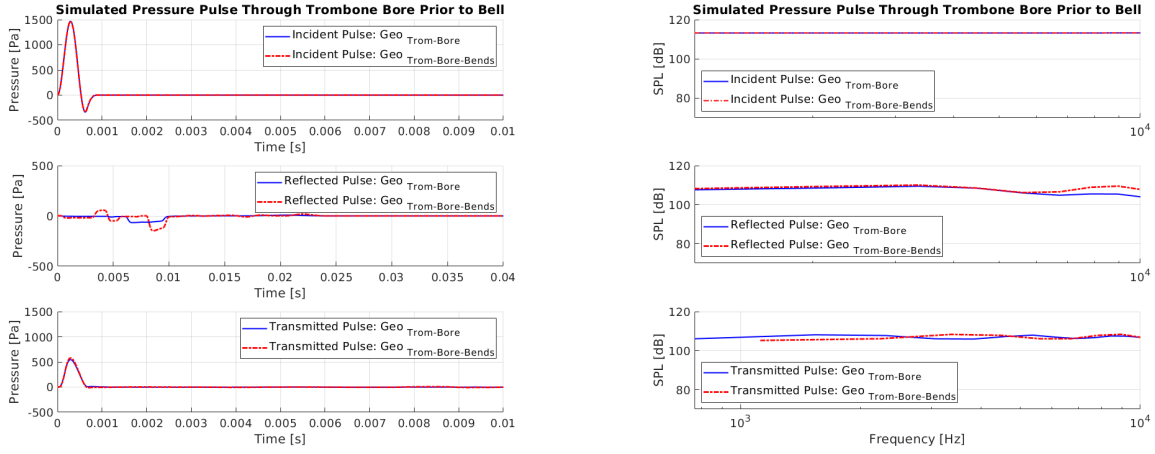

Figure 5.35: Computed impulse response curves of $p_i(t)$ (top) and $p_r(t)$ (middle) at the inlet as well as the $p_t(t)$ at the bell exit obtained on Geo $_{\text{Trom-Bore}}$ and Geo $_{\text{Trom-Bore-Bends}}$. The computed pressure (left) and harmonic spectra (right) are shown.

5.6.3 Setup for the Entire Instrument

.

The simulations that will now be reviewed are an extension of the work done in Section 5.5. More specifically, the new computational trumpet is modelled by using Geo.3 $_{\text{Trumpet}}$ as its blueprint. The beginning portion, the flare, and domain in front of the bell are identical to that of Geo.3 $_{\text{Trumpet}}$ (bottom of Figure 5.16), but the new geometry includes the first trumpet bend 37.5 cm from the inlet boundary. This new geometry (Figure 5.36) will be referred to as Geo.4 $_{\text{Trumpet}}$.

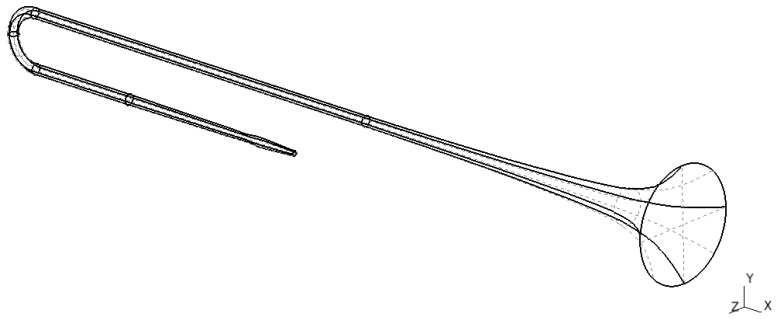

Figure 5.36: Picture of the computational trumpet constructed in GMSH with a bend that was used in Sections 5.6.3 and 5.6.4.

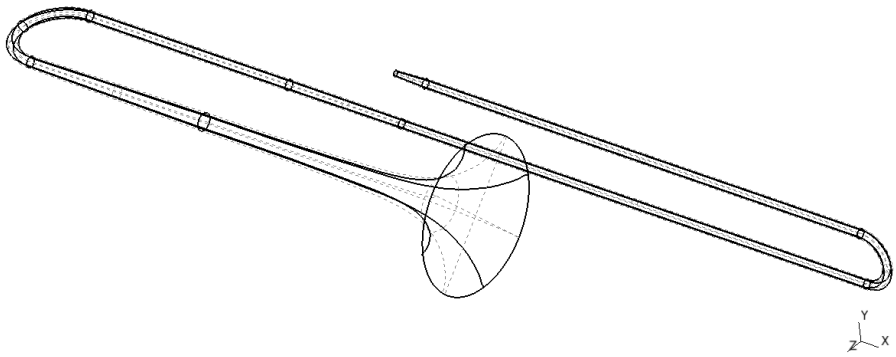

Figure 5.37: Picture of the computational trombone constructed in GMSH with both bends that was used in Sections 5.6.3 and 5.6.4.

Similarly, for the trombone, bend 1 and 2 positioned 69.58 cm and 194.07 cm from the inlet were incorporated into Geo.2 $_{\text{Trombone}}$ (Figure 5.37), and the new geometry will be referred to as Geo.3 $_{\text{Trombone}}$. We note that the slide of the trombone (which includes the first bend) is in front of the bell regardless of the playing position. To deal with this, a volume outlining the first bend was constructed in GMSH such that a gap was created between the exterior of the bend and the volume that the bell opens into[22].

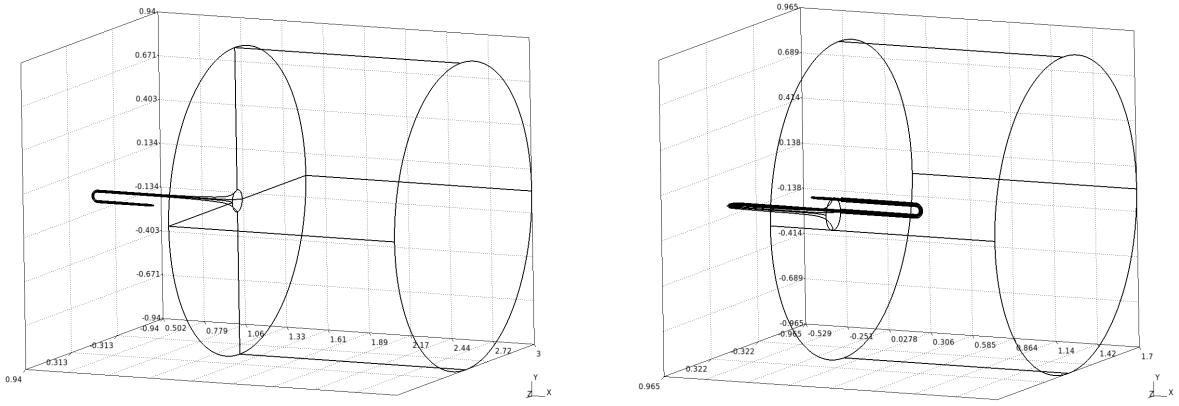

Figure 5.38: Computational domain for the trumpet and trombone shown in Figures 5.36 and 5.37 where the bends are included. Left: Geo.4 $_{\text{Trumpet}}$. Right: Geo.3 $_{\text{Trombone}}$.

Table 5.5: Properties of the computational domains shown in Figure 5.38 with the corresponding number of elements, minimum radius of the inscribed sphere (r_{min}), and memory required.

Geometry	Bore Shape	Number of Cells	r_{min}	Memory
Geo.3 $_{\text{Trumpet}}$	MSM	1,317,219	26.7 μm	1.75 GB
Geo.4 $_{\text{Trumpet}}$	MSM+1 Bend	1,898,949	55.4 μm	2.51 GB
Geo.2 $_{\text{Trombone}}$	MSM	2,234,905	51.2 μm	2.97 GB
Geo.3 $_{\text{Trombone}}$	MSM+2 Bends	4,064,662	13.5 μm	5.40 GB

Both the trumpet and trombone domains can be seen in Figure 5.38 and information for each mesh can be found in Table 5.5 (the Geo.3 $_{\text{Trumpet}}$ and Geo.2 $_{\text{Trombone}}$ information

[22] This basically can be thought of as creating a trombone wall with a certain thickness that is filled with empty space.

is also reported for comparative purposes). At the mouthpiece boundary, the musical note simulated on Geo.4 $_{\text{Trumpet}}$ and Geo.3 $_{\text{Trombone}}$ was the B_3^b played at f[23].

5.6.4 Simulation Results on the Entire Instrument Shape

For both the trumpet and trombone, the numerical solutions were sampled both before and after the bend positions. Recall that at the mouthpiece boundary, the waveform generated represents a steady B_3^b. As the disturbance propagates through the computational instruments, reflections will occur as the radius of the bore changes. Moreover, the majority of the lower harmonic components will reflect throughout the bell region and travel back toward the mouthpiece. These backward moving waves will interact with the forward ones and produce a 'new' steady state solution. Therefore, we will compare and discuss the numerical results before the initial reflections occur at the flare.

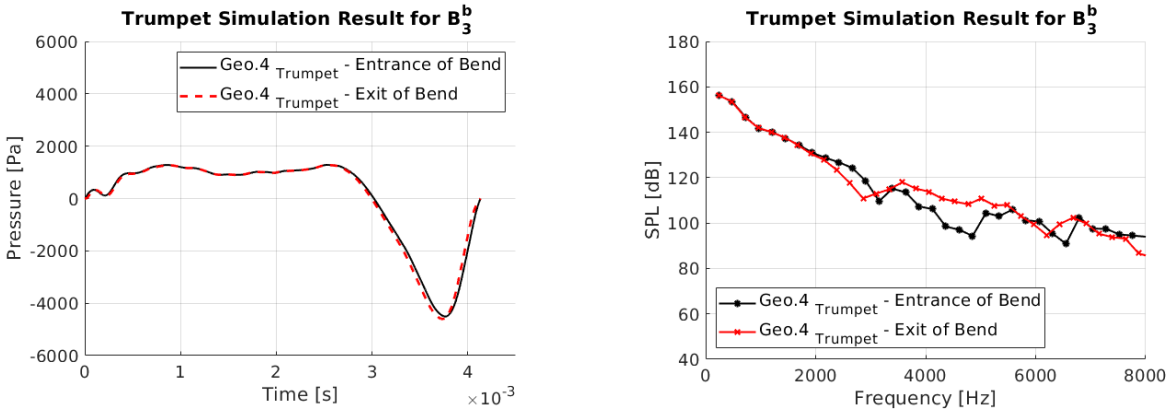

Figure 5.39: Computed pressure (left) and corresponding frequency spectra (right) when simulating the loudly played B_3^b on Geo.4 $_{\text{Trumpet}}$ before entering and after exiting the bend.

The numerical solution obtained on Geo.3 $_{\text{Trombone}}$ entering and exiting the first and second trombone bend is shown in Figures 5.40 and 5.41, respectively. We observe little difference between the computed pressure before and after travelling through bend 1. Any variation between the computed spectra is seen where the SPL has dropped by 45+ dB. Now comparing the numerical solution entering and exiting bend 2, we observe even less

[23] Note the B_3^b trombone note considered in this section has a dynamic level of *f*, not *ff* as in Section 5.5. This is because we wanted to examine a note where shocks were not produced. The *ff* B_3^b trombone note will be examined in after in Section 5.6.5.

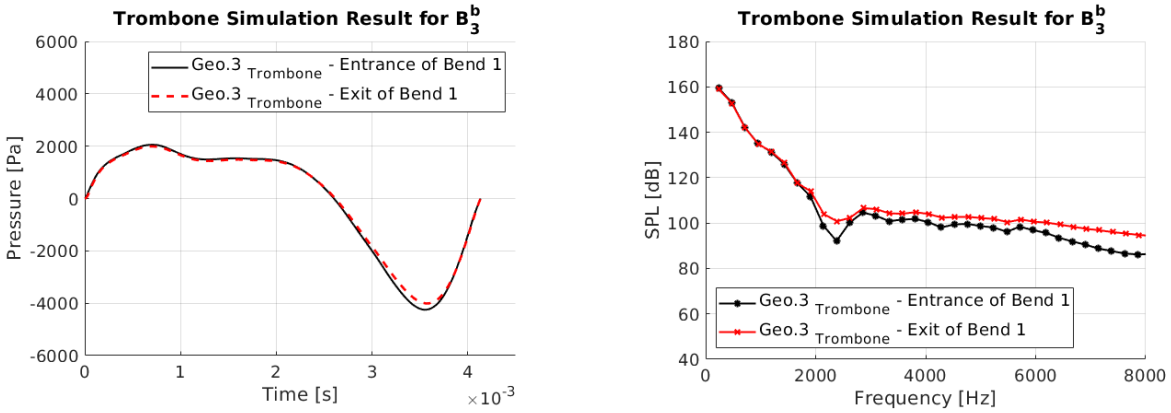

Figure 5.40: Computed pressure (left) and corresponding frequency spectra (right) when simulating the loudly played B_3^b on Geo.3 $_{\text{Trombone}}$ before entering and after exiting Bend 1.

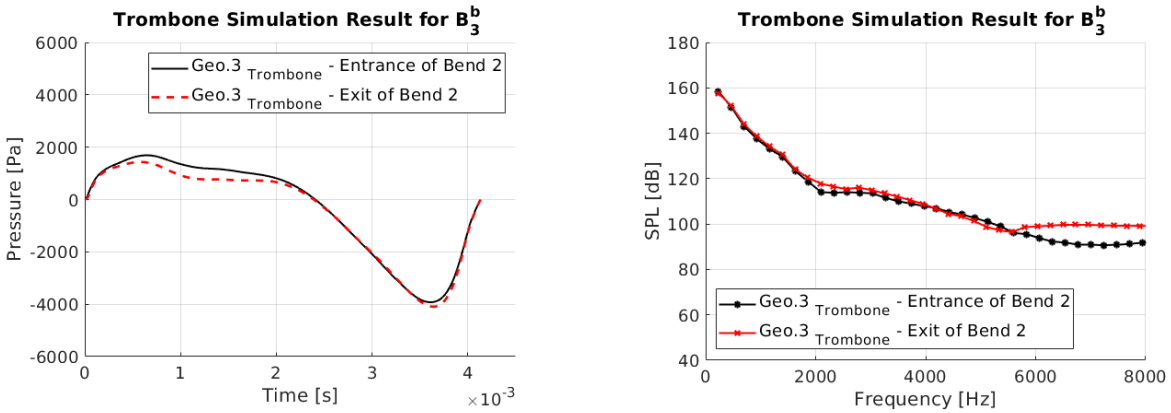

Figure 5.41: Computed pressure (left) and corresponding frequency spectra (right) when simulating the loudly played B_3^b on Geo.3 $_{\text{Trombone}}$ before entering and after exiting Bend 2.

variation between the wave profile in both the time-domain and frequency-domain. The most noticeable difference is observed in the SPLs for spectral components in-between 4000 Hz - 5000 Hz. However, the amplitude values corresponding to these frequencies is down by least 35+ dB and therefore, has little influence.

5.6.5 Further Discussion About the Bends

To verify that the bends do not greatly influence the wave propagation after travelling through the entire instruments (and hence, the numerical solution outside the bell), we now compare the numerical results against the experimental data at Mic $_{\text{Outside-Bell}}$. First, we will review the f B_3^b trumpet note depicted in Figure 5.42.

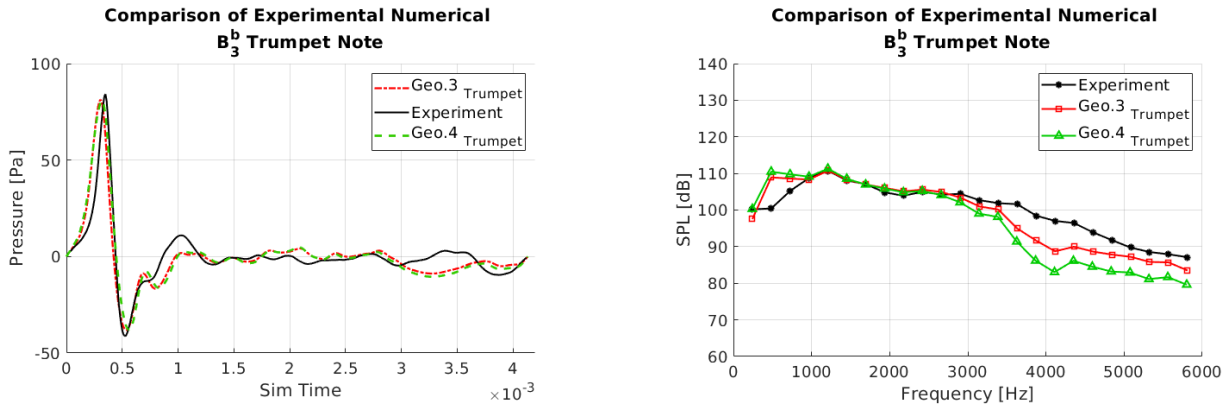

Figure 5.42: Comparison between the experimental data with the computed pressure (left) and corresponding frequency spectra (right) when simulating the loudly played B_3^b on Geo.3 $_{\text{Trumpet}}$ and Geo.4 $_{\text{Trumpet}}$.

Overall, we found that both computational trumpets produce similar solution curves. In particular, the spectral components in-between 900 Hz - 2800 Hz are the same and align well with the experimental SPLs. For frequencies above 2800 Hz, the Geo.3 $_{\text{Trumpet}}$ solution better agrees with the experiment. The Geo.4 $_{\text{Trumpet}}$ output has the same harmonic distribution for the frequencies in this range, yet are slightly lower in amplitude compared to the Geo.3 $_{\text{Trumpet}}$ spectrum.

We also simulated the B_4^b played at f on Geo.3 $_{\text{Trumpet}}$ and Geo.4 $_{\text{Trumpet}}$ out of curiosity to determine if the numerical results for a higher pitch would better match. The corresponding outputs were sampled at Mic $_{\text{Outside-Bell}}$ and can be found in Figure 5.43. We do indeed observe better agreement between the numerical solutions for the B_4^b. For instance, the SPLs corresponding to $f_1 - f_4$ match, and although there is a slight variation between the amplitudes of the higher components, this difference is much smaller compared to the B_3^b solutions.

For the trombone, the B_3^b trombone note played at ff was simulated on Geo.2 $_{\text{Trombone}}$ and Geo.3 $_{\text{Trombone}}$. The solutions sampled at Mic $_{\text{Outside-Bell}}$ are plotted against the exper-

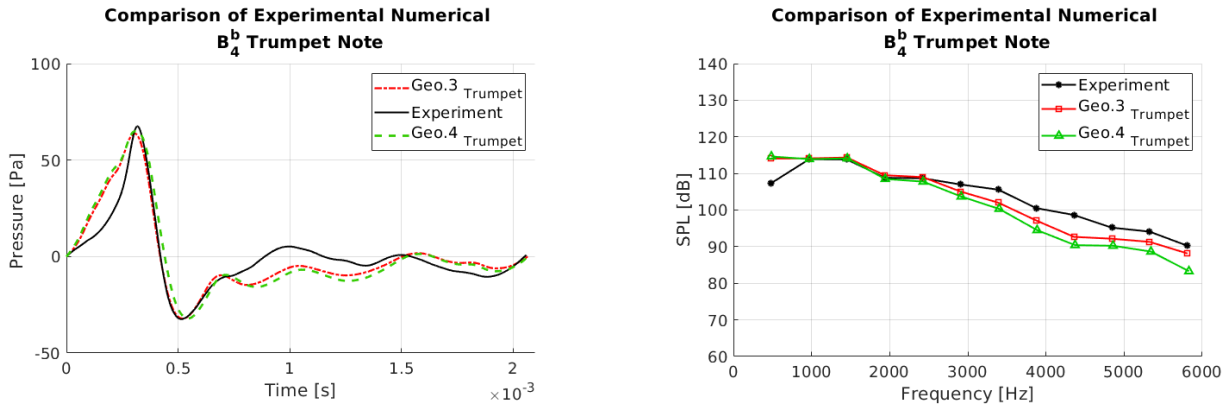

Figure 5.43: Comparison between the experimental data with the computed pressure (left) and corresponding frequency spectra (right) when simulating the loudly played B_4^b on Geo.3 $_{\text{Trumpet}}$ and Geo.4 $_{\text{Trumpet}}$.

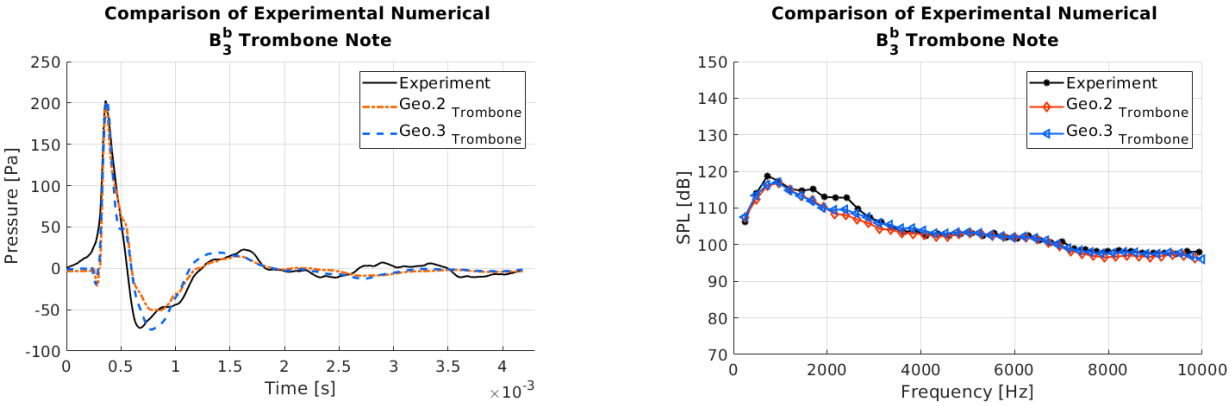

Figure 5.44: Comparison between the experimental data with the computed pressure (left) and corresponding frequency spectra (right) when simulating the loudly played B_3^b on Geo.2 $_{\text{Trombone}}$ and Geo.3 $_{\text{Trombone}}$.

imental data in Figure 5.44. Compared to the trumpet, we observe even less deviations between the trombone solutions. For both computed pressures, before the main peak we see the presence of Gibbs type oscillations in the wave profiles. Again, this is due to the production of computational shock waves. In addition, it appears that the Geo.3 $_{\text{Trombone}}$ shock is slightly stronger due to the sharper change in pressure after $t = 0.0005$ s.

In conclusion, as demonstrated in the 2D numerical study presented in [184], we found

that modelling the trumpet and trombone bends does not greatly influence the numerical solutions. Therefore, it does not seem worthwhile to incorporate them into the computational instruments' geometry[24]. Furthermore, including the trombone bends requires considerably more mesh cells and is not worth the computational expense. To run the B_3^b simulation on Geo.3 $_{\text{Trombone}}$ took 52 days, whereas the Geo.2 $_{\text{Trombone}}$ simulation finished in six and a half days.

5.7 Axisymmetric versus 3D Simulations

Simplifying a 3D problem of modelling sound propagation in a musical instrument is frequently done by exploiting the symmetry and reducing the problem to 2D or even 1D. Previously in [184], we considered a 2D model and examined the consequences of neglecting the third spatial dimension since the spreading of waves in 2D and 3D differs. We calculated that the 2D - 3D dimensionality difference (which we call the *dimension factor*) in our results would be approximately 14 dB. We arrived at this value by assuming that the axial pressure in both 2D and 3D is a good measure of the total energy leaving the bell[25]. After taking this amplitude difference into account, we obtained a good match between the experimental and numerical data for the frequency components that are transmitted from the trumpet bell. The lower spectrum of the musical notes however did not align well with our experimental data. We suspected from our results that the bell could not be approximated in 2D since the pressure amplitude spreads proportionally as $\frac{1}{\sqrt{r}}$, whereas in 3D, the amplitude varies as $\frac{1}{r}$.

Thus, the 2D model was expanded to the full 3D problem. The results of our numerical study demonstrated that all three spatial dimensions are crucial to ensure the reflections from the bell region are properly modelled [185]. This is supported by recent work done by Harrison [89][26]. To illustrate the drastic difference between modelling a trumpet using a 2D and 3D model, as well as properly modelling the cross-sectional area of the bore, we include Figure 5.45. This graph represents the progression of the various models we used to simulate a realistic B_3^b trumpet note played at *f*. Since the bends do not substantially influence the wave propagation through the computational instruments, they have radial

[24] Furthermore, with respect to the trumpet, we suspect that the valves would be more influential to the wave propagation than the bends.

[25] A full derivation of the dimension factor value can be found in [184].

[26] Harrison concluded that the back-scattering from the flare expansion was important to consider so that interactions between the forward and backward moving waves could be better modelled.

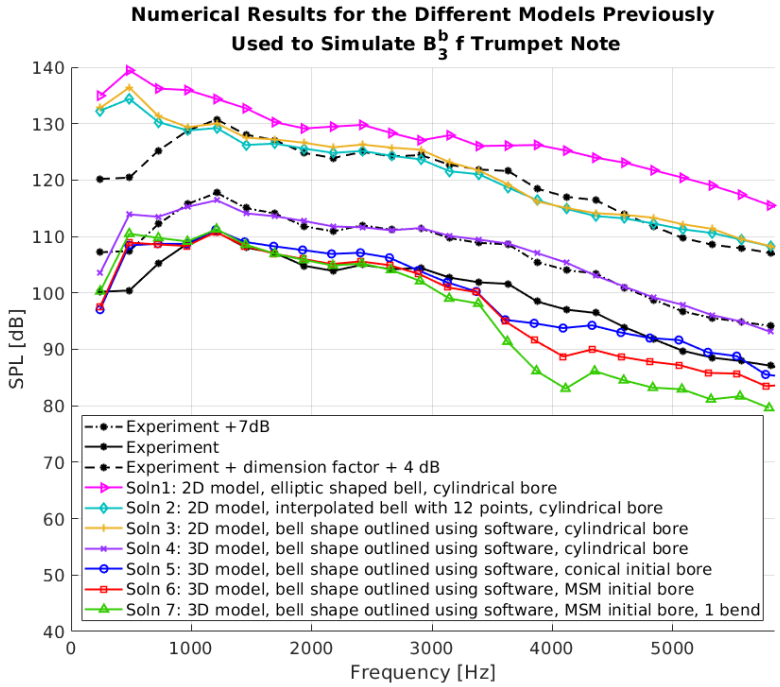

Figure 5.45: Previous 2D and 3D numerical results obatined for the B_3^b played on the trumpet at *f*.

symmetry. So we will now investigate if reducing the 3D problem to a 2D axisymmetric one is sufficient, and whether there are significant differences between the models.

5.7.1 Known Advantages of Axisymmetric Formulations

The main advantage of axisymmetric simulations is the reduction in computing time and required memory. Exploiting such symmetry means that the five equations in the Euler system describing the motion for an inviscid compressible fluid reduces to four equations, and the 3D domain is simplified to a 2D one. The reduction of one spatial dimension allows us to create finer meshes and improve the solution's resolution. Conversely, the required number of elements is reduced by several orders of magnitude for the same resolution. This might be of importance for GPU computing where memory is limited (which was the bottleneck we encountered for the trombone).

While the 3D and axisymmetric equations of motion are the same from an analytical

point of view, simulation results may slightly differ due to the presence of numerical artifacts. For instance, unstructured tetrahedral meshes lack axial symmetry. As a result, the 3D numerical solution will also lack axial symmetry. This is due to numerical diffusion which depends on the size and orientation of the tetrahedra in the mesh. For the flows we are interested in, the differences should be small. A more important numerical artifact is due to imperfect approximation of the physical domain by a computational one. The surface of the computational domain in 3D consists of triangular faces of tetrahedra, i.e., it is not smooth when straight faced tetrahedral discretization is used. It is well known that the accuracy of the simulations will then suffer from spurious entropy production at the vertices and edges of the mesh. The proper way to treat such geometry is to use higher order mesh elements. But, this does not always work well for complicated geometries and is difficult to deal with numerically. Axisymmetric simulations do not suffer from this problem, except possibly at the expansion of the flare [186].

5.7.2 Setup and Discretization of the Conservation Laws

We want to simulate the wave propagation of a musical note through the trumpet and trombone when a 2D axisymmetric model is used. We will then compare the 2D and 3D numerical simulations along with the experimental data. For the 3D representations of the trumpet and trombone, Geo.3 $_{\text{Trumpet}}$ and Geo.2 $_{\text{Trombone}}$ were used and will be referred to as Geo $_{\text{Trumpet-3D}}$ and Geo $_{\text{Trombone-3D}}$ in this Section. For the 2D axisymmetric computational instruments, the curves used in GMSH to create the 3D geometries (such as those shown in Figures 5.18 and 5.19) were used. A line was just added along the axis of symmetry and at the far-field. To avoid confusion, the corresponding axisymmetric meshes will be denoted by Geo $_{\text{Trumpet-Axi}}$ and Geo $_{\text{Trombone-Axi}}$. An image of each mesh is shown in Figure 5.46 and Table 5.6 summarizes the information about each mesh. On each computational trumpet, the loudly played B_3^b was prescribed at the inlet boundary. For the trombone geometries, a quieter B_3^b was simulated.

5.7.3 Axisymmetric versus 3D Simulation Results

All numerical solutions were sampled at Mic $_{\text{Outside-Bell}}$. The computed pressure waveforms obtained on the axisymmetric and 3D domains are shown in Figure 5.47. For both instruments, the numerical curves are very similar. However, the magnitude of the Geo $_{\text{Trumpet-Axi}}$ and Geo $_{\text{Trombone-Axi}}$ pressure profiles are slightly larger than the equivalent 3D ones. For the computational trumpet, this is mainly observed at the main peak and dip, whereas

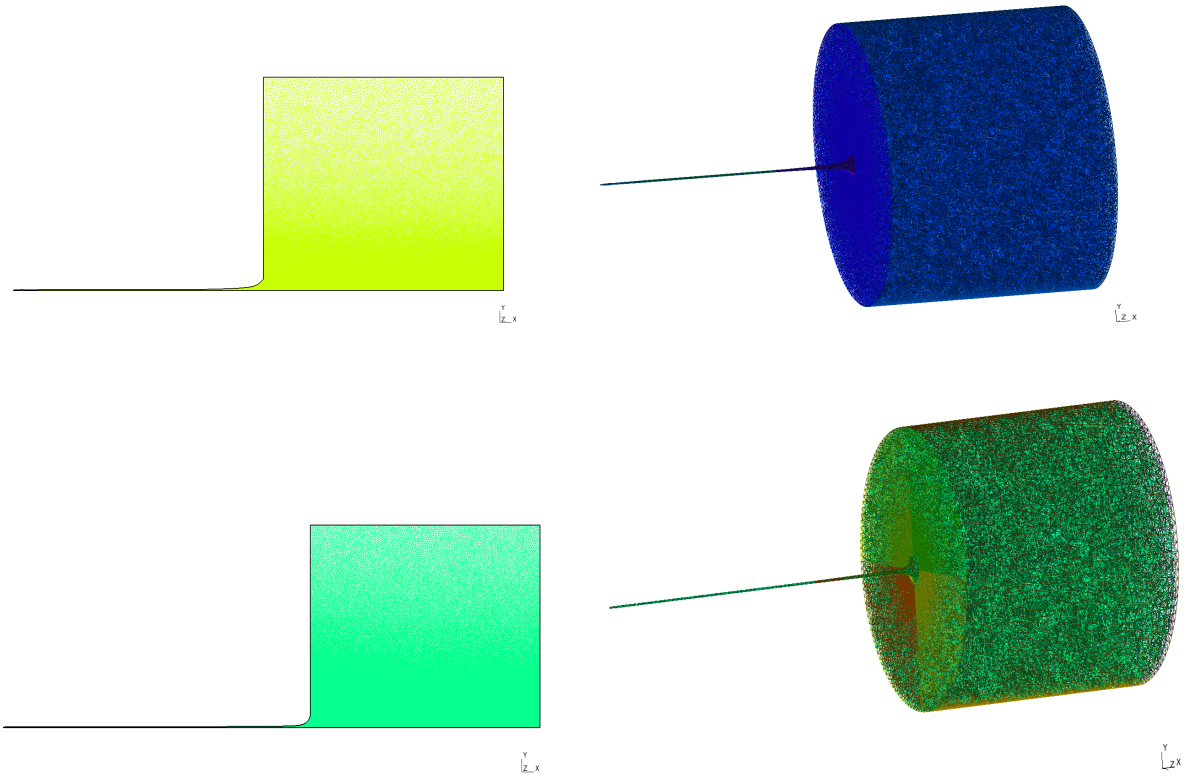

Figure 5.46: A picture of the meshes generated in GMSH used in Sections 5.7.2 and 5.7.3. Top-left: Geo $_{\text{Trumpet-Axi}}$. Top-right: Geo $_{\text{Trumpet-3D}}$. Bottom-left: Geo $_{\text{Trombone-Axi}}$. Bottom-right: Geo $_{\text{Trombone-3D}}$. Information about the meshes can be found in Table 5.6.

Table 5.6: Names of each computational domain shown in Figure 5.46 for the simulations discussed in Sections 5.7.2 and 5.7.3. The corresponding number of elements, minimum inscribed circle or sphere and total memory are reported.

Geometry	Number of Cells	r_{min}	Memory Required
Geo $_{\text{Trumpet-Axi}}$	743,424	32.8 μm	885 MB
Geo $_{\text{Trumpet-3D}}$	1,317,219	26.7 μm	1.75 GB
Geo$_{\text{Trombone-Axi}}$	935,366	75.4 μm	901MB
Geo$_{\text{Trombone-3D}}$	2,234,905	51.2 μm	2.97 GB

for the trombone, there is consistently a difference of 1 Pa - 2 Pa between the computed

pressures (except at the beginning and end of the period). Though, the note simulated on the trombone geometries will suffer slightly more from numerical diffusion, as the dynamic level of the B_3^b was only *mp* (the maximum pressure at Mic $_{\text{Outside-Bell}}$ is only 14 Pa).

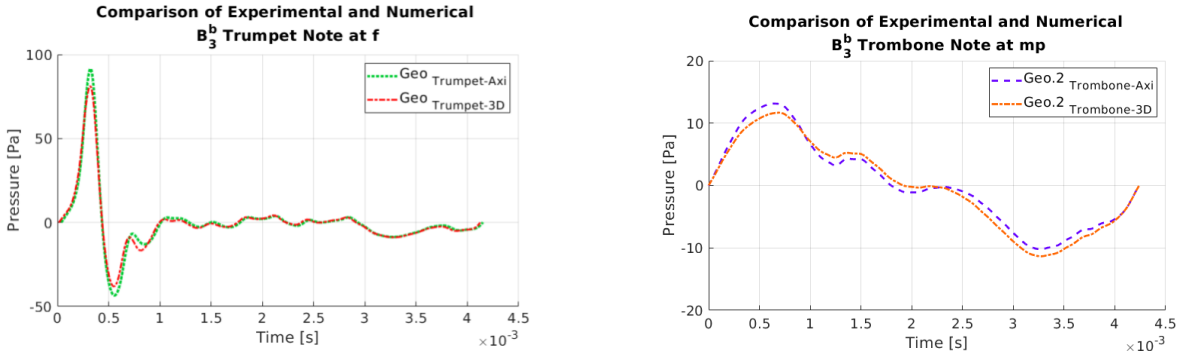

Figure 5.47: Comparison between the computed pressure waveforms of the *f* B_3^b trumpet note (left) and *mp* B_3^b trombone note (right) sampled at Mic $_{\text{Outside-Bell}}$ and simulated on the Geo $_{\text{Axi}}$ and Geo $_{\text{3D}}$ geometries.

Figure 5.48 then shows the computed spectra against the measured data. We find that the axisymmetric simulations align slightly better with the measured notes compared to the 3D results. For instance, the fundamental frequency obtained on Geo $_{\text{Trumpet-Axi}}$ is only 1 dB below the measured value, whereas the 3D value is off by -3 dB. Similarly for the trombone note, the SPL for f_4 obtained on Geo $_{\text{Tromhone-3D}}$ underestimates the experimental SPL by 3 dB, whereas there is no variations between the experimental and Geo $_{\text{Tromhone-Axi}}$ value. More so for the trumpet, the highest frequency components corresponding to the axisymmetric simulations do not appear to suffer as much from numerical diffusion and consequently, the deviation from the experiment is not as large. It is harder to make such a statement for the trombone however, as the higher spectra contains mostly noise.

These differences between the models are small, yet the results clearly indicate that the straight-sided mesh elements better approximate the complex geometry of the instruments in 2D rather than 3D. This is especially evident for the trumpet. That being said, making a true comparison between the models is difficult because mesh generation slightly differs in 2D and 3D, particularly for local refinement [64]. In conclusion, our results demonstrate that axisymmetric simulations can offer better resolution for our problem while greatly reducing runtimes and memory requirements.

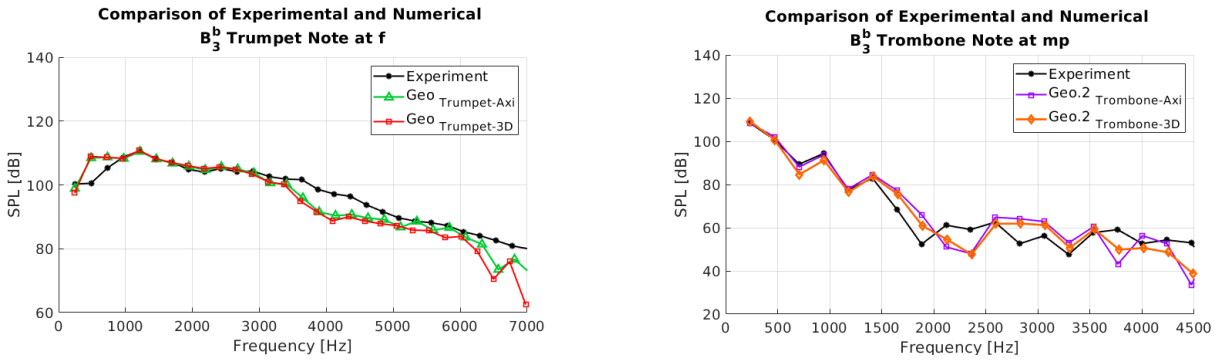

Figure 5.48: Comparison between measured and computed spectra of pressure of the f B_3^b trumpet note (left) and mp B_3^b trombone note (right) sampled at Mic $_{\text{Outside-Bell}}$ and simulated on the Geo $_{\text{Axi}}$ and Geo $_{\text{3D}}$ geometries.

5.8 Reflection and Transmission Properties

Whether it be simulating a single short duration pulse through a computational instrument, or generating the pulse repetitively at the inlet, numerically solving pulse reflectometry problems can be time consuming. This is because the numerical solution needs to return to the equilibrium state (if a single pulse is being considered), or reach a steady state solution (if the pulse is being generated repetitively). Otherwise, the true reflective propagation behaviour of the signal cannot be properly examined.

In Section 5.6, the influence of the bends were analyzed via pulse reflectometry methods. We conduct a similar numerical investigation to study the effects of the various other brass instrument components, except using an axisymmetric model. In particular, the flare, the changes in cross-sectional area, and the mouthpiece cup will be examined by simulating a short duration pulse down different computational trombone and trumpet geometries. For each numerical test case, the pressure pulse originally defined in equation (5.11) was prescribed as follows,

$$p = \begin{cases} 1.0 + 0.01\left(1 - \cos\big(1500t\big)\right), & \text{if t} < \frac{2\pi}{1500} \\ 1.0, & \text{otherwise.} \end{cases}$$

This produced a pulse at the entrance of the computational instruments with a duration of 0.66 ms and an amplitude that is 2% of atmospheric pressure. Better understanding the behaviour associated with the different regions of the trumpet or trombone can be achieved in part by finding the reflection and transmission coefficients defined in Section 5.3.2.

To carry out a thorough comparison between the trumpet and trombone flare expansion only (which includes determining their cutoff frequencies and comparing our findings with the literature), we modelled the tubing prior to the flares as uniform cylindrical tubes[27]. These 2D computational domains will be referred to as Geo.1 $_{\text{Trumpet-Axi}}$ and Geo.1 $_{\text{Trombone-Axi}}$. To establish how the reflective and transmissive properties are influenced by the initial tubing shapes near the mouthpiece-shank, pressure pulse simulations were also done on Geo.2 $_{\text{Trumpet-Axi}}$, Geo.3 $_{\text{Trumpet-Axi}}$ and Geo.2 $_{\text{Trombone-Axi}}$[28].

Table 5.7: Names of each computational domain used in Section 5.8 as well as the corresponding number of elements, minimum radius of the inscribed circle (r_{min}), and the total memory required.

Geometry	Number of Cells	r_{min}	Memory Required
Geo.1 $_{\text{Trumpet-Axi}}$	545,626	73.7 μm	669 MB
Geo.2 $_{\text{Trumpet-Axi}}$	734,808	34.8 μm	868 MB
Geo.3 $_{\text{Trumpet-Axi}}$	743,424	32.8 μm	898 MB
Geo.1 $_{\text{Trombone-Axi}}$	909,955	72.7 μm	899 MB
Geo.2 $_{\text{Trumpet-Axi}}$	935,366	75.4 μm	901 MB

5.8.1 Influence of the Flare and Cross-Sectional Area

In Figure 5.49, the computed acoustic pulses sampled at the inlet of Geo.1 $_{\text{Trumpet-Axi}}$, Geo.2 $_{\text{Trumpet-Axi}}$ and Geo.3 $_{\text{Trumpet-Axi}}$ are plotted. All trumpet simulations were run until $\tau = 40$, which in real time corresponds to 11.66 ms. However, to more easily see the main reflection sequence, the computed pressure only up to $\tau = 14$ is shown. For the numerical impulse response curves obtained on Geo.1 $_{\text{Trombone-Axi}}$ and Geo.2 $_{\text{Trombone-Axi}}$, the final simulation time was $\tau = 80$, which corresponds to 23.32 ms. The numerical trombone solutions are plotted to $\tau = 25$ in Figure 5.50.

The computed trumpet impulse response curves (Figure 5.49) depict significant differences when the initial tubing shape is better modelled, i.e., not cylindrical. For instance, the incident unipolar pulses (p_i) immediately undergo reflections when simulated on Geo.2 $_{\text{Trumpet-Axi}}$ or Geo.3 $_{\text{Trumpet-Axi}}$, which can be seen between $\tau \in [0.22, 0.6]$. This is much more evident for the trumpet versus the trombone because the radius varies for the

[27] The axisymmetric computational geometries used are equivalent to Geo.1 $_{\text{Trumpet}}$ and Geo.1 $_{\text{Trombone}}$

[28] Recall that Geo.3 $_{\text{Trumpet}}$ and Geo.2 $_{\text{Trombone}}$ were the most realistic representations of the instruments with respect to how their cross-sections change and are depicted in Figures 5.16 and 5.17.

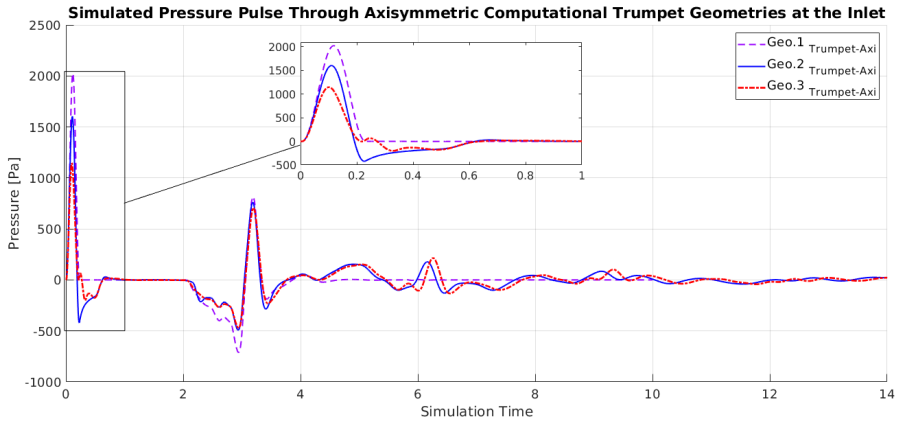

Figure 5.49: Simulated pressure pulse through axisymmetric computational trumpets Geo.1 $_{\text{Trumpet}}$, Geo.2 $_{\text{Trumpet}}$ and Geo.3 $_{\text{Trumpet}}$ sampled at the inlet.

initial 24 cm of tubing but only 4.5 cm for the trombone. As the acoustic pulses enter the trumpet flare, the pressure disturbance undergoes continuous reflection as it travels through the entire bell. These reflections can be seen near $\tau = 2.1$ for all computational trumpets, whereas the reflection sequence corresponding to the computational trombones (Figure 5.50) are different. For instance, for Geo.2 $_{\text{Trombone-Axi}}$, the reflection sequence is first observed near $\tau = 3.9$, whereas for Geo.1 $_{\text{Trombone-Axi}}$, it starts at approximately $\tau = 4.4$. This is because prior to the flare region, as discussed in Section 5.5, there is a small conical section of tubing[29]. For all computational instruments, these times align well with the time required for the reflected pressure pulses (p_r) to return to the mouthpiece boundary. For the Geo.1 $_{\text{Trumpet-Axi}}$ simulation, p_r mostly vanishes by $\tau = 4.5$ (since the bore prior to the flare is cylindrical), whereas for the other geometries, it takes much longer (approximately until $\tau = 15$). Although the Geo.2 $_{\text{Trumpet-Axi}}$ and Geo.3 $_{\text{Trumpet-Axi}}$ reflection sequences are similar in character, their differences are indisputable. With respect to the computational trombone geometries, echos from additional reflections are observed until almost $\tau = 23$. As expected, the reflection sequence of Geo.2 $_{\text{Trombone-Axi}}$ is more complicated compared to Geo.1 $_{\text{Trombone-Axi}}$, yet it is more segregated relative to Geo.2 $_{\text{Trumpet-Axi}}$ or Geo.3 $_{\text{Trumpet-Axi}}$. In other words, there appear to be distinct echos near $\tau = 4.4$, $\tau = 10.5$, $\tau = 16.3$, $\tau = 22.1$. These intervals of six, i.e., 1.7 ms, corresponds to the time it would take for the pressure disturbance to make a round trip from the inlet, to the bell, and back to the inlet. The trumpet curves in Figure 5.49 also have this feature but due to the length of the trumpet,

[29] This is also why the initial dip of the Geo.2 $_{\text{Trombone-Axi}}$ reflection sequence is less pronounced relative to Geo.1 $_{\text{Trombone-Axi}}$.

it appears more muddled.

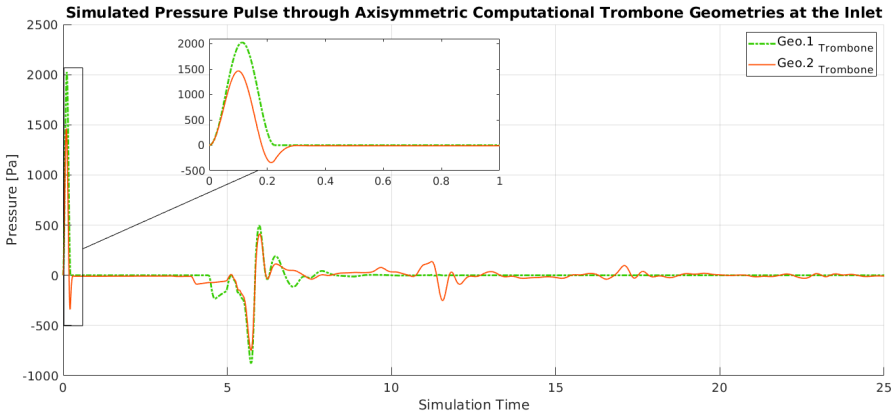

Figure 5.50: Simulated pressure pulse through axisymmetric computational trombones Geo.1 $_{\text{Trombone-Axi}}$ and Geo.2 $_{\text{Trombone-Axi}}$ sampled at the inlet.

Recall that we denote the frequency content of the incident, reflected and transmitted portion of the acoustic pulses by $\mathcal{P}_i$, $\mathcal{P}_r$ and $\mathcal{P}_t$, respectively. The numerical reflection coefficient (or the reflected transfer data), $R(f)$ is a representation of the power that is reflected by the computational flares. The complement of $R(f)$ is the transmission coefficient (or transmission transfer function), $T(f) = 1 - R(f)$, and corresponds to the power that is radiated from the bell. Examining these coefficients for the Geo.1 $_{\text{Trumpet-Axi}}$ and Geo.1 $_{\text{Trombone-Axi}}$ solutions show the influence only of the flare expansion. At low frequencies, the sound waves undergo a relatively abrupt acoustic change when travelling to the bell exit and as a result, are largely reflected out of phase. In this case, $R(f)$ is approximately equal to one (zero in frequency-space) [58].

The computed $R(f)$ and $T(f)$ for both Geo.1 $_{\text{Trumpet-Axi}}$ and Geo.1 $_{\text{Trombone-Axi}}$ are depicted in Figure 5.51. The position where they cross at -3 dB corresponds to the reduction of sound power by 50%. For Geo.1 $_{\text{Trumpet-Axi}}$ and Geo.1 $_{\text{Trombone-Axi}}$, respectively, this position is approximately at 900 Hz and 780 Hz. The frequency at which the $R(f)$ have dropped by -6 dB is near 1050 Hz and 920 Hz for Geo.1 $_{\text{Trumpet-Axi}}$ and Geo.1 $_{\text{Trombone-Axi}}$. The spectral components greater than these values are almost completely transmitted from the bell. According to the literature, components above 1200 Hz - 1600 Hz mostly propagate directly out of the trumpet flare, whereas for the trombone, it is for frequencies near 700 Hz - 850 Hz [20], [55], [58], [112], [180]. Our results are therefore in relatively

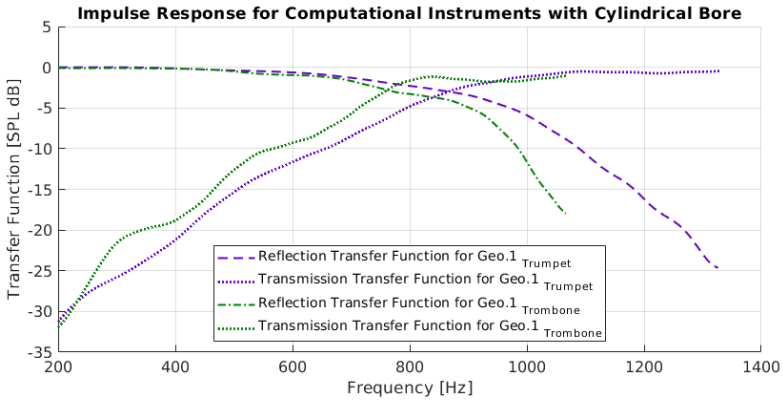

Figure 5.51: Computed reflection and transmission coefficient obtained when simulating a pressure pulse on Geo.1 $_{\text{Trumpet-Axi}}$ and Geo.1 $_{\text{Trombone-Axi}}$.

good agreement with the values reported in the literature[30]. Furthermore, the transmission function we calculated for Geo.1 $_{\text{Trombone-Axi}}$ displays similar character to the $T(f)$ curve reported in [55].

5.8.2 Inclusion of the Mouthpiece Cup

The mouthpiece cup of a brass instrument is said to have a vital role in sound generation [66]. For instance, experiments have been done measuring the impedance peaks for the trumpet and trombone with and without the mouthpiece being coupled to the instruments. It has been found that the impedance peaks of the trumpet are much more affected when the mouthpiece is included compared to the trombone. For the trombone, the mouthpiece pushes the cutoff frequency from 700 Hz to approximately 850 Hz. Whereas for the trumpet, the mouthpiece amplifies the impedance peaks until a maximum is reached near 800 Hz[31]. However, for the numerical simulations presented in this thesis, the cup was not incorporated. We justify this for a couple of reasons. Firstly, we are interested in numerically solving a system already in a quasi-steady state, i.e., the input waveform simulated at the inlet is a representation of a musical note that was recorded once a standing wave

[30] It is important to note that the transfer functions depicted in Figure 5.51 correspond specifically to the Geo.1 $_{\text{Trumpet-Axi}}$ and Geo.1 $_{\text{Trombone-Axi}}$ geometries, so the values will not be identical to those published in the literature (since any changes in the cross-sectional area are not modelled for these geometries).

[31] In [55] for instance, the maximum impedance peaks for the trumpet were measured to be approximately 400 MΩ near 800 Hz. For the trombone, the maximum peak was 55 MΩ and corresponded to the initial peak.

pattern was achieved. In this case, the contribution of the mouthpiece cup (as well as the lip coupling) is encoded in the periodic waveform. Secondly, the lips protrude into the mouthpiece cup effectively reducing its volume [119][32]. Thirdly, from a computational perspective, incorporating the mouthpiece cup could be problematic due to the rapid change in radius. In particular, the diameter of the mouthpiece cup is larger than anywhere else along the bore, excluding the flare[33] and is connected to the narrowest region, i.e., the throat[34]. It could therefore be challenging to obtain good quality meshes, especially for the trumpet. For these reasons, we believe our simplification of the instruments' shape is adequate.

Despite this, it still may be of benefit to examine how the inclusion of the mouthpiece cup would change the impulse response curves obtained above. Although we have not come across such numerical results in the literature, physical experiments measuring the impulse response curves have been performed and hence, could be compared against analogous simulations. For instance, Elliott, Bowsher and Watkinson carried out such measurements on the trombone when the mouthpiece was and was not attached [55]. This was also done for the trumpet but only when the mouthpiece was not connected, as the authors came across several challenges related to the physical structure of the trumpet mouthpiece and throat. They claim for instance that if the particle velocity surpasses a certain limit (which is highest in the mouthpiece throat), the airflow can become turbulent [55][35]. Similar claims about turbulence in brass instruments have also been made in [20], [47], [86], [159], [167], [188].

Figure 5.52: A picture of the mouthpiece cup region of the axisymmetric computational trumpet (left) and trombone (right) produced in GMSH used in Section 5.8.2.

[32] For higher pitches and increased dynamic levels, the lips protrude more into the cup. In such situations, it is possible for the lip opening area to be comparable to that of the mouthpiece throat [47].

[33] The effective volume of a standard mouthpiece cup has been reported to be approximately 4.7 ml and 1.2 ml for the trombone and trumpet, respectively [55].

[34] For our trombone and trumpet, the throat radius is 0.35 cm and 0.18 cm, respectively.

[35] Elliot *et al.* explain that when the particle velocity is sufficiently large, it results in a resistance, which at 20 m/s was measured to be 0.3 MΩ and 0.53 MΩ in the throat of the trombone and trumpet, respectively. To put this into perspective, the magnitude of the standard acoustical impedance is 20 MΩ [55].

Table 5.8: Names of each computational domain shown in Figure 5.52 and the corresponding number of elements, minimum inscribed circle (r_{min}) and total memory required.

Geometry	Number of Cells	r_{min}	Memory Required
Geo.3 $_{\text{Trumpet-Axi-Cup}}$	1,335,436	33.0 μm	1.28 GB
Geo.2 $_{\text{Trombone-Axi-Cup}}$	937,431	75.1 μm	901 MB

Geo.3 $_{\text{Trumpet-Axi-Cup}}$ and Geo.2 $_{\text{Trombone-Axi-Cup}}$ refer to the additional computational instruments constructed which incorporate the cups to Geo.3 $_{\text{Trumpet-Axi}}$ and Geo.2 $_{\text{Trombone-Axi}}$. A close up near the shank is shown in Figure 5.52. Although we were able to generate good quality meshes for both the computational instruments, to my surprise, when I attempted to simulate an acoustic pulse through Geo.3 $_{\text{Trumpet-Axi}}$ and Geo.2 $_{\text{Trombone-Axi}}$, a physical solution was only obtained for the trombone. Regardless of how we constructed the mesh, or how the impulse was generated, i.e., as an inflow boundary condition on pressure or as a source term[36], it always resulted in a nonphysical solution (i.e., the code crashed). Hypothetically speaking, if the claims in [55] about turbulent flow developing in the mouthpiece throat are true, then it make sense that our simulation would crash since we do not incorporate turbulence. Although this is only speculation, it seems to provide some sort of merit to such claims made in [20], [47], [55], [86], [159], [167], [188].

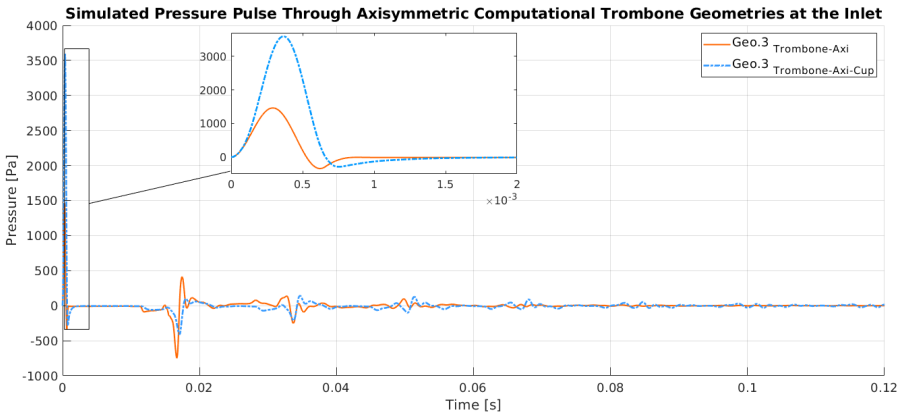

Figure 5.53: Simulated pressure pulse through axisymmetric computational trombones Geo.1 $_{\text{Trombone-Axi-Cup}}$ and Geo.2 $_{\text{Trombone-Axi-Cup}}$ at the inlet.

Nonetheless, the simulation result acquired on Geo.2 $_{\text{Trombone-Axi-Cup}}$ appeared to be a reasonable solution that eventually settled back to the equilibrium state. The final

[36] See Section 6.4.1 for a full discussion on the source term.

simulation time was $\tau = 80$ or, 23.32 ms. The computed impulse response up until 0.12 ms can be seen in Figure 5.53. We found that when the cup was included in the trombone geometry, the numerical solution took much longer to reach the initial state, which is of course due to the additional reflections occurring near the mouthpiece cup. We also found that the cup greatly increases the amplitude of p_i and also, lengthens the duration of the pulse. This seems reasonable because from the literature, we know that connecting the mouthpiece to the bore shifts the impedance peaks.

5.8.3 Reflectometry Results and Comparison with the Literature

For comparative purposes, $\mathcal{P}_i$ and $\mathcal{P}_r$ for all six computational instruments are plotted in Figure 5.54. In addition, the numerical transfer functions, i.e., the ratio between $\mathcal{P}_t$ and $\mathcal{P}_i$, were calculated and are shown in Figure 5.55. The most obvious difference between the transfer functions is that for Geo.1 $_{\text{Trumpet-Axi}}$ and Geo.1 $_{\text{Trombone-Axi}}$, the curves are flat in the lower frequency range. All other geometries have little spikes or peaks in the same range, which are a consequence to the changes in cross-sectional area near the inlet, and before the trombone flare. For Geo.2 $_{\text{Trombone-Axi-Cup}}$, the spikes do not completely die off near 1000 Hz compared to the other numerical results but rather, become less pronounced as the frequency increases. In addition, the transfer function is shifted downward relative to the other trombone results.

As mentioned, one of the main reasons for running the simulations discussed in Sections 5.8.1 and 5.8.2 was that we found equivalent experiments published in the literature, e.g., [55], [179], [180]. This provided an opportunity to verify whether our numerical simulations were producing reasonable results. For instance, $\mathcal{P}_i$ curves found in [179][37] for the trombone (where the mouthpiece was not included) are qualitatively similar to our computed $\mathcal{P}_i$ output when a pulse was simulated on Geo.2 $_{\text{Trombone-Axi}}$ (Figure 5.54). In addition, measurements of $\frac{\mathcal{P}_t}{\mathcal{P}_i}$ for both the trumpet and trombone can be found in [55] (when the backbore of the mouthpieces were sealed off), which would be equivalent to the Geo.3 $_{\text{Trumpet-Axi}}$ and Geo.2 $_{\text{Trombone-Axi}}$ geometries. Our computed transfer functions in Figure 5.55 also display similar behaviour to the results shown in [55]. For instance, both our pressure transfer functions and the measurements of Elliott's *et al.* display spikes for frequencies up to 1000 Hz (more precisely, around 1000 Hz for the trumpet and 850 Hz for the trombone) and then begin to die away[38]. Impulse response curves for the trombone

[37] Pulses of roughly 1% - 2% of atmospheric pressure were generated where the duration of the pulses were approximately 0.008s [179].

[38] The authors do not present the pressure transfer functions when the mouthpieces are coupled to the bore.

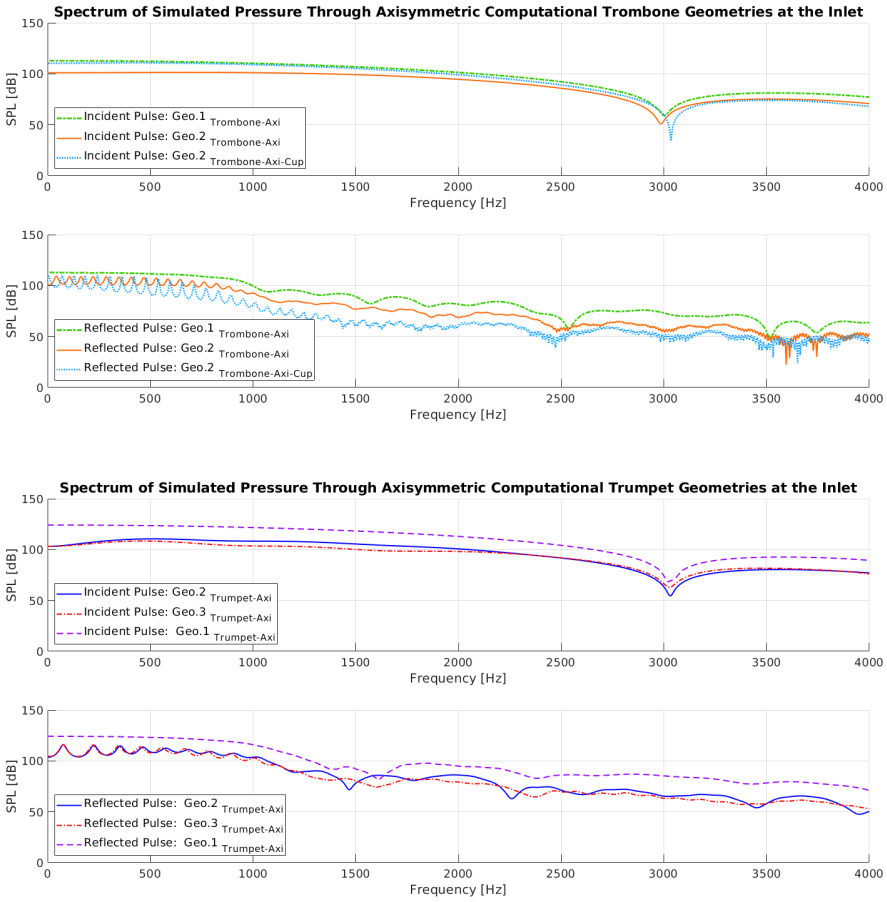

Figure 5.54: Computed $\mathcal{P}_i$ and $\mathcal{P}_r$ curves obtained from simulating a pressure pulse on Geo.1 $_{\text{Trombone-Axi}}$, Geo.2 $_{\text{Trombone-Axi}}$, Geo.2 $_{\text{Trombone-Axi-Cup}}$ and Geo.1 $_{\text{Trumpet-Axi}}$, Geo.2 $_{\text{Trumpet-Axi}}$, Geo.3 $_{\text{Trumpet-Axi}}$ discussed in Sections 5.8.1 and 5.8.2.

reported in [55][39] also resemble our Geo.2 $_{\text{Trombone-Axi-Cup}}$ results found in Figure 5.53. The authors also found that the addition of the mouthpiece cup greatly increases the pressure values and produces a longer reflection sequence that dies away roughly 200 ms later. In conclusion, these experiments give us some confidence that the chosen model and numerical method used to describe the sound propagation through the computational trumpet and trombone (at the very least) are qualitatively producing reasonable outputs.

[39] The authors also applied an inverse Fourier transform on their measured impedance curves to obtain the impulse response curves in the time-domain.

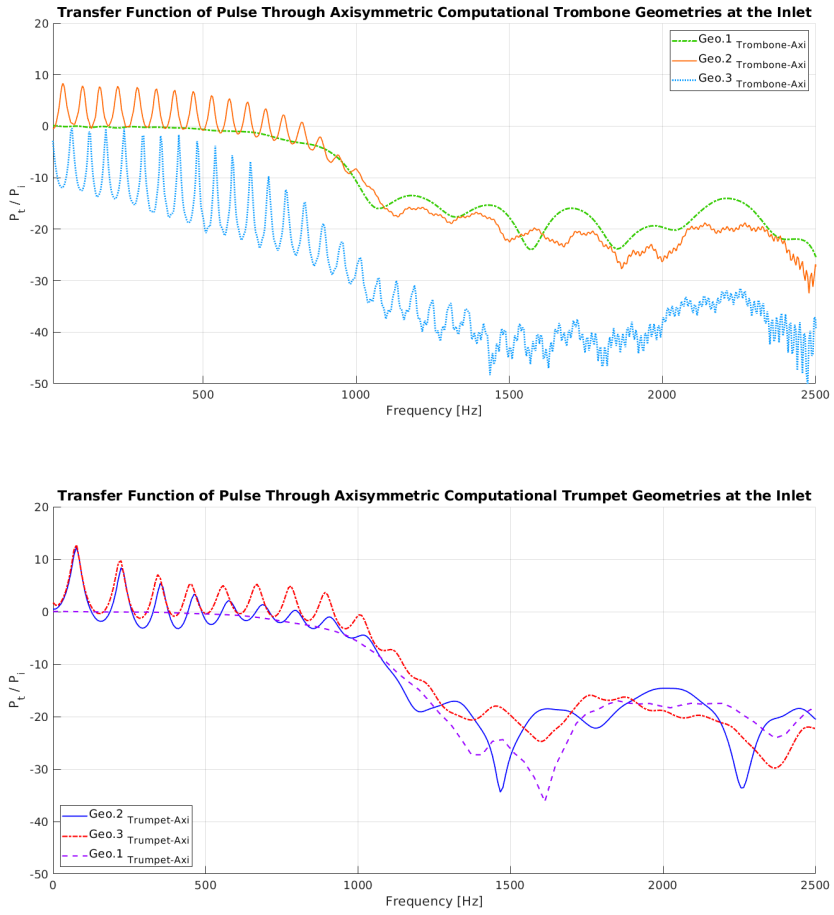

Figure 5.55: Computed $\frac{\mathcal{P}_i}{\mathcal{P}_r}$ function simulated pressure pulse obtained on Geo.1 $_{\text{Trombone-Axi}}$, Geo.2 $_{\text{Trombone-Axi}}$, Geo.2 $_{\text{Trombone-Axi-Cup}}$ (top) and Geo.1 $_{\text{Trumpet-Axi}}$, Geo.2 $_{\text{Trumpet-Axi}}$, Geo.3 $_{\text{Trumpet-Axi}}$ (bottom) discussed in Sections 5.8.1 and 5.8.2.

5.9 Numerical Verification of Spectral Enrichment

As discussed in [161], the bore of the instrument is the main factor to influence the timbre of a musical note. But, musicians can also control the level of brassiness by adjusting their embouchure and manipulating their lip tension, the angle of the instrument and hence, the angle that the lips couple to the bore. Experiments from [161] demonstrate that this gives the player the ability to adjust the rate of pressure that enters the instrument but without necessarily changing the maximum/minimum amplitude of the waveform. As a

consequence, the pressure wave will undergo a greater degree of wave steepening and thus, spectral enrichment. However, a wave can only steepen so much at certain playing levels. So even if a player can produce a 'brassier' p note for instance, this does not necessarily mean that a shock wave will be produced.

Upon analyzing the sound pressure measurements for various notes in Chapter 2, we were able to verify that increasing the playing level results in a brassier timbre. The literature states this is due to exciting the higher spectral components by 'the shifting the energy' from the lower to higher frequencies [38], [99]. Experimentally, this is very difficult to observe due to the nature of sound production in musical instruments [1]. Even if one musician is used for all experimental trials, exactly reproducing a note at the exact same volume is improbable [171], [190]. For this reason, we numerically investigate the outcomes due to spectral enrichment and how the harmonic distribution of a musical note is influenced.

5.9.1 Setup of Spectral Enrichment Simulations

The pressure waveform of a B_3^b played at f was prescribed at the inlet boundary for both Geo.3 $_{\text{Trumpet-3D}}$ and Geo.2 $_{\text{Trombone-3D}}$ as usual[40]. An additional simulation was run where the same musical note was considered but with only 10% of the original amplitude level. This ensured that the pressure amplitude would be sufficiently small so that the wave would not undergo steepening. Once the second numerical solution was obtained, the output was multiplied by ten, evaluated and then compared with the first simulation. We are not concerned here with how well the computed pressures sampled outside the bell matches the experimental data but rather, we are focused on the variation between the solutions for each instrument. For convenience, the simulations with the original pressure amplitude will be referred to as the *nonlinear simulation* or *nonlinear note*. The simulations that consider only 10% of the pressure level at the inlet will be called the *linear simulation* or *linear note*. Recall that the B_3^b trumpet note did not generate any shocks within the tubing but the B_3^b trombone note did.

5.9.2 Results Obtained for Spectral Enrichment Simulations

Reviewing the trumpet results (left of Figure 5.56), we observe a 3 dB difference in the SPLs between the linear and nonlinear simulations for components f_1, f_2 and f_3. Due to their

[40] These notes were previously used for numerical simulations discussed in Sections 5.5, 5.6, and 5.7 and the information for each of these computational instruments can be found in Table 5.3.

wavelengths, the majority of the sound energy is not transmitted from the bell. The f_4, f_5, f_6 and f_7 components match between the two numerical results. These frequencies are able to propagate further into the bell with little reflection, whereas the spectral components above this radiate from the flare without significant, if any, reflections. For the transmitted harmonics, we notice that the linear spectral curve quickly drops off in SPL compared to the nonlinear result. Thus, the consequences due to wave steepening are quite distinct. In particular, we clearly observe an emphasis toward the higher spectrum, which is how spectral enrichment is characterized in the literature (e.g., [20], [38], [167], [159], [99]).

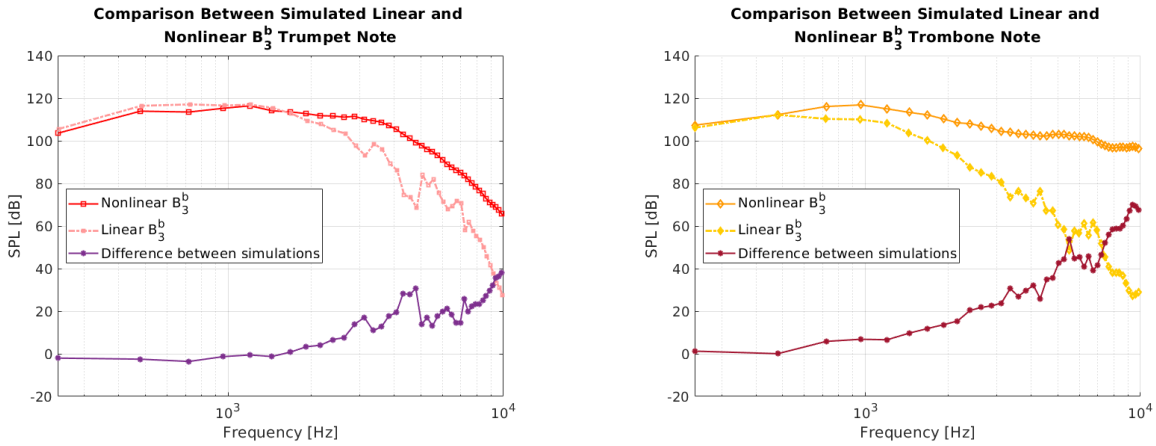

Figure 5.56: Comparison between measured and computed *linear* and *nonlinear* frequency spectra of the loudly played B_3^b trumpet (left) and trombone (right) notes simulated on Geo.3 $_{\text{Trumpet-3D}}$ and Geo.2 $_{\text{Trombone-3D}}$ (and discussed in Section 5.9).

Examining the trombone outcomes (right of Figure 5.56), we found that the SPLs below the cutoff frequency of the flare, i.e., f_1 and f_2, are equal. For f_3, f_4 and f_5, the linear result is approximately 6 dB lower than the nonlinear spectrum and then quickly drops off in amplitude (whereas the nonlinear spectrum remains relatively flat). Although the trombone outputs are similar to the trumpet's (in the sense that the linear solution decreases faster in SPL compared to the nonlinear result), the lowest spectral trombone components are equal[41]. The exact reason for this is a little unclear but we believe it illustrates the difference between the strength of nonlinear effects. In other words, our results demonstrate how the harmonic distribution of a sound wave is influenced when the

[41] There does not appear to be a redistribution of the energy content but rather, just further emphasis on the radiated components.

nonlinear behaviour leads to wave steepening, compared to when it is strong enough to form shock waves.

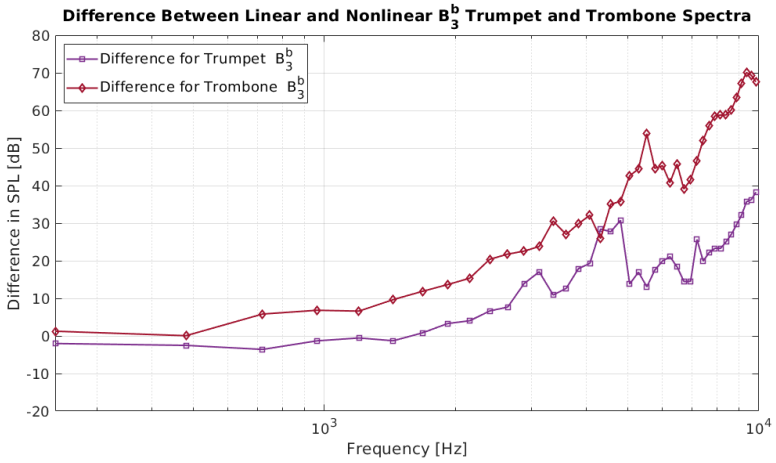

Figure 5.57: Spectral-difference curves between numerical *linear* and *nonlinear* outputs simulated on Geo.3 $_{\text{Trumpet-3D}}$ and Geo.2 $_{\text{Trombone-3D}}$ shown in Figure 5.56.

The difference between the linear and nonlinear numerical spectral outputs have been calculated and plotted for both the trumpet and trombone in Figure 5.57. Both spectral-difference curves show similar behaviour, but overall, the difference between the linear and nonlinear trombone outputs is larger than that of the trumpet. This numerical evidence gives further merit to the hypotheses discussed in Section 2.3.1 regarding the consequences of wave steepening and the production of shock waves. To our knowledge, similar numerical experiments have not been previously published.

5.10 Summary of Findings

In this chapter, several numerical investigations have been reviewed. Their purpose was to explore which aspects are most important to reproduce the timbre of a musical tone produced on a trumpet or trombone. In particular, our findings have indicated the following:

i. The computational domain behind the flare of the instrument does not need to be included for our purposes. We also determined that modelling the space directly in front of the bell as a cylinder minimizes the number of mesh elements while preserving the mesh quality.

ii. In this chapter and Chapter 2, we examined experimental, theoretical, and numerical evidence regarding the production of shock waves in the trumpet and trombone. At least for loudly played $B_3^\flat$ notes that we measured in the lab, shock waves were produced in the trombone but not in the trumpet. Numerical simulations confirmed this and also agreed with the theoretical approximation of x_s for the trombone.

iii. We numerically determined the cutoff frequency of the constructed computational trumpet and trombone flares. We found that our results agreed well with the ranges published in the literature and we interpret this to mean that the geometry is sufficiently modelled.

iv. The initial tubing near the mouthpiece-shank needs to be accurately modelled. In addition, properly modelling this section of the instrument is more important than including the bends or mouthpiece cup.

v. A 2D axisymmetric model is a reasonable simplification to make and slightly improves the numerical simulations (as the 2D computational domain better approximates the physical 3D domain).

vi. Numerical pulse reflectometry tests produced qualitatively similar outputs to equivalent physical experiments previously published in the literature. This served as a good verification test to see if our simulations were producing reasonable results.

vii. The consequences due to spectral enrichment were examined numerically thereby verifying claims made in the literature as well as the hypotheses put forward in Section 2.3.1.

Chapter 6

Examination of Boundary Conditions

For all the simulations presented in Chapter 5, sound waves were introduced into the computational domain by prescribing an inflow boundary condition. In this chapter, we will review the choices made in Section 5.3 and examine how reasonable our assumptions were. For the remaining numerical simulations that will be discussed in this thesis, the axisymmetric model will be used. Hence, the simulations will be run on either Geo.3 $_{\text{Trumpet}}$ or Geo.2 $_{\text{Trombone}}$ shown in Figure 5.46. The information about these 2D computational instruments can be found in Table 5.6.

6.1 Inlet Boundary Condition

One approach to define the inflow boundary condition is to prescribe it with respect to acoustic pressure. This would allow us to use the experimental data, p_{exp} (from Chapter 2) as an input for the simulations. The density can then be related to p_{exp} using the adiabatic relation. However, properly prescribing the velocity is not so easy.

In an ideal situation, the acoustic velocity would have been measured simultaneously along with the pressure at the mouthpiece-shank. Unfortunately, almost no such data exists due to the technical difficulty involved in carrying out such an experiment. The only studies we found with such data were in [47] and [54]. In [54], Elliot and Browsher used hot-wire anemometry to measure the particle velocity in the mouthpiece throat of the trumpet and trombone for notes played around *mf* - *f*[1]. The issue with hot-wires is that

[1] This method uses a very thin wire (usually around 5μm) where each end is connected to an electric device via a needle. The device supplies a heating current to a sensor that is convectively cooled as the air passes it. In taking temperature measurements, the speed of the airflow can be obtained [54].

they are very fragile, can be difficult to calibrate and ultimately, their presence influences the flow as the wire and sensor would be placed in the center of the tube. Elliot *et al* also measured pressure along with velocity and found that regardless of the octave, both displayed very similar behaviour. The authors concluded that "*the same mechanisms must be at work in the various frequency ranges in each case*" [54]. Cullen instead used laser Doppler anemometry (LDA), which has better resolution, is less intrusive and is generally more accurate[2]. However, the best results were obtained for notes where the SPL was around 105 dB - 140 dB. Cullen found however that the velocity profiles were rather noisy, even after applying filters[3] and attributed this to turbulence. For this thesis, accurate velocity measurements could not be obtained with the available equipment. The velocity therefore needs to be approximated and written as a function of p_{exp}.

6.1.1 Bernoulli's Equation

The standard approach taken in the literature to describe the pressure-velocity relationship is by using Bernoulli's equation (e.g., [1], [31], [47], [69], [168], [171]), which at any arbitrary point along a streamline is

$$\frac{1}{2}u^2 + gh + \frac{p}{\rho} = \text{constant}, \tag{6.1}$$

where u is the fluid flow speed, g is the acceleration due to gravity, h is the height above a reference plane, p is pressure, and ρ is the density of the fluid. Relating the flow properties to the pressure in this manner assumes the flow through the lips is incompressible, frictionless and quasi-stationary [47]. The justification in the literature for this choice is that when a musician is producing a note, the lungs serve as a source of constant pressure. It is then argued that the alternating flow through the lip opening produces a time varying Bernoulli pressure that forces the lips to move. Additionally, it is assumed that the flow depends on the area of the lip opening, but not the lip speed, and is time independent. The volume flow can then be expressed as

$$U = \sqrt{\frac{2\Delta p}{\Delta \rho}}\ell h, \tag{6.2}$$

[2] The idea behind LDA is utilizing the Doppler shift of a laser beam to measure the velocity. In particular, if a particle crosses the path of the laser, it scatters the light with a frequency shift that is measured. The velocity of the particle can then be determined from the Doppler shift of the frequency of the laser beam [47].

[3] The author stated this was due to "*the turbulent intensity tended to increase with the velocity of the air flow*" [47].

where ℓ is the length of the lip opening and h is the height (i.e., how much the lips separate). The velocity of the flow is then defined by

$$u = \sqrt{\frac{2\Delta p}{\Delta \rho}}, \tag{6.3}$$

and the inflow boundary condition is

$$U = \begin{cases} p & = p_{\,\text{exp}}, \\ \rho & = \gamma p^{\frac{1}{\gamma}}, \\ u & = \sqrt{\frac{2\Delta p}{\Delta \rho}}, \\ v & = 0, \\ w & = 0, \end{cases} \tag{6.4}$$

However, compressibility effects cannot be neglected, especially in this region. For the trumpet in particular, the shape of the tubing from the mouthpiece cup to the mouthpiece-shank is a converging-diverging channel (also known as a Ventari-nozzle). This means the Mach number will increase as the flow travels toward the throat. Some researchers claim that the flow even becomes turbulent in this region[4], e.g., [20], [47], [55], [86], [159], [167]. Recently, Giordano published a thorough analysis investigating when it is appropriate to use Bernoulli's equation to relate the pressure and velocity flow. From his experimental and numerical work [83], he concluded that this relationship "*fails significantly*" in most situations such as during much of the lip oscillation cycle. The only situation where Giordano found Bernoulli's equation to be reasonably accurate was when the lips were fully open, and this only accounts for a small portion of the oscillation period.

6.1.2 Planar Relationship

Due to the findings in [83], a more qualitatively accurate way to relate pressure and velocity near the entrance of the instrument is required. We know from the experimental data published in [54] that the pressure and velocity waveform profiles should be similar in shape. Since the majority of the bore before the flare is cylindrical, the flow will mainly be

[4] The author of [47] states that the jet of air travels into the bore expanding and creating a turbulent flow where the turbulent dissipation of kinetic energy implies that there is no pressure recovery across the turbulent region. However, further down the mouthpiece, they assume the velocity is uniform throughout the entire cross-section of the bore.

in the horizontal direction. As discussed in Chapter 5, for a 1D planar wave $p = p_0 + \rho_0 c_0 u$. Setting $p = p_{\text{exp}}$, the velocity in the horizontal direction would be defined as

$$u = \frac{p_{\text{exp}} - p_0}{\rho_0 c_0}.$$

This approximation has also been used in the literature (e.g., [24], [111], [184], [188]) and gives the inflow boundary condition (5.10). However, this too is an idealization of the pressure-velocity relationship, but at least reproduces p_{exp} at the mouthpiece boundary.

6.1.3 Riemann Invariants

Since we are solving the Euler equations, the inflow condition could be prescribed with respect to characteristic curves, which has also been considered in the literature (e.g., [90]). This approximation relies on the flow being *homentropic*, i.e., the entropy, denoted by S, is spatially uniform and $S = S_0$. In such a case,

$$p = k\rho^{\gamma}, \tag{6.5}$$

where $k = \kappa e^{\frac{S_0}{c_v}} = \text{constant}$. The conservation of mass and momentum laws can then be expressed as

$$\frac{\partial \rho}{\partial t} + \vec{v} \cdot (\rho \vec{v}) = 0,$$
$$\frac{\partial \vec{v}}{\partial t} + \vec{v} \cdot \nabla \vec{v} + k\gamma\rho^{(\gamma-2)} \nabla \rho = 0.$$

Considering the flow to be 1D for convenience, the equations are expressed as

$$\frac{\partial \rho}{\partial t} + \frac{\partial}{\partial x}(\rho u) = 0, \tag{6.6}$$
$$\frac{\partial u}{\partial t} + u\frac{\partial u}{\partial x} + k\gamma\rho^{(\gamma-2)}\frac{\partial \rho}{\partial x} = 0. \tag{6.7}$$

The easiest way to construct characteristic curves for this system is to write (6.6) and (6.7) in terms of u, and the local sound speed, c, i.e.,

$$c = \sqrt{\left(\frac{\partial p}{\partial \rho}\right)_S} = \sqrt{k\gamma\rho^{(\gamma-1)}} \implies \rho = \left(\frac{c^2}{k\gamma}\right)^{\frac{1}{\gamma-1}}.$$

Once (6.6) and (6.7) are written this way, they can be subtracted to obtain[5]

$$\frac{\partial}{\partial t}\left(u \pm \frac{2c}{\gamma - 1}\right) + (u \pm c)\frac{\partial}{\partial x}\left(u \pm \frac{2c}{\gamma - 1}\right) = 0.$$

The functions defined by

$$\mathcal{R}_{\pm}(u, c) = u \pm \frac{2c}{\gamma - 1}$$

are called the *Riemann invariants* of the system and are constant on the two sets of characteristic curves[6] [29], [164]

$$\mathcal{C}_{\pm} = \frac{dX_{\pm}}{dt} = u \pm c.$$

In our case, the type of flow we are considering at the inlet is subsonic,[7] and to obtain the Riemann invariant boundary condition (RIBC), we consider the computational domain depicted in Figure 6.1. The inner portion of the computational domain (i.e., the right hand side) is referred to as the *interior state*, denoted by $\mathcal{I}$. Outside the computational domain is the *physical state*, denoted by $\mathcal{O}$. The Riemann invariant $\mathcal{R}_{-}$ corresponds to $\mathcal{I}$, and $\mathcal{R}_{+}$ corresponds to $\mathcal{O}$. The interior, exterior, and interface of these two states must be physically consistent for the wave propagation to transport information in-between $\mathcal{I}$ and $\mathcal{O}$ to achieve a steady state. Thus, to evaluate the flux at a boundary, information within $\mathcal{I}$ combines with the problem's physical constraints.

The primitive variables are the pressure (p), density (ρ), and velocity (u)[8]. The variables within the interior state will be denoted with subscript i; whereas at the boundary, the variables will have the subscript b. Within the computational instrument, p_i, ρ_i and u_i will be determined from the PDE system. At the boundary, we have that $p_b = p_{\text{exp}}$, which also gives ρ_b. However, u_b is unknown.

The two families of characteristic curves physically represent left and right moving waves. At the inlet where the flow is subsonic, the waves travelling at u and $(u + c)$ are

[5] See Appendix D.6 for a complete derivation.

[6] Given an initial value problem, for the solution to be well-defined, a single $\mathcal{C}_{+}$ and $\mathcal{C}_{-}$ characteristic must pass through each point in the domain of the solution. The values of u and ρ at each point can then be determined from the initial values of $\mathcal{R}_{\pm}$ on each characteristic.

[7] This implies that the $\mathcal{C}_{-}$ characteristic has a negative slope and information from inside the domain reaches the boundary along $\mathcal{C}_{-}$. So, no boundary condition associated with $\mathcal{C}_{-}$ can be fixed arbitrarily. A subsonic outlet boundary condition also has the $\mathcal{C}_{-}$ characteristic with a negative slope implying one BC would be fixed [164].

[8] At the mouthpiece boundary, we are really only have u since $v = w = 0$ in our situation.

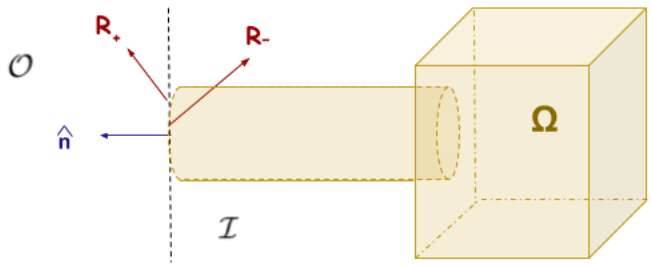

Figure 6.1: Interface of computational boundary to derived the RIBC.

entering the interior, but the wave travelling at $(u-c)$ is not, as illustrated in Figure 5.1. Thus, u, p or ρ will be determined by $\mathcal{R}_-$ and transported at velocity $(u-c)$ along $\mathcal{C}_-$. This implies that

$$\begin{aligned} u_b - \frac{2c_b}{\gamma-1} &= u_i - \frac{2c_i}{\gamma-1}, \\ u_b &= u_i + \frac{2}{\gamma-1}\left(c_b - c_i\right), \end{aligned} \tag{6.8}$$

where

$$c_b = \sqrt{\frac{\gamma p_b}{\rho_b}}, \qquad c_i = \sqrt{\frac{\gamma p_i}{\rho_i}}.$$

Hence, the flow is entering the bore, $\mathcal{C}_0$, and $\mathcal{C}_+$ are travelling into the tube, whereas $\mathcal{C}_-$ is propagating out, i.e.,

$$\text{Inflow BC for } \mathcal{I}: \begin{cases} p_b &= p_{\text{exp}}, \\ \rho_b &= \gamma p_b^{\frac{1}{\gamma}}, \\ c_b &= \sqrt{\frac{\gamma p_b}{\rho_b}}, \\ u_b &= u_i + \frac{2}{(\gamma-1)}(c_b - c_i n), \\ v_b &= v_i, \\ w_b &= w_i, \end{cases}$$

For the outflow, $\mathcal{C}_0$ and $\mathcal{C}_+$ travel in the reverse direction, i.e., there is an outflow from the

mouthpiece boundary. In this case, we have

$$\text{Inflow BC for } \mathcal{O}: \begin{cases} p_b &= p_{\text{exp}}, \\ \rho_b &= \gamma p_b^{\frac{1}{\gamma}}, \\ c_b &= \sqrt{\frac{\gamma p_b}{\rho_b}}, \\ u_b &= u_i, \\ v_b &= v_i, \\ w_b &= w_i, \end{cases}$$

However, a slight modification can be made so that the physical state is more consistent with the acoustics. In particular, instead of setting $\vec{u}_b = \vec{u}_i$ at the mouthpiece boundary itself, we set $\vec{u}_b = \vec{0}$. This choice is more aligned with previous findings such as the measured velocity profiles from [47] and [54], which are always positive. Physically, this makes sense because when a musician produces a steady note, the airflow is consistently moving from the lungs, into the mouthpiece and then, into the bore of the instrument. When a player takes a breath, the coupling of the lips with the instrument is momentarily broken[9]. In addition, it has been argued by some (e.g., [16], [90]) that the coupling between the backward and forward propagating nonlinear waves are weak, and the forward moving waves are most important. In particular, Bednarik states in [16], that "*the relative weakness of the nonlinear processes allows us to suppose that wave profiles of the counter-propagating waves vary slowly with time and propagation distance.*" The ghost state for the RIBC can then be defined as

$$U_{\text{right}} = \begin{cases} \rho_b, \\ u_b \rho_b, \\ v_b \rho_b, \\ w_b \rho_b, \\ \frac{p_b}{\gamma - 1} + \frac{\rho_b}{2}\left(u_b^2 + v_b^2 + w_b^2\right). \end{cases} \tag{6.9}$$

6.2 Numerical Test Case Using the Different BCs

To compare the different boundary conditions used in the literature, we simulated a loudly played B_3^b on Geo.3 $_{\text{Trumpet}}$ and Geo.2 $_{\text{Trombone}}$ using the inflow conditions (6.4), (5.10) and (6.9). The numerical results were sampled at Mic $_{\text{Outside-Bell}}$ and plotted against the experimental data (Figures 6.2 and 6.3). When prescribing (6.4), i.e., the BC with Bernoulli's

[9] Air would only travel back into the mouth if the player took a breath through the instrument, which is not how one breathes when playing a brass instrument.

equation, we obtained the most deviation between the numerical and experimental data (which is in agreement with [83]). We see from comparing the results in the time-domain (Figure 6.3), that the numerical pressure amplitude is severely underestimated for both instruments, especially the computational trombone. This implies that the effects due to spectral enrichment will not be well modelled, as clearly seen in the spectral curves (Figure 6.2).

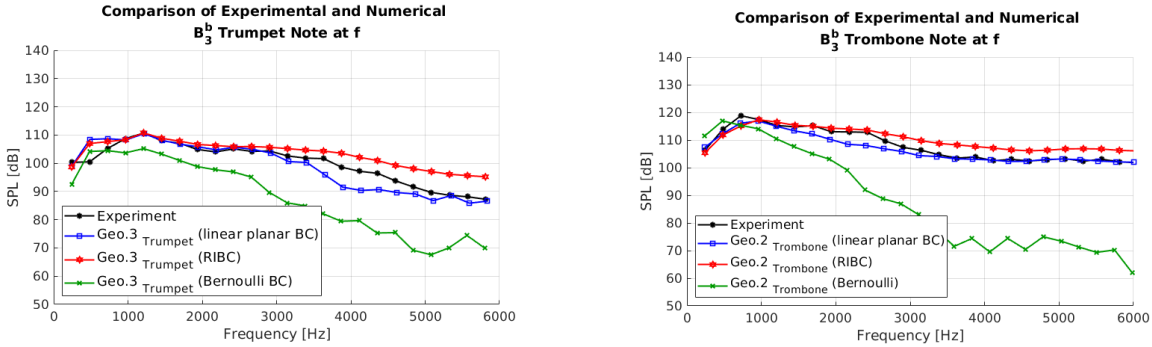

Figure 6.2: A comparison between the experimental and numerical spectra for the loudly played B_3^b on the trumpet (left) and trombone (right) when the different boundary conditions were used.

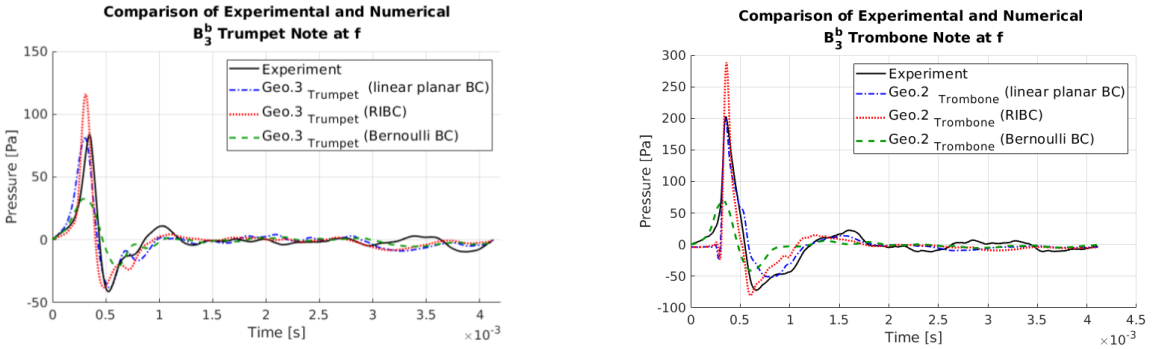

Figure 6.3: A comparison between the experimental and numerical pressure waveforms for the loudly played B_3^b on the trumpet (left) and trombone (right) when the different boundary conditions were used.

When using either the planar relationship (5.10) or the Riemann invariants (6.9) to define the inflow boundary conditions, the wave propagation was better modelled in Geo.3 $_{\text{Trumpet}}$

and Geo.2 $_{\text{Trombone}}$. Furthermore, both boundary conditions produced relatively similar results. For instance, for the spectral components less that 3000 Hz and 1500 Hz for the computational trumpet and trombone, respectively, the SPLs closely align (Figure 6.2). For Geo.3 $_{\text{Trumpet}}$ however, we notice there is less deviation from the measured spectrum when the RIBC was used. For the higher harmonic components, (5.10) yields a good match with the experimental spectrum corresponding to the B_3^b trombone note. However, in-between 1500 Hz - 3000 Hz, the simulation underestimates the experimental SPLs. When (5.10) was used for the computational trumpet, the SPLs for frequencies in-between 3500 Hz - 5000 Hz were also underestimated. Conversely, when prescribing (6.9) on Geo.2 $_{\text{Trombone}}$, the computed spectrum matches the experiment for frequencies 1500 Hz - 2500 Hz. Above this however, the numerical result overestimates the experimental spectrum. For the computational trumpet, the RIBCs also overestimates the SPLs for components greater than 3300 Hz, where the deviation increases slightly with frequency.

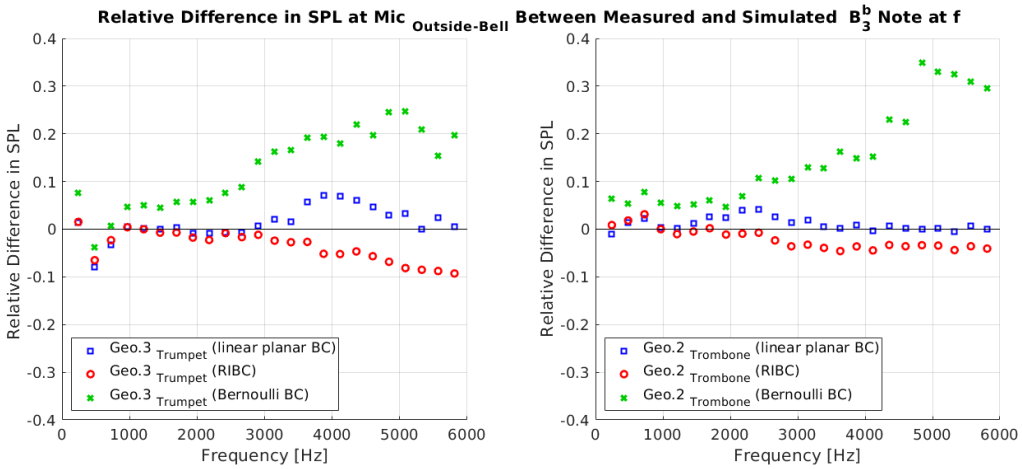

Figure 6.4: Relative difference in SPL between measured and simulated B_3^b notes shown in Figure 6.2 sampled at Mic $_{\text{Outside-Bell}}$ for the trumpet (left) and trombone (right).

The relative difference between the experimental spectrum and numerical solutions are plotted in Figure 6.4. We observe that (5.10), i.e., the planar BC, best models the B_3^b notes, especially when played on the trombone. The RIBC, i.e., (6.9), seems to be best suited for the computational trumpet. This seems reasonable, as the initial tubing geometry of the trumpet is more complex than the trombone.

6.3 Numerical Simulations of Realistic Musical Notes

In Section 6.2, simulations of the loudly played B_3^b were run on the computational trumpet and trombone to compare the validity of the different inflow boundary conditions. Between the three boundary conditions that were tested, the numerical simulations matched the experimental data most when the planar relationship between pressure and velocity was used. Although this locally assumes linearity, everywhere else in the computational domain, the pressure and velocity were determined by the PDE system. Some have suggested in the literature that this is a reasonable approximation [110], [141], [179].

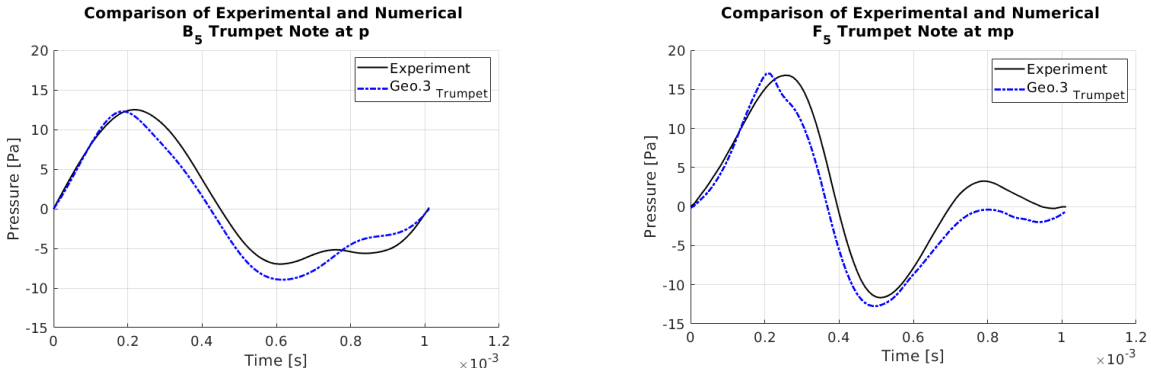

Figure 6.5: A comparison between the experimental and computed pressure for the B_5 and F_5 played at p and mp on Geo.3 $_{\text{Trumpet}}$ when the planar inflow boundary condition was used.

To further test the robustness of this boundary condition, several other musical notes were simulated on Geo.3 $_{\text{Trumpet}}$ and Geo.2 $_{\text{Trombone}}$ and then compared against the measured data at Mic $_{\text{Outside-Bell}}$. On Geo.3 $_{\text{Trumpet}}$ for instance, a B_5 and F_5 played at p and mp, respectively, were considered. As displayed in Figure 6.5, we obtained that the measured and computed pressure in the time-domain aligns reasonably well. Although losses were not modelled, we do not observe detrimental discrepancies between the measured and simulated pressure amplitudes. To test if this also holds true for the computational trombone, a B_3^b played at mp was simulated on Geo.2 $_{\text{Trombone}}$. The computed and measured spectral curves for these quiet trumpet and trombone notes are plotted in Figures 6.6 and 6.7. For the mp trombone note, the SPLs corresponding to $f_1 - f_6$ (i.e., less than 1500 Hz) match the experimental data[10]. For the mp F_5 trumpet note, with the exception of a slight

[10] These components are most important since the higher harmonics appear to contain mostly noise. We therefore dismiss this portion of the spectrum.

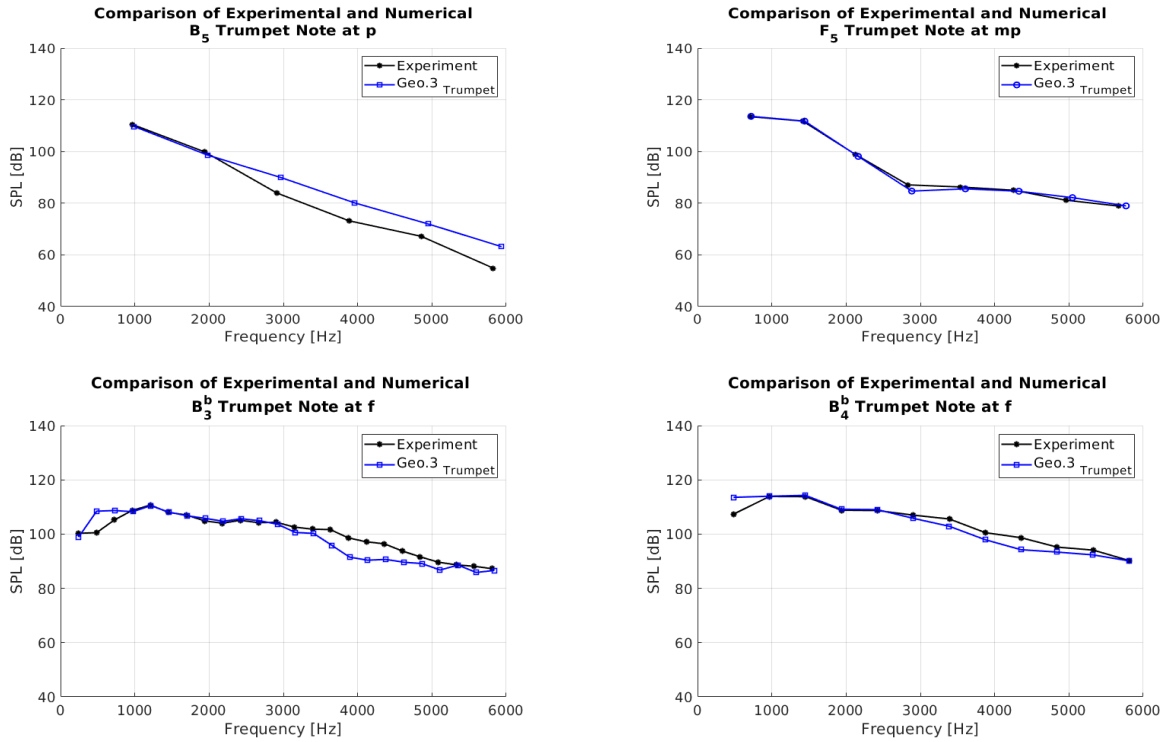

Figure 6.6: A comparison between the experimental and computed frequency spectra of the B_5 played at p (top-left), F_5 played at mp (top-right), B_3^b played at f (bottom-left) and B_4^b played at f (bottom-right) simulated on Geo.3 $_{\text{Trumpet}}$ when the planar inflow boundary condition was used.

deviation in the SPL associated with f_4, all numerical components match the experimental SPLs. As for the B_5 trumpet note at p, the f_1 and f_2 frequencies (i.e., less than 2000 Hz) match the measured spectrum. For tones of this playing dynamic, recall that only the first couple harmonics characterize the timbre [37]. Thus for both instruments, the timbre associated with p or mp notes is well modelled.

To evaluate whether brassy timbres could be reproduced, several f notes were also simulated on Geo.3 $_{\text{Trumpet}}$ and Geo.2 $_{\text{Trombone}}$. The computed spectra are again plotted against the experimental spectral curves (Figures 6.6 and 6.7). For both the trumpet and trombone, the B_3^b and B_4^b played at f were considered. For the computational trombone, these simulated notes match the measured data exceptionally well for all frequencies below 2800 Hz. A lower, louder pitch, the F_3^b played at ff, was also simulated on Geo.2 $_{\text{Trombone}}$.

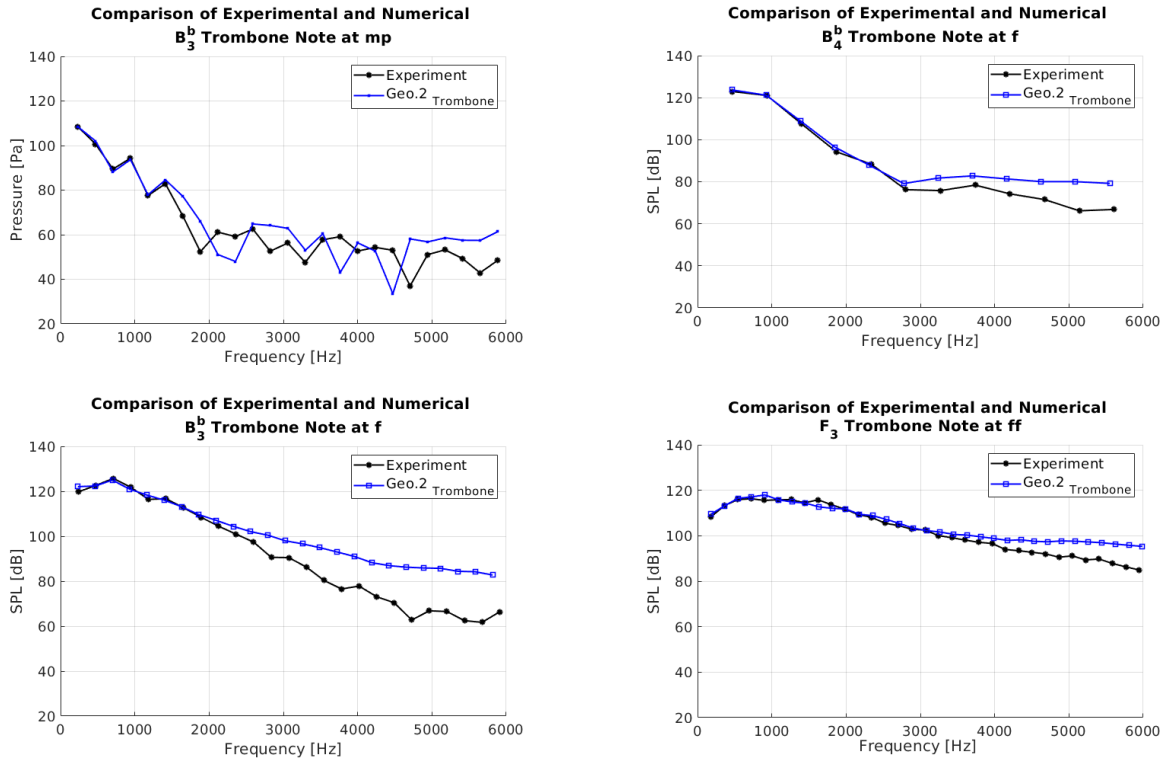

Figure 6.7: A comparison between the experimental and computed frequency spectra of the B_3^b played at *mp* (top-left), B_4^b played at f (top-right), B_3^b played at f (bottom-left) and F_3 played at *ff* (bottom-right) simulated on Geo.2 $_{\text{Trombone}}$ when the planar inflow boundary condition was used.

In this case, we obtained even better results for frequencies up to 4000 Hz. With respect to the f trumpet notes, we obtained reasonable qualitative agreement with the experiment for SPLs in-between 900 Hz - 3200 Hz, and greater than 5000 Hz. However, for the B_4^b, f_1 was overestimated by 6 dB. This frequency corresponds to the f_2 for the B_3^b, which was also 6 dB too high (the f_3 of the B_3^b spectrum was also off by +2 dB). However, for both trumpet notes, harmonics approximately in-between 3200 Hz - 5000 Hz are underestimated by the model.

6.4 The Relationship Between Pressure and Velocity

All simulations thus far have been based on a homogeneous system which introduces sound into the computational instrument via an inflow boundary condition (where $p = p(u)$). However, once the reflected waves from the bell travel back to the mouthpiece boundary, a new steady state will form. This will influence the other pressure fields and ultimately, alter the numerical solution. In a real brass instrument, the sound pressure waveform that forms within the instrument is a result of a volume velocity source, i.e., the pressure measured within an instrument is the result of the acoustic velocity. Thus, another way to generate a sound field is by defining a source term at the entrance of the bore.

Mathematically, sound sources correspond to the right hand side of the equations of motion being nonzero. This implies that conservation does not hold, e.g., mass is injected into the system[11] or a force is exerted on the acoustic material[12]. The mass source and exerted force will be denoted as $Q(t)$ and $F(t)$, respectively. The creation of mass per unit volume is associated with the continuity equation, and when a sound field is driven by the volume occupied by the injected mass, it takes work. Hence, a term on the right hand side of the energy equation is needed if a mass source is to be considered. In particular, the rate of change of energy will correspond to the rate at which the product of atmospheric pressure and volume changes. This means that the right hand side of the energy equation would be the product of atmospheric pressure and $Q(t)$[13]. Comparatively, the force $F(t)$ is associated with the momentum equation, and if a force is put upon a fluid, a pressure dipole wave is generated.

6.4.1 Alternative Approach using a Source Term

Let's consider the problem more carefully. When a player produces a note, they introduce periodic puffs of air, i.e., mass, into the system at a certain rate of kg/s. The lips exhibit oscillatory motion which creates an oscillatory pressure disturbance. From a modelling perspective, this means that optimally, a moving boundary would be considered at the

[11] This type of acoustic source creates matter, i.e., motionless mass, creating more material at p_{atm} with no drift velocity.

[12] This is the other type of acoustic source which forces matter to move.

[13] That is, if V denotes volume, then

$$\frac{dE}{dt} = \frac{d(pV)}{dt} = p_{\text{atm}} \frac{dV}{dt} = p_{\text{atm}} Q(t).$$

inlet of the computational instrument. However, this is difficult to deal with numerically. Instead, we can approximate a moving boundary by considering a source within a small region near the mouthpiece boundary and then, at the boundary itself, a solid-wall condition can be prescribed. At the mouthpiece, we require the total velocity, which would be written as

$$u_{\text{total}} = u_{\text{specified}} + u_{\text{reflection}}. \tag{6.10}$$

Numerically speaking, if we continuously introduce mass into the computational instrument (via the continuity equation), the PDE system should produce a corresponding acoustic velocity and pressure that eventually, will settle into a steady state. Pressure and velocity could then be obtained at any position along the instrument. This provides a way to determine the velocity profile at the inlet which induces the p_{exp} waveform measured at Mic $_{\text{Mouthpiece}}$.

Whether a source term or an inflow boundary condition is used to introduce sound into the computational domain, if they are physically representative of the system, they should function in a similar manner. However, although it is true that a sound field produced by a sound source is unique, a source cannot be described with certainty from a measured sound field. In other words, regardless of the equipment used, analyzing the structure of a sound source by examining the associated sound field cannot be done reliably [53][14]. Therefore, we first seek to validate the previous approach of using an inflow boundary condition rather than a source term.

6.4.2 Justification of the Inflow Boundary Condition

A small amplitude acoustic pulse was simulated through the computational trumpet[15] in two different ways. The first method prescribed a pressure pulse as an inflow boundary condition (this numerical result was already presented in Section 5.8.1). The second approach used a mass source term to inject a puff of air into the instrument to create an acoustic pressure pulse. For this numerical test to be physically valid however, the relationship between pressure and velocity is required to prescribe the inflow boundary condition properly. If the bore prior to the bell of the computational instrument is uniform, then the relationship is known, i.e., $p = p_0 + \rho_0 c u$. Therefore, the Geo.1 $_{\text{Trumpet}}$ geometry was used for the numerical test.

As seen in Figure 6.8 (left), the computed pressure and velocity in the horizontal direction midway through Geo.1 $_{\text{Trumpet}}$ are equivalent for both simulations. We observe

[14] A mathematical example demonstrating this can be found in [53].

[15] Since the trumpet is shorter, this numerical test was only done for the trumpet.

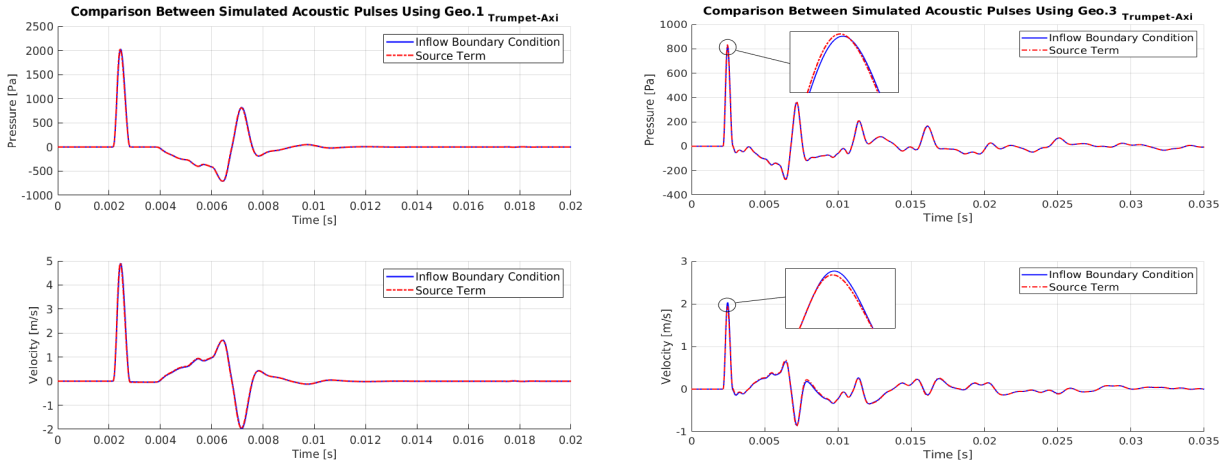

Figure 6.8: Computed impulse response curves sampled midway through Geo.1 $_{\text{Trumpet}}$ (left) and Geo.3 $_{\text{Trumpet}}$ (right) when generating a pulse at the inlet of the computational trumpet using an inflow boundary condition and a mass source term.

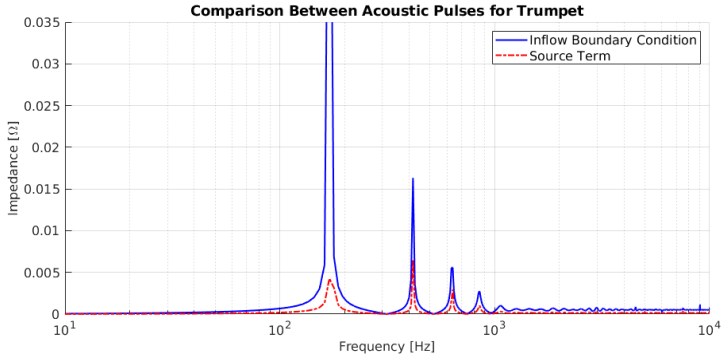

Figure 6.9: Numerical impedance corresponding to the Geo.3 $_{\text{Trumpet}}$ pulse simulations shown in Figure 6.8.

the incident pulse at $t = 0.002$ s and the reflections from the bell can be seen near $t = 0.004$ s[16]. These pulse simulations were repeated on the Geo.3 $_{\text{Trumpet}}$ (right of Figure 6.8) to investigate whether the outcomes would greatly differ. As expected, the reflection sequence is much longer but overall, the numerical solutions are rather similar. The main difference between them is a slight variation in the peak values. This difference would correspond to

[16] The character of the pressure and velocity are similar, which agrees with the observations made in [54] and [47].

the source term simulation having lower impedance peaks (computed impedance plots are shown in Figure 6.9).

Therefore, from a mathematical perspective, the approach outlined in Section 6.1 (i.e., using an inflow boundary condition) is consistent[17]. However, the problem still remains, for nonlinear waves propagating through a nonuniform bore, the precise relationship between the pressure and velocity is unknown. In addition, from an acoustic perspective, it is the velocity that is supposed to impose a pressure, i.e., $p = p(u)$, rather than $u = u(p)$. As alluded to in Section 6.4.1, we will now outline a procedure that theoretically, could be used to determine an approximate functional form of the velocity needed at the inlet to generate p_{exp} at Mic $_{\text{Mouthpiece}}$. We will refer to this procedure as the *T-Method*.

6.4.3 The Theoretical Setup of the T-Method

For the T-Method to work, the computational instruments Geo.3 $_{\text{Trumpet}}$ and Geo.2 $_{\text{Trombone}}$ need to be extended at the inlet. Instead of the computational domains beginning in the shaded region originally shown in Figures 5.14 and 5.15, the throat of the mouthpieces were also included. For the trumpet and trombone, this corresponds to the computational domains beginning 1.5 cm and 2.25 cm from the mouthpiece cup entrance. With this in mind, we will consider the setup of the T-Method as illustrated in Figure 6.10 by first defining the necessary variables.

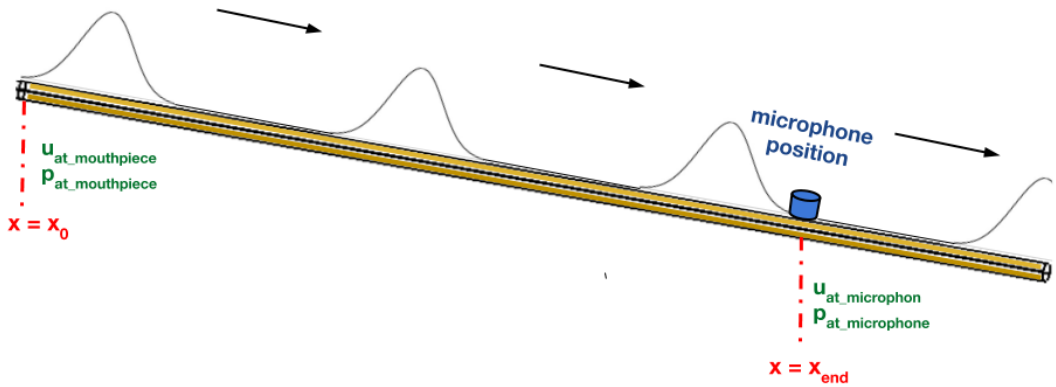

Figure 6.10: A diagram illustrating the setup of the T-Method.

[17] This agrees with previous claims made stating that the "*behaviour expected of velocity-controlled nonlinear oscillators are very similar to that of pressure controlled instruments*" [17].

Let x denote the length of the bore where $x = 0$ corresponds to the entrance of each computational bore, and $x = x_{\text{end}}$ be the location where the microphone was mounted, i.e., the Mic $_{\text{Mouthpiece}}$ position. Let $p_{\text{exp}}(t)$ denote the experimental time pressure waveform measured at Mic $_{\text{Mouthpiece}}$, where the fundamental frequency of the tone is f_0. We consider a continuously generated unipolar pulse, denoted by $Q_{\text{inlet}}(t)$, at the inlet of the computational instrument that repeats every $\frac{1}{f}$ s. The width of the pulse itself is one sixth the wavelength of f[18]. This produces a velocity profile at the inlet, denoted by $u_{\text{inlet}}(t)$, as well as a pressure wave that can be sampled at the microphone position of the computational instruments. The computed pressure wave at Mic $_{\text{Mouthpiece}}$ will be denoted as $p_{\text{sim}}(t)$.

We want $u_{\text{inlet}}(t)$ to produce $p_{\text{exp}}(t)$ at the microphone position. To find the proper form of $u_{\text{inlet}}(t)$, we will assume the following:

1. Linearity holds between the inlet position and the first microphone position. This is a relatively short distance, so there is not 'enough length' for any disturbances to undergo wave steepening.

2. Pressure and velocity can be written as sums of sinusoidal waves, i.e.,

$$p = \sum_{i=1}^{\frac{f_s}{2}} A_i \cos\left(2\pi f_i t + \phi_i\right), \tag{6.11}$$

$$u = \sum_{i=1}^{\frac{f_s}{2}} B_i \cos\left(2\pi f_i t + \psi_i\right), \tag{6.12}$$

   where N is the number of points in the period, and $\frac{f_s}{2}$ is the Nyquist frequency.

3. By linearity, for each frequency component i, pressure and velocity (even at different locations) are related by a constant. More precisely, if $\mathcal{P} = \texttt{fft}(p(t))$, $\mathcal{U} = \texttt{fft}(u(t))$ and $\mathcal{T} \in \mathbb{C}$, we have that

$$\mathcal{P}_{\text{at-microphone}} = \mathcal{T}\,\mathcal{U}_{\text{at-inlet}}. \tag{6.13}$$

Under these assumptions, we now obtain two equations

$$\mathcal{P}_{\text{sim}} = \mathcal{T}\,\mathcal{U}_{\text{inlet-sim}} \tag{6.14}$$

$$\mathcal{P}_{\text{exp}} = \mathcal{T}\,\mathcal{U}_{\text{inlet-actual}}. \tag{6.15}$$

[18] Since our measurements were taken while the instrument was being played by a musician, we used a periodic pulse. However, a single unipolar pulse or wide-band pulse could also be implemented, which is better for the "filled-in" transfer function.

From equation (6.14) we have

$$\mathcal{T} = \frac{\mathcal{P}_{\text{sim}}}{\mathcal{U}_{\text{inlet-sim}}}, \tag{6.16}$$

and from (6.15),

$$\mathcal{U}_{\text{inlet-actual}} = \frac{\mathcal{P}_{\text{exp}}}{\mathcal{T}}. \tag{6.17}$$

Substituting equation (6.16) into (6.17), we obtain the derived velocity expression in the time-domain

$$u_{\text{derived}} = \texttt{ifft}(\mathcal{U}_{\text{inlet-actual}}). \tag{6.18}$$

6.4.3.1 An Example Determining the Pressure and Velocity Profiles of the B_3^b

For both the computational trumpet and trombone, a continuous unipolar pulse with $f = 242$ Hz was generated at the inlet. This resulted in an acoustic pressure that built up until a steady, standing wave pattern was achieved. A computational acoustic velocity profile was also obtained. These wave profiles sampled by the inlet and at Mic $_{\text{Mouthpiece}}$ are shown in Figure 6.11.

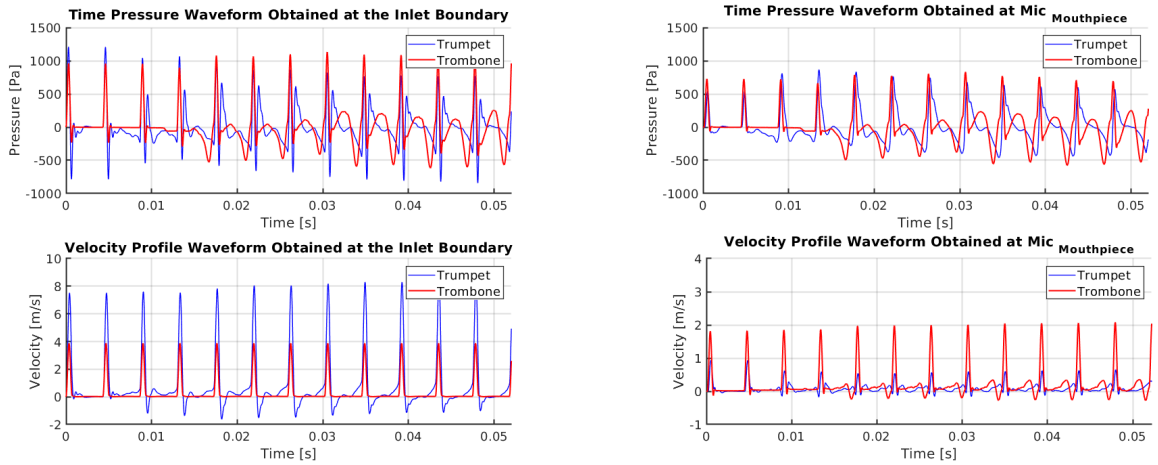

Figure 6.11: Computed pressure and velocity results obtained from simulating a periodic pulse source term through the computational trumpet and trombone at the inlet (left) and at Mic $_{\text{Mouthpiece}}$ (right).

The output of the simulation then allows us to find the relationship between the acoustic velocity and pressure at any point in the computational instrument, as modelled by the

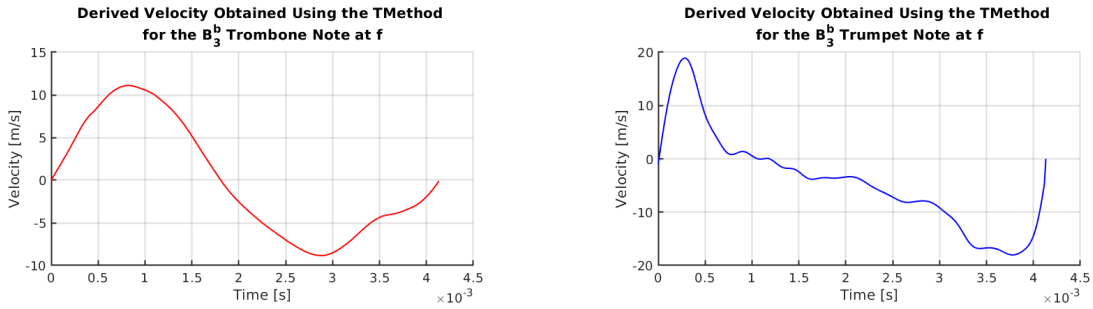

Figure 6.12: The derived velocity (obtained from using the T-Method) required at the inlet of the trombone (left) and trumpet (right) to produce the loudly played B_3^b at Mic $_{\text{Mouthpiece}}$.

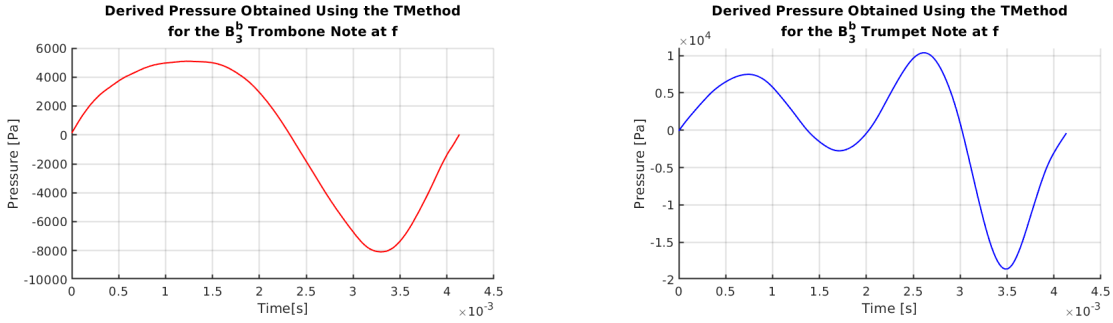

Figure 6.13: The derived pressure (obtained from using the T-Method) required at the inlet of the trombone (left) and trumpet (right) to produce the loudly played B_3^b at Mic $_{\text{Mouthpiece}}$.

compressible Euler equations. For instance, the derived inlet velocity for the loudly played B_3^b on both computational instruments is shown in Figure 6.12[19]; the pressure waveforms are depicted in Figure 6.13. These velocity plots are within the range of the measured velocity profiles found in [54] (i.e., just below 20 m/s).

Theoretically, once this derived velocity is found, it could be used to prescribe a momentum source term, which physically creates kinetic energy and describes how the instrument is 'forced' into resonance to produce the sound pressure waveform for a certain note. Alternatively, an inflow boundary condition could be prescribed so long as the pressure is

[19] This would allow one to determine the relationship between pressure and velocity in a nonuniform bore if the wave propagation was linear. However, the wave propagation does not have to be linear, just more-or-less linear. The initial correction will be small, but perhaps we can do this as an iterative procedure and use linearity to guide the iteration.

not specified.

Chapter 7

Conclusion and Discussion

7.1 Discussion Regarding the Simplified Boundary Condition

In the literature, it is typical to consider six to ten harmonics when analyzing the timbre of f notes, [1], [13], [99], [168], [179]. By these standards, our proposed model is able to reproduce the brassiness of the mentioned notes rather well. For the trombone in particular, regardless of the playing dynamic, deviations from the experimental data were observed mainly for the highest frequencies. In particular, the computed SPLs were too high and we found that this error increased with frequency. However, the lower and mid-frequencies of the trombone notes matched the experimental spectra very well. This makes it tempting to suggest that the observed variation is due to neglecting thermoviscous effects (since losses are more efficient for higher frequencies).

Interpreting the trumpet results however is more difficult. What we can say is for the f notes, the sound energy contained in the lower spectra does not seem to be properly distributed to the higher components. I hypothesize there are two main factors at play here. Firstly, the initial tubing shape of the trumpet is more complicated. This implies the wave motion is more complex and we suspect that the simplified planar condition does a poor job properly modelling the wave interactions. This idea seems to be supported by examining the higher pitch trumpet results, which are better modelled (especially the F_5). Although this could be due to the playing dynamic, I suspect the more significant factor is the value of f_1. In particular, for the B_3^b and B_4^b, $f_1 = 242$ Hz and $f_1 = 484$ Hz, whereas $f_1 = 720$ Hz and $f_1 = 989$ Hz for the F_5 and B_5, respectively. The wavelengths of the latter

pitches are significantly shorter and hence, not as influenced by the change in curvature near the mouthpiece-shank or flare expansion. This means the harmonic waves will be less affected by the changes in cross-sectional area and a larger portion of sound energy will be transmitted rather than reflected. Secondly, the trumpet is almost half the length of the trombone, i.e., effects due to nonlinearities are not as prominent. Consequently, the degree of spectral enrichment in the trumpet is much lower compared to the trombone. This may also explain why the SPLs of the f B_3^b and B_4^b notes are too high below the cutoff frequency, but too small for the higher components.

With respect to the literature, although there is a good portion of publications dedicated to modelling nonlinear wave propagation within brass instruments, most models do not attempt to simulate realistic musical notes. Typically, acoustic pulses (e.g., [179], [180]) or simplifications of musical notes, such as generating the fundamental frequency only (e.g., [1], [69]), are considered. So overall, most models have not yet been validated experimentally [82], [134].

The few examples we could find in the literature where the authors attempted to simulate measured notes can be found in [188] for the bassoon, [161] for the french horn, and [204] for the trombone. For the bassoon, Richter used pressure measurements to prescribe both the inflow and outflow boundary conditions. Although the simulation results were qualitatively similar to the measured data, the computed pressure greatly underestimated the measurements (pressure peaks differed by approximately 1000 Pa). Nonetheless, the author concluded that although some harmonics were under- or overestimated, "*the characteristics of the instrument could be reproduced successfully*" [188]. For the french horn results presented by Norman *et al.*, the input data for their simulation was prescribed to be the pressure measured at the backbore (near the shank) of the horn. In the paper however, the computational geometry used was not described. The obtained numerical results according to the authors were "*qualitatively comparable to that of the measured data*" [161]. However, we found that their model overestimated the experimental spectral curve by 20 dB. Finally, the model proposed by Thompson *et al.* for the trombone was previously mentioned in Section 1.2. Both a linear and nonlinear model were considered. For the loudly played note that was simulated, both models obtained a good match for the SPLs corresponding to f_1 and f_2. However, the linear model (as the authors expected) greatly underestimated all other frequencies. The nonlinear model deviated from the experiment for frequencies in-between 800 Hz - 6000 Hz by approximately 10 dB. For the larger components, specifically frequencies greater than 8000 Hz, the authors concluded that "*the nonlinear model is reasonably accurate in its predictions*" [204].

Therefore, with respect to previous findings published in the literature, even with the simplified boundary condition, our model yields the most accurate results. For the trom-

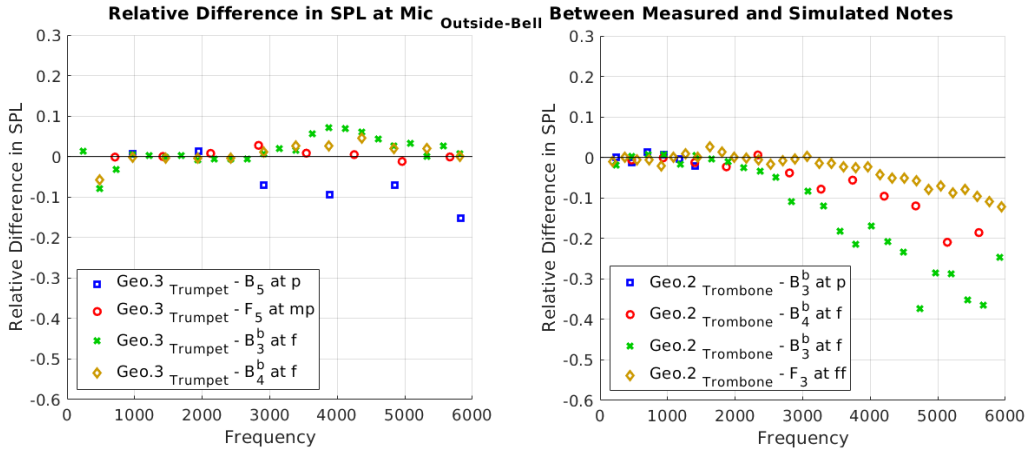

Figure 7.1: Relative difference in SPLs between the measured and simulated trumpet (left) and trombone (right) notes shown in Figures 6.6 and 6.7, i.e., when the linear planar inlet boundary condition is used.

bone, this is true both qualitatively and quantitatively. Once the SPLs have dropped by roughly +30 dB, the computed spectra overestimates the measured values. For the trumpet, the model gives good qualitative results and reasonably accurate quantitative results, particularly for higher frequency notes[1]. The relative difference in the SPLs between our computed and measured notes presented in Section 6.3 are plotted in Figure 7.1.

7.2 Summary of Other Obtained Results

Within this thesis, we carried out several numerical studies. The purpose of these investigations was to determine how we could simplify our proposed problem, verify previous claims or findings within the literature, and finally, to examine whether our numerical outputs were producing reasonable results. This is similarly true for the acoustic experiments done in the lab. In particular, we obtained sound pressure measurements at various locations along the trumpet and trombone to better understand the acoustic differences between the instruments, to examine independently if shock waves could form within the bore of either instrument, to verify claims made in the literature, and to collect data for numerical simulations. Accelerometers were also placed on the bell of each instrument to study the vibroacoustic effects and to determine whether these oscillations were strong enough to

[1] Implying that the transmitted frequencies are very well modelled.

influence the sound wave propagation. Within this thesis, we have achieved the following:

1. Confirmed both experimentally and numerically that the degree of spectral enrichment increases with dynamic level, which results in the played sound having a brassier timbre (Sections 2.3.1 and 5.9).

2. By collecting sound pressure measurements, we were able to observe shock waves in the trombone. For the trumpet however, at least for the musical notes we considered, only wave steepening was observed (Section 2.3). The same musical notes were then simulated, which allowed us to verify that the nonlinearities were not strong enough in Geo.3 $_{\text{Trumpet}}$ for the steepening waves to form a shock. Although, we did find that shock waves were generated when simulating the musical note on Geo.2 $_{\text{Trombone}}$ (Section 5.5.3). To our knowledge, we are the first to numerically reproduce (with reasonably good results (see right plot in Figure 6.4) the development of shock waves when modelling the propagation of a musical note from real data[2] and hence, providing numerical verification of the work published by Hirschberg *et al.* in [99].

3. Using accelerometers, we measured the vibrations of the bells and then approximated how large the corresponding pressure fluctuations would be from their oscillations. The purpose of this was to establish whether such effects were strong enough to influence the played sound measured at Mic $_{\text{Outside-Bell}}$ (Section 4.1.2). Our findings demonstrated that vibroacoustic effects have little to no influence (especially compared to the bore shape) on the timbre of the produced sound outside the bell when the instrument is being played by a musician. A full summary of our results can be found in Section 4.1.2.3.

4. The influence due to thermoviscous losses and the consequences of neglecting them were examined (Sections 4.2.2 and 4.2.3). This was done from a theoretical perspective using the work outlined in [146] by Morse and Ingard. In addition, we used COMSOL to simulate a sinusoidal wave through uniform tubes of varying radii where the wave propagation was modelled by the linearized Navier-Stokes and Euler equations. We found both numerically and theoretically that for a small-amplitude wave, an error of approximately 5% is to be expected when the losses are neglected in the brass instruments prior to the bell.

5. From our numerical studies, we determined that the 2D axisymmetric model does not suffer as much from numerical diffusion compared to the full 3D system. Conse-

[2] Fulfilling my personal goal to describe nonlinear wave propagation in brass instruments, which included being able to numerically reproduce shock waves if they formed within the real instrument [184].

quently, a much finer mesh can be constructed (if the axisymmetric model is used) to better approximate the curvature of the instrument's walls (Section 5.7). We also determined that the space behind the computational instrument does not need to be modelled to obtain good numerical results in front of the instrument along the central axis (Section 5.5).

6. The cutoff frequency (or transition range) of the computational trumpet bell is almost double that of the computational trombone flare. This is in agreement with values reported in the literature (Section 5.8).

7. From our numerical investigations, we determined that the bends do not greatly influence the wave propagation and therefore, can be neglected (Section 5.6). Moreover, it is inadequate to model the tubing before the bell as a uniform cylindrical bore. For the trumpet in particular, this shifts the amplitude of the harmonic distribution up by approximately 6 dB - 7 dB. Although this is also true for the trombone, the difference in the SPLs is much lower and only observed for components above the cutoff frequency (Section 5.5).

7.3 Future Work

Between the physical experiments measuring the vibroacoustic effects of the bell and the numerical experiments investigating the prominence of thermoviscous losses, our findings indicate that of the various types of energy losses, the most influential is the sound dissipation undergone in the boundary layers[3]. However, loss effects due to viscosity and thermal conductivity are frequency dependent and therefore, easiest to incorporate with a frequency-domain model. However, this is not optimal for nonlinear wave propagation. Thus, future work would include taking the thermoviscous losses written with respect to frequency and expressing them within the time-domain. This would entail working with fractional time derivatives [210]. One of the major issues with fractional derivatives is that they are non-local in time, i.e., the past history of the solution must be stored [28]. This is expensive from a computational perspective, especially when considering a 3D model. Fortunately, with advances in computing, technology soon will be able to deal with this bottleneck.

One model that attempts to take such an approach was proposed by Berjamin *et al.* [24] in 2017. The model attempts to include both nonlinearities and thermoviscous losses by

[3] Though these effects are still relatively small as shown in Chapter 4.

taking a frequency-domain model based on generalized Burgers' equations and then transforming it into the time-domain. Due to the computational power required, the authors considered the problem in 1D and approximated the shape of the instrument as a Bessel horn. Even with such simplifications, the authors commented on the difficulties dealing with memory requirements. Nonetheless, the model proposed by Berjamin *et al.* truly represents the embodiment of the current state of realistic brass instrument modelling and how much progress has been made. However, as shown in this thesis, properly modelling the instrument's geometry, specifically the initial bore shape and the flare, is essential to accurately model the instrument during play. Furthermore, either a 2D axisymmetric or a 3D model would be needed to accurately describe how the sound waves spread out and reflect within the bell region. The results presented throughout this thesis have indicated[4] that these factors are more important than including boundary layer losses.

Another problem that could not be fully addressed within this thesis is determining a general nonlinear relationship between pressure and velocity at the inlet boundary. Although the T-Method theoretically is sound, several issues arose when attempting to implement the boundary condition without specifying the pressure (once a velocity expression was derived)[5]. If this could be successfully done, recall that the T-Method does not exactly require linearity, the propagation just has to be more-or-less linear. An iterative procedure could then be used to keep making small corrections to the velocity expression where we use linearity to guide the iteration. So even if the wave propagation is undergoing effects due to nonlinear behaviour, we still have a path to see what is happening and what the nonlinearities are doing to alter the wave propagation. That being said however, there is no mathematical guarantee that a general nonlinear relationship between pressure and velocity can be obtained.

[4] Specifically, comparing the $\text{Geo.1}_{\text{Trumpet}}$ / $\text{Geo.3}_{\text{Trumpet}}$ and $\text{Geo.1}_{\text{Trombone}}$ / $\text{Geo.2}_{\text{Trombone}}$ numerical results presented in Section 5.5.

[5] In particular, we were able to run simulations, but a steady state was never achieved.

Bibliography

[1] Adachi, S., & Sato, M. A., (1995). "Timedomain simulation of sound production in the brass instrument." *Journal of the Acoustical Society of America*, **97**(6), 3850-3861.

[2] Adachi, S., & Sato, M. A., (1996). "Trumpet sound simulation using a twodimensional lip vibration model." *Journal of the Acoustical Society of America*, **99**(2), 1200-1209.

[3] Acheson, David J., (2009). *Elementary Fluid Dynamics* (Clarendon, Oxford).

[4] Adachi, S., (2009). "Principles of Sound Production in Wind Instruments." *Acoustic Society and Technology* **25**(5), 400-05.

[5] Appelö, D., (2003). "Non-reflecting Boundary Conditions for Wave Propagation Problems." Thesis. *Royal Institute of Technology.*

[6] Ayers, R. D., Eliason, L. J., & Salem, M. M. B., (1985). "An acoustic pulse generator for wind instrument bores." *Journal of the Acoustical Society of America*, **77**(S1), S90-S90.

[7] Ayers, R. D., Eliason, L. J., & Lee, A. S., (1985). "Multiple reflections in simple bore shapes." *Journal of the Acoustical Society of America*, **77**(S1), S90-S90.

[8] Babuska, I., & Guo, B.Q., (1992). "The h, p and h-p version of the finite element method: basis theory and applications." *Advances in Engineering Software*, **15**(3-4).

[9] Backus, J., (1964). "Effect of Wall Material on the Steady-State Tone Quality of Woodwind Instruments." *Journal of the Acoustical Society of America*, **36**(10), 1881-1887.

[10] Backus, J., (1965). "Wall vibrations in organ pipes and their effect on tone." *Journal of the Acoustical Society of America*, **38**(5), 912-912.

[11] Backus, J., & Hundley, T. C., (1966). "Wall vibrations in flue organ pipes and their effect on tone." *Journal of the Acoustical Society of America*, **39**(5A), 936-945.

[12] Backus. J., (1970). *The Acoustical Foundations of Music* (Murray, London).

[13] Backus, J., & Hundley, T. C., (1971). "Harmonic generation in the trumpet." *Journal of the Acoustical Society of America*, **49**, 509-519.

[14] Balasubramanian, S., & Kausel, W., (2015). "Pitch shifts in wind instruments due to changes in air composition." Proceedings of the Third Vienna Talk on Music Acoustics, **16**, 19.

[15] Beauchamp, J. W., (2012). "Trombone transfer functions: Comparison between frequency-swept sine wave and human performer input." *Archives of Acoustics*, **37**(4), 447-454.

[16] Bednarik, M., & Cervenka, M., (2014). "Equations for description of nonlinear standing waves in constant-cross-sectioned resonators." *Journal of the Acoustical Society of America*, **135**(3), EL134-EL139.

[17] Benade, A. H., & Gans, D. J., (1968). "Sound production in wind instruments." *Annals of the New York Academy of Sciences*, **155**(1), 247-263.

[18] Benade, A. H., & Smith, J. H., (1981). "Brass wind instrument impulse response measurements." *Journal of the Acoustical Society of America*, **70**(S1), S22-S22.

[19] Benade, A. H., & Keefe, D.H., (1983). "Wave propagation in strongly curved ducts." *Journal of the Acoustical Society of America* **74**, 320-332.

[20] Benade, A. H., (1900). *Fundamentals of Musical Acoustics* (Dover Publications, New York).

[21] Beltman, W. M., (1999). "Viscothermal wave propagation including acoustoelastic interaction, Part I: Theory and Part II: Applications." *Journal of Sound and Vibration*, **227**(3), 555-586 (part I) and 587-609 (part II).

[22] Beranek, L., (1986). *Acoustics* (American Institute of Physics for the Acoustical Society of America, New York).

[23] Berggren, M., Bernland, A., & Noreland, D., (2018). "Acoustic boundary layers as boundary conditions." *Journal of Computational Physics*, **371**, 633-650.

[24] Berjamin, H., Lombard, B., Vergez, C., & Cottanceau, E., (2017). "Time-domain numerical modeling of brass instruments including nonlinear wave propagation, viscothermal losses, and lips vibration." *Acta Acustica united with Acustica*, **103**(1), 117-131.

[25] Bilbao, S., (2011, September). "Modelling of brass instrument valves." In Proceedings of the 14th International Conference on Digital Audio Effects, 337-343.

[26] Bilbao, S. (**2012**). Personal conversation, *University of Edinburgh*.

[27] Bilbao, S., & Chick, J., (2013). "Finite difference time domain simulation for the brass instrument bore." *Journal of the Acoustical Society of America*, **134**(5), 3860-3871.

[28] Bilbao, S & Harrison, R. L., (2016). "Passive time-domain numerical models of viscothermal wave propagation in acoustic tubes of variable cross section." *Journal of the Acoustical Society of America*, **140** pp. 728-740.

[29] Billingham, J., & A. C. K., (2001). *Wave Motion* (Cambridge UP, Cambridge)

[30] Blackstock, D. T., Hamilton, M. F., & Pierce, A. D., (1998). *Nonlinear Acoustics*, edited by M. F. Hamilton and D. T. Blackstock (Academic, San Diego).

[31] Boutin, H., Fletcher, N., Smith, J., & Wolfe, J., (2015). "Relationships between pressure, flow, lip motion, and upstream and downstream impedances for the trombone." *Journal of the Acoustical Society of America*, **137**(3), 1195-1209.

[32] Brackett, D., (2011). "The optimisation of brass istruments to include wall vibration effects." PhD Thesis, *Loughborough University*.

[33] Broch, J. T., (1980). Mechanical vibration and shock measurements.

[34] Cabelli, A., (1979). "The Acoustic Characteristics of Duct Bends." *Journal Sound and Vibration*, **68**, 369-88.

[35] Campbell D. M., (1999). "Nonlinear dynamics of musical reed and brass wind instruments." *Contemporary Physics,* **114**, 415-431.

[36] Campbell, M., Myers, A., & Chick, J., (2013). "Influence of the bell profile of the trombone on sound reflection and radiation." In Proceedings of Meetings on Acoustics ICA2013 **19**(1), 035068.

[37] Campbell, M., Chick, J., Gilbert, J., Kemp, J., Myers, A., & Newton, M., (2014). "Spectral enrichment in brass instruments due to nonlinear sound propagation; a comparison of measurements and predictions." Proceedings of ISMA, Le Mans.

[38] Chick, J., Logie, S., Campbell, M., & Gilbert, J., (2012). "Spectral enrichment and wall losses in trombones played at high dynamic levels." In Acoustics 2012.

[39] Christensena, R., Juhlb, P., & Henriquezb, V. C., (2008). "Practical modeling of acoustic losses in air due to heat conduction and viscosity." aries, **1**(2), 3-4.

[40] Churchhill, R. V., (1963). *Fourier Series and Boundary Value Problems*, 2nd ed. (McGraw-Hill Incorporated, New York).

[41] Cockburn, B. & Shu, C. W., (1989). "TVB Runge-Kutta local projection discontinuous Galerkin finite element method for conservation laws II: General framework." *Mathematics of Computation*, **52**(186), 411-435.

[42] Cockburn, B. & Shu, C. W., (1998). "The Runge-Kutta discontinuous Galerkin finite element method for conservation laws V: Multidimensional systems." *Journal of Computational Physics*, **141** 119-224.

[43] Cockburn, B., (2003). "Discontinuous galerkin methods." *Journal of Applied Mathematics and Mechanics*, **83**, 731-754.

[44] Cockburn, B., Karniadakis, G., & Shu, C. W., (2000). "The development of discontinuous Galerkin methods." UMSI research report/University of Minnesota (Minneapolis, Mn).

[45] Copley, D. C.,& Strong, W. J., (1996). "A stroboscopic study of lip vibrations in a trombone." *Journal of the Acoustical Society of America*, **99**(2), 1219-1226.

[46] Coyle, W. L., (2016). "A study of the acoustical properties of the clarinet in order to predict playing frequencies." PhD Thesis, *Pennsylvania State University.*

[47] Cullen, J. S., (2000). "Study of brass instrument acoustics using an artificial lip reed mechanism, laser doppler anemometry and other techniques." PhD Thesis, *University of Edinburgh.*

[48] Cutanda-Henríquez, V., & Juhl, P. M., (2013). "An axisymmetric boundary element formulation of sound wave propagation in fluids including viscous and thermal losses." *Journal of the Acoustical Society of America*, **134**(5), 3409-3418.

[49] Dalmont, J. P., Nederveen, C. J., & Joly, N., (2001). " Radiation impedance of tubes with different flanges: numerical and experimental investigations." *Journal of Sound and Vibration*, **244**(3): 505-534.

[50] Darlington. P., & Simpson. A., (1992). "Cooling Rate of the B^b Trumpet" *Applied Acoustics*, **36** 145-157.

[51] Deane, A. M., (1986). "Time domain work on brass instruments." PhD thesis, *University of Surrey.*

[52] Dokumaci, E., (1995). "Prediction of the effects of entropy fluctuations on sound radiation from vibrating bodies using an integral equation approach." *Journal of sound and vibration*, **186**(5), 805-819.

[53] Dowling, A. P., & Ffowcs Williams, J. E., (1983). *Sound and sources of sound* (Ellis Horwood Publishers, Sussex).

[54] Elliott, S.J., & Bowsher, J. M., (**1982**). "Regeneration in brass wind instrument." *Journal of Sound and Vibration*, **83**, 181-217.

[55] Elliott, S., Bowsher, J., & Watkinson, P., (1982). "Input and transfer response of brass wind instruments." *Journal of the Acoustical Society of America*, **72**(6), 1747-1760.

[56] Enflo, B. O., and Hedberg, C. M., (2002). *Theory of Nonlinear Acoustics in Fluids* (Kluwer Academic, Dordrecht).

[57] Erickson, R. R.. & Zinn, B. T., (2003). "Modeling of finite amplitude acoustic waves in closed cavities using the Galerkin method," *Journal of the Acoustical Society of America* **113**(4), 1863-1870.

[58] Eveno, P., Dalmont, J. P., Caussé, R., & Gilbert, J., (2012). "Wave propagation and radiation in a horn: Comparisons between models and measurements." *Acta Acustica united with Acustica*, **98**(1), 158-165.

[59] Eveno, P., Petiot, J. F., Gilbert, J., Kieffer, B., & Causse, R., (2014). "The relationship between bore resonance frequencies and playing frequencies in trumpets." *Acta Acustica united with Acustica*, **100**(2), 362-374.

[60] Farassat, F., & Myers, M. K., (1988). "Extension of Kirchhoff's formula to radiation from moving surfaces." *Journal of Sound and Vibration*, **123**(3), 451-460.

[61] Félix, S., & Pagneux, V., (2004). "Sound attenuation in lined bends." *Journal of the Acoustical Society of America*, **116**(4), 1921-1931.

[62] Félix, S., Dalmont, J. P., & Nederveen, C. J., (2012). "Effects of bending portions of the air column on the acoustical resonances of a wind instrument." *Journal of the Acoustical Society of America*, **131**(5), 4164-4172.

[63] Feynman, R., (1900). *The Feynman Lectures on Physics* (California).

[64] Flaherty, J. E., Krivodonova, L., Remacle, J. F., & Shephard, M. S., (2002). "Some aspects of discontinuous Galerkin methods for hyperbolic conservation laws." *Journal of Finite Elements in Analysis and Design*, **38**(10): 889-908.

[65] "FFT based method for advection type models (Burgers)". https://wiki.math.uwaterloo.ca/sheets/matlab/html/PDE_bugers_filt.html.

[66] Fletcher, N. H., and Rossing, T. D., (1991). *The Physics of Musical Instruments* (Springer-Verlag, New York).

[67] Fletcher, N.H., (1998). "The nonlinear physics of musical instruments." *Reports on Progress in Physics*, **62**, 723-765.

[68] Fletcher, N. H., and A. Tarnopolsky., (1998). "Blowing pressure, power, and spectrum in trumpet playing." *Journal of the Acoustical Society of America* **105**, 874-881.

[69] Fréour, V., & Scavone, G. P., (2013). "Trombone sound simulation under varying upstream coupling conditions." In Proceedings SMAC.

[70] Fuhry, M., Giuliani, A., & Krivodonova, L., (2014). "Discontinuous Galerkin methods on graphics processing units for nonlinear hyperbolic conservation laws." *International Journal of Numerical Methods in Fluids*. **76**(12): 982-1003.

[71] French, A. P., (1971). *Vibrations and Waves* (W.W Norton and Company, New York).

[72] Fuhry, M., (2013). "An Implementation of the Discontinuous Galerkin Method on Graphics Processing Units." Master's Thesis, *University of Waterloo*.

[73] Gautier, F., Nief, G., Gilbert, J., & Dalmont, J. P., (2012). "Vibro-acoustics of organ pipesRevisiting the Miller experiment (L)." *Journal of the Acoustical Society of America*, **131**(1), 737-738.

[74] Goldstein, M. E., (1976). *Aeroacoustics* (McGraw-Hill, New York).

[75] Gilbert, J., Dalmont, J., and Guimezanes, T., (2005). "Nonlinear wave propagation in woodwinds." Forum Acusticum, Budapest, 1369-1372.

[76] Gilbert, J., (2006). "Differences between cylindrical and conical brass instruments; the nonlinear propagation point of view from experiments and simulations." *Journal of the Acoustical Society of America*, **120**(5), 3332-3332.

[77] Gilbert, J., Campbell, M., Myers, A., & Pyle, B., (2007). "Differences between brass instruments arising from variations in brassiness due to nonlinear propagation." In International Symposium on Musical Acoustics (ISMA).

[78] Gilbert, J., Menguy, L., & Campbell, M., (2008). "A simulation tool for brassiness studies," *Journal of the Acoustical Society of America*. **123**(4): 1854-1857.

[79] Godlewski, E., Raviart, P. A. (**1996**). *Numerical Approximation of Hyperbolic Systems of Conservation Laws*, Volume 118 (Springer, New York).

[80] Gautier, F., & Tahani, N., (1998). "Vibroacoustics of cylindrical pipes: internal radiation modal coupling." *Journal of Sound and Vibration*, **215**(5), 1165-1179.

[81] Gautier, F., & Tahani, N., (1998). "Vibroacoustic behaviour of a simplified musical wind instrument." *Journal of Sound and Vibration*, **213**(1), 107-125.

[82] Giordano, N., (2018). "Physical modeling of a conical lip reed instrument." *Journal of the Acoustical Society of America*, **143**(1), 38-50.

[83] Giordano, N., (2019). "Force on the lips of a trumpet player." *Journal of the Acoustical Society of America*, **145**(3), 1521-1528.

[84] Giuliani, A., (2018). "A parallel, adaptive discontinuous Galerkin method for hyperbolic problems on unstructured meshes." PhD Thesis, *University of Waterloo*.

[85] Goldstein, M. E., (1976). Aeroacoustics. New York, McGraw-Hill International Book Co., 305 p.

[86] Gupta, P., & Scalo, C., (2018). "Spectral energy cascade and decay in nonlinear acoustic waves." Physical Review E, **98**(3), 033117.

[87] Haberman, R., (2004). *Applied Partial Differential Equations with Fourier Series and Boundary Value Problems* (Pearson Prentice Hall, Upper Saddle River, N.J).

[88] Hargather, M. J., Settles, G. S., & Madalis, M. J., (2010). "Schlieren imaging of loud sounds and weak shock waves in air near the limit of visibility." *Shock Waves*, **20**(1), 9-17.

[89] Harrison-Harsley, R. L., & Bilbao, S., (2018). "Separability of wave solutions in nonlinear brass instrument modelling." *Journal of the Acoustical Society of America*, **143**(6), 3654-3657.

[90] Harrison-Harsley, R. L., (2018). "Physical modelling of brass instruments using finite-difference time-domain methods." PhD Thesis, *University of Edinburgh.*

[91] Hélie, T., & Smet, V., (2008). "Simulation of the weakly nonlinear propagation in a straight pipe: application to a real-time brassy audio effect." In 2008 16th Mediterranean Conference on Control and Automation (pp. 1580-1585). IEEE.

[92] Hélie, T., & Smet, V., (2008). "Simulation of the weakly nonlinear propagation in a straight pipe: application to a real-time brassy audio effect." In 2008 16th Mediterranean Conference on Control and Automation (pp. 1580-1585). IEEE.

[93] Helmholtz, H., (1863). "Verhandlungen des Nattrrhistorisch-medicinischert." *Vereins zu Heidelberg*, **3**, 16

[94] Henrquez, V. C., Andersen, P. R., Jensen, J. S., Juhl, P. M., & Sánchez-Dehesa, J., (2017). "A Numerical Model of an Acoustic Metamaterial Using the Boundary Element Method Including Viscous and Thermal Losses." *Journal of Computational Acoustics*, *25.*

[95] Hentschel, K., & Zhu, (2017). Gustav Robert Kirchhoff's Treatise On the Theory of light Rays (1882) English Translation, Analysis and Commentary (World Scientific, New York).

[96] Henry, P. S. H., (1931). "The tube effect in sound-velocity measurements. Proceedings of the Physical Society." **43**(3), 340.

[97] Hirsch, C., (1990). *Numerical computation of internal and external flows: Computational methods for inviscid and viscous flows* (Wiley, Brussels).

[98] Hirschberg, A. J., Gilbert, J., and Wijnands, A. P. J., (1994). "Musical aero-acoustics of the clarinet." *Journal De Physique.* **44**, 559-568.

[99] Hirschberg, A. J., Gilbert, J., Msallam, R., and Wijnands, A. P. J., (1995). "Shock waves in trombones," *Journal of the Acoustical Society of America* **99**(3), 1754-1758.

[100] Holland , K. R., & Morfey, C. L., (1996). "A model of nonlinear wave propagation in horns." *Journal of the Audio Engineering Society*, **44**(7-8), 569-580.

[101] Honzík, P., Durand, S., Joly, N., & Bruneau, M., (2013). "On the acoustic transfer function of slowly tapered small horns filled with thermo-viscous fluid." *Acta Acustica united with Acustica*, **99**(5), 694-702.

[102] Hopkin, B., (1996). *Musical Instrument Design Practical Information for Instrument Making* (Sharp Press, New York).

[103] Hunt, F. V., (1955). "Notes on the exact equations governing the propagation of sound in fluids." *Journal of the Acoustical Society of America*, **27**(6), 1019-1039.

[104] Illinskii, Y. A., Lipkens, B., Lucas, T. S., Van Doren, T. W., & Zabolotskaya, E. A., (1998). "Nonlinear standing waves in an acoustical resonator." *Journal of the Acoustical Society of America*, **104**: 2664-2674.

[105] Jensen, M. H., (2017). "Modeling Aeroacoustics with the Linearized Navier-Stokes Equations." https://www.comsol.com/blogs/modeling-aeroacoustics-with-the-linearized-navier-stokes-equations/.

[106] Kampinga, W. R., Wijnant, Y. H., & de Boer, A., (2010). "Performance of several viscothermal acoustic finite elements." *Acta Acustica united with Acustica*, **96**(1), 115-124.

[107] Karra, C., & Tahar, M. B., (1997). "An integral equation formulation for boundary element analysis of propagation in viscothermal fluids." *Journal of the Acoustical Society of America*, **102**(3), 1311-1318.

[108] Kausel, W., Mayer, A., & Nachtmann, G., (2007). "Experimental demonstration of the effect of wall vibrations on the radiated sound of the horn and a search for possible explanations." In Proceedings of International Symposium on Musical Acoustics.

[109] Kausel, W., Zietlow, D. W., & Moore, T. R., (2010). "Influence of wall vibrations on the sound of brass wind instruments." *Journal of the Acoustical Society of America*, **128**(5), 3161-3174.

[110] Kausel, W., Beauchamp, J. W., & Carral, S., (2013). "Brass instrument power efficiency and the relationship between input impedance and transfer function." In Proceedings of Meetings on Acoustics ICA2013 (**19**(1), p. 035069). ASA.

[111] Kausel, W., & Geyer, C. B., (2013). "Time-domain simulation of standing waves in brass wind instruments taking non-linear wave steepening into account." In Proceedings of the Stockholm Music Acoustics Conference, Stockholm, Sweden.

[112] Kausel. W., Chatziioannou. B., Gorman. B., Rokni. M., & Moore. T., (2014). "Vibroacoustic modeling of wall vibrations of a trumpet bell." ISMA 2014 France, 90-93

[113] Kausel, W., Chatziioannou, V., Moore, T. R., Gorman, B. R., & Rokni, M., (2015). "Axial vibrations of brass wind instrument bells and their acoustical influence: Theory and simulations." *Journal of the Acoustical Society of America*, **137**(6), 3149-3162.

[114] Keefe, D. H., (1984). "Acoustical wave propagation in cylindrical ducts: Transmission line parameter approximations for isothermal and nonisothermal boundary conditions." *Journal of the Acoustical Society of America*, **75**(1), 58-62.

[115] Keller, J. B., (1954). "Geometrical acoustics. I. The theory of weak shock waves." *Journal of Applied Physics*, **25**(8), 938-947.

[116] Kemp, J., (2002). "Theoretical and experimental study of wave propagation in brass musical instruments." PhD Thesis, *University of Edinburgh*.

[117] Kemp, J. A., Van Walstijn, M., Campbell D. M., & Smith, R. A., (2010). "Time domain wave separation using multiple microphones." *Journal of the Acoustical Society of America*, **128**:195-205.

[118] Kemp, J. A., & Smith, R., (2012). "Measuring the effect of the reflection of sound from the lips in brass musical instruments." Acoustics 2012 Joint meeting : 11th Congreès Français d'Acoustique and 2012 IOA annual meeting, 1767-1773.

[119] Kemp, J., (2014). "Sensing lip protrusion and vibratory motion in the mouthpiece during trumpet playing using a theremin." In Proceedings of the International Symposium on Musical Acoustics (ISMA) (pp. 137-142).

[120] Kemp, J. A., López-Carromero, A., & Campbell, M., (2017). "Pressure fields in the vicinity of brass musical instrument bells measured using a two dimensional grid array and comparison with multimodal models." In Proceedings of the 24th International Congress on Sound and Vibration. International Institute of Acoustics and Vibration.

[121] Kirchhoff, C., (1868). "Ueber den Eincuss der Warmeleitung in einem Gas aug die Schallbewegung"(About the entrance of the heat pipe in a gas aug the sound movement). *Pogg. Ann.*, **123**, 177-193.

[122] Kirchhoff, G. (1868). "Ueber den Einfluss der Wärmeleitung in einem Gase auf die Schallbewegung" (On the influence of heat conduction in a gas on the sound movement). *Annalen der Physik*, **210**(6), 177-193. (On the influence of heat conduction in a gas on the sound movement)

[123] Klippel, W., (1995). "Nonlinear wave propagation in horns and ducts." *Acta Acustica united with Acustica*, **98**(1): 431-436.

[124] Krivodonova, L., (2010). "An Efficient Local Time Stepping Scheme for Solution of Nonlinear Conservation Laws." *Journal of Computational Physics*. **229**, 8537-8551.

[125] Kundu, P. K., Cohen, I. M., (2008). *Fluid Mechanics*, 4th ed. (Elsevier Incorporated, London).

[126] Kundt, A., (1866). "Ueber eine neue Art Akustischer Staubfiguren und ber die Anwendung derselben zur Bestimmung der Shallgeschwindigkeit in festen Krpern und Gasen" (About a new sound, acoustic dust tube and the application of the same sound velocity in solid bodies and gases). *Annalen der Physik*. Leipzig: J. C. Poggendorff. **12**(4): 497-523.

[127] Kundt, A., (1868). *III. Acoustic Experiments.* The London, Edinburgh, and Dublin Philosophical Magazine and Journal of Science, **35**(234), 41-48.

[128] Lambert, R. F., (1951). "Wall viscosity and heat conduction losses in rigid tubes." *Journal of the Acoustical Society of America*, **23**(4), 480-481.

[129] Lambert, R. F., (1953). "A Study of the Factors Influencing the Damping of an Acoustical Cavity Resonator." *Journal of the Acoustical Society of America*, **25**(6), 1068-1083.

[130] Lefebvre, A., & Scavone, G. P., (2012). "Characterization of woodwind instrument toneholes with the finite element method." *Journal of the Acoustical Society of America*, **131**(4), 3153-3163.

[131] Liepmann, H. W., & Roshko, A., (2001). *Elements of Gasdynamics* (Dover Publications, Mineola).

[132] Logie, S. M., (2013). "Acoustical study of the playing characteristics of brass wind instruments." PhD Thesis, *University of Edinburgh*.

[133] Lombard, B., Matignon, D., & Le Gorrec, Y., (2013). "A fractional Burgers' equation arising in nonlinear acoustics: theory and numerics." IFAC Proceedings Volumes, **46**(23), 406-411.

[134] López-Carromero, A., Campbell, D. M., Rendón, P. L., & Kemp, J., (2016). "Validation of brass wind instrument radiation models in relation to their physical accuracy using an optical Schlieren imaging setup." In Proceedings of Meetings on Acoustics 22ICA (**28**(1), p. 035003). ASA.

[135] Luo, C., Huang, X. Y., & Nguyen, N. T., (2005). "Effect of resonator dimensions on nonlinear standing waves." *Journal of the Acoustical Society of America*, **117**(1), 96-103.

[136] *Math Works*. http://www.mathworks.com/.

[137] Mattsson, A. E., & Rider, W. J., (2013). "Artificial viscosity: back to basics." https://www.osti.gov/servlets/purl/1115027.

[138] Marshall, I., (1992). "Acoustic reflectometry for airway measurement." PhD Thesis, *University of Edinburgh*.

[139] Martin, D. W., (1942). "Directivity and the acoustic spectra of brass wind instruments." *Journal of the Acoustical Society of America*, **13**(3), 309-313.

[140] Martin, P. A., (2004). "On Websters horn equation and some generalizations," *Journal of the Acoustical Society of America*,**116**(3) , 1381-1388.

[141] Menguy, L., & Gilbert, J., (2000). "Weakly nonlinear gas oscillations in air-filled tubes; solutions and experiments." *Acta Acustica united with Acustica*, **86**(5), 798-810.

[142] Miller. D. C., (1909) "The influence of the material of wind-instruments on the tone quality." *Science*, **29**, 161-171.

[143] Milne-Thomson, L. M., (1973). *Theoretical aerodynamics*. (Courier Corporation).

[144] Moore, T. R., Shirley, E. T., Codrey, I. E., & Daniels, A. E., (2005). "The effects of bell vibrations on the sound of the modern trumpet." *Acta Acustica united with Acustica*, **91**(3), 578-589.

[145] Moore, T., Kausel, W., Chatziioannou, V., Etchenique, N., & Gorman, B., (2013). "Axial vibrations of brass wind instruments." Proceedings of Meetings on Acoustics ICA2013, **19**(1): 035073.

[146] Morse. P. M., & Ingard. K. I., (1968). Theoretical Acoustics

[147] Msallam, R., Dequidt, S., Causse, R., & Tassart, S., (2000). "Physical model of the trombone including nonlinear effects. Application to the sound synthesis of loud tones." *Acta Acustica united with Acustica*, **86**(4), 725-736.

[148] Mulder, W. A., (1999). "Spurious modes in finite-element discretizations of the wave equation may not be all that bad." Applied Numerical Mathematics **30**(4), 425-445.

[149] Munson, B. R., Donald F. Y., and Theodore H. O., (2005). *Fundamentals of Fluid Mechanics* (Wiley, New York).

[150] *Music and Computers*. www.music.columbia.edu/cmc/musicandcomputers/.

[151] Myers, A., Gilbert, J., Pyle, B., & Campbell, M., (2007). "Non-linear propagation characteristics in the evolution of brass musical instruments design." In International Congress on Acoustics (19th ICA).

[152] Myers, A., Pyle Jr, R. W., Gilbert, J., Campbell, D. M., Chick, J. P., & Logie, S., (2012). "Effects of nonlinear sound propagation on the characteristic timbres of brass instruments." *Journal of the Acoustical Society of America*, **131**(1), 678-688.

[153] Naugolnykh, K., & Ostrovskii, L. A., (1998). *Nonlinear Wave Processes in Acoustics* (Cambridge University Press, Cambridge).

[154] Nederveen, C. J., (1998). "Influence of a toroidal bend on wind instrument turning." *Journal of the Acoustical Society of America*, **104**, 1616-1626.

[155] Neittaanmäki, P., Rossi, T., Majava, K., Pironneau, O., Périaux, J., & Krzek, M., (2004). "A Finite element method for the modelig of thermoviscous effects in acoustics." In Proceedings of the European Congress on Computational Methods in Applied Science and Engineering (ECCOMAS 2004).

[156] Nief. G., Gautier. F., Dalmont. J.P., & Gilbert. J., (2008). "Influence of wall vibrations on the behavior of a simplified wind instrument." *Journal of the Acoustical Society of America*, **124**(2).

[157] Nief. G., Gautier. F., Dalmont. J.P., & Gilbert. J., (2008). "External sound radiation of vibrating trombone bells." *Journal of the Acoustical Society of America, 123*(5), 3237-3237.

[158] Noreland D., (2002). "A Numerical Method for Acoustic Waves in Horns." *Acta Acustica united with Acustica*, **88**(4), 576-586.

[159] Noreland, D., (2003). "Numerical techniques for acoustic modelling and design of brass wind instruments." PhD Thesis, *Acta Universitatis Upsaliensis*.

[160] Noreland, J.D., Udawalpola, M.R., & Berggren, O.M., (2010). "A hybrid scheme for bore design optimization of a brass instrument." *Journal of the Acoustical Society of America*, **128**(3): 1391-1400.

[161] Norman, L., Chick, J. P., Campbell, D. M., Myers, A., & Gilbert, J., (2010). "Player control of 'Brassiness' at intermediate dynamic levels in brass instruments." *Acta Acustica united with Acustica*, **96**(4), 614-621.

[162] Official COMSOL website. https://www.comsol.com/.

[163] Official COMSOL website - Acoustics Module. https://www.comsol.com/acoustics-module.

[164] Official NASA website. https://www.nasa.gov/centers/glenn/home/index.html.

[165] Official NVIDIA website. https://developer.nvidia.com/about-cuda.

[166] Olson, H. F., (1980). *Music, Physics and Engineering*. 2nd ed. (Dover Publications, New York).

[167] Pandya, B. H., Settles, G. S., and Miller, J. D., (2003). "Schlieren imaging of shock waves in a trumpet." *Journal of the Acoustical Society of America*, **114**, 3363-3367.

[168] Petiot, J. F., & Gilbert, J., (2013). "Comparison of Trumpets' Sounds Played by a Musician or Simulated by Physical Modelling." *Acta Acustica united with Acustica*, **99**(4), 629-641.

[169] Pico, R., Gautier, F., & Redondo, J., (2007). "Acoustic input impedance of a vibrating cylindrical tube." *Journal of Sound and Vibration*, **301**(3-5), 649-664.

[170] Pierce, A. D., & Beyer, R. T., (1990). *Acoustics: An introduction to its physical principles and applications*. 1989 Edition (Springer).

[171] Poirson, E., Petiot, J. F., & Gilbert, J., (2005). "Study of the brightness of trumpet tones." *Journal of the Acoustical Society of America*, **118**(4), 2656-2666.

[172] Prieur, F., (2018). "On the signal amplitude asymmetry in nonlinear propagation." In Proceedings of Meetings on Acoustics 21ISNA, **34**(1), 045006.

[173] Pyle Jr, R. W., (1998). "The effect of wall materials on the timbre of brass instruments." *Journal of the Acoustical Society of America*, **103**(5), 2834-2834.

[174] Pyle Jr, R. W., & Myers, A., (2006). "Scaling of brasswind instruments." *Journal of the Acoustical Society of America*, **119**(5), 3259-3259.

[175] Pyle, R., (2010). *The influence of mouthpiece cup shape on brassiness* (University of Music and Performing Arts Wienna, Austria).

[176] Rasmussen, A. R., (2009). "Thermoviscous model equations in nonlinear acoustics: analytical and numerical studies of shocks and rarefaction waves." PhD Thesis, *Technical University of Denmark*.

[177] Rayleigh, J. W. S., and Robert B. Lindsay., (1976). *The Theory of Sound, Volume One Unabridged Second Revised Edition* (Dover Publications, Minneapolis).

[178] Rayleigh, J. W. S., and Robert B. Lindsay., (1976). *The Theory of Sound, Volume Two (Dover Classics of Science and Mathematics)* (Dover Publications, Minneapolis).

[179] Rendón, P. L., Narezo, D., Bustamante, F. O., and Lopez, A. P., (2009). "Nonlinear progressive waves in a slide trombone resonator." *Journal of the Acoustical Society of America*, **127**(2), 1096-1103.

[180] Rendón, P. L., Ezeta, R., & Pérez-López, A., (2013). "Nonlinear sound propagation in trumpets." *Acta Acustica united with Acustica*, **99**(4), 607-614.

[181] Rendón, P. L., Malanche, C.G. & Orduña-Bustamante, F., (2016). "Effect of input signal shape on the nonlinear steepening of transient acoustic waves in a cylindrical tube." 22nd International Congress on Acoustics.

[182] Rendón, P. L., Velasco-Segura, R., Echeverría, C., Porta, D., Pérez-López, A., Vázquez-Turner, R. T., & Stern, C., (2018). "Using Schlieren imaging to estimate the geometry of a shock wave radiated by a trumpet bell." *Journal of the Acoustical Society of America*, **144**(4), EL310-EL314.

[183] Resch, J., (2013). "Nonlinear Wave Propagation in Brass Instruments." Master's Thesis, *University of Waterloo*.

[184] Resch, J., Krivodonova, L., & Vanderkooy, J., (2014). "A two-dimensional study of finite amplitude sound waves in a trumpet using the discontinuous Galerkin method." *Journal of Computational Acoustics*, **22**(03), 1450007.

[185] Resch, J., Krivodonova, L., & Vanderkooy, J., (2016). "A comparison between two and three-dimensional simulations of finite amplitude sound waves in a trumpet." In *Mathematical and Computational Approaches in Advancing Modern Science and Engineering*. Springer International Publishing, 481-492.

[186] Resch, J., Giuliani, A., Krivodonova, L., & Vanderkooy, J., (2017). "Axisymmetric Simulations of Nonlinear Sound Propagation in a Trumpet." In *Recent Advances in Mathematical and Statistical Methods*. Springer International Publishing, 229-238.

[187] Richter, A., Stiller, J., & Grundmann, R., (2007). "Stabilized discontinuous Galerkin method for flow-sound interaction." *Journal of Computational Acoustics*, **15**: 123-143.

[188] Richter, A., (2012). "Numerical investigations of the gas flow inside the bassoon." *Journal of Fluids Engineering*, **134**(4), 041104.

[189] Richards, S. K., Zhang, X., Chen, X. X., & Nelson P. A., (2004). "The evaluation of non-reflecting boundary conditions for duct acoustic computation." *Journal Sound and Vibration*, **270**(3): 539-557.

[190] Rocamora, M., Lopez, E., & Jure, L., (2009). "Wind instruments synthesis toolbox for generation of music audio signals with labeled partials." In Proceedings of 2009 Brazilian Symposium on Computer Music **2**, 2-4.

[191] Rose, N., & Holloway, D. S., (2012). "Finite element modeling of brass musical instruments." In Acoustics 2012 Fremantle: Acoustics, Development and Environment, 1-8.

[192] Scavone, G. P., (1997). "An acoustic analysis of single-reed woodwind instruments with an emphasis on design and performance issues and digital waveguide modeling techniques." PhD Thesis, *Stanford University*.

[193] Schlichting, H., (1979). *Boundary Layer Theory*, 7th ed. (McGraw-Hill Book, New York).

[194] Scott, F. S., (2012). "Measurement and synthesis of the trombone." PhD Thesis, *School of Computing Science*.

[195] Sharp, D. B., (1996). "Acoustic pulse reflectometry for the measurement of musical wind instruments." PhD Thesis, *University of Edinburgh*.

[196] Sharp, D. B., & Campbell, D. M. (1997). "Leak detection in pipes using acoustic pulse reflectometry." *Acta Acustica united with Acustica*, **83**(3), 560-566.

[197] Sharp, D. B., Myers, A., & Campbell, D. M., (1997). "Using pulse reflectometry to compare the evolution of the cornet and the trumpet in the 19th and 20th centuries." Proceedings-Institute of Acoustics, **19**, 541-548.

[198] Skudrzyk, E., (1971). *The foundations of acoustics: basic mathematics and basic acoustics* (Springer, New York).

[199] Smith, R. A., (1978). "Recent developments in trumpet design." *International Trumpet Guild Journal*, **3**, 1-8.

[200] Smith, R., (1986). "The effect of material in brass instruments: a review." Proceedings of the Institute of Acoustics, **8**(1), 91-96.

[201] 'Sound.' *ThinkQuest*. https://library.thinkquest.org/C005705/English/sound/history.htm.

[202] Stevenson, S., Campbell, M., Bromage, S., Chick, J., & Gilbert, J., (2009). "Motion of the lips of brass players during extremely loud playing." *Journal of the Acoustical Society of America*, **125**(4), 152-157.

[203] Sugimoto, N., (1991). "Burgers' equation with a fractional derivative; hereditary effects on nonlinear acoustic waves." *Journal of Fluid Mechanics*, **225**, 631-653.

[204] Thompson, M. W., and Strong, W. J., (2001). "Inclusion of wave steepening in a frequency-domain model of trombone sound production." *Journal of the Acoustical Society of America*, **110**(1), 556-562.

[205] Thompson, S. C., Gabrielson, T. B., & Warren, D. M., (2014). "Analog model for thermoviscous propagation in a cylindrical tube." *Journal of the Acoustical Society of America*, **135**(2), 585-590.

[206] Tournemenne, R., Petiot, J. F., Talgorn, B., Kokkolaras, M., & Gilbert, J., (2017). "Brass instruments design using physics-based sound simulation models and surrogate-assisted derivative-free optimization." *Journal of Mechanical Design*, **139**(4), 041401.

[207] Tripathi, B., (2015). "Discontinuous Galerkin method for propagation of acoustical shock waves in complex geometry." PhD Thesis, *Université Pierre et Marie Curie-Paris VI*.

[208] Välimäki, V., Tolonen, T., & Karjalainen, M., (1998). "Signal-dependent Nonlinearities for Physical Models Using Time-varying Fractional Delay Filters." In ICMC.

[209] Van Walstijn, M., & Campbell, M., (2003). "Discrete-time modeling of woodwind instrument bores using wave variables." *Journal of the Acoustical Society of America*, **113**(1), 575-585.

[210] Vanderkooy, J., Personal conversation, *University of Waterloo*.

[211] Velasco-Segura, R., & Rendón, P. L., (2015). "A finite volume approach for the simulation of nonlinear dissipative acoustic wave propagation." *Wave Motion*, **58**, 180-195.

[212] Warburton, T., and Hesthaven, J. S., (2008). *Nodal Discontinuous Galerkin Methods: Algorithms, Analysis, and Applications* (Springer, New York).

[213] Watkinson, P. S., & Bowsher, J. M., (1982). "Vibration characteristics of brass instrument bells." *Journal of Sound and Vibration*, **85**(1), 1-17.

[214] Watson, A. P., & Bowsher, J. M., (1988). "Impulse measurements on brass musical instruments." *Acta Acustica united with Acustica*, **66**(3), 170-174.

[215] Webster A. G., (1919). "Acoustical impedance and the theory of horns and of the phonograph." Proceedings of National Academy of Science, **5**(7): 275-282.

[216] Weiner, S., (1966). "Standing sound waves of finite amplitude." *Journal of the Acoustical Society of America*, **40**, 240-243.

[217] Weston, D. E., (1953). "The theory of the propagation of plane sound waves in tubes." Proceedings of the Physical Society, **66**(8), 695.

[218] "What Is the Psd?" *Vru Vibration Testing - Power-spectral-density*. https://vru.vibrationresearch.com/lesson/what-is-the-psd/.

[219] Whitehouse, J., (2003). "A study of the wall vibrations excited during the playing of lip-reed instruments." PhD Thesis, *Open University*.

[220] Wolfe, J., "Brass Instrument Acoustics An Introduction." *Brass Instrument (lip Reed) Acoustics: An Introduction*. www.phys.unsw.edu.au/jw/brassacoustics.html.

[221] Wolkov, A. V., & Petrovskaya, N. B., (2010). "Higher order discontinuous Galerkin method for acoustic pulse problem." *Computer Physics Communications*, **181**(7): 1186-1194.

[222] Wu, Z., Xu, Y., Wang, W., & Hu, R., (2013). "Review of shock wave detection method in CFD post-processing." *Chinese Journal of Aeronautics*, **26**(3): 501-513.

[223] Yan, J., & Shu, C. W., (2002). "Discontinuous Galerkin Methods for Partial Differential Equations with Higher Order Derivatives." *Journal of Scientific Computing*, **17**(1-4), December 2002, 27-47.

[224] Yazaki, T., Tashiro, Y., & Biwa, T., (2007). "Measurements of sound propagation in narrow tubes." Proceedings of the Royal Society A: Mathematical, Physical and Engineering Sciences, **463**(2087), 2855-2862.

[225] Yoshikawa, S., & Muto, Y., (2003). "Lip-wave generation in horn players and the estimation of lip-tissue elasticity." *Acta Acustica united with Acustica*, **89**(1), 145-162.

[226] Young, J. E., (1955). "Heat Conduction Losses in the Acoustic Boundary Layer." *Journal of the Acoustical Society of America*, **27**(6), 1039-1043.

Appendix A

Microphone and Accelerometer Calibration

Experiment #1

This calibration applies to the measurement of the trumpet and was carried out by an 114 dB signal at 1 kHz. This signal is 10.0 Pa rms.

Channel 0: $\frac{1}{4}$ inch GRAS 40BH

On preamplifier with special gain switch set to 0 dB. Calibration factor: 1,895 Pa/V.

Channel 1: $\frac{1}{4}$ inch B&K 4135

On B&K 2610 preamplifier set to 0 dB input gain, 0 dB output gain, and set to 28 V polarization. Note that this microphone signal was inverted. Calibration factor: -1,776 Pa/V.

Channel 2: $\frac{1}{2}$ inch B&K 4133

On preamplifier with special gain switch set to 10 dB gain. Calibration factor: 26.65 Pa/V.

Experiment #2

This calibration applies to the measurement of the trombone where all channels were set to 200 V polarization.

Channel 0: $\frac{1}{4}$ inch B&K 4136

Preamplifier set to -10 dB input gain, 0 dB output gain. Calibration factor: 2,633 Pa/V.

Channel 1: $\frac{1}{4}$ inch GB&K 4135

Preamplifier set to -10 dB dB input gain, 0 dB output gain. Calibration factor: 272 Pa/V.

Channel 2: $\frac{1}{4}$ inch GRAS 40BP

Preamplifier set to 10 dB input gain, 0 dB output gain. Calibration factor: 595 Pa/V.

Channel 3: $\frac{1}{2}$ inch B&K 4133

Preamplifier set to 20 dB input gain, 0 dB output gain. Calibration factor: 80 Pa/V.

Experiment # 3

This calibration applies to the measurements for the trumpet and trombone where all channels were set to 200 V polarization.

Channel 0: $\frac{1}{4}$ inch B&K 4136

Preamplifier set to -10 dB input gain, 0 dB output gain. Note that this microphone signal was inverted. Calibration factor: -2,638 Pa/V.

Channel 1: $\frac{1}{2}$ inch GRAS 40BP

Preamplifier set to -10 dB input gain, 0 dB output gain. Note that this microphone signal was inverted. Calibration factor: -2,136 Pa/V.

Channel 2: $\frac{1}{4}$ inch B&K 4133

Preamplifier set to 0 dB input gain, 0 dB output gain. Calibration factor: 82 Pa/V.

Channel 3: Knowles BU 1771 Accelerometer

Produced about 4.1 mV/g. Calibration factor: 243 g/V.

Experiment # 4

This calibration applies to the measurements for the trumpet and trombone where all channels were set to 200 V polarization.

Channel 0: $\frac{1}{4}$ inch GRAS 40BP

Preamplifier set to -20 dB input gain, 0 dB output gain. Note that this microphone signal was inverted. Calibration factor: -25,000 Pa/V.

Channel 1: $\frac{1}{4}$ inch B&K 4136

Preamplifier set to -10 dB input gain, 0 dB output gain. Note that this microphone signal was inverted. Calibration factor: -8,547 Pa/V.

Channel 2: $\frac{1}{2}$ inch B&K 4133

Preamplifier set to 0 dB input gain, 0 dB output gain. Note that this microphone signal was inverted. Calibration factor: -81 Pa/V.

Channel 3: Knowles BU 1771 Accelerometer # 1

Produced about 4.1 mV/g. Calibration factor: 243 g/V.

Channel 4: Knowles BU 1771 Accelerometer # 2

Note that this microphone signal was inverted and produced about 5.2 mV/g. Calibration factor: -192 g/V.

Appendix B

Prerequisites of Acoustic Measuring and Analysis Techniques

B.1 Sensors

In general, when using microphones or sensors, low sensitivity sensors may require amplification of their output. In terms of sample rate, typically 10,000 Hz for shock testing, over 5000 Hz for general vibration, and around 1000 Hz for slower vibration or movement is the general rule.

The resolution of a sensors is usually specified as bits, which can then be used to calculate the resolution in acceleration units. For instance, consider an accelerometer system that has 16-bit resolution. This implies that there are 2^{16} (65,536) acceleration levels or bins that can be measured.

B.2 Filters

Filters are data processing techniques that can smooth out high or low frequency fluctuations in data or remove periodic trends of a specific frequency from data. For instance, high pass filters remove lower frequency vibration[1]. In some cases, digital filters can be

[1]Low pass filters are usually used to prevent aliasing which cannot be filtered out in software. Aliasing causes a signal to become indistinguishable or to look like a completely different signal. It is important to realize that an analog lowpass filter is needed to prevent aliasing. Once a signal is aliased, it cannot be filtered out digitally in software.

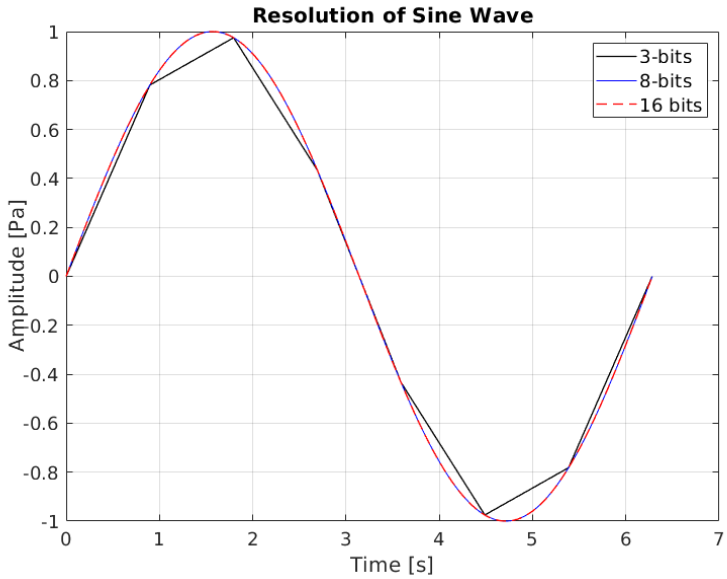

Figure B.1: A 1 Pa sine wave plotted with different bit resolutions.

designed with infinite impulse response, known as an IIR filter, which is a recursive filter, i.e., is a filter that reuses one or more of its outputs as an input. IIR filters are particularly useful if one needs to save computation time. However, there are situations where the phase response of the filter is very important. In such cases it might be more useful to use a finite impulse response, known as a FIR filter, because they can be designed with a linear phase, i.e., the phase response of the filter is a linear function of frequency which usually causes a phase delay. FIR filtered are carried out via convolution.

This ideal filter would have a perfectly linear phase response to the same upper frequency limit. But ideal filters don't exist; there is some compromise that needs to be made on a filter's amplitude and phase response. There are four main different types of filters:

Butterworth:

A Butterworth filter is known for its maximally flat amplitude response and a reasonably linear phase response. The Butterworth filter is the most popular for vibration testing.

Bessel:

The Bessel filter has nearly perfect phase linearity so it is best suited for transient

events like shock testing. It has a fairly good amplitude response but its amplitude roll-off is slower than the Butterworth or Chebyshev filter.

Chebyshev:

The Chebyshev has a faster roll-off in the amplitude response which is achieved by introducing a ripple before the roll-off. They have a relatively nonlinear phase response.

Elliptic:

The Elliptical filter has the steepest roll-off in the amplitude response but it has a ripple in both the pass band and stop band. In addition, its phase response is highly nonlinear. This is only used for applications where phase shift or ringing is not of a concern; it should generally be avoided to the common test engineer because of its tendency to distort complex time signals.

Butterworth filters offer the best of both worlds with a relatively sharp amplitude drop off. Bessel has the best phase response and a reasonably good amplitude response but note begins filtering rather early. In general, the Butterworth filter is best for vibration and the Bessel is best for shock testing.

B.3 Windowing

If a signal is not periodic (starts and ends at 0), there will be leakage in the frequency domain because the signal is distorted. In order to minimize this error, windows are used to better make the signal appear periodic for the FFT process. The most common windows are the rectangular window, the Hanning window, the flattop, and the force/exponential window. However, any window will distort the data. Once a window function is chosen, multiply the window function, point by point, into the signal of interest. Then the FFT can be taken. Sometimes if more samples are considered, the unwindowed data can get better or worse; whereas the windowed data tends to mainly get better.

Appendix C

Derivation of Shock Distance

Although in reality, attenuation would occur as the wave propagates due to thermoviscous losses, we want to obtain the minimal possible shock distance and so, losses will also be neglected. For similar reasons, it will be assumed that the tubing before the flare is cylindrical. Under these assumptions, an expression for the shock distance, denoted by x_s, can be approximated. Using the method of characteristics, x_s can be derived for a simple finite-amplitude wave. Since we are assuming the bore is a uniform cylindrical tube, the exact solution for finite-amplitude sound waves will be used in addition to the ideal gas lawon Eulerian coordinates using a velocity potential.

Consider a piston at a fixed point x_o that has a velocity $u(x_o, t)$ for all time, t. Then, the wave propagation for outgoing waves in the positive x-direction can be described by the following wave equation

$$\frac{\partial u}{\partial t} + (c_o + \beta u)\left(\frac{\partial u}{\partial x}\right) = 0, \tag{C.1}$$

where u is the particle velocity, c_o is the sound speed and β is the coefficient of nonlinearity[1] [30]. The solution to (C.1) is

$$u = F\left(t - \frac{x}{c + \beta u}\right), \tag{C.2}$$

where F is a function determined by the initial condition [30]. The solution (C.2) is known as Poisson's solution and is valid until the shock forms in which a discontinuity develops,

[1] The coefficient of linearity in gas is defined as $\beta = \frac{1}{2}(1 + \gamma)$, where γ is the specific heat ratio which is approximately equal to 1.4 in air [30].

i.e., when $\frac{\partial u}{\partial t} = \infty$ [30]. Taking

$$u(0,t) = F(t) \tag{C.3}$$

and differentiating (C.2) gives

$$\frac{\partial u}{\partial t} = F' \left(1 + \frac{\beta x \frac{\partial u}{\partial t}}{(c+\beta u)^2} \right). \tag{C.4}$$

Solving for $\frac{\partial u}{\partial t}$, we obtain

$$\frac{\partial u}{\partial t} = \frac{F'}{1 - \frac{\beta x F'}{(c+\beta u)^2}}. \tag{C.5}$$

Note that $\frac{\partial u}{\partial t} = \infty$ when $1 - \frac{\beta x F'}{(c+\beta u)^2} = 0$, so we obtain

$$x_{vertical} = \frac{(c+\beta u)^2}{\beta F'}. \tag{C.6}$$

The smallest $x_{vertical}$ is the distance desired. Assuming $\beta|u| << c$ which is satisfied by nonlinear acoustics, the second term in the numerator can be ignored [30]. To obtain the smallest $x_{vertical}$, F' must be the maximum positive slope giving

$$x_s = \frac{c^2}{\beta \left(\frac{\partial F}{\partial t}\right)_{max}}. \tag{C.7}$$

Writing the shock formation distance in terms of pressure yields

$$x_s = \frac{\rho c^3}{\beta \left(\frac{\partial p}{\partial t}\right)_{max}}. \tag{C.8}$$

Notice that the shock distance is reciprocally dependent on the maximum change of the mouthpiece pressure with time. For an adiabatic gas, a further simplification can be made since we know that $c^2 = \frac{\gamma p}{\rho}$ and $\beta = \frac{1}{2}(\gamma + 1)$. Substituting these relations into (C.7), the following expression from [99] is obtained,

$$x_s = \frac{2\gamma p_0 c}{(1+\gamma)\left(\frac{\partial p}{\partial t}\right)_{max}}. \tag{C.9}$$

Expression (C.9) will allow us to determine if it is possible for shock waves to form within a certain range given a specific $\frac{\partial p}{\partial t}$.

Appendix D

Mathematical Prerequisites

D.1 The Material Derivative

Lets consider a fluid particle with position $\vec{x}(t)$ at some time t.
Let $f(x, y, z, t)$ or $f(\vec{x}, t)$ denote any property of interest for the fluid in motion.
The rate of change of f 'following the fluid' is denoted by $\frac{Df}{Dt}$ and defined as

$$\frac{Df}{Dt} = \frac{d}{dt}\left(f(x(t), y(t), z(t), t)\right.$$

where $x(t)$, $y(t)$, $z(t)$ change with time at the local flow velocity $\vec{u}$, where

$$\frac{dx}{dt} = u, \quad \frac{dy}{dt} = v, \quad \frac{dz}{dt} = w,$$

so as to 'follow the fluid'. By the chain rule we obtain

$$\begin{aligned}
\frac{Df}{Dt} &= \frac{\partial f}{\partial x}\frac{dx}{dt} + \frac{\partial f}{\partial y}\frac{dy}{dt} + \frac{\partial f}{\partial z}\frac{dz}{dt}\frac{\partial f}{\partial t} \\
&= \underbrace{(u, v, w)}_{=\vec{u}(t)} \cdot \underbrace{\left(\frac{\partial f}{\partial x}, \frac{\partial f}{\partial y}, \frac{\partial f}{\partial z}\right)}_{=\nabla f} + \underbrace{\frac{\partial f}{\partial t}}_{f_t} \\
&= \underbrace{f_t}_{\text{RoC in t}} + \underbrace{\vec{u} \cdot \nabla f}_{\text{RoC of f following the fluid}}
\end{aligned}$$

This operator is known as the *material derivative* and accounts for the rate of change with time and the motion of fluid particles. If we apply this definition to u, v and w, the acceleration of the fluid element at position $\vec{x}$ is defined as

$$\frac{D\vec{u}}{Dt} = \frac{\partial \vec{u}}{\partial t} + \vec{u} \cdot \nabla \vec{u}. \tag{D.1}$$

D.2 The Laws of Thermodynamics

A *thermodynamic system* is a quantity of matter separated from the environment by an enclosure. If a system is not given any mass, heat or work for a long time, it will reach equilibrium, i.e., the system will be independent of time. The *variables of state* are pressure, p; volume, V; and temperature, denoted by T. We will also need to include internal energy, denoted by E; and entropy, denoted by S which leads to:

Zeroth Law of Thermodynamics:

> There exists a variable of state, in this case temperature, T. If two systems are in thermal contact (i.e., separated by an enclosure that transmits heat) and in a state of thermal equilibrium, then the temperature in both systems has to be equal.

D.2.1 Internal energy for air

In classical kinetic theory, the Theorem of Equipartition of Energy says there is an average internal energy $E = \frac{1}{2}kT$ associated with every degree of freedom of the molecules in an ideal gas (where there is no intermolecular attraction). The variable k is called the Boltzmann's constant.

An atom in translational motion has 3 degrees of freedom, so the internal energy is $\frac{3}{2}kT$. For one mole of these atoms (which is expressed by the Avogadro constant N_A) the energy is

$$\frac{3}{2}T \underbrace{kN_A}_{=R \approx 8.3 \frac{J}{k\ mol}}$$

where R is the Universal gas constant. So the internal energy of a mole is

$$E = \frac{3}{2}RT. \tag{D.2}$$

For a mole of molecules composed of two atoms (known as diatomic molecules), there are 3 translational degrees of freedom, and 2 rotational degrees of freedom. So the internal energy is $E = \frac{5}{2}RT$. Since air mostly consists of nitrogen and oxygen, we can consider it as a diatomic gas. So a reasonable approximation for the internal energy of air is

$$E = \frac{5}{2}RT. \tag{D.3}$$

We will now examine what happens when a gas is heated and its volume is allowed to vary. In turn, this will tell us how temperature and pressure change.

Denoting Q to be the amount of heat that is absorbed or given up by a volume of gas, and denoting W to be the work done on the volume. The change in internal energy is given by the first law of thermodynamics.

First Law of Thermodynamics:

> There exists a variable of state, in this case internal energy, E. Heat, denoted by Q, and work, denoted by W, are forms of energy transfer. All the energy associated with a system must be accounted for as heat, work, chemical energy etc., Therefore, the difference in energy of a system must be equal to the sum of the work and heat, i.e.,
>
> $$dE = dQ + dW. \tag{D.4}$$

We then define work as

$$W = \int \vec{F} \cdot d\vec{r}, \tag{D.5}$$

where $\vec{F}$ is the force vector, and $d\vec{r}$ is a displacement vector. We can relate this force to the pressure p and surface area, A, to give

$$W = \int pAd\vec{r} = -\int pdV, \tag{D.6}$$

with the convention that $dV > 0$ if the volume of the system is increasing. Using this relation for work, we obtain

$$dE = dQ - pdV. \tag{D.7}$$

If we neglect viscous and magnetic effects then $W = pdV$ and

$$dE = Q - pdV. \tag{D.8}$$

D.2.2 Entropy of a gas

All natural/spontaneous processes are *irreversible*. If we suddenly stir a fluid or add heat, it induces currents in the system (currents refers to the flux of a quantity like heat, mass, momentum, etc.). A system is in equilibrium if it has no currents. A process leading from one state to another is called *reversible* if the system remains in equilibrium the whole time (i.e., if $W + Q$ are added but no currents are produced).

Entropy, denoted by S, is a measure of randomness. For a gas, it is the amount of thermal energy that is not available to be converted into mechanical energy. If the amount of heat Q is absorbed at an absolute temperature T, then S increases by the amount

$$dS = \frac{Q}{T}. \tag{D.9}$$

Second Law of Thermodynamics:

> There exists an extensive variable of state, in this case entropy, S; and an intensive variable, T, the absolute temperature. The entropy difference between state A and state B is
>
> $$S_b - S_a = \int_A^B \frac{dQ}{T} \quad \text{or} \quad dE = TdS - pdV \tag{D.10}$$

D.3 Derivation for Internal Energy:

Let's consider $E = E(S, V)$, then we can write

$$dE = \underbrace{\left(\frac{\partial E}{\partial S}\right)_V}_{=T} dS + \underbrace{\left(\frac{\partial E}{\partial V}\right)_S}_{=-p} dV \tag{D.11}$$

There are two other energies that measure how much energy the gas has available to exchange with its surroundings.

1. Enthalpy: Amount of heat content used/released in system

$$H = E + pV. \tag{D.12}$$

2. Free energy: Amount of energy is the system that can be converted to do work

$$F = E - TS. \tag{D.13}$$

We have that

$$\begin{aligned} dH &= dE + pdV + Vdp \\ &= \left(\frac{\partial E}{\partial S}\right)_V dS + \left(\frac{\partial E}{\partial V}\right)_S dV + pdV + Vdp \\ &= TdS - pdV + pdV + Vdp \\ &= TdS + Vdp. \end{aligned}$$

If we also consider $H = H(S, p)$, then we can write

$$\begin{aligned} dH &= \underbrace{\left(\frac{\partial H}{\partial S}\right)_p}_{=T} dS + \underbrace{\left(\frac{\partial H}{\partial p}\right)_S}_{=V} dp \\ &= TdS + Vdp \end{aligned}$$

Assuming smoothness of the second partial derivatives of the enthalpy and free energy respectively gives

$$\left(\frac{\partial T}{\partial p}\right)_S = \left(\frac{\partial V}{\partial S}\right)_p, \qquad \left(\frac{\partial p}{\partial T}\right)_V = \left(\frac{\partial S}{\partial V}\right)_T.$$

If the gas absorbs an amount of heat Q and its temperature raised by dT, we can define the specific heat as

$$c = \frac{Q}{dT}. \tag{D.14}$$

And the first law of thermodynamics states that

$$dE = c\ dT - p\ dV$$

so if this heat absorption takes place at a constant volume, we have $c = c_V$ and the specific heat at a constant volume for an ideal gas is

$$\begin{aligned} dE &= c_v dT \\ c_v &= \left(\frac{\partial E}{\partial T}\right)_V \approx \frac{5}{2}R. \end{aligned}$$

If absorption of the heat takes place at a constant pressure, we have $c = c_p$ (and $dp = 0$) and the specific heat at a constant pressure for diatomic ideal gas is

$$\begin{aligned} dE &= cdT - pdV \\ \left(\frac{\partial E}{\partial T}\right)_p &= c_p - p\left(\frac{\partial V}{\partial T}\right)_p \\ c_p &= \left(\frac{\partial E}{\partial T}\right)_p + p\left(\frac{\partial V}{\partial T}\right)_p \\ c_p &= \frac{\partial}{\partial T}\left(\underbrace{E + pV}_{=H}\right)_p \\ c_p &= \left(\frac{\partial H}{\partial T}\right)_p \approx \frac{7}{2}R. \end{aligned}$$

We now need to determine the relationship between c_p and c_V. Consider $E = E[V(p,T),T]$, then

$$\begin{aligned} c_p &= \left(\frac{\partial H}{\partial T}\right)_p \\ c_p &= \frac{\partial}{\partial T}\left(E[V(p,T),T] + pV(p,T)\right)_p \\ c_p &= \underbrace{\left(\frac{\partial E}{\partial V}\right)_T}_{=c_V}\left(\frac{\partial V}{\partial T}\right)_p + \left(\frac{\partial HE}{\partial T}\right)_V + p\left(\frac{\partial V}{\partial T}\right)_p \\ c_p &= c_V + \left(\frac{\partial V}{\partial T}\right)_p\left[\left(\frac{\partial E}{\partial T}\right)_V + p\right] \qquad (*) \end{aligned}$$

From the second law of thermodynamics we have

$$\begin{aligned} dE &= TdS - pdV \\ \left(\frac{\partial E}{\partial V}\right)_T &= T\left(\frac{\partial S}{\partial V}\right)_T - p \end{aligned}$$

and substituting this into $(*)$ gives

$$
\begin{aligned}
c_p &= c_V + \left(\frac{\partial V}{\partial T}\right)_p \left[\left(T\left(\frac{\partial S}{\partial V}\right)_T - \not{p}\right) + \not{p}\right] \\
c_p &= c_V + \left(\frac{\partial V}{\partial T}\right)_p T \underbrace{\left(\frac{\partial S}{\partial V}\right)_T}_{\left(\frac{\partial p}{\partial T}\right)_V} \\
c_p &= c_V + T\left(\frac{\partial V}{\partial T}\right)_p \left(\frac{\partial p}{\partial T}\right)_V \qquad (**)
\end{aligned}
$$

For one mole of an ideal gas $pV = RT$ where $\left(\frac{\partial p}{\partial T}\right)_V = \frac{R}{V}$ and $\left(\frac{\partial V}{\partial T}\right)_p = \frac{R}{p}$. Hence we can write $(**)$ as

$$
\begin{aligned}
c_p &= c_V + T\frac{R}{p}\frac{R}{V} \\
c_p &= c_V + \frac{(\not{p}\not{V})}{\not{p}}\frac{R}{\not{V}} \\
c_p &= c_V + R
\end{aligned}
$$

From the second law of thermodynamics we also have

$$
\begin{aligned}
dE &= TdS - pdV \\
TdS &= dE + pdV \\
dS &= c_V\frac{dT}{T} + \frac{p}{T}dV \\
dS &= c_V\frac{dT}{T} + R\frac{dV}{V} \\
dS &= c_V\frac{dT}{T} + (c_p - c_V)\frac{dV}{V} \\
dS &= c_V\frac{dT}{T} + c_V\left(\frac{c_p}{c_V} - 1\right)\frac{dV}{V} \\
\frac{dS}{c_V} &= \frac{dT}{T} + \left(\underbrace{\frac{c_p}{c_V}}_{=\gamma} - 1\right)\frac{dV}{V} \\
\frac{dS}{c_V} &= \frac{dT}{T} + (\gamma - 1)\frac{dV}{V}
\end{aligned}
$$

where γ is the ratio of specific heats. Next we integrate to yield

$$\begin{aligned}
\int \frac{dS}{c_V} &= \int \frac{dT}{T} + (\gamma - 1) \int \frac{dV}{V} \\
\frac{S}{c_V} &= \log(T) + (\gamma - 1)\log(V) + C \\
\frac{S}{c_V} &= \log(T) + \log(V)^{(\gamma-1)} + C \\
\frac{S}{c_V} &= \log(TV^{(\gamma-1)}) + C \\
e^{\frac{S}{c_V}} &= TV^{(\gamma-1)} \cancel{e^{C}}^{1} \qquad p = \rho RT, \;\; pV = RT \\
e^{\frac{S}{c_V}} &= \left(\frac{p}{\rho \cancel{R}}\right)\left(\frac{\cancel{R}T}{p}\right)^{(\gamma-1)} \\
e^{\frac{S}{c_V}} &= \left(\frac{p}{\rho}\right)\left(\frac{1}{\rho R}\right)^{(\gamma-1)}
\end{aligned}$$

$$\begin{aligned}
e^{\frac{S}{c_V}} &= \left(\frac{p}{\cancel{\rho}}\right)\left(\frac{1}{\rho^{(\gamma-1)}}\right)\left(\frac{1}{\cancel{R}^{(\gamma-1)}}^{\text{const}}\right) \\
e^{\frac{S}{c_V}} &= \left(\frac{p}{\rho^{\gamma}}\right) C
\end{aligned}$$

So, we obtain

$$\begin{aligned}
\frac{S}{c_V} &= \log\left(\left(\frac{p}{\rho^{\gamma}}\right) C\right) \\
\frac{S}{c_V} &= \log\left(\frac{p}{\rho^{\gamma}}\right) + \text{const} \\
p &= \kappa e^{\frac{S}{c_V}} \rho^{\gamma} \qquad \kappa = \text{const}
\end{aligned}$$

For a diatomic ideal gas, $\gamma \approx 1.4$. The entropy of a gas satisfies this equation. The internal energy of a unit mass of can be written as

$$E = c_V T = \frac{p}{(\gamma - 1)\rho}. \tag{D.15}$$

D.4 Derivation of Equations of Motion

D.4.1 Conservation of Mass

Consider a fixed volume, V, inside of a fluid. The net mass in V at any time, t, can be taken as the volume integral of a density, $\rho(\vec{x}, t)$. This represents the local average of mass per unit volume around $\vec{x}$. By conservation of mass,

$$\begin{pmatrix}\text{time rate}\\ \text{of change}\end{pmatrix} = \begin{pmatrix}\text{net mass per unit time entering}\\ V \text{ through the confined surface } S\end{pmatrix} + \begin{pmatrix}\text{source}\\ \text{term}\end{pmatrix}.$$

The net mass per unit time leaving through a small area element ΔS, with outward normal vector $\hat{n}(\vec{x}_s)$ centered at point $\vec{x}_s$ on S can be expressed as

$$\rho(\vec{x}_s, t)\vec{v}(\vec{x}_s, t) \cdot \hat{n}(\vec{x}_s)\Delta S,$$

where $\vec{v}(\vec{x}_s, t)$ is the fluid velocity at $\vec{x}$. The net mass leaving V per unit time is the surface integral over S of $(\rho\vec{v} \cdot \hat{n})$ and so, conservation of mass requires

$$\frac{\mathrm{d}}{\mathrm{dt}} \underbrace{\int\int\int_V \rho \, \mathrm{d}V}_{\text{total mass}} = \underbrace{-\int\int_S \rho\vec{v} \cdot \hat{n} \, \mathrm{dS}}_{\text{mass flux out through surface}} + \underbrace{\int\int\int_V Q \, \mathrm{d}V}_{\text{source term}}$$

$$\int\int\int_V \rho_t \, \mathrm{d}V = \underbrace{-\int\int\int_V \nabla \cdot (\rho\vec{v}) \, \mathrm{d}V}_{\text{by Gauss' Theorem}} + \int\int\int_V Q \, \mathrm{d}V$$

$$\int\int\int_V [\rho_t + \nabla \cdot (\rho\vec{v}) - Q] \, \mathrm{d}V = 0$$

$$\rho_t + \nabla \cdot (\rho\vec{v}) = Q \quad \text{Continuity Equation.} \tag{D.16}$$

If there is no source term, then the right hand side is set to zero, i.e., $Q(t) = 0$.

D.4.2 Conservation of Momentum

Next, consider a fluid particle that consists of all fluid within some moving volume V. Each point is moving with local fluid velocity $\vec{v}(\vec{x}_s, t)$. The mass in such a fluid particle

is constant and so, $(m\vec{a})$ is the time rate of change of momentum within the particle. Therefore, by Newton's second law,

$$\begin{pmatrix}\text{rate of change of}\\ \text{momentum in V}\end{pmatrix} = \begin{pmatrix}\text{total net}\\ \text{forces}\end{pmatrix} + \begin{pmatrix}\text{momentum flux}\\ \text{through surface S}\end{pmatrix}.$$

The net influx of momentum per unit time leaving through a small area element ΔS, with outward normal vector $\hat{n}(\vec{x}_s)$ centered at point $\vec{x}_s$ on S can be expressed by

$$[\rho(\vec{x}_s,t)\vec{v}(\vec{x}_s,t)]\vec{v}(\vec{x}_s,t)\cdot\hat{n}(\vec{x}_s)\Delta S,$$

where $\vec{v}(\vec{x}_s,t)$ is the fluid velocity at $\vec{x}$. The net influx of momentum leaving V per unit time is the surface integral over S of $\rho\vec{v}\cdot\hat{n}$. Conservation of momentum thus requires

$$\frac{\mathrm{d}}{\mathrm{dt}}(m\vec{v}) = \vec{f}_{\text{Body}} + \vec{f}_{\text{Surface}} + \int\int_S \rho\vec{v}\cdot\hat{n}\ \mathrm{dS}$$

$$\frac{\mathrm{d}}{\mathrm{dt}}\underbrace{\int\int\int_V \rho\vec{v}\ \mathrm{d}V}_{\text{total momentum}} = \underbrace{\int\int\int_V \rho\vec{f}_{\text{grav}}\ \mathrm{d}V}_{\text{total body force e.g., gravity}} + \underbrace{\int\int_S \vec{\tau}\cdot\hat{n}\ \mathrm{dS}}_{\text{viscous force, }\vec{\tau}\text{ stress tensor}} + \underbrace{\int\int_S \rho\vec{v}\cdot\hat{n}\ \mathrm{dS}}_{\text{net influx of momentum}}$$

For a compressible fluid with thermodynamic pressure, p, the stress tensor is defined as

$$\tau_{ij} = -\left(p + \frac{2}{3}\mu\nabla\cdot\vec{v}\right)\delta_{ij} + 2\mu e_{ij}, \tag{D.17}$$

where $i = 1,2,3$, μ is the shear viscosity, and e_{ij} is the deformation tensor defined by

$$e_{ij} = \frac{1}{2}\left(\frac{\partial u_i}{\partial x_j} + \frac{\partial u_j}{\partial x_i}\right). \tag{D.18}$$

Using the fact that the pressure produces a normal force on the control surface, we obtain

$$\frac{\mathrm{d}}{\mathrm{dt}}\int\int\int_V \rho\vec{v}\ \mathrm{d}V = \int\int\int_V \rho\ \underbrace{\vec{f}_{\text{Body}}}_{\text{e.g. gravity}}\ \mathrm{d}V + \underbrace{\int\int_S \vec{f}_{\text{Surface}}\ \mathrm{dS}}_{\int\int_S p\vec{e}\cdot\hat{n}\ \mathrm{dS}}$$

$$+ \int\int_S \vec{\tau}\cdot\hat{n}\ \mathrm{dS} + \int\int_S \rho\vec{v}\cdot\hat{n}\ \mathrm{dS}$$

$$\frac{\mathrm{d}}{\mathrm{dt}}\int\int\int_V \rho\vec{v}\ \mathrm{d}V = \underbrace{\int\int_S p\vec{e}\cdot\hat{n}\ \mathrm{dS} + \int\int_S \vec{\tau}\cdot\hat{n}\ \mathrm{dS} + \int\int_S \rho\vec{v}\cdot\hat{n}\ \mathrm{dS}}_{\text{by Gauss' Theorem}}$$

$$\int\int\int_V (\rho\vec{v})_t \, \mathrm{d}V = -\int\int\int_V \nabla\cdot(p\vec{e}) \, \mathrm{d}V + \int\int\int_V \nabla\cdot\tau \, \mathrm{d}V - \int\int\int_V \nabla\cdot(\rho\vec{v}) \, \mathrm{d}V$$

$$0 = \int\int\int_V [(\rho\vec{v})_t + \nabla p - \nabla\cdot\tau + \nabla\cdot(\rho\vec{v})] \, \mathrm{d}V$$

$$0 = \int\int\int_V \left[\rho\frac{D\vec{v}}{Dt} - \nabla p + \nabla\cdot\tau\right] dV$$

$$\rho\frac{D\vec{v}}{Dt} = -\nabla p + \nabla\cdot\tau \qquad \text{Navier-Stokes Equation.} \tag{D.19}$$

D.4.3 Conservation of Energy

Using equations (D.16) and (D.19), the conservation of energy equation for an ideal, inviscid flow can be derived. The energy per unit mass of the gas consists of the internal energy, E, and the kinetic energy, $E_k = \frac{1}{2}, \vec{u}\cdot\vec{u}$. i.e.,

$$\begin{pmatrix}\text{total}\\ \text{energy}\end{pmatrix} = \begin{pmatrix}\text{internal}\\ \text{energy}\end{pmatrix} + \begin{pmatrix}\text{kinetic}\\ \text{energy}\end{pmatrix}$$

The energy conservation equation relates the flux of this energy to the rate of work of the pressure forces, i.e.,

$$\frac{d}{dt}\rho\left(E + \frac{1}{2}\vec{u}\cdot\vec{u}\right) + \nabla\cdot\left(\rho E + \frac{1}{2}\rho\vec{u}\cdot\vec{u} + p\right)\vec{u} = 0$$

$$\frac{d}{dt}\left(\rho E + \frac{1}{2}\rho\vec{u}\cdot\vec{u}\right) + \nabla\cdot\left(\rho E + \frac{1}{2}\rho\vec{u}\cdot\vec{u}\right)\vec{u} + \nabla\cdot(p\vec{u}) = 0$$

$$\frac{D}{Dt}\left(\rho E + \frac{1}{2}\rho\vec{u}\cdot\vec{u}\right) + \left(\rho E + \frac{1}{2}\rho\vec{u}\cdot\vec{u}\right)\nabla\cdot\vec{u} + \nabla\cdot(p\vec{u}) = 0$$

$$\frac{D\rho}{Dt}E + \frac{DE}{Dt}\rho + \frac{D\rho}{Dt}\frac{1}{2}\vec{u}\cdot\vec{u} + \rho\vec{u}\cdot\underbrace{\frac{D\vec{u}}{Dt}}_{=-\frac{1}{\rho}\nabla p} + \left(\rho E + \frac{1}{2}\rho\vec{u}\cdot\vec{u}\right)\underbrace{\nabla\cdot\vec{u}}_{=-\frac{1}{\rho}\frac{D\rho}{Dt}} + p\nabla\cdot\vec{u} + \vec{u}\cdot\nabla p = 0$$

$$\frac{D\rho}{Dt}E + \frac{DE}{Dt}\rho + \frac{D\rho}{Dt}\frac{1}{2}\vec{u}\cdot\vec{u} - \left(E + \frac{1}{2}\vec{u}\cdot\vec{u}\right)\frac{D\rho}{Dt} + p\nabla\cdot\vec{u} = 0$$

$$\frac{D\rho}{Dt}\underbrace{\left(E + \frac{1}{2}\vec{u}\cdot\vec{u} - \left(E + \frac{1}{2}\vec{u}\cdot\vec{u}\right)\right)}_{\to 0} + \frac{DE}{Dt}\rho + p\underbrace{\nabla\cdot\vec{u}}_{=-\frac{1}{\rho}\frac{D\rho}{Dt}} = 0$$

This yields equation for conservation of energy, i.e.,

$$\frac{DE}{Dt} - \frac{p}{\rho^2}\frac{D\rho}{Dt} = 0. \tag{D.20}$$

It is assumed that the flow is adiabatic, i.e., energy is transferred only as work. From Appendix D, we know that

$$TdS = dE - pdV$$
$$TdS = dE - \frac{p}{\rho^2}d\rho \implies \frac{DS}{Dt} = 0$$

which is an equation describing conservation of energy for an ideal, inviscid flow. Physically, this means that entropy is advected with the flow and hence, is constant on streamlines. Assuming we have an ideal gas implies two things: firstly, that $c^2 = \frac{\gamma p}{\rho}$ and secondly, the molecular diffusivity is zero, i.e., no heat can be transferred between fluid particles, which means entropy must be in a thermodynamic equilibrium. This type of flow is called *isentropic*.

D.5 Compressible Bernoulli's Equations

D.5.1 Bernoulli's Theorem

In regions of flow, if there is no heat transfer along streamlines and the net friction forces are small, then the main forces acting along the z-direction are due to pressure.

Assuming we are concerned with the z-direction, an unsteady flow is considered, then $u = u(z,t)$ and by Newton's second law,

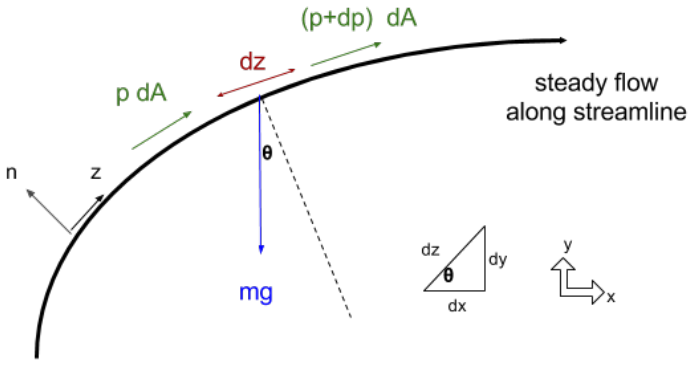

$$\sum F_z = ma_z$$

$$p\,dA - (p+dp)\,dA - mg\sin(\theta) = m\left(u\,\frac{du}{dz} + \frac{du}{dt}\right)$$

$$p\,dA - (p+dp)\,dA - (\rho\,dA\,dz\,g)\,\frac{dy}{dz} = \rho\,dA\,dz\,\left(u\,\frac{du}{dz} + \frac{du}{dt}\right)$$

$$-dp - \rho g\,dy = \rho u\,du + \rho\,\frac{du}{dt}\,dz$$

$$0 = \frac{dp}{\rho} + g\,dy + \frac{1}{2}\,d(u^2) + \frac{du}{dt}\,dz$$

$$C = \int \frac{dp}{\rho} + gy + \frac{1}{2}u^2 + \int \frac{du}{dt}\,dz.$$

Assuming that gravity can be ignored, integrating yields

$$C = \int \frac{dp}{\rho} + \frac{1}{2}u^2 + \int \frac{du}{dt}\,dz \tag{D.21}$$

which is is Bernoulli's equation for an unsteady compressible flow [1]. For an isentropic flow[2], we know that

$$\frac{p}{\rho^\gamma} = C \implies \rho = C^{-\frac{1}{\gamma}} p^{\frac{1}{\gamma}},$$

and so we can write

$$\begin{aligned}
\int \frac{dp}{\rho} &= \int C^{\frac{1}{\gamma}} p^{-\frac{1}{\gamma}}\,dp \\
&= \frac{1}{1-\frac{1}{\gamma}} C^{\frac{1}{\gamma}} p^{1-\frac{1}{\gamma}} \\
&= \frac{\gamma}{\gamma-1}\left(\frac{p}{\rho^\gamma}\right)^{\frac{1}{\gamma}} p^{1-\frac{1}{\gamma}} \\
&= \frac{\gamma}{\gamma-1}\left(\frac{p}{\rho}\right).
\end{aligned}$$

[1] Bernoulli's equation can be viewed as mechanical energy balance.

[2] A reversible and adiabatic process with no heat transfer, no heat generated from internal friction and with constant entropy. Note that in a duct, the pressure and temperature of the gas may change. For dry air, the specific heat ratio is $\gamma \approx 1.4$.

Using this in D.21, we can write Bernoulli's equation as for an unsteady, compressible flow as follows,

$$C = \frac{\gamma}{\gamma - 1}\left(\frac{p}{\rho}\right) + \frac{1}{2}u^2 + \int \frac{du}{dt}\, dz. \tag{D.22}$$

If it is further assumed that

i. The flow is steady, i.e., $\int \frac{du}{dt}\, dz = 0$,

ii. The gas is ideal, i.e., $p = \rho RT$, $c = \sqrt{\frac{\gamma p}{\rho}} = \sqrt{\gamma RT}$,

ii. The gas accelerates from rest isentropically, i.e., there is a stagnation point in the first state (so the kinetic energy has been converted to pressure energy), i.e., $u_1 = 0$.

Then, in such a situation, using (D.21), we have that

$$\frac{\gamma}{\gamma - 1}\left(\frac{p_1}{\rho_1}\right) = \frac{\gamma}{\gamma - 1}\left(\frac{p_2}{\rho_2}\right) + \frac{1}{2}u_2^2 \tag{D.23}$$

This expression holds for adiabatic flow. Considering a isentropic flow, we can state that

$$\frac{p_2}{\rho_2^\gamma} = \frac{p_1}{\rho_1^\gamma}$$

and using this relationship, we can eliminate ρ_2 in (D.23), i.e.,

$$\begin{aligned}
\frac{\gamma}{\gamma - 1}\left[\frac{p_1}{\rho_1}\left(\frac{p_2}{p_1}\right)^{\frac{\gamma-1}{\gamma}}\right] + \frac{1}{2}u_2^2 &= \frac{\gamma}{\gamma - 1}\left(\frac{p_1}{\rho_1}\right) \\
\frac{1}{2}u_2^2 &= \frac{\gamma}{\gamma - 1}\left(\frac{p_1}{\rho_1}\right)\left[1 - \left(\frac{p_2}{p_1}\right)^{\frac{\gamma-1}{\gamma}}\right] \\
u_2 &= \sqrt{\frac{2\gamma}{\gamma - 1}\left(\frac{p_1}{\rho_1}\right)\left[1 - \left(\frac{p_2}{p_1}\right)^{\frac{\gamma-1}{\gamma}}\right]}.
\end{aligned} \tag{D.24}$$

Equation (D.24) is Bernoulli's equation for a steady, compressible flow.

D.6 Derivation of Riemann Invariants

If the entropy, denoted by S, is spatially uniform, the flow is called *homentropic*, i.e., a homentropic flow with no shock waves, $S = S_0$, then

$$p = k\rho^{\gamma}, \tag{D.25}$$

where $k = \kappa e^{\frac{S_0}{c_V}} =$ constant. This is the relationship between pressure and density that we used for linear waves. Furthermore, it allows us to write conservation of mass and momentum as

$$\begin{aligned}
\frac{D\rho}{Dt} + \rho\nabla\cdot\vec{u} &= 0 \\
\frac{\partial\rho}{\partial t} + \vec{u}\cdot\nabla\rho + \rho\nabla\cdot\vec{u} &= 0 \\
\frac{\partial\rho}{\partial t} + \nabla\cdot(\rho\vec{u}) &= 0
\end{aligned}$$

$$\begin{aligned}
\frac{D\vec{u}}{Dt} + \frac{1}{\rho}\nabla p &= 0 \\
\frac{\partial\vec{u}}{\partial t} + \vec{u}\cdot\nabla\vec{u} + \frac{1}{\rho}\nabla(k\rho^{\gamma}) &= 0 \\
\frac{\partial\vec{u}}{\partial t} + \vec{u}\cdot\nabla\vec{u} + k\gamma\rho^{(\gamma-2)}\nabla\rho &= 0.
\end{aligned}$$

Considering a 1D flow for convenience, we can write conservation of mass and momentum as

$$\frac{\partial\rho}{\partial t} + \frac{\partial}{\partial x}(\rho u) = 0 \tag{D.26}$$

$$\frac{\partial u}{\partial t} + u\frac{\partial u}{\partial x} + k\gamma\rho^{(\gamma-2)}\frac{\partial\rho}{\partial x} = 0 \tag{D.27}$$

The easiest way to construct characteristic curves for this system is to consider the system in terms of u and the local sound speed, i.e.,

$$\begin{aligned}
c &= \sqrt{\left(\frac{\partial p}{\partial\rho}\right)_S} = \sqrt{k\gamma\rho^{(\gamma-1)}} \\
\implies \rho &= \left(\frac{c^2}{k\gamma}\right)^{\frac{1}{\gamma-1}}.
\end{aligned}$$

In terms of c, the equations can be written as

$$\begin{aligned}
\frac{\partial \rho}{\partial t} + \frac{\partial}{\partial x}(\rho u) &= 0 \\
\frac{\partial}{\partial t}\left(\frac{c^2}{k\gamma}\right)^{\frac{1}{\gamma-1}} + \frac{\partial}{\partial x}\left(\left(\frac{c^2}{k\gamma}\right)^{\frac{1}{\gamma-1}} u\right) &= 0 \\
\frac{\partial}{\partial t}\left(c^2\right) + \frac{\partial}{\partial x}\left(c^2 u^{(\gamma-1)}\right) &= 0 \\
2\frac{\partial c}{\partial t} + 2\frac{\partial c}{\partial x} u^{(\gamma-1)} + (\gamma-1)c^2 \frac{\partial u^{(\gamma-2)}}{\partial x} &= 0 \\
2\frac{\partial c}{\partial t} + 2u\frac{\partial c}{\partial x} + (\gamma-1)c\frac{\partial u}{\partial x} &= 0 \\
\frac{\partial u}{\partial t} + u\frac{\partial u}{\partial x} + k\gamma\rho^{(\gamma-2)}\frac{\partial \rho}{\partial x} &= 0 \\
\frac{\partial u}{\partial t} + u\frac{\partial u}{\partial x} + k\gamma\left(\left(\frac{c^2}{k\gamma}\right)^{\frac{1}{\gamma-1}}\right)^{(\gamma-2)} \frac{\partial}{\partial x}\left(\left(\frac{c^2}{k\gamma}\right)^{\frac{1}{\gamma-1}}\right) &= 0 \\
\frac{\partial u}{\partial t} + u\frac{\partial u}{\partial x} + k\gamma\left(\frac{c}{k\gamma}\right)^{\frac{(2(\gamma-2))}{\gamma-1}} \frac{2}{k\gamma(\gamma-1)}\frac{\partial c^{\frac{-\gamma}{(\gamma-1)}}}{\partial x} &= 0
\end{aligned}$$

$$\begin{aligned}
\frac{\partial u}{\partial t} + u\frac{\partial u}{\partial x} + \frac{2}{(\gamma-1)}\left(\frac{c}{k\gamma}\right)^{\frac{2(\gamma-2)}{\gamma-1}} \frac{\partial c}{\partial x} &= 0 \\
\frac{\partial u}{\partial t} + u\frac{\partial u}{\partial x} + \frac{2c}{(\gamma-1)}\frac{\partial c}{\partial x} &= 0
\end{aligned}$$

Subtracting these equations, we obtain

$$\frac{\partial}{\partial t}\left(u \pm \frac{2c}{\gamma-1}\right) + (u \pm c)\frac{\partial}{\partial x}\left(u \pm \frac{2c}{\gamma-1}\right) = 0$$

Thus, the functions

$$\mathcal{R}_{\pm}(u,c) = u \pm \frac{2c}{\gamma-1}$$

are called the *Riemann invariants* of the system and constant on the two sets of characteristic curves, $X_{\pm}(t)$, where

$$\frac{dX_{\pm}}{dt} = u \pm c,$$

where these are not necessarily straight lines. On the C_+ characteristic, given by $\frac{dX_+}{dt} = (u + c)$, the C_+ invariant

$$\mathcal{R}_+ = \left(u + \frac{2c}{\gamma - 1} \right) \text{ is const.}$$

On the $\mathcal{C}_-$ characteristic, given by $\frac{dX_-}{dt} = (u - c)$, the $\mathcal{C}_-$ invariant

$$\mathcal{R}_- = \left(u - \frac{2c}{\gamma - 1} \right) \text{ is const.}$$

Given an initial value problem, for the solution to be well-defined, a single $\mathcal{C}_+$ and $\mathcal{C}_-$ characteristic must pass through each point in the domain of the solution. The values of u and ρ at each point can then be determined from the initial values of $\mathcal{R}_\pm$ on each characteristic.

Appendix E

Matlab Code

```
% Read in experimental data
% Initialize variables.
filename   = '/home/jr/Documents/MATLAB/Exp/.txt';
delimiter  = ',';
startRow   = 8;
% Format for each line of text:
formatSpec = '%*s%*s%f%f%f%f%*s%[^\n\r]';
% Open the text file.
fileID = fopen(filename,'r');
% Read columns of data according to the format.
dataArray = textscan(fileID, formatSpec, 'Delimiter', delimiter, ...
    'TextType', 'string', 'EmptyValue', NaN, 'HeaderLines' ...
    ,startRow-1, 'ReturnOnError', false, 'EndOfLine', '\r\n');
% Close the text file.
fclose(fileID);
% Create output variable
data = [dataArray{1:end-1}];
% Clear temporary variables
clearvars filename delimiter startRow formatSpec fileID dataArray ans;

% Read in pressure wanted, e.g.: let x be column wanted
pressurePosition = data(:,x); % This is in voltage
PressureAt- = pressurePosition*cal_factor; % Convert from voltage to Pa
```

```
% Filters used for accelerometer data and bell data when low ...
    frequency noise needed to be filtered
```

```
% Apply filter for bell
Fs          = 100000;            % Sampling frequency
Order_bell  = 5;                 % Order
Fc_bell     = 230;               % Cutoff frequency
fnorm_bell  = Fc_bell / (Fs/2);  % Normalized cutoff frequency

% Apply filter for accelerometer
Order       = 5;                 % Order
Fc          = 5000;              % Cutoff frequency
fnorm       = Fc / (Fs/2);       % Normalized cutoff frequency

% Create butterworth filter
[b,a] = butter(Order_bell,fnorm_bell,'high');
low_pass_data_bell = filtfilt(b,a,bell);

[b1,a1] = butter(Order,fnorm,'low');
low_pass_data_acc1 = filtfilt(b1,a1,acc1);

[b2,a2] = butter(Order,fnorm,'low');
low_pass_data_acc2 = filtfilt(b2,a2,acc2);
```

```
%Get Path where sim results are
path    = 'G:\Acoustics_Research\PhD\';

dir     = '\SimOfInterest\';
tempDir = strcat(path,dir);

%Get sensors from simulation result
SensorOfInterest   = 'sensor_x.txt';

%Read in sensor data
data = load(fullfile(tempDir,SensorOfInterest));
% Use function plotDataAxi or plotData, e.g.:
[realtime,rho,u,v,E,point1,point2,mPressure] = plotDataAxi(data, n, ...
    startpoint, endpoint)
```

```
function [realtime,rho,u,v,E,point1,point2,mPressure] = ...
    plotDataAxi(data, n, startpoint, endpoint)
% Read in file and preforms Fourier analysis.
% Plots the data in the time and frequency domain.
% The time and frequency space parameters are given as outputs

```

```
gamma=1.4;
n=randi([0 20]); % Randomize the colour for the plots
col=hsv(20);

% Initialize variables.
if nargin<=2
    startpoint = 0;
    endpoint = length(data(:,1));
    n=1;
end

% Get columns from data file
time    = data(:,1);
rho     = data(:,2);
u_rho   = data(:,3);
v_rho   = data(:,4);
E       = data(:,5);
u       = u_rho./rho;
v       = v_rho./rho;
p       = (gamma-1).*E-0.5*rho.*((u.*u)+(v.*v));

% Plot raw data
figure(1)
hold on
plot(time,101325*p-101325,'color',col(n,:));
grid on
title('Pressure wrt Sim Time')
xlabel('Sim Time')
ylabel('Pressure [Pa]')

% State what the first and last point of the selected period is
if startpoint == 0
    point1 =1;
else
    point1=floor((length(data)/time(length(data)))*(startpoint));
end

if endpoint == length(data(:,1))
    point2=length(time);
else
    point2=floor((length(data)/time(length(data)))*(endpoint));
end

% Find the number of points in the period
diff        = point2-point1;
```

```
51
52 % Find real time and pressure in proper units
53 realtime    = (0.002915451)*data(:,1);
54 pabs        = (gamma-1).*E - 0.5*((u_rho.*u_rho)+(v_rho.*v_rho))./rho;
55 p           = 101325*(pabs - 1);
56 mPressure   = 101325*pabs(point1:point2)-101325;
57 mVelocity   = 343*u(point1:point2);
58
59 % Plot pressure period of interest in proper units
60 figure(2)
61 hold on
62 plot(realtime(point1:point2),mPressure,'color',col(n,:));
63 grid on
64 title('Pressure Waveform wrt Time')
65 xlabel('Time [s]')
66 ylabel('Pressure [Pa]')
67
68 % Plot velocity in proper units
69 figure(3)
70 hold on
71 plot(realtime,343*u,'color',col(n,:));
72 grid on
73 title('Velocity Waveform wrt Time')
74 xlabel('Time [s]')
75 ylabel('Velocity [m/s]')
76
77 % Find parameters for FFT in proper units
78 N           = length(p);
79 nnyquist    = floor((diff/2)+1);
80 fs          = 343*floor(length(data(:,1))/data(length(data(:,1)),1));
81 freq        = ([1:nnyquist]-1)*(fs/diff);
82
83 % Get FFT
84 myFFT       = (1/diff)*fft(mPressure);
85 myFFTv      = (1/diff)*fft(mVelocity);
86
87 % Get FFT in SPL dB and the frequency and phase angle (ignoring DC)
88 pFFT            = 20*log10(sqrt(2)*abs(myFFT(2:nnyquist))/abs(2*10^-5));
89 vFFT            = 20*log10(sqrt(2)*abs(myFFTv(2:nnyquist))/abs(2*10^-5));
90 freq            = freq(2:nnyquist);
91 phi             = angle(myFFT(1:31));
92
93 % Plot FFT in frequency vs SPL dB
94 figure(4)
95 hold on
```

```
semilogx(freq,pFFT,'marker','s','color',col(n,:));
grid on
title('Frequency Spectrum of Pressure Waveform')
xlabel('Frequency [Hz]')
ylabel('SPL [dB]')
```

```
% Transfer vector analysis (T-Method Set Up)
clear all; clc; close all;
format long

try
  pkg load signal
catch
end

csound  = 343;
gamma   = 1.4;
fs      = 100000; % for experimental datatime
Po      = 101325; % atmospheric pressure

load 'SimulationResultOfPeriodicPulse.mat'

% Get 1 period of the experimental data at Mic_Mouthpiece
% 'mouthpiece' is the experimental data for the trombone obtained ...
    from the microphone mounted to the mouthpiece shank.
Data_1period = mouthpiece;
N            = point2-point1; % length of period
nnyquist     = floor(N/2+1);  % nyquist frequency
freq         = ([1:floor(N_22/2)+1]-1)*(fs/N_22); % frequency
P_experiment = (1/N)*(fft(Data_1period)); % Find fft (complex amplitudes)

%--------------------------------

% 'data_at_inlet' is the simulation data at the inlet
% 'data_at_microphone' is the simulation data sampled at the ...
    microphone position
data = data_at_inlet;

% Get columns from data file
time    = data(:,1);
rho     = data(:,2);
u_rho   = data(:,3);
v_rho   = data(:,4);
w_rho   = data(:,5);
```

```
E       = data(:,6);
u       = u_rho./rho;
v       = v_rho./rho;
w       = w_rho./rho;
p       = (gamma-1).*E-0.5*rho.*((u.*u)+(v.*v)+(w.*w));

%----number of sim samples in 1 expt sample-----
n_fs = (csound/fs)*(length(time)-1)/(time(length(time))-time(1));
disp(['# of sim samples per data acquisition sample: ' num2str(n_fs)])
%-------------------------------------

% Plot raw sim time and pressure in proper units
figure(10)
subplot(2,1,1)
hold on
plot(time,Po*(p-1),'-r');
grid on
xlabel('Sim Time')
ylabel('Pressure [Pa]')
title('Time Pressure Waveform at Inlet Boudary')
subplot(2,1,2)
hold on
plot(time,343*u,'-r');
grid on
xlabel('Sim Time')
ylabel('Velocity [m/s]')
title('Velocity Profile Waveform at Inlet Boudary')

%----resample the sim data to experimental fs------
% we can round index to nearest sim sample, or use fractional interpolate
N_max=floor(length(data)/n_fs) %number of complete periods you will ...
    get in data

for k=1:N_max
    index=1+(k-1)*n_fs;%this will be fractional
    rdata(k,:)=data(round(index),:); %rounding to nearest sim sample
    frac=(index-floor(index));
    datalo=data(floor(index),:);
    datahi=data(floor(index)+1,:);
    rfdata(k,:)=datalo+frac*(datahi-datalo); %interpolated resampling
end
%----------------------nearest sample resampling-----------------
time    = rdata(:,1);
rho     = rdata(:,2);
u_rho   = rdata(:,3);
```

```
v_rho    = rdata(:,4);
w_rho    = rdata(:,5);
E        = rdata(:,6);
u        = u_rho./rho;
v        = v_rho./rho;
w        = w_rho./rho;
p        = (gamma-1).*E-0.5*rho.*((u.*u)+(v.*v)+(w.*w));

% Plot resampled sim time and pressure in proper units
% repeat interval is about 432 samples
figure(20)
subplot(2,1,1)
hold on
plot(time,Po*(p-1),'-r');
grid on
xlabel('Sim Time')
ylabel('Pressure [Pa]')
title('Time Pressure Waveform at Inlet Boudary')
subplot(2,1,2)
hold on
plot(time,343*u,'-r');
grid on
xlabel('Sim Time')
ylabel('Velocity [m/s]')
title('Velocity Profile Waveform at Inlet Boudary')

%-----------------data using interpolated resampling-----------------
time     = rfdata(:,1);
rho      = rfdata(:,2);
u_rho    = rfdata(:,3);
v_rho    = rfdata(:,4);
w_rho    = rfdata(:,5);
E        = rfdata(:,6);
u        = u_rho./rho;
v        = v_rho./rho;
w        = w_rho./rho;
p        = (gamma-1).*E-0.5*rho.*((u.*u)+(v.*v)+(w.*w));
simvelocity = csound*u;

% Plot resampled sim time and pressure in proper units
figure(30)
subplot(2,1,1)
hold on
plot(time,Po*(p-1),'-r');
grid on
```

```
126 xlabel('Sim Time')
127 ylabel('Pressure [Pa]')
128 title('Time Pressure Waveform at Inlet Boudary')
129 subplot(2,1,2)
130 hold on
131 plot(time,csound*u,'-r');
132 grid on
133 xlabel('Sim Time')
134 ylabel('Velocity [m/s]')
135 title('Velocity Profile Waveform at Inlet Boudary')
136
137 %-------------------large plot of inlet velocity------------------
138 figure(35)
139 hold on
140 plot(343*u,'-r');
141 grid on
142 xlabel('10usec samples')
143 ylabel('Pressure [Pa]')
144 title('Time Pressure Waveform at Inlet Boundary')
145
146 %---------------------------get sim repeat length----------------------
147 % repeat length is from sample 3 to 434, 432 samples, so N=431
148 %-----------now sim at microphone position----------
149 % 'data_at_microphone' is the simulation data sampled at the ...
      microphone position
150 data = data_at_microphone;
151
152 %Get columns from data file
153 gamma   = 1.4;
154 time    = data(:,1);
155 rho     = data(:,2);
156 u_rho   = data(:,3);
157 v_rho   = data(:,4);
158 w_rho   = data(:,5);
159 E       = data(:,6);
160 u       = u_rho./rho;
161 v       = v_rho./rho;
162 w       = w_rho./rho;
163 p       = (gamma-1).*E-0.5*rho.*((u.*u)+(v.*v)+(w.*w));
164
165 %---------- Plot resampled sim time and pressure in proper units
166 figure(100)
167 subplot(2,1,1)
168 hold on
169 plot(time,Po*(p-1),'-r');
```

```
170 grid on
171 xlabel('Sim Time')
172 ylabel('Pressure [Pa]')
173 title('Time Pressure Waveform at Inlet Boudary')
174 subplot(2,1,2)
175 hold on
176 plot(time,csound*u,'-r');
177 grid on
178 xlabel('Sim Time')
179 ylabel('Velocity [m/s]')
180 title('Velocity Profile Waveform at Inlet Boudary')
181
182 %-----resample the sim data to experimental fs-----
183 % we can round index to nearest sim sample, or use fractional interpolate
184 % N_max=floor(length(data)/n_fs);
185
186 for k=1:N_max
187     index=1+(k-1)*n_fs; %this will be fractional
188     rdata(k,:)=data(round(index),:); %rounding to nearest sim sample
189     frac=(index-floor(index));
190     datalo=data(floor(index),:);
191     datahi=data(floor(index)+1,:);
192     rfdata(k,:)=datalo+frac*(datahi-datalo); %interpolated resampling ...
            (fractional)
193 end
194
195 %---------------------------------
196 time    = rfdata(:,1);
197 rho     = rfdata(:,2);
198 u_rho   = rfdata(:,3);
199 v_rho   = rfdata(:,4);
200 w_rho   = rfdata(:,5);
201 E       = rfdata(:,6);
202 u       = u_rho./rho;
203 v       = v_rho./rho;
204 w       = w_rho./rho;
205 p       = (gamma-1).*E-0.5*rho.*((u.*u)+(v.*v)+(w.*w));
206
207 simpressure = Po*(p-1);
208 simVelocityMic = csound*u;
209
210 % Plot raw sim time and pressure in proper units
211
212 figure(120)
213 subplot(2,1,1)
```

```
214 hold on
215 plot(time,Po*(p-1),'-r');
216 grid on
217 xlabel('Sim Time')
218 ylabel('Pressure [Pa]')
219 title('Time Pressure Waveform at Microphone')
220 subplot(2,1,2)
221 hold on
222 plot(time,343*u,'-r');
223 grid on
224 xlabel('Sim Time')
225 ylabel('Velocity [m/s]')
226 title('Velocity Profile Waveform at Microphone')
227
228 %repeat interval is about 432 samples
229 N=431; % see near line 159
230 startn=3858; % manually find in sim
231
232 simpressperiod=simpressure(startn:startn+N-1);
233 simvelperiod=simvelocity(startn:startn+N-1);
234 simvelperiodMic=simVelocityMic(startn:startn+N-1);
235
236 %-----------------plot both sim mic pressure and inlet velocity
237 figure(200)
238 subplot(2,1,1)
239 hold on
240 plot(time,simpressure,'-r');
241 grid on
242 xlabel('Sim Time')
243 ylabel('Pressure [Pa]')
244 title('Time Pressure Waveform at Microphone')
245 subplot(2,1,2)
246 hold on
247 plot(time,csound*u,'-r');
248 grid on
249 xlabel('Sim Time')
250 ylabel('Velocity [m/s]')
251 title('Velocity Profile Waveform at Inlet')
252
253
254 %-------now for experimental mic data------
255 %Pick the data you want
256 data = mouthpiece;
257 etime=(1e-5:1e-5:1);
258
```

```
%-------------------------------------------------
% Plot mic pressure in Pa
figure(310)
plot(etime,data,'-r');
grid on
xlabel('Time')
ylabel('Pressure [Pa]')
title('Pressure Waveform at Microphone')

figure(320)
plot(data(2894:3310),'-r');
grid on
xlabel('Time sample')
ylabel('Pressure [Pa]')
title('Pressure Waveform at Microphone')
%-----------------------------------
% plot 310 shows repeat occurs from 1 to 417
Nx=416;
% choose data from 2894-3310
p_mic=data(2894:2894+Nx);
% however, the sim data is from 1 to 432, N=431, so we will "bend" ...
    expt for now!

for k=1:N
    index=1+(k-1)*(Nx-1)/(N-1); %this will be fractional
    frac=(index-floor(index));
    datalo=p_mic(floor(index));
    datahi=p_mic(floor(index)+1);
    rfp_mic(k)=datalo+frac*(datahi-datalo); %interpolated resampling
end
rfp_mic=rfp_mic';

%------------------T-analysis-----------------------------
% data has already been selected for 1 period, N=431
time=(0:1/fs:(N-1)/fs);
freq=(0:fs/N:fs*(N-1)/N);

% the transfer vector is defined in the frequency domain
SimPressPeriod=fft(simpressperiod);
SimVelPeriod=fft(simvelperiod);
Rfp_mic=fft(rfp_mic);
T=SimPressPeriod./SimVelPeriod; %defining the transfer vector


figure(400)
```

```
plot(real(T),'r')
hold on
plot(imag(T),'c')
grid on
xlabel('freq bin')
ylabel('T-matrix')
legend('real', 'imag')
title('Linear acoustic transfer vector')


Rfv_mic=Rfp_mic./T; %obtaining the linear projected velocity response
rfv_mic=ifft(Rfv_mic); %back to the time domain

figure(420)
plot(rfv_mic)
grid on
xlabel('time sample')
ylabel('T-vector')
title('Derived inlet velocity')

figure(421) %Janelle added
plot(rfv_mic_JR)
grid on
xlabel('time sample')
ylabel('T_u-vector')
title('Derived inlet pressure')

%------------get analytical expression for u ------------
waveformReconstructionAxi2(Period,rfv_mic,numOfHarmonics);
```

```
function [T, timesum, amplitudeOfWaveform, phaseOfWaveform, ...
    frequencyOfWaveform, harmonics, harmonicsSim] = ...
    waveformReconstructionAxi2(timeEnd, pressure, numOfHarm)

%%%%%%%%%%%%%%%%%%%%%%%%%%%%%%%%%%%%%%%%%%%%%%%%%%%%%%%%
% Inputs:  data        - simulation text file that has been imported
%          mPressure   - pressure obtained from plotDataAxi()
%          numOfHarm   - number of harmonics for waveform
%
% Ouputs:  timesum             - reconstructed waveform as vector
%          amplitudeOfWaveform - amplitude values for each harmonic
%          phaseOfWaveform     - phase values for each harmonic
%          frequencyOfWaveform - frequency values for each harmonic
%          harmonics           - sum of harmonics in proper units
```

```
%          harmonicsSim        - sum of scaled harmonics for sim
%%%%%%%%%%%%%%%%%%%%%%%%%%%%%%%%%%%%%%%%%%%%%%%%%%%%%%%%%%%%

% Set up fs and frequency as a checker
N        = length(pressure);
time     = linspace(0, timeEnd, N);
time     = time';
fs       = 1/(time(2)-time(1));
nnyquist = floor(N/2+1);
freq     = ([1:floor(N/2)+1]-1)*(fs/N);
y1f          = (1/N)*(fft(pressure));
y1i          = N*ifft(y1f);

figure(2);
hold on
plot(freq(2:nnyquist),20*log10(sqrt(2)*abs(y1f(2:nnyquist))/abs(2*10^-5)));
grid on;
title('SPL of waveform to be represented as sum of cosines')
ylabel('SPL [dB]')
xlabel('Frequency [Hz]')

%Now we write the pressure as a sum of harmonics
amplitude       = abs(y1f(1:nnyquist));
amplitudePercent= amplitude/101325;
phi             = angle(y1f(1:nnyquist));
timesum         = zeros(N,1);  % Initialize time array
timesum(1:N)    = amplitude(1);  % DC into array

% Harmonics excluding DC, which has a factor of 1, not 2.
% start from 2 for velocity
for k=2:1:numOfHarm+1
timesum = timesum + 2*amplitude(k)*cos(2*pi*freq(k)*time + phi(k));
       amplitudeOfWaveform(k) =  amplitude(k);
       phaseOfWaveform(k) =  phi(k);
       frequencyOfWaveform(k) = freq(k);
    end

amplitudeOfWaveform = amplitudeOfWaveform(1:numOfHarm+1 )';
phaseOfWaveform = phaseOfWaveform(1:numOfHarm+1)';
frequencyOfWaveform = frequencyOfWaveform(1:numOfHarm+1 )';

for i=1:1:numOfHarm %comsol version
    a = strcat('2*',num2str(amplitudeOfWaveform(i), ...
        15),'*cos(2*pi*t*',num2str(frequencyOfWaveform(i), ...
        15),'[Hz]+',num2str(phaseOfWaveform(i), 15),')+');
```

```
56          terms(i)= cellstr(a);
57  end
58  harmonics = strjoin(terms)
59
60  for i=1:1:numOfHarm
61     a = strcat('2*',num2str(amplitudeOfWaveform(i)/101325 , ...
           15),'*cos(2*PI*t*',num2str(frequencyOfWaveform(i)/340, ...
           15),'+',num2str(phaseOfWaveform(i), 15),')+');
62     termsS(i)= cellstr(a);
63  end
64  harmonicsSim = strjoin(termsS)
65
66  figure(50)
67  hold on
68  plot(time,smooth(pressure),'b')
69  plot(time,timesum ,'-.r')
70  legend('original',sprintf('%d harmonics', numOfHarm))
71  title('Number of Harmonics Needed to Reconstruct Note')
72  ylabel('Pressure [Pa] ')
73  xlabel('Time [s]')
74
75  % Calculate total SPL
76  DC_power_correction = -3*amplitude(1)^2; % removes overcal in sum()
77  harmonic_power = sum(2*amplitude.^2);
78  total_SPL = 10*log10((DC_power_correction+harmonic_power)/4E-10);
79
80  end
```